DEVELOPMENT OF MESHFREE METHODS FOR THREE-DIMENSIONAL AND ADPATIVE ANALYSES OF SOLID MECHANICS PROBLEMS

ZHANG GUIYONG

NATIONAL UNIVERSITY OF SINGAPORE

2007

DEVELOPMENT OF MESHFREE METHODS FOR THREE-DIMENSIONAL AND ADAPTIVE ANALYSES OF SOLID MECHANICS PROBLEMS

ZHANG GUIYONG

(B.Eng., DUT, CHINA)

A THESIS SUBMITTED

FOR THE DEGREE OF DOCTOR OF PHILOSOPHY

DEPARTMENT OF MECHANICAL ENGINEERING

NATIONAL UNIVERSITY OF SINGAPORE

2007

Acknowledgements

I would like to express my deepest gratitude and appreciation to my supervisor, Professor Liu Gui-Rong for his dedicated support, invaluable guidance, and continuous encouragement in the duration of the study. His influence on me is far beyond this thesis and will benefit me in my future research work. I am much grateful to my co-supervisor, Dr. Wang Yu-Yong, for his inspirational help and valuable guidance in my research wrok.

I would also like to thank Dr. Gu Yuan-Tong for his helpful discussion, suggestion, recommendations and valuable perspectives. To my friends and colleagues in the ACES research center, Miss Zhang Ying-Yan, Miss Cheng Yuan, Dr. Dai Ke-Yang, Mr. Li Zi-Rui, Dr. Li Wei, Dr. Deng Bin, Mr. Zhou Cheng-En, Dr. Zhao Xin, Mr. Kee Buck Tong Bernard, Mr. Zhang Jian, Mr. Song Cheng-Xiang, Mr. Khin Zaw, Mr. Nguyen Thoi Trung, I would like to thank them for their friendship and help.

To my family, my parents and my elder sister, I appreciate their encouragement and support in the duration of this thesis. With their love, it is possible for me to finish the work smoothly.

I appreciate the National University of Singapore for granting me the research scholarship which makes my study in NUS possible. Many thanks are conveyed to Center for Advanced Computations in Engineering Science (ACES) and Department of Mechanical Engineering, for their material support to every aspect of this work.

Table of contents

Summary

Meshfree methods have been developed and achieved remarkable progress in recent years. These methods have been shown to be effective for different classes of problems. These methods have provided us many numerical techniques and extended our minds in the quest for more effective and robust computational methods.

This thesis focuses on the development of new meshfree methods and the application of these methods for three-dimensional problems and adaptive analysis. The work of the present study can be devided into three parts: the first is to extend the meshfree radial point interpolation method (RPIM) for three-dimensional problems; the second is to develop a stabilized nodal integration scheme for the meshfree RPIM; the third is to develop a linearly conforming point interpolation method (LC-PIM) for both 2D and 3D problems, and to apply it to adaptive analysis.

The RPIM was originally proposed for 2D problems and applied for different types of problems. The first contribution of the thesis is to formulate the RPIM to 3D solid mechanics problems. In the 3D RPIM, basis functions composed of radial basis functions (RBFs) augmented with polynomial terms and a set of nodes in the local support domain of the point of interests have been employed to construct the shape functions. The RPIM shape function possesses the Delta function property and essential boundary conditions can be imposed straightforwardly at nodes. Some 3D numerical cases are studied and effects of the shape parameters are investigated via the numerical results. The results show that the RPIM has a very good performance for the analysis of 3D elastic problems.

To improve the efficiency of the RPIM, a nodal integration scheme based on Taylor expansion is proposed in place of the original Gauss integration. The second part is focusing on developing a nodal integration scheme for the RPIM (NI-RPIM). In this method, RPIM shape function is used and Gakerkin weak form is used for creating discretized system equations, in which a nodal integration scheme is employed for numerical integration. The nodal integration scheme is stabilized by using Taylor's expansion up to the second order. The NI-RPIM can obtain stable numerical results. Compared with the RPIM using Gauss integration, the NI-RPIM achieves higher convergence rate and efficiency; compared with the FEM with linear triangular elements, the NI-RPIM obtains better accuracy and higher efficiency.

To obtain the compatibility and to achieve monotonic convergence in energy norm in the numerical results for the polynomial PIM, a linearly conforming point interpolation method (LC-PIM) is developed in the final part of the thesis. The LC-PIM has been formulated for both 2D and 3D elastic problems and applied to the adaptive analysis. In the LC-PIM, linear polynomial terms are employed for the construction of shape function using point interpolation. The generalized Galerkin weak form is used to discretize the system equations and a stabilized nodal integration scheme with strain smoothing operation is used for numerical integration. The LC-PIM can guarantee the linear exactness and monotonic convergence for the numerical solutions. Furthermore, the LC-PIM possesses a very important property of upper bound on strain energy which is demonstrated with a number of numerical examples. Results of the examples also show that the LC-PIM can obtain better accuracy and higher convergence rate compared with the FEM with linear triangular elements, especially for stress calculation. An adaptive

analysis procedure using the LC-PIM is finally proposed, in which an error estimate based on residual error and a simple refinement scheme have been introduced. Some benchmark problems for adaptive analysis have been studied to demonstrate the validity and effectiveness of the adaptive procedure for the LC-PIM.

In the thesis, the numerical implementation issues and effect of parameters for these methods are described and discussed in detail. A large number of numerical examples are studied using these methods and the results are compared with analytical solutions or those obtained using other numerical methods. Theoretical analysis together with these numerical examples have shown that the meshfree techniques presented in this study are very effective and robust for three-dimensions and adaptive analysis of various solid mechanics problems.

Nomenclature

$\mathbf{a}$	Coefficient vector
A	Area of the domain
$\mathbf{b}$	Body force vector
$\mathbf{B}$	Strain matrix
d_c	Average nodal spacing
d_s	Dimension of the local support domain
$\mathbf{D}$	The stress-strain matrix of isotropic linear elasticity
E	Young's modulus
e_d	Error in displacement norm
e_e	Error in energy norm
$\mathbf{f}$	Force vector
$\mathbf{G}$	Shear modulus
I	Moment of inertia of section
$\mathbf{K}$	Stiffness matrix
$\mathbf{L}$	Matrix of differential operator
$\mathbf{L}_n$	Matrix of unit outward normal
$\mathbf{n}$	Unit outward normal vector
n	Number of nodes in a local support domain
N	Total number of nodes located in the problem domain
$P(\mathbf{x})$	Polynomial basis function

$\mathbf{P}_n$, $\mathbf{P}_m$	Polynomial moment matrix
q	Parameter of MQ radial basis function
r	Distance
$R(\mathbf{x})$	Radial basis function
$\mathbf{R}_q$	Moment matrix of RBFs
$\bar{\mathbf{t}}$	Specified traction vector
$\mathbf{U}$	Displacement vector
$\bar{\mathbf{u}}$	Specified displacement vector
u^h	Approximation of function u
$\widehat{w}$	Smoothing function
$\mathbf{x} = [x \quad y \quad z]^T$	Cartesian coordinates
α_c	Parameter of MQ radial basis function
α_s	Coefficient for local support domain
Γ	Boundary of domain
Γ_t	Natural boundary
Γ_u	Essential boundary
δ	Kronecker delta
$\boldsymbol{\varepsilon}$	Strain vector
$\widetilde{\boldsymbol{\varepsilon}}$	Smoothed strain vector
φ_i	Shape function component
$\boldsymbol{\Phi}$	Shape function vector

v	Poisson ratio
$\boldsymbol{\sigma}$	Stress vector
θ	Rotation angle
Ω	Problem domain
Ω_k	Smoothing domain for node k

List of figures

List of tables

Chapter 1

Introduction

1.1 Overview of meshfree methods

1.1.1 Introduction

In the process of designing an advanced engineering system, engineers must undertake the courses of modeling, simulation, analysis and visualization. Differential equations and boundary conditions are abstract, and often highly approximate, characterizations of physical process in engineering. However, exact solutions to these differential equations are often possible only for problems defined in simple geometrical domains and mostly constrained to linear problems. To solve differential equations governing the engineering processes occurring mostly in practice, many types of numerical methods have been proposed and developed such as the finite difference method (FDM), the finite element method (FEM) and the boundary element method (BEM), etc.

FEM possesses many attractive features and has become one of the most important advances in the field of numerical methods (Zienkiewicz and Taylor, 2000; Liu and Quek, 2003). A salient feature of FEM is that it divides a continuum into a finite number of elements to model the problem. The individual elements are connected together by a topological map called mesh. The common characteristic of the meshes is that each of them has several connecting nodes and there is some information concerning the relation

of nodes. The continuity of field variables within the domain spreads through the adjacent meshes and related nodes. The governing differential equations, whether ordinary differential equations (ODEs) or partial differential equations (PDEs), can be transformed into weak-form formulations on the discretized sub-domains by means of certain principles, such as variational method, minimum potential energy principle or principle of virtual work. Using the properly predefined meshes and the field discretization method, a set of algebraic equations are generated. After assembling the equations of all the meshes and imposing of proper boundary conditions, the system equations governing the problem domain can be formed and thereafter solved. The FEM has been thoroughly developed and is widely used in engineering field due to its versatility for complex geometry and flexibility for many types of problems. Most practical engineering problems related to solids and structures are currently solved using well developed FEM commercial packages.

Despite of the robustness in numerical analysis, there are still some limitations or inconveniences in the FEM (Liu, 2002; Liu and Gu, 2005). For example the data preparation in the course of mesh generation and model conversion from physical model to finite element data is an extremely burdensome and time-consuming task. Another factor may be that the secondary variables such as strains and stresses by the FEM are much less accurate than the primary variables such as displacements, temperature, etc. At the same time, the problems of computational mechanics grow ever more challenging. For instance, in the simulation of manufacturing processes, such as extrusion and modeling, it is necessary to deal with extremely large deformations of the mesh; while in computations of castings the propagation of interfaces between solids and liquids is

crucial. In simulations of failure processes, it is required to model the propagation of cracks with arbitrary and complex paths. In the development of advanced materials, methods which can track the growth of phase boundaries and extensive micro-cracking are required. However, these problems are not well suited to conventional computational methods such as the finite element method.

To overcome these problems, meshfree or meshless methods have been developed and achieved remarkable progress in recent years. Meshfree methods use a set of nodes scattered within the problem domain as well as sets of nodes scattered on the boundaries of the domain to represent the problem domain and its boundaries (Liu, 2002). For most meshfree methods, these sets of scattered nodes do not form a mesh, which means no priori information on the relationship between the nodes is required for at least the interpolation or approximation of the unknown functions of field variables. So far, many meshfree methods have found very good applications and shown great potential to become powerful numerical tools.

1.1.2 Features and properties of meshfree methods

Compared with the traditional FEM, meshfree methods possess some unique features that are summarized as follows (Liu, 2002).

1) The shape function of the FEM relies on the type of the element and hence constrained by the connectivity of the mesh. Most meshfree methods, however, can freely and dynamically choose surrounding nodes to construct the shape functions based on the nature of the problem. The shape functions of meshfree methods change

generally from point to point and it can be constructed during the process of an analysis, which is important in adaptive analysis.

2) The shape function of a meshfree method may or may not satisfy Kronecker delta conditions, depending on the method used. If not, like the MLS-based meshfree methods, special techniques are required to impose the essential boundary conditions (Belytschko et al., 1994a).

3) Some meshfree methods may require background cells that cover the problem domain for the numerical integration of the weak-form formulations over the problem domain, such as the global weak-form methods. Typical methods include the element-free Galerkin method (Belytschko et al., 1994a), the meshfree point interpolation method (Liu and Gu, 2001a; Wang and Liu, 2002a), and so on. Some meshfree methods need local cells, such as the local weak-form methods which include the meshless local Petrov-Galerkin (MLPG) method (Atluri and Zhu, 1998), the local point interpolation method (LPIM) (Liu and Gu, 2001b) and the local radial point interpolation method (LRPIM) (Liu and Gu, 2001c; Liu et al., 2002b). There are also meshfree methods that need no integration, like the strong-form methods which include the smooth particle hydrodynamics (SPH) (Lucky, 1977; Gingold and Monaghan, 1977), the general finite difference method (GFDM) (Girault, 1974), and so on.

4) For most of the meshfree methods, mesh automation and adaptive analysis can be implemented easily, as no predefined connections between the nodes are required. Meshfree methods are suitable for solving problems related to large deformation, crack propagation or elastodynamic for the same reason.

5) Results of meshfree methods can be more accurate than that of the FEM especially for stresses.
6) Meshfree methods are generally more expensive than the FEM due to the complexity in construction of shape functions and imposition of boundary conditions.

1.2 Literature review

The starting point of meshfree methods may be traced to 1970s when Smoothed Particle Hydrodynamics (SPH) was developed. The SPH was used for modeling astrophysical phenomena without boundaries such as exploding stars and dust clouds. Most of earlier research work on SPH was reflected in the publications of Lucy and Monaghan and their coworkers (Lucy, 1977; Gingold and Monaghan, 1977; Monaghan and Lattanzio, 1985; Liberskuy and Petscheck, 1991; Monaghan, 1992). A detailed and systemic description on SPH has been given by Liu and Liu (2003). Rapid development on meshfree methods was from the early 1990s when weak form was used in the formulation. Since then, more and more research efforts were devoted to the study of meshfree methods and a group of meshfree methods have been proposed and developed.

According to the formulation procedures used, meshfree methods can be largely categorized into three major categories (Liu and Gu, 2005): meshfree methods based on strong form of partial differential equations (PDEs); meshfree methods based on Galerkin weak form of PDEs and methods based on both strong form and weak form such as the Meshfree Weak-Strong (MWS) form method (Liu and Gu, 2003b).

1.2.1 Meshfree shape function construction techniques

One of the most important issues in meshfree methods is the construction of shape functions. Before reviewing various meshfree methods, approximation techniques used in meshfree methods will be briefly introduced.

1) SPH approximation

The SPH method uses an integral form of function approximation (Lucy 1977; Gingold and Monaghan, 1977), in which a field function of $u(\mathbf{x})$ at a point $\mathbf{x}$ is approximated using

$$u^h(\mathbf{x}) = \int_{\Omega_\xi} u(\xi)\hat{w}(\mathbf{x}-\xi,h)d\Omega_\xi \tag{1.1}$$

where $\hat{w}$ is called smoothing or weight function, and h is termed the smoothing length in SPH.

Monaghan (1982) gave the five conditions that the smoothing funcion should satisfy. The kernels often used in SPH can be found in the papers of Monaghan (1982, 1992), Belytschko et al. (1996a), and more completely in the book by Liu and Liu (2003). The consistency of SPH approximation function was also discussed in the paper of Belytschko et al. (1996a). They concluded that although the continuous form of SPH has second order consistency, the discrete form of SPH does not ensure the linear consistency. More detailed discussions on some of the recent developments for SPH can be found in the book by Liu and Liu (2003).

2) MLS approximation

The moving least squares (MLS) approximation originated from mathematicians in data fitting and surface construction (Mclain, 1974; Gordon and Wixom, 1978). An excellent description of MLS can be found in the landmark paper by Lancaster and Salkausdas (1981). The MLS approximation is now widely used in meshfree methods for constructing shape functions. Nayroles et al. (1992) used MLS in a meshfree method that was called the diffuse element method (DEM).

The MLS approximation is given as

$$u^h(\mathbf{x}) = \sum_{i=1}^{m} p_i(\mathbf{x}) a_i(\mathbf{x}) = \mathbf{P}^{\mathrm{T}}(\mathbf{x})\mathbf{a}(\mathbf{x}) \tag{1.2}$$

where $\mathbf{P}(\mathbf{x})$ is the basis and is a function of the space coordinates. The coefficients $\mathbf{a}(\mathbf{x})$ in equation (1.2) are also functions of $\mathbf{x}$, which can be obtained at the point $\mathbf{x}$ by minimizing a weighted discrete $\mathbf{L}_2$ norm as

$$J = \sum_{j=1}^{n} \hat{w}(\mathbf{x} - \mathbf{x}_j)\left[\mathbf{P}^{\mathrm{T}}(\mathbf{x}_j)\mathbf{a}(\mathbf{x}) - u_j\right]^2 \tag{1.3}$$

where n is the number of nodes in the support domain of $\mathbf{x}$ for which the weight function $\hat{w}(\mathbf{x} - \mathbf{x}_j) \neq 0$, and u_j is the nodal value of u at $\mathbf{x} = \mathbf{x}_j$.

The major advantage of MLS approximation is that its continuity is mainly related to the continuity of the chosen weight function (Belytschko et al., 1994a; Liu, 2002). In other words, a low order polynomial basis, e.g., a linear basis, may be used to generate higher continuous approximations by choosing an appropriate weight function. The main disadvantages of MLS are the lack of Kronecker delta function property and it is computationally expensive (Belytschko et al., 1996a). Detailed discussions of MLS approximation will be presented in Chapter 2.

3) RKPM approximation

Liu et al. (1995) developed a method that ensures the required degree of consistency in the SPH integral approximation, and named it the reproducing kernel particle method (RKPM). The reproducing property is achieved by adding a correction function to the kernel in Equation (1.1). This correction function is particularly useful in improving the SPH approximation near the boundaries as well as to make it linearly or C^1 consistent. The integral representation of a function with correction function can be given by

$$u^h(\mathbf{x}) = \int_{\Omega_\xi} u(\xi) C(\mathbf{x}, \xi) \tilde{w}(\mathbf{x} - \xi, h) d\Omega_\xi \tag{1.4}$$

where $C(\mathbf{x}, \xi)$ is the correction function.

An example of the correction function in one dimension is

$$C(\mathbf{x}, \xi) = c_1(\mathbf{x}) + c_2(\mathbf{x})(\xi - \mathbf{x}) \tag{1.5}$$

where $c_1(\mathbf{x})$ and $c_2(\mathbf{x})$ are coefficients. The coefficients can be obtained by enforcing the corrected kernel to reproduce the function required (Liu et al., 1995).

4) Partition of unity method

Melenk and Babuska (1996) proposed the following approximation technique which is called the partition of unity finite element method (PUFEM).

$$u^h(\mathbf{x}) = \sum_I \Phi_I^0(\mathbf{x}) \sum_j \beta_{jI} p_j(\mathbf{x}) \tag{1.6}$$

where β_{jI} are the unknowns (several per node) and p_j is the basis which typically will include monomial terms up to a certain degree and possibly some enhancement functions.

Φ^0 is a function that satisfies conditions of partition of unity. It can be constructed from an MLS shape function.

Durarte and Oden (1995) have proposed a slightly more general partition of unity method, called the *hp* method. In *hp* approximation, MLS shape functions of order k are employed instead of the partition of unity functions of PUFEM. The formulation of *hp* approximation is

$$u^h(\mathbf{x}) = \sum_I \Phi_I^k(\mathbf{x}) \left(u_I + \sum_i b_{iI} q_{iI}(\mathbf{x}) \right) \tag{1.7}$$

The functions $q_{iI}(\mathbf{x})$ are either high order monomials or enhancement functions for a node i. A major advantage of this formulation is that it allows the basis q to vary from node to node and thus make *p*-adaptivity easier.

5) Point interpolation method (PIM)

Point interpolation method (PIM) is a meshfree interpolation technique that was originally proposed by Liu and his co-workers (2001a). In the PIM, nodes located locally in a support domain are used to approximate the variable and construct shape functions. The PIM shape functions possess the Kronecker delta function property and hence essential boundary conditions can be applied straightforwardly at nodes (Liu, 2002). Two different types of PIM using the polynomial basis and the radial basis functions (RBF) and related techniques have been developed (Liu and Gu, 2001a; Wang and Liu, 2002a). Details of the PIM will be discussed in Chapter 2.

1.2.2 Meshfree methods based on strong forms

In this thesis, the research work is focused on the meshfree methods which are formulated based on Galerkin weak forms. Hence strong form meshfree methods are only briefed in this section.

To approximate the strong form of a PDE using meshfree methods, the PDE is usually discretized by a specific collocation technique. One of the most famous meshfree methods based on the strong form is the smooth particle hydrodynamics (SPH) (Lucy, 1977; Gingold and Monaghan, 1977). The basic idea of SPH is that the state of a system can be discretized by arbitrarily distributed particles, and then the SPH approximation, Equation (1.1), is used in the strong form of the PDEs of the problem. The earliest applications of SPH were mainly focused on astrophysical problems and fluid dynamics related areas, such as, the simulation of binary stars and stellar collisions (Benz, 1988; Monaghan, 1992), elastic flow (Swegle et al., 1995), gravity currents (Monaghan, 1995), heat transfer (Cleary, 1998), and so on. Recently, the SPH method has been applied for the simulations of high velocity impact (HVI) problems. Libersky and his co-workers have made outstanding contributions in the application of SPH to impact problems (Libersky and Petscheck, 1991; Libersky et al., 1995; Randles and Libersky, 1996).

The main shortcomings of the SPH method include tensile instability, lack of interpolation consistency, zero-energy mode, and difficulty in enforcing essential boundary condition (Liu and Liu, 2003). Some improvements and modifications of the SPH have been developed (Monaghan and Lattanzio, 1985; Swegle et al., 1995; Morris, 1996).

There are some other meshfree methods (particle methods) developed based on the strong forms, such as, the vortex method (Chorin, 1973), the general finite difference method (GFDM) (Girault, 1974, Pavlin and Perrone, 1975, Liszka and Orkisz, 1980, Cheng and Liu, 2002), meshfree collocation method (Kansa, 1990, Zhang et al., 2000), the finite point method (Onate et al., 1996), the least-squares radial point collocation method (LS-RPCM) (Liu and Kee, 2006), and so on.

Meshfree strong form methods generally have some attractive advantages including: simple algorithm, computational efficiency, and no need of background mesh. However, meshfree strong form methods are usually unstable and less accurate, especially for problems with derivative boundary conditions (Liu, 2002).

1.2.3 Meshfree methods based on Galerkin weak forms

Unlike SPH, meshfree methods based on Galerkin weak forms are relatively young. From the early 1990s, more and more research efforts have been devoted to the study of meshfree methods based on Galerkin weak forms. Several landmark papers were published in this period of time. The first one was proposed by Nayroles et al. (1992). They basically rediscovered the MLS interpolant proposed by Lancaster and Salkauskas (1981). Foreseeing its potential use in numerical computations, they named it the diffuse element method (DEM). Belytschko et al. (1994a) published another landmark paper to propose the element free Galerkin (EFG) based on the DEM. After this publication, the meshfree methods based on the Galerkin weak forms had significant advancement. It is reflected by the large number of new meshfree methods proposed. Several reviews

(Belytschko et al., 1996a; Liu et al., 1996; Liu, 2002) are available. Some typical meshfree methods based on Galerkin weak forms will be briefly reviewed in this section.

1) Element free Galerkin (EFG) method

Belytschko et al. (1994a) proposed the element free Galerkin (EFG) method, in which the MLS approximation was used for the first time in the Galerkin procedure to establish the weak form of PDEs. In the EFG method, the problem domain is discretized by properly scattered nodes. The MLS is used to construct shape functions based on only a group of arbitrarily distributed nodes. A background cell is required to evaluate the integrals in the global Gakerkin weak forms.

The EFG method has been reported to be accurate and stable for numerical analysis (Belytschko et al., 1994a; 1996b). The rates of convergence of the EFG method are higher than that of FEM (Belytschko et al., 1994a). In addition, no volumetric locking occurs in the process of computing using EFG (Lu et al., 1994). The irregular arrangement of nodes does not affect the performance of the EFG method (Belytschko et al., 1994a). The EFG method has been rapidly developed after it was proposed. It has been successfully applied to a large variety of problems including two-dimensional and three-dimensional problems of linear and nonlinear materials (Belytschko et al., 1997; Lu et al., 1994; Jun, 1996), the fracture and crack growth problems (Belytschko et al., 1994b; Belytschko et al., 1995a, b; Lu et al., 1995), plate and shell problems (Krysl and Belytschko, 1995; 1996; Liu and Chen, 2001), electromagnetic field problems (Cingoski et al., 1998), and so on. Furthermore, techniques of coupling EFG with FEM have also been developed (Belytschko et al., 1995c; Hegen, 1996). All these applications indicate

that the EFG method is gradually becoming a mature and practical computational approach in the area of computational mechanics.

2) Reproducing Kernel particle method (RKPM)

RKPM was proposed by Liu and his co-workers in 1995 (Liu et al., 1995). The main idea of RKPM is to improve the SPH approximation to satisfy consistency requirements via a correction function. The method produces a smoother shape function and consequently provides higher accuracy of solution for large deformation problems. There are two forms of RKPM: the strong form (Aluru, 2000) and the Galerkin weak form (Liu et al., 1995). The moving least square reproducing kernel method (MLSRKM) (Liu et al., 1997a) was also developed based on RKPM. In MLSRKM, the procedure of constructing MLS interpolation is attained by using the notion of the reproducing kernel formulation to establish a continuous basis function.

RKPM is especially effective in treating nonlinear and large deformation problems (Chen et al., 1996; Chen et al., 1998; Liu and Jun, 1998), inelastic structures (Chen et al., 1997), structural acoustics (Uras et al., 1997), fluid dynamics (Liu et al., 1997b), and so on.

3) Meshfree point interpolation methods

Liu and his co-workers have proposed the meshfree point interpolation methods (PIM) based on the Galerkin weak form. In PIM, the problem domain is presented with distributed nodes and shape functions are constructed using PIM based on a set of nodes located in the support domain. A background cell is needed for numerical integration in

the Galerkin weak forms. Two types of PIMs have been developed by using polynomial basis and radial basis functions (RBFs) as mentioned previously, i.e. polynomial PIM and RPIM.

In the polynomial PIM, the moment matrix can be singular. A matrix triangularization algorithm (MTA) has been proposed to overcome this problem (Liu and Gu, 2003a). However, the polynomial PIM is not very robust for irregular nodal distribution due to the incompatibility nature of PIM shape functions (Liu and Gu, 2005). The RPIM is very stable and robust for arbitrary nodal distributions and has been successfully applied to various types of problems, including 2D and 3D solid mechanics (Wang and Liu, 2000, 2002a, b; Liu and Gu, 2001c; Liu et al., 2005b), inelastic analysis (Dai et al., 2006), problems of smart materials (Liu and Dai, 2002, 2003; Liu et al., 2002a), plate and shell structures (Liu and Tan, 2002; Chen, 2003), material non-linear problems in civil engineering (Wang et al., 2001; 2002).

4) Local meshfree Galerkin methods

Atluri and Zhu (1998) developed a meshfree method called the meshless local Petrov-Galerkin (MLPG) method. In the MLPG, a local quadrature domain is defined around each node for the integration of the local weak form based on the Petrov-Galerkin procedure, in which the trial and test functions can be chosen from different spaces to develop discrete system equations. It makes it possible for the MLPG method to choose test functions purposely to simplify the local integration. Like the EFG, the MLPG also uses the MLS approximation to construct its shape functions.

The MLPG does not need a global mesh for either interpolation or integration (only local integration in local quadrature is required). The implementation procedure of the MLPG is node based, which is as simple as methods based on strong forms yet it possesses as high accuracy as methods based on weak forms. For the simplicity and efficiency, the MLPG has been developed and extended by Atluri's group and other researchers over the years. These extensions and applications include the Laplace equation, Poisson equation and potential flow problem (Atluri and Zhu, 1998), the elasto-static problems (Atluri and Zhu, 2000), 4^{th} order thin beams (Atluri et al., 1999a) and thick beams (Cho et al., 2001), linear fracture problems (Ching and Batra, 2001), fluid mechanics problems (Lin and Atluri, 2001), and so on. The MLPG method was thoroughly assessed by Atluri in his book named "The meshless method (MLPG) for domain & BIE discretizations" which was printed in 2004 (Atluri, 2004).

Liu and his co-workers used the concept of MLPG and developed two meshfree local weak form methods: the local point interpolation method (LPIM) (Liu and Gu, 2001b) and the local radial point interpolation method (LRPIM) (Liu and Gu, 2001c; Liu et al., 2002b), in which polynomial PIM shape functions and RPIM shape functions are used respectively. Since the PIM shape functions possess the Delta function property, essential boundary conditions in the LPIM and the LRPIM can be imposed straightforwardly at nodes. LRPIM is very robust for domains with randomly distributed nodes because of the excellent interpolation stability of RBFs and has been successfully applied to solid mechanics (Liu and Gu, 2001c, 2002; Liu et al., 2002b; Xiao and Mccarthy, 2003a), fluid mechanics (Wu and Liu, 2003), 4^{th} order ODEs for beam structures (Gu and Liu, 2001), microelectronic mechanical system (MEMS) (Li et al., 2004), and so on.

5) Boundary type meshfree methods

Boundary type meshfree methods were developed by combining the boundary integral equation (BIE) with the meshfree techniques. Mukherjee and his co-worker proposed the boundary node method (BNM) (Mukherjee and Mukherjee, 1997; Kothnur et al., 1999). In BNM, the boundary of the problem domain is discrtetized by properly scattered nodes. The BIEs of problems considered are discretized using the MLS approximation based only on a group of arbitrarily distributed boundary points. The BNM has been applied to three dimensional problems of potential theory and elasto-statics (Chati et al., 1999; Chati and Mukherjee, 2000). Very good results were reported. However, because the MLS shape functions lack of delta function properties, it is difficult to accurately satisfy the essential boundary conditions in BNM. This problem actually becomes more serious in BNM because a large number of boundary conditions are required to be satisfied. The method used by Kothnur et al. (1999) imposes boundary conditions doubles the number of system equations. It makes BNM computationally much more expensive than the original one.

Zhu et al. has developed another boundary type meshfree method which is called the local boundary integral equation (LBIE) method (Zhu et al., 1998a). In LBIE, the domain and the boundary of the problem are discretized by properly distributed nodes. For each node, the BIE is locally used to construct system equations of the problem. The LBIE has been successfully used to solve linear and non-linear boundary problems (Zhu et al., 1998a, b; Zhu et al., 1999; Atluri et al., 2000).

By using the PIM and RPIM shape functions in BIEs of PDEs, Liu and Gu have developed two boundary-type meshfree methods: the boundary point interpolation

method (BPIM) (Gu and Liu, 2002) and the boundary radial point interpolation method (BRPIM) (Gu and Liu, 2003). In these two methods, since the shape functions have the Kronecker delta function property, the essential boundary condition can be imposed as easily as in the BEM. So the BPIM and BRPIM are more efficient than the methods using MLS shape functions (Liu and Gu, 2005).

6) Other meshfree Galerkin methods

Beside the meshfree methods mentioned above, there are some other meshfree methods have also been developed, such as, the *hp* cloud method (Armando and Oden, 1995), the partition of unity finite element method (PUFEM) (Melenk and Babuska, 1996; Babuska and Kelenk, 1997), the finite point method (FPM) (Onate et al., 1996), the finite spheres method (De and Bathe, 2000), the point assembly method (PAM) (Liu, 2002), and so on.

1.2.4 Meshfree methods based on combination of weak and strong forms

Liu and Gu (2003b) have developed a meshfree method called meshfree weak-strong (MWS) form method, which is formulated based on the combination of weak form and strong form. The key idea of the MWS method is that both the strong form and local weak form are used for establishing the discretized system equations, but these two forms are used for different group of nodes carrying different equations and conditions (Liu and Gu, 2005). In detail, the local weak form is used for all the nodes that are on or near the boundaries with derivative conditions and the strong form is used for all the other nodes.

A background cell is needed for the numerical integration. The MWS obtains very stable and accurate solutions for PDEs with derivative boundary conditions (Liu and Gu, 2005). It has been successfully applied in solid mechanics (Liu and Gu, 2003b; Gu and Liu, 2005) and fluid mechanics problems (Liu et al., 2004).

1.3 Objectives and significance of the study

This thesis will focus on the development of meshfree methods for three-dimensional problems, the formation of the nodal integration scheme and the application of meshfree methods in adaptive analysis. Major works reported in this thesis are as follows.

1) Extend the meshfree radial point interpolation method (RPIM) to three-dimensions and discuss the effect of the shape parameters;
2) Develop a stabilized nodal integration scheme for meshfree radial point interpolation method (RPIM), which is based on Taylor series extension of the integrands;
3) Develop a linearly conforming point interpolation method (LC-PIM), which can guarantee linear exactness and monotonic convergence in energy norm for the numerical solutions and possess the important property of upper bound on strain energy;
4) Extend the linearly conforming point interpolation method (LC-PIM) to three-dimensions;
5) Develop a suitable adaptive procedure and perform an adaptive analysis using the linearly conforming point interpolation method (LC-PIM).

These works will be thoroughly discussed in the following chapters.

1.4 Organization of the thesis

The thesis consists of eight chapters and the contents of each chapter are as follows.

In Chapter 1, an overview of meshfree methods is first presented. A literature review of different types of meshfree methods is carried out in terms of the approximation techniques, and different formulation procedures.

In Chapter 2, meshfree interpolation methods, polynomial point interpolation method (polynomial PIM) and radial point interpolation method (RPIM) are introduced, together with the MLS approximation method. The PIMs (polynomial PIM and RPIM) will be used for shape function construction in the meshfree methods developed in the thesis. The formulations of the shape functions will be introduced in detail and the properties of them have also been discussed.

In Chapter 3, meshfree radial point interpolation method (RPIM) is extended for three-dimensional problems. Formulations of the RPIM for three-dimensional problems are developed, effects of parameters are investigated and some 3D numerical examples are studied using the 3D RPIM.

In Chapter 4, a nodal integration technique for meshfree radial point interpolation method is developed (NI-RPIM). Formulations of the nodal integration scheme have been introduced for both 1D and 2D problems. The effect of shape parameters and dimension of the local support domain on the results of NI-RPIM is investigated. A number of numerical examples including an automobile mechanical component are studied using the NI-RPIM.

In Chapter 5, a linearly conforming point interpolation method (LC-PIM) is developed. Formulations of construction of PIM shape functions based on background cells and a

stabilized nodal integration scheme with strain smoothing operation are introduced. The generalized Galerkin weak form for the LC-PIM is then derived. A thorough theoretical study has been conducted. The LC-PIM is proved to be variationally consistent, and possesses the upper bound property on strain energy for elasticity problems. A number of numerical examples are studied to demonstrate the properties of the LC-PIM.

In Chapter 6, the linearly conforming point interpolation method (LC-PIM) is formulated for three-dimensional problems. The stabilized integration scheme with strain smoothing operation is extended for three-dimensions. A standard patch test is first studied to prove the stability of the nodal integration scheme and the convergence property of the LC-PIM for 3D problems. Some 3D numerical examples, including a riser connector which comes from a real offshore project, are analyzed using the 3D LC-PIM.

In Chapter 7, an adaptive analysis procedure using the linearly conforming point interpolation method (LC-PIM) is presented. Formulations of the LC-PIM are first introduced briefly, and a proper error estimate and the associated refinement scheme are introduced for the adaptive analysis using the LC-PIM. Some benchmark problems for adaptive analysis are studied. The numerical results of adaptive procedure are compared with the results of uniform refinement to investigate the validity and efficiency of the adaptive procedure for the LC-PIM.

The final Chapter 8 presents conclusion remarks and recommendations for future research work.

Chapter 2

Point interpolation method (PIM)

2.1 Introduction

The interpolation technique plays a key role in numerical methods. In the traditional finite element method (FEM), the shape functions are created using interpolation techniques based on elements formed by a set of fixed nodes. This type of interpolation is termed as stationary element based interpolation (Liu and Gu, 2005). In meshfree methods, the problem domain is usually represented by field nodes that are, in general, arbitrarily distributed. The field variables at an arbitrary point in the problem domain are mostly approximated using a group of field nodes in a local domain. This type of interpolation is called moving domain based interpolation (Liu and Gu, 2005).

Most meshfree methods developed so far are based on the moving least squares (MLS) approximation. Although MLS method has seen great success in constructing the shape functions for arbitrarily distributed nodes, two techniques associated with it are still not well solved: the first is the difficulty in implementation of the essential boundary conditions for its lacking of delta function property (Belytschko et al., 1994a); another is the complexity in numerical algorithm for computing its shape functions and derivatives (Liu, 2002).

A point interpolation method (PIM) was originally proposed by Liu and his coworkers (Liu and Gu, 1999, 2001a; Wang and Liu, 2002). The PIM obtains the approximation of a

variable by letting the function pass through the nodal values exactly at each scattered node within the local support domain of the interesting point. The PIM shape functions show three main features compared with the MLS-based ones (Liu, 2002). The first is that the PIM shape functions possess the Kronecker delta function property, which allows straightforward imposition of essential boundary conditions at nodes as easily as in the conventional FEM. The second is that the PIM shape function and its derivatives can be developed in a much more efficient and simpler way than in the MLS procedure. The third is that the constructed PIM shape function and its derivatives have a very simple form.

Two types of PIM shape functions have been formulated so far using different forms of basis functions. PIM using polynomial basis functions was originally developed by Liu and Gu (2001a) and it is termed as polynomial PIM. PIM using radial basis functions (RBFs) was developed by Wang and Liu (2000; 2002a) and it is termed as RPIM. The PIM has been established using both Galerkin and Petrov-Galerkin formulations (Liu and Gu, 2001 a, b, c), thus they are accordingly termed as global weak form and local weak form. The PIM has also been formulated in meshfree weak-strong (MWS) form, in which the method is formulated based on the combination of strong and local weak forms (Liu and Gu, 2003a). In the present work, only global weak form PIM is employed.

Formulations of PIMs and properties of the PIM shape functions will be presented in the following sections. In addition, the MLS method will also be briefly introduced.

2.2 Polynomial point interpolation method (Polynomial PIM)

2.2.1 Polynomial PIM formulation

Polynomials have been used as basis functions in the interpolation to create shape functions in many numerical methods, such as the FEM. In the FEM, however, the interpolation is based on elements that are perfectly (no gap and overlapping) connected. In the polynomial PIM, the interpolation is based on a small set of nodes in a local support domain that can overlap with other support domains.

$$u^h(\mathbf{x}) = \sum_{i=1}^{n} p_i(\mathbf{x}) a_i = \mathbf{p}^T(\mathbf{x})\mathbf{a} \tag{2.1}$$

where $p_i(\mathbf{x})$ is the basis function of monomials in the space coordinates $\mathbf{x} = [x, y]^T$, n is the number of polynomial terms, and a_i is the corresponding coefficient yet to be determined. The polynomial basis $p_i(\mathbf{x})$ is usually built utilizing the Pascal's triangle (as shown in Figure 2.1), and a complete basis is preferred because of the requirement of consistency. The complete polynomial basis of order 1 and 2 can be written in the following forms.

$$\begin{aligned} &\mathbf{p}^{\mathrm{T}}(\mathbf{x}) = \{1 \quad x \quad y\} && \text{Basis of complete } 1^{\text{st}} \text{ order} \\ &\mathbf{p}^{\mathrm{T}}(\mathbf{x}) = \{1 \quad x \quad y \quad xy \quad x^2 \quad y^2\} && \text{Basis of complete } 2^{\text{nd}} \text{ order} \end{aligned} \tag{2.2}$$

In the PIM, a local support domain containing of n field nodes is formed for the point of interest $\mathbf{x}$ (Liu, 2002), and in which, a circle or rectangle will be usually used as the shape of the local support domain (as shown in Figure 2.2). The coefficients a_i in

Equation (2.1) can then be determined by enforcing $u(\mathbf{x})$ to be the values of field variables at these n nodes. Leading to the following n equations:

$$\begin{cases} u(x_1,y_1) = a_1 + a_2x_1 + a_3y_1 + a_4x_1y_1 + ... + a_n p_n(\mathbf{x}_1) \\ u(x_2,y_2) = a_1 + a_2x_2 + a_3y_2 + a_4x_2y_2 + ... + a_n p_n(\mathbf{x}_2) \\ \vdots \\ u(x_n,y_n) = a_1 + a_2x_n + a_3y_n + a_4x_ny_n + ... + a_n p_n(\mathbf{x}_n) \end{cases} \tag{2.3}$$

In matrix form, it can be written as

$$\mathbf{U}_s = \mathbf{P}_n\mathbf{a} \tag{2.4}$$

where $\mathbf{U}_s$ is the vector of nodal values of field variables,

$$\mathbf{U}_s = \{u_1 \quad u_2 \quad u_3 \quad ... \quad u_n\}^{\mathrm{T}} \tag{2.5}$$

$\mathbf{a}$ is the vector of unknown coefficients,

$$\mathbf{a} = \{a_1 \quad a_2 \quad a_3 \quad ... \quad a_n\}^{\mathrm{T}} \tag{2.6}$$

$\mathbf{P}_n$ is the polynomial moment matrix.

$$\mathbf{P}_n = \begin{bmatrix} 1 & x_1 & y_1 & x_1y_1 & \dots & p_n(\mathbf{x}_1) \\ 1 & x_2 & y_2 & x_2y_2 & \dots & p_n(\mathbf{x}_2) \\ 1 & x_3 & y_3 & x_3y_3 & \dots & p_n(\mathbf{x}_3) \\ \vdots & \vdots & \vdots & \vdots & \ddots & \vdots \\ 1 & x_n & y_n & x_ny_n & \dots & p_n(\mathbf{x}_n) \end{bmatrix} \tag{2.7}$$

Assuming the existence of $\mathbf{P}_n^{-1}$, a unique solution for $\mathbf{a}$ can be obtained as

$$\mathbf{a} = \mathbf{P}_n^{-1}\mathbf{U}_s \tag{2.8}$$

Substituting Equation (2.8) back into Equation (2.1) yields

$$u^h(\mathbf{x}) = \mathbf{P}^{\mathrm{T}}(\mathbf{x})\mathbf{P}_n^{-1}\mathbf{U}_s = \sum_{i=1}^{n}\varphi_i u_i = \mathbf{\Phi}^{\mathrm{T}}(\mathbf{x})\mathbf{U}_s \tag{2.9}$$

where $\mathbf{\Phi}(\mathbf{x})$ is the vector of PIM shape functions:

$$\mathbf{\Phi}^{\mathrm{T}}(\mathbf{x}) = \{\varphi_1(\mathbf{x}) \quad \varphi_2(\mathbf{x}) \quad \dots \quad \varphi_n(\mathbf{x})\} \tag{2.10}$$

The derivatives of the shape functions can be easily obtained because the PIM shape function is of polynomial form. The l^{th} derivatives of PIM shape functions can be written as

$$\mathbf{\Phi}^{(l)}(\mathbf{x}) = \left\{\varphi_1^{(l)}(\mathbf{x}) \quad \varphi_2^{(l)}(\mathbf{x}) \quad \dots \quad \varphi_n^{l}(\mathbf{x})\right\}^{\mathrm{T}} = \frac{\partial^l \mathbf{P}^{\mathrm{T}}(\mathbf{x})}{\partial \mathbf{x}^l}\cdot\mathbf{P}_n^{-1} \tag{2.11}$$

2.2.2 Properties of polynomial PIM shape functions

1) Consistency

The consistency of the polynomial PIM shape function depends on the complete orders of the monomial used in Equation (2.1), and hence on number of nodes included in the support domain. For example, if the complete order of the monomials is n, the shape function will possess C^n consistency (Liu, 2002).

To make it clear, a field function is expressed as the linear combination of the first k^{th} monomials in the Pascal triangle:

$$f(\mathbf{x}) = \sum_{i=1}^{k} p_i(\mathbf{x})b_i \qquad k \le n \tag{2.12}$$

Such a function can also be written using Equation (2.1) by employing all the n basis terms as

$$f(\mathbf{x}) = \sum_{i=1}^{n} p_i(\mathbf{x}) b_i = \mathbf{P}^{\mathrm{T}}(\mathbf{x})\mathbf{b} \tag{2.13}$$

where $\mathbf{b}^{\mathrm{T}} = \begin{bmatrix} b_1 & b_2 & \cdots & b_k & 0 & \cdots & 0 \end{bmatrix}$.

Using the n nodes in the support domain of point $\mathbf{x}$, one can obtain the vector of nodal function value $\mathbf{U}_s$ as

$$\mathbf{U}_s = \begin{Bmatrix} f_1 \\ f_2 \\ \vdots \\ f_k \\ f_{k+1} \\ \vdots \\ f_n \end{Bmatrix} = \begin{bmatrix} p_1(\mathbf{x}_1) & p_2(\mathbf{x}_1) & \cdots & p_k(\mathbf{x}_1) & p_{k+1}(\mathbf{x}_1) & \cdots & p_n(\mathbf{x}_1) \\ p_1(\mathbf{x}_2) & p_2(\mathbf{x}_2) & \cdots & p_k(\mathbf{x}_2) & p_{k+1}(\mathbf{x}_2) & \cdots & p_n(\mathbf{x}_2) \\ \vdots & \vdots & \vdots & \vdots & \vdots & \vdots & \vdots \\ p_1(\mathbf{x}_k) & p_2(\mathbf{x}_k) & \cdots & p_k(\mathbf{x}_k) & p_{k+1}(\mathbf{x}_k) & \cdots & p_n(\mathbf{x}_k) \\ p_1(\mathbf{x}_{k+1}) & p_2(\mathbf{x}_{k+1}) & \cdots & p_k(\mathbf{x}_{k+1}) & p_{k+1}(\mathbf{x}_{k+1}) & \cdots & p_n(\mathbf{x}_{k+1}) \\ \vdots & \vdots & \vdots & \vdots & \vdots & \vdots & \vdots \\ p_1(\mathbf{x}_n) & p_2(\mathbf{x}_n) & \cdots & p_k(\mathbf{x}_n) & p_{k+1}(\mathbf{x}_n) & \cdots & p_n(\mathbf{x}_n) \end{bmatrix} \begin{Bmatrix} b_1 \\ b_2 \\ \vdots \\ b_k \\ b_{k+1} \\ \vdots \\ b_n \end{Bmatrix} \tag{2.14}$$

$$= \mathbf{P}_n \mathbf{b}$$

Substituting the above equation into Equation (2.9), one can get the approximate function value

$$u^h(\mathbf{x}) = \mathbf{P}^{\mathrm{T}}(\mathbf{x})\mathbf{P}_n^{-1}\mathbf{U}_s = \mathbf{P}^{\mathrm{T}}(\mathbf{x})\mathbf{P}_n^{-1}\mathbf{P}_n\mathbf{b} = \mathbf{P}^{\mathrm{T}}(\mathbf{x})\mathbf{b} = \sum_{i=1}^{k} p_i(\mathbf{x}) b_i \tag{2.15}$$

which is exactly the same as that in Equation (2.12). This demonstrates that any field given in Equation (2.12) will be exactly reproduced by the polynomial PIM, as long as the function is included in the basis for interpolating the shape functions. In particular, in order to make polynomial PIM exhibit linear consistency, what one needs to do is to include the constant and linear monomials into the basis functions. Another important feature that can be obtained from the above procedure is that any function appearing in the basis can be reproduced exactly.

2) Delta function property

Polynomial PIM shape functions have the Kronecker delta function property, that is

$$\varphi_i\left(\mathbf{x}=\mathbf{x}_j\right)=\begin{cases}1 & i=j,\quad i,j=1,2,\cdots n\\ 0 & i\neq j,\quad i,j=1,2,\cdots n\end{cases} \tag{2.16}$$

3) Partitions of unity

If the constant is included in the basis, polynomial PIM shape functions is partitions of unity, i.e.

$$\sum_{i=1}^{n}\varphi_i\left(\mathbf{x}\right)=1 \tag{2.17}$$

4) Compatibility

In using the polynomial PIM shape functions, the compatibility in the global domain is not ensured when the local support domain is used, as the field function approximation could be discontinuous when nodes enter or leave the moving support domain (Liu and Gu, 2005). Fortunately, this problem has been successfully resolved in my work by using the nodal integration scheme with strain smoothing technique. It will be presented in detail in Chapter 5.

2.2.3 Techniques to overcome singularity in moment matrix

Although the polynomial PIM possesses many excellent properties, its shape functions may not be retrieved if the singularity of moment matrix $\mathbf{P}_n$ occurs in Equation (2.8). After the selection of nodes and basis functions, the moment matrix is completely determined by the structure of scattered nodes in a predefined coordinates system. This

means that two factors dominate whether the inverse matrix $\mathbf{P}_n^{-1}$ exists or not, i.e., the node distribution and the coordinate system. When using polynomial basis function, it is difficult to guarantee the existence of $\mathbf{P}_n^{-1}$ in all circumstances especially for a group of arbitrarily scattered nodes. A number of methods have been proposed by Liu and his co-workers to deal with the problem of singularity.

The simplest method to obtain a non-singular moment matrix is to move the nodes in the support domain by a small distance randomly in terms of both directions. The method is simple and effective for most situations (Liu and Gu, 2001a). However, there are still chances for the moment matrix to be ill conditioned or to be singular. The coordinate transformation method (Wang et al., 2001) was also proposed to avoid the singular problem. This approach is developed making use of the fact that the singularity of the moment matrix depends on the coordinates system where the moment matrix is formed. The singularity can be avoided by rotating the local coordinate system. This method works for many cases, but does not provide full proof for the problem. A matrix triangularization algorithm (MTA) is proposed by Liu and Gu (2003a). The MTA is very efficient and works well for most of the situations. The employment of radial basis functions in constructing the polynomial PIM shape function is another method (Wang and Liu, 2000, 2002a). This method always works and ensures the existence of the inversion of the moment matrix. The major drawback is that it is computationally more expensive as more nodes are required to obtain accurate results compared to that of the polynomial PIM. This method will be presented in the following section.

In my work, a scheme of nodes selection on the background cell is proposed for the construction of polynomial PIM shape function. The method is very simple and can overcome the singularity problem efficiently. It will be presented in Chapter 5 for details.

2.3 Radial point interpolation method (RPIM)

2.3.1 RPIM formulation

Radial basis functions (RBFs) are useful for function approximation based on arbitrary distributed nodes (Powell, 1992), and RPIM shape functions can be created using RBFs for meshfree methods following a simple procedure given, for example in (Liu, 2002). A field function $u(\mathbf{x})$ is first approximated as follows using RBFs augmented with polynomials in the local support domain of the point of interest.

$$u^h(\mathbf{x}) = \sum_{i=1}^{n} R_i(\mathbf{x}) a_i + \sum_{j=1}^{m} P_j(\mathbf{x}) b_j = \mathbf{R}^T(\mathbf{x})\mathbf{a} + \mathbf{P}^T(\mathbf{x})\mathbf{b} \tag{2.18}$$

where $R_i(\mathbf{x})$ and $P_j(\mathbf{x})$ are radial basis functions and polynomial basis functions respectively, a_i and b_j are corresponding constants, n is the number of field nodes in the local support domain and m is the number of polynomial terms. When $m = 0$, pure RBFs are used. Otherwise, the RBF is augmented with m terms of polynomial basis functions.

There are several types of RBFs (as shown in Table 2.1), and the multi-quadrics (MQ) (Hardy, 1990) is used in the present work. The MQ-RBF is a function of nodal distance r_i defined as follows (Liu, 2002),

$$R_i(\mathbf{x}) = (r_i^2 + (\alpha_c d_c)^2)^q \tag{2.19}$$

where d_c is the average nodal spacing near the point of interest $\mathbf{x}$; α_c and q are two arbitrary real numbers of dimensionless parameters, and

$$r_i = \sqrt{(x - x_i)^2 + (y - y_i)^2} \tag{2.20}$$

To perform the interpolation, a local support domain of the point of interest will be taken and the field values at the nodes in this domain will be used to implement the interpolation. In this work, a circular domain centered at the point of interest is used. The dimension of the local support domain, defined as the radius of the circle, is given by,

$$d_s = \alpha_s d_c \tag{2.21}$$

where α_s is a positive real number of dimensionless size of the local support domain.

For 2D cases, the average nodal spacing is usually defined as follows (Liu, 2002),

$$d_c = \frac{\sqrt{A_s}}{\sqrt{n_{A_s}} - 1} \tag{2.22}$$

where A_s is an estimated area that is covered by the support domain of dimension d_s (the estimate does not have to be very accurate but should be known and a reasonable good estimate), and n_{A_s} is the number of nodes that are covered by the estimated domain with the area of A_s.

Constants a_i and b_j in Equation (2.18) can be determined by enforcing the field function pass through all n field nodes in the local support domain. At the k^{th} point, it has the following form,

$$u^h(x_k, y_k) = \sum_{i=1}^{n} R_i(x_k, y_k) a_i + \sum_{j=1}^{m} p_j(x_k, y_k) b_j \qquad k = 1, 2, \ldots, n \tag{2.23}$$

The matrix form of the above equation can be expressed as

$$\mathbf{U}_s = \mathbf{R}_q \mathbf{a} + \mathbf{P}_m \mathbf{b} \tag{2.24}$$

where $\mathbf{U}_s$ is the vector of function values at the nodes in the local support domain.

$$\mathbf{U}_s = \{u_1 \quad u_2 \quad \ldots \quad u_n\}^T \tag{2.25}$$

$\mathbf{R}_q$ is the moment matrix of RBFs,

$$\mathbf{R}_q = \begin{bmatrix} R_1(r_1) & R_2(r_1) & \ldots & R_n(r_1) \\ R_1(r_2) & R_2(r_2) & \ldots & R_n(r_2) \\ \ldots & \ldots & \ldots & \ldots \\ R_1(r_n) & R_2(r_n) & \ldots & R_n(r_n) \end{bmatrix}_{(n \times n)} \tag{2.26}$$

$\mathbf{P}_m$ is the polynomial moment matrix,

$$\mathbf{P}_m = \begin{bmatrix} 1 & x_1 & y_1 & \ldots & p_m(\mathbf{x}_1) \\ 1 & x_2 & y_2 & \ldots & p_m(\mathbf{x}_2) \\ \ldots & \ldots & \ldots & \ldots & \ldots \\ 1 & x_n & y_n & \ldots & p_m(\mathbf{x}_n) \end{bmatrix}_{(n \times m)} \tag{2.27}$$

$\mathbf{a}$ is the vector of unknown coefficients for RBFs,

$$\mathbf{a}^T = \{a_1 \quad a_2 \quad \ldots \quad a_n\} \tag{2.28}$$

$\mathbf{b}$ is the vector of unknown coefficients for polynomial basis functions,

$$\mathbf{b}^T = \{b_1 \quad b_2 \quad \ldots \quad b_m\} \tag{2.29}$$

To obtain unique solutions of Equation (2.24), the constraint conditions should be applied as follows (Golberg et al., 1999),

$$\sum_{i=1}^{n} p_j(\mathbf{x}_i)a_i = \mathbf{P}_m^T\mathbf{a} = 0, \qquad j = 1,2,...,m \tag{2.30}$$

Combination of Equations (2.24) and (2.30) yields the following equations in the matrix form,

$$\begin{bmatrix} \mathbf{U}_s \\ \mathbf{0} \end{bmatrix} = \begin{bmatrix} \mathbf{R}_q & \mathbf{P}_m \\ \mathbf{P}_m^T & \mathbf{0} \end{bmatrix} \begin{Bmatrix} \mathbf{a} \\ \mathbf{b} \end{Bmatrix} = \mathbf{G}\mathbf{a}_0 \tag{2.31}$$

From Equation (2.24), $\mathbf{a}$ can be expressed as

$$\mathbf{a} = \mathbf{R}_q^{-1}\mathbf{U}_s - \mathbf{R}_q^{-1}\mathbf{P}_m\mathbf{b} \tag{2.32}$$

Substitution of Equaiton (2.32) into (2.30) yields

$$\mathbf{b} = \mathbf{S}_b\mathbf{U}_s \tag{2.33}$$

where

$$\mathbf{S}_b = \left[\mathbf{P}_m^T\mathbf{R}_q^{-1}\mathbf{P}_m\right]^{-1}\mathbf{P}_m^T\mathbf{R}_q^{-1} \tag{2.34}$$

Substituting Equation (2.33) into Equation (2.32), $\mathbf{a}$ can be further expressed as

$$\mathbf{a} = \mathbf{S}_a\mathbf{U}_s \tag{2.35}$$

where

$$\mathbf{S}_a = \mathbf{R}_q^{-1}\left[1 - \mathbf{P}_m\mathbf{S}_b\right] \tag{2.36}$$

Substituting the derived vectors $\mathbf{a}$ and $\mathbf{b}$ into Equation (2.18), the interpolation can be expressed as,

$$u^h(\mathbf{x}) = \left[\mathbf{R}^T(\mathbf{x})\mathbf{S}_a + \mathbf{P}^T(\mathbf{x})\mathbf{S}_b\right]\mathbf{U}_s = \mathbf{\Phi}(\mathbf{x})\mathbf{U}_s \tag{2.37}$$

where the shape function $\mathbf{\Phi}(\mathbf{x})$ is defined as

$$\mathbf{\Phi}(\mathbf{x}) = \{\varphi_1(\mathbf{x}) \quad \varphi_2(\mathbf{x}) \quad ... \quad \varphi_n(\mathbf{x})\} = \mathbf{R}^T(\mathbf{x})\mathbf{S}_a + \mathbf{P}^T(\mathbf{x})\mathbf{S}_b \tag{2.38}$$

The derivatives of $u(\mathbf{x})$ can be easily obtained as,

$$u^h_{,k}(\mathbf{x}) = \mathbf{\Phi}_{,k}(\mathbf{x})\mathbf{U}_s = \left[\mathbf{R}^T_{,k}(\mathbf{x})\mathbf{S}_a + \mathbf{P}^T_{,k}(\mathbf{x})\mathbf{S}_b\right]\mathbf{U}_s \tag{2.39}$$

where k denotes the coordinates x or y. A comma designates a partial differentiation with respect to the indicated spatial coordinate that follows.

Note that $\mathbf{R}_q^{-1}$ usually exists for arbitrarily scattered nodes (Hardy, 1990; Schaback, 1994; Wendland, 1998). Therefore, there is no singularity problem in the RPIM because only a small number of nodes (usually 10~40 for 2D problems) are used in the local support domain (Liu, 2002; Liu and Gu, 2005).

2.3.2 Properties of RPIM shape function

The RPIM shape functions have been found to possess the following properties (Liu, 2002; Liu and Gu, 2005):

1) The RPIM shape functions have the Kronecker delta function properties.
2) The RPIM shape functions are of partition unity.
3) The RPIM shape functions are of compact support as long as they are constructed using nodes in a compact support domain.
4) The RPIM shape functions usually possess higher continuity because of the high continuity of the radial basis function.

5) Mathematicians have proven the moment matrix of RBFs is always invertible, so the RPIM shape functions can completely solve the singularity problem, which occurrs in the polynomial PIM shape functions.

Although the RPIM shape functions successfully resolve the problem of singularity, it still has some disadvantages compared to the polynomial shape function (Liu 2002; Liu and Gu, 2005).

1) The RPIM is usually less accurate compared to the polynomial PIM.
2) Some parameters are required to be determined carefully because they will affect the accuracy and the performance of the RPIM.
3) The RPIM is usually computationally much more expensive than the polynomial PIM because more nodes are required in the approximation procedure.

2.3.3 Implementation issues

1) Augment of polynomial terms in the RBF basis function

In the preceding formulation, if the polynomial terms are not augmented in the basis function, the RPIM shape function is not consistent due to the fact that the RBF cannot produce the polynomial exactly. Adding polynomial basis functions to RBFs for interpolation was proposed by Powell (1992) for function approximation. The idea was extended to the RPIM by Wang and Liu (2001). It was found that adding polynomial terms in the RBF basis functions has the following advantages (Liu, 2002):

- Adding polynomial terms up to the linear order can ensure the C^1 consistency.

- In general, adding polynomial can always improve the accuracy of the results, at least no negative effect has been observed for meshfree weak-form methods.
- Adding polynomial reduces the influence of the shape parameters on the accuracy of the results, and will provide much more freedom in choosing shape parameters.
- Adding polynomial can improve the interpolation stability.

In my work, a linear polynomial is used to augment the RBFs.

2) Values of dimensionless parameters in the RPIM shape function

There are some dimensionless parameters used in the constructing of RPIM shape functions. The values of these parameters should be determined carefully as they affect the performance of the RPIM. Much work has been done on the investigation of the parameters (Wang and Liu, 2001b; Liu, 2002; Liu and Gu, 2005). The following values are recommended for the MQ-RBF, i.e., $\alpha_c = 4.0, q = 1.03$ and $\alpha_s = 3.0$ for a circular support domain.

2.4 Moving least square (MLS) approximation

Moving least square method was originally proposed by mathematicians for data and surface fitting (Mclain, 1974; Gordon and Wixom, 1978; Lancaster and Salkauskas, 1981), which is also termed as local regression. The MLS approximation has two major advantages that make it very popular (Liu, 2002): one is the approximated field function is continuous and smooth in the entire problem domain, and the other is that it is capable

of producing a function with desired order of consistency. In particular, It has at least C^1 continuity and thus is attractive for plates and shells problems (Belytschko et al., 1996a).

MLS approximation is now widely used to construct shape functions for meshfree methods. Nayroles et al. (1992) used MLS method to construct the shape functions in their diffuse element method (DEM). Belytschko et al. (1994) refined and modified the method and named it the element-free Galerkin (EFG) method. Their major findings in EFG are as follows: the EFG method does not seem to exhibit any volumetric locking even when the basis functions are linear; the convergence rate is faster than that of FEM; and a high resolution of localized steep gradients can be achieved.

2.4.1 MLS formulation

In this method, the general displacement of a point of interest $\mathbf{x}$, say $u(\mathbf{x})$, is approximated in the following form

$$u^h(\mathbf{x}) = \sum_{j=1}^{m} p_i(\mathbf{x}) a_i(\mathbf{x}) = \mathbf{P}^T(\mathbf{x})\mathbf{a}(\mathbf{x}) \tag{2.40}$$

where $\mathbf{P}(\mathbf{x})$ is a complete basis of monomials of the lowest order of m. The coefficients $\mathbf{a}(\mathbf{x})$ are functions of $\mathbf{x}$, which can be determined using the function values at a set of nodes that are included in the local support domain of $\mathbf{x}$. A function of weighted residue is constructed using the approximated values of the field function, say at node i

$$u^h(\mathbf{x}_i) = \mathbf{P}^T(\mathbf{x}_i)\mathbf{a}(\mathbf{x}), \quad i = 1,2,\cdots,n \tag{2.41}$$

and

$$J = \sum_{i=1}^{n} \hat{w}(\mathbf{x} - \mathbf{x}_i)\left[\mathbf{P}^{\mathrm{T}}(\mathbf{x}_i)\mathbf{a}(\mathbf{x}) - u_i\right]^2 \tag{2.42}$$

where n is the number of nodes in the neighborhood of $\mathbf{x}$, which is also called the influence domain of $\mathbf{x}$. $\hat{w}(\mathbf{x} - \mathbf{x}_i)$ is a weight function. u_i is the nodal parameter at node i. Equation (2.42) is a function of weighted residual that is constructed using the approximated values and the nodal parameters of the unknown field function. Because the number of nodes, n, used in the MLS approximation is usually much larger than that of unknown coefficient, m, the approximated function, u^h, does not pass through the nodal values (as shown in Figure 2.3).

At an arbitrary point $\mathbf{x}$, $\mathbf{a}(\mathbf{x})$ is chosen by minimizing the functional of weighted residual. The minimum condition requires

$$\frac{\partial J}{\partial \mathbf{a}} = 0 \tag{2.43}$$

which leads to the following equation system

$$\mathbf{A}(\mathbf{x})\mathbf{a}(\mathbf{x}) = \mathbf{B}(\mathbf{x})\mathbf{U}_s \tag{2.44}$$

where $\mathbf{U}_s$ is the vector that collects the nodal parameters of field function for all the nodes in the support domain and $\mathbf{A}$ is called the weighted moment matrix. Matrix $\mathbf{A}$ is symmetric whereas matrix $\mathbf{B}$ is non-symmetric and they are in the expressions of

$$\mathbf{A}(\mathbf{x}) = \sum_{i=1}^{n} \hat{w}(\mathbf{x} - \mathbf{x}_i)\mathbf{P}(\mathbf{x}_i)\mathbf{P}^{\mathrm{T}}(\mathbf{x}_i) \tag{2.45}$$

$$\mathbf{B}(\mathbf{x}) = \left[\hat{w}(\mathbf{x} - \mathbf{x}_1)\mathbf{P}(\mathbf{x}_1) \quad \hat{w}(\mathbf{x} - \mathbf{x}_2)\mathbf{P}(\mathbf{x}_2) \quad \cdots \quad \hat{w}(\mathbf{x} - \mathbf{x}_n)\mathbf{P}(\mathbf{x}_n)\right] \tag{2.46}$$

Solving Equation (2.44) and substituting $\mathbf{a}(\mathbf{x})$ into Equation (2.40) leads to

$$u^h(\mathbf{x}) = \sum_{i=1}^{n} \mathbf{P}^{\mathrm{T}}(\mathbf{x})\mathbf{A}^{-1}(\mathbf{x})\mathbf{B}_i(\mathbf{x})u_i = \sum_{i=1}^{n} \varphi_i(\mathbf{x})u_i \tag{2.47}$$

where φ_i is the MLS shape function given by

$$\varphi_i(\mathbf{x}) = \mathbf{P}^{\mathrm{T}}(\mathbf{x})\mathbf{A}^{-1}(\mathbf{x})\mathbf{B}_i(\mathbf{x}) \tag{2.48}$$

Let $\Phi(\mathbf{x}) = [\varphi_1(\mathbf{x}) \quad \varphi_2(\mathbf{x}) \quad \cdots \quad \varphi_n(\mathbf{x})]$ and $\boldsymbol{\gamma}(\mathbf{x}) = \mathbf{A}^{-1}(\mathbf{x})\mathbf{P}(\mathbf{x})$, it arrives

$$\boldsymbol{\Phi}(\mathbf{x}) = \boldsymbol{\gamma}^{\mathrm{T}}(\mathbf{x})\mathbf{B}(\mathbf{x}) \tag{2.49}$$

The partial derivatives of $\boldsymbol{\gamma}(\mathbf{x})$ can be obtained by

$$\mathbf{A}\boldsymbol{\gamma}_{,i} = \mathbf{P}_{,i} - \mathbf{A}_{,i}\boldsymbol{\gamma} \tag{2.50}$$

$$\mathbf{A}\boldsymbol{\gamma}_{,ij} = \mathbf{P}_{,ij} - \left(\mathbf{A}_{,i}\boldsymbol{\gamma}_{,j} + \mathbf{A}_{,j}\boldsymbol{\gamma}_{,i} + \mathbf{A}_{,ij}\boldsymbol{\gamma}\right) \tag{2.51}$$

where the subscripts (i, j) denote the coordinate (x, y), respectively. The partial derivatives of shape function $\boldsymbol{\Phi}$ can be obtained as follows

$$\boldsymbol{\Phi}_{,i} = \boldsymbol{\gamma}_{,i}^{\mathrm{T}}\mathbf{B} + \boldsymbol{\gamma}^{\mathrm{T}}\mathbf{B}_{,i} \tag{2.52}$$

$$\boldsymbol{\Phi}_{,ij} = \boldsymbol{\gamma}_{,ij}^{\mathrm{T}}\mathbf{B} + \boldsymbol{\gamma}_{,i}^{\mathrm{T}}\mathbf{B}_{,j} + \boldsymbol{\gamma}_{,j}^{\mathrm{T}}\mathbf{B}_{,i} + \boldsymbol{\gamma}^{\mathrm{T}}\mathbf{B}_{,ij} \tag{2.53}$$

It should be noted that the MLS shape functions do not satisfy the Kronecker delta criterion, i.e., $\varphi_i(\mathbf{x}_j) \neq \delta_{ij}$ which accordingly results in $u^h(\mathbf{x}_i) \neq u_i$. Hence, they are not values of interpolation, but rather approximations of a function.

2.4.2 Weight function

The weight function plays an important role in the formulation of the MLS method. One is to provide weightings for residues at different nodes within the support domain, and the other is to ensure that nodes leave and enter the influence domain in a gradual and smooth manner when the point of interest moves.

In order to function properly, the weight function needs to satisfy the following conditions (Monaghan, 1982):

1) $\hat{w}(\mathbf{x}-\mathbf{x}_i)>0$ over Ω (Positivity); it is essential to ensure a meaningful representation of physical phenomena, though not required mathematically.

2) $\hat{w}(\mathbf{x}-\mathbf{x}_i)=0$ outside Ω (Compactness); it enables the approximate function to be generated using nodes in a local domain. Hence banded system matrices can be formed.

3) $\int_{\Omega}\hat{w}(\mathbf{x}-\mathbf{x}_i)d\Omega=1$ (Partition of unity); it ensures the zero-order consistency (C^0) of the integral form representation of the continuous function.

4) $\hat{w}$ is a monotonically decreasing function (Decay); it ensures that nodes nearer the considered point have greater effect on it than those farther form it in the same local support domain.

5) $\hat{w}(s,h)\to\delta(s)$ as $h\to 0$ (Dirac delta function behavior). Actually, if a function satisfies the four conditions mentioned above, it will naturally satisfy this condition. In fact, the smoothing length h never goes to zero in practical computations.

The exponential function and spline functions are often used as weight function in practice. Among them, the most commonly used weight functions are listed below.

W1: The cubic spline weight function

$$\hat{w}(\mathbf{x}-\mathbf{x}_i)=\begin{cases} 2/3-4\bar{r}_i^2+4\bar{r}_i^3 & (\bar{r}_i\le 0.5) \\ 4/3-4\bar{r}_i+4\bar{r}_i^2-4/3\bar{r}_i^3 & (0.5<\bar{r}_i\le 1) \\ 0 & (\bar{r}_i>1) \end{cases} \tag{2.54}$$

W2: The quartic spline weight function

$$\hat{w}(\mathbf{x}-\mathbf{x}_i)=\begin{cases} 1-6\bar{r}_i^2+8\bar{r}_i^3-3\bar{r}_i^4 & \bar{r}_i\le 1 \\ 0 & \bar{r}_i>1 \end{cases} \tag{2.55}$$

W3: The exponential weight function

$$\hat{w}(\mathbf{x}-\mathbf{x}_i)=\begin{cases} e^{-\left(\bar{r}_i^2/\alpha\right)^2} & \bar{r}_i\le 1 \\ 0 & \bar{r}_i>1 \end{cases} \tag{2.56}$$

where α is a constant of shape parameter, and

$$\bar{r}_i=\frac{d_i}{r_w}=\frac{\left|\mathbf{x}-\mathbf{x}_i\right|}{r_w} \tag{2.57}$$

in which $d_i=\left|\mathbf{x}-\mathbf{x}_i\right|$ is the distance from node $\mathbf{x}_i$ to the sampling point $\mathbf{x}$, and r_w is the size of the support domain for the weight function.

2.4.3 Properties of MLS shape functions

1) Consistency

By the definition, the consistency of the meshfree shape functions is the capability of shape functions to reproduce the complete order of polynomial (Liu, 2002). The consistency of MLS approximation depends on the complete order of the monomial

employed in the polynomial basis if the complete order of monomial is k, the shape function will possess C^k consistency (Krongauz and Belytschko, 1996; Liu, 2002).

2) Partitions of unity

If the constant is included in the basis, the MLS shape function is of partitions of unity.

3) Lack of Kronecker delta function property

The MLS approximation is obtained by a special least squares method. The function obtained by the MLS is a smooth curve (or surface) and it does not pass through the nodal values (as shown in Figure 2.3). Therefore, the MLS shape functions do not, in general, satisfy the Kronecker delta condition.

Table 2.1 Radial Basis Functions with dimensionless shape parameters

Item	Name	Expression	Shape parameters
1	Multiquadrics (MQ)	$R_i(\mathbf{x}) = (r_i^2 + (\alpha_c d_c)^2)^q$	$\alpha_c \geq 0, q$
2	Gaussian (EXP)	$R_i(\mathbf{x}) = \exp\left[-\alpha_c (\frac{r_i}{d_c})^2\right]$	α_c
3	Thin plate spline (TPS)	$R_i(\mathbf{x}) = r_i^\eta$	η
4	Logarithmic RBF	$R_i(r_i) = r_i^\eta \log r_i$	η

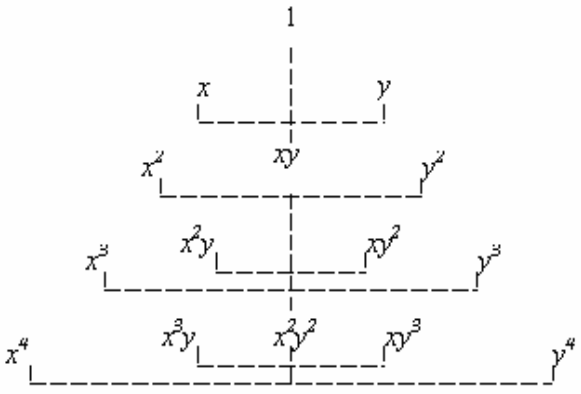

Figure 2.1 The Pascal's triangle.

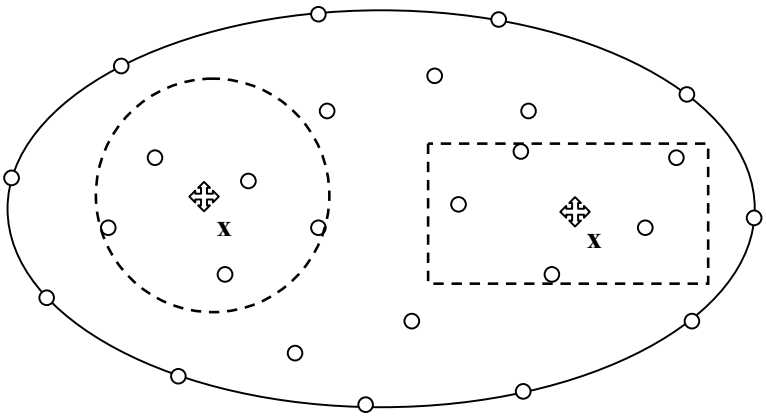

Figure 2.2 Illustration of local support domain

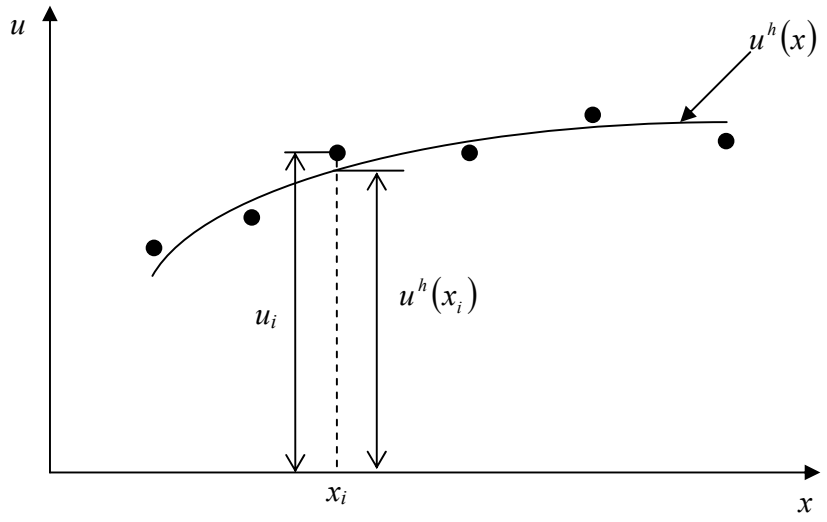

Figure 2.3 The approximation function and the nodal parameters in the MLS approximation

Chapter 3

Meshfree radial point interpolation method (RPIM) for three-dimensional problems

3.1 Introduction

The meshfree radial point interpolation method (RPIM) has been developed for 2D problems and shown very good performance for different types of problems (Liu, 2002). As it has been presented in Chapter 2, the RPIM employs the RBFs as the basis function which is a function of only the distance between the point of interest and a field node used for approximation. So the formulation of the RPIM can be easily extended to three dimensions. In this chapter, the 3D RPIM is formulated based on three dimensional RPIM approximation and global Galerkin weak form. Similar as in two dimensions, a background cell is needed to perform the numerical integration, in which Gauss integration scheme is used.

3.2 Radial point interpolation method (RPIM) in three-dimensions

As presented in Chapter 2, the only variable in the Radial Basis Functions (RBFs) is the distance r, so it is easy to extend RPIM shape function to to three-dimensions. Consider a function $u(\mathbf{x})$ defined in a 3D problem domain Ω. The function can be

approximated in a local support domain of the point of interest **x** with a set of arbitrarily distributed nodes using radial basis function $R_i(\mathbf{x})$ augmented with polynomial basis function $p_j(\mathbf{x})$ (Powell, 1992; Liu, 2002).

$$u^h(\mathbf{x}) = \sum_{i=1}^{n} R_i(\mathbf{x})a_i + \sum_{j=1}^{m} P_j(\mathbf{x})b_i = \mathbf{R}^T(\mathbf{x})\mathbf{a} + \mathbf{P}^T(\mathbf{x})\mathbf{b} \tag{3.1}$$

where n is the number of RBFs and is also identical to the number of nodes in the local support domain of the point of interest **x**, and m is the number of polynomial basis functions. In the following work, a linear polynomial basis is augmented to the RBFs, i.e., $m = 4$ is used in Equation (3.1). Coefficients a_i and b_i are constants yet to be determined.

In the radial basis function $R_i(\mathbf{x})$, the variable is only the distance between the point of interest (x, y, z) and a node at (x_i, y_i, z_i),

$$r = \sqrt{(x-x_i)^2 + (y-y_i)^2 + (z-z_i)^2} \tag{3.2}$$

There are four types of radial basis functions (RBFs) presented in Table 2.1, and the multi-quadrics (MQ) function with real number of parameters is used to construct RPIM shape functions in the present work.

In order to determine the constants a_i and b_j, Equation (3.1) is enforced to be satisfied at these n nodes in the local support domain, which leads to a set of n equations. The matrix form of these equations can be expressed as

$$\mathbf{U}_s = \mathbf{R}_q\mathbf{a} + \mathbf{P}_m\mathbf{b} \tag{3.3}$$

where the vector of function values $\mathbf{U}_s$ is

$$\mathbf{U}_s = \{u_1 \quad u_2 \quad ... \quad u_n\}^T \tag{3.4}$$

The moment matrix of RBFs is

$$\mathbf{R}_q = \begin{bmatrix} R_1(r_1) & R_2(r_1) & ... & R_n(r_1) \\ R_1(r_2) & R_2(r_2) & ... & R_n(r_2) \\ ... & ... & ... & ... \\ R_1(r_n) & R_2(r_n) & ... & R_n(r_n) \end{bmatrix}_{(n\times n)} \tag{3.5}$$

The polynomial moment matrix is

$$\mathbf{P}_m = \begin{bmatrix} 1 & x_1 & y_1 & z_1 & ... & p_m(\mathbf{x}_1) \\ 1 & x_2 & y_2 & z_2 & ... & p_m(\mathbf{x}_2) \\ ... & ... & ... & ... & ... & ... \\ 1 & x_n & y_n & z_n & ... & p_m(\mathbf{x}_n) \end{bmatrix}_{(n\times m)} \tag{3.6}$$

The vector of unknown coefficients for RBFs is

$$\mathbf{a}^T = \{a_1 \quad a_2 \quad ... \quad a_n\} \tag{3.7}$$

The vector of unknown coefficients for polynomial is

$$\mathbf{b}^T = \{b_1 \quad b_2 \quad ... \quad b_m\} \tag{3.8}$$

There are $(n+m)$ unknowns in Equation (3.3), and here m additional equations need to be added. Following m constraint conditions are applied to obtain the additional unknowns (Golberg et al., 1999).

$$\sum_{i=1}^{n} p_j(x_i)a_i = \mathbf{P}_m^T\mathbf{a} = 0, \qquad j = 1,2,...,m \tag{3.9}$$

Combining Equation (3.3) and Equation (3.9) yields the following set of equations in the matrix form,

$$\begin{bmatrix} \mathbf{U}_s \\ \mathbf{0} \end{bmatrix} = \begin{bmatrix} \mathbf{R}_q & \mathbf{P}_m \\ \mathbf{P}_m^T & \mathbf{0} \end{bmatrix} \begin{Bmatrix} \mathbf{a} \\ \mathbf{b} \end{Bmatrix} = \mathbf{G}\mathbf{a}_0 \tag{3.10}$$

where

$$\mathbf{G} = \begin{bmatrix} \mathbf{R}_q & \mathbf{P}_m \\ \mathbf{P}_m^T & 0 \end{bmatrix} \tag{3.11}$$

$$\mathbf{a}_0^T = \{a_1 \quad a_2 \quad \ldots \quad a_n \quad b_1 \quad b_2 \quad \ldots \quad b_m\} \tag{3.12}$$

Because the moment matrix $\mathbf{R}_q$ is symmetric, the matrix $\mathbf{G}$ will also be symmetric. Solving Equation (3.10), the unknowns can be obtained as

$$\mathbf{a} = \mathbf{R}_q^{-1}\mathbf{U}_s - \mathbf{R}_q^{-1}\mathbf{P}_m\mathbf{b} \tag{3.13}$$

Substituting Equation (3.13) into Equation (3.9) leads to

$$\mathbf{b} = \mathbf{S}_b\mathbf{U}_s \tag{3.14}$$

where

$$\mathbf{S}_b = \left[\mathbf{P}_m^T\mathbf{R}_q^{-1}\mathbf{P}_m\right]^{-1}\mathbf{P}_m^T\mathbf{R}_q^{-1} \tag{3.15}$$

Substituting Equation (3.14) into Equation (3.13), it arrives at

$$\mathbf{a} = \mathbf{S}_a\mathbf{U}_s \tag{3.16}$$

where

$$\mathbf{S}_a = \mathbf{R}_q^{-1}\left[1 - \mathbf{P}_m\mathbf{S}_b\right] \tag{3.17}$$

Substituting the derived vectors **a** and **b** into Equation (3.1), the interpolation can be expressed as,

$$u^h(\mathbf{x}) = \left[\mathbf{R}^T(\mathbf{x})\mathbf{S}_a + \mathbf{P}^T(\mathbf{x})\mathbf{S}_b\right]\mathbf{U}_s = \mathbf{\Phi}(\mathbf{x})\mathbf{U}_s \tag{3.18}$$

where the shape function $\mathbf{\Phi}(\mathbf{x})$ is defined as

$$\mathbf{\Phi}(\mathbf{x}) = \{\varphi_1(\mathbf{x}) \quad \varphi_2(\mathbf{x}) \quad \ldots \quad \varphi_n(\mathbf{x})\} = \mathbf{R}^T(\mathbf{x})\mathbf{S}_a + \mathbf{P}^T(\mathbf{x})\mathbf{S}_b \tag{3.19}$$

The derivatives of $u(\mathbf{x})$ can be easily obtained as,

$$u_{,l}(\mathbf{x}) = \mathbf{\Phi}_{,l}(\mathbf{x})\mathbf{U}_s = \left[\mathbf{R}_{,l}^T(\mathbf{x})\mathbf{S}_a + \mathbf{P}_{,l}^T(\mathbf{x})\mathbf{S}_b\right]\mathbf{U}_s \tag{3.20}$$

where l denotes the coordinates x, y or z. A comma designates a partial differentiation with respect to the indicated spatial coordinate that follows.

3.3 Formulations

Consider the static problem defined in the 3D domain Ω boundary by Γ. The standard partial differential equation and boundary conditions for a 3D solid mechanics problem can be given as the follows (Liu, 2002).

Equilibrium equation:

$$\mathbf{L}^T\boldsymbol{\sigma} + \mathbf{b} = 0 \qquad \text{in } \Omega \tag{3.21}$$

Natural boundary condition:

$$\boldsymbol{\sigma}\cdot\mathbf{n} = \bar{\mathbf{t}} \qquad \text{on } \Gamma_t \tag{3.22}$$

Essential boundary condition:

$$\mathbf{u} = \bar{\mathbf{u}} \qquad \text{on } \Gamma_u \tag{3.23}$$

where $\mathbf{L}$ is differential operator; $\boldsymbol{\sigma}^T = \{\sigma_{xx} \quad \sigma_{yy} \quad \sigma_{zz} \quad \tau_{xy} \quad \tau_{yz} \quad \tau_{zx}\}$ is the stress vector, $\mathbf{u}^T = \{u \quad v \quad w\}$ is the displacement vector, $\mathbf{b}^T = \{b_x \quad b_y \quad b_z\}$ is the body force vector, $\bar{\mathbf{t}}$ is the prescribed traction on the natural boundaries, $\bar{\mathbf{u}}$ is the prescribed displacement on the essential boundaries, and $\mathbf{n}$ is the vector of unit outward normal at a point on the neutral boundary.

The unconstrained Galerkin weak form of Equation (3.21) is posed as the follows (see, e.g., Liu, 2002)

$$\int_{\Omega} (\mathbf{L}\delta\mathbf{u})^T (\mathbf{D}\mathbf{L}\mathbf{u}) d\Omega - \int_{\Omega} \delta\mathbf{u}^T \mathbf{b} d\Omega - \int_{\Gamma_t} \delta\mathbf{u}^T \bar{\mathbf{t}} d\Gamma = 0 \tag{3.24}$$

where $\mathbf{D}$ is the matrix of elastic constants. For 3-D isotropic solids, it is in the following form

$$\mathbf{D} = \frac{E(1-\nu)}{(1+\nu)(1-2\nu)} \begin{bmatrix} 1 & & & & & \\ \frac{\nu}{1-\nu} & 1 & & & & \\ \frac{\nu}{1-\nu} & \frac{\nu}{1-\nu} & 1 & & & \\ 0 & 0 & 0 & \frac{1-2\nu}{2(1-\nu)} & & \\ 0 & 0 & 0 & 0 & \frac{1-2\nu}{2(1-\nu)} & \\ 0 & 0 & 0 & 0 & 0 & \frac{1-2\nu}{2(1-\nu)} \end{bmatrix} \tag{3.25}$$

where E and ν are Young's modulus and Poisson's radio respectively.

It should be mentioned that Equation (3.24) is a weak-form defined over the global problem domain Ω. Although theoretically the constrained Galerkin weak form should be used to enforce the global compatibility, it has been found that the unconstrained

Galerkin weak form works well with RPIM shape functions (Liu, 2002). Hence, the unconstrained Galerkin weak form is used in this work.

Substituting Equation (3.18), the approximations of $u(\mathbf{x})$, into Equation (3.24) yields

$$\mathbf{Kd} = \mathbf{f} \tag{3.26}$$

where **K** is the stiffness matrix

$$\mathbf{K}_{ij} = \int_{\Omega} \mathbf{B}_i^T \mathbf{D} \mathbf{B}_j d\Omega \tag{3.27}$$

in which **B** is a strain matrix defined as

$$\mathbf{B}_i = \begin{bmatrix} \varphi_{i,x} & 0 & 0 \\ 0 & \varphi_{i,y} & 0 \\ 0 & 0 & \varphi_{i,z} \\ \varphi_{i,y} & \varphi_{i,x} & 0 \\ 0 & \varphi_{i,z} & \varphi_{i,y} \\ \varphi_{i,z} & 0 & \varphi_{i,x} \end{bmatrix} \tag{3.28}$$

In Equation (3.26), **d** is the vector that collects nodal displacements at all the unconstrained nodes and **f** is the nodal force vector given by

$$\mathbf{f}_i = \int_{\Omega} \varphi_i \mathbf{b} d\Omega + \int_{\Gamma_t} \varphi_i \bar{\mathbf{t}} d\Gamma \tag{3.29}$$

3.4 Implementation issues

3.4.1 Background mesh and numerical integration

To perform a meshfree method that is based on the global Galerkin weak form, such as the EFG method and the present RPIM, a background mesh is required for the purpose of numerical integration. In the following work, both 8-node hexahedron-shaped and 4-node

tetrahedron-shape background mesh are used. For both types of background mesh, the mesh vertices have been used as the field nodes in the problem domain. Although the cells of the integration mesh can be independent of the field nodes, there is no harm in having them linked together (Liu, 2002). Furthermore, mature algorithms available in the public domain can be used for the construction of background cells and field nodes together. Based on the background mesh, Gauss integration scheme is used for numerical integration.

3.4.2 Two models of support domain

In order to perform the interpolation, a local support domain must be taken into account. Two different models of local support domain are considered, i.e., Model-1 and Model-2. Model-1 is simply defined as a spherical domain entered at the point of interest (which is often a quadrature point). Then the field nodes within the sphere are used for constructing shape functions. The dimension of the support domain is naturally defined by the radii of the sphere, which is determined as follows

$$d_s = \alpha_s d_c \tag{3.30}$$

where α_s is dimensionless size of the support domain, and d_c is the nodal spacing near the point of interest **x**. If the nodes are uniformly distributed, d_c is simply the distance between two neighboring nodes. In the case where the nodes are non-uniformly distributed, d_c can be defined as an "average" nodal spacing in the support domain (see, e.g., Liu, 2002).

For Model-2, the number of field nodes in the local support domain will be predefined, i.e., n. Then according to the different distances between the field nodes and the point of interest, the n nodes which are the nearest to the point of interest are used for constructing shape functions.

In the present work, both these two different models of the support domain are examined via the numerical example in the following section.

3.5 Numerical examples

In order to validate the present method, the RPIM is used for displacement and stress analysis of 3D solids. The units are all taken as international standard units through the thesis and the material of the problems studied is linear elastic.

3.5.1 Analysis of shape parameters through function fitting

The solutions obtained using the RPIM may first depend on the quality of its shape functions. Hence, in this section, the interpolation errors using RBF shape functions are examined through fitting a given function. The MQ-RBF is employed for interpolation and linear polynomial terms are included in the following studies.

In the analysis of function fitting, a domain of $(x, y, z) \in [0,1] \times [0,1] \times [0,1]$ is considered and 729 uniformly distributed field nodes with a constant nodal distance $d_c = 0.125$ are used to represent the domain. A total of 512 regularly distributed points of $(x, y, z) \in [0.05,0.95] \times [0.05,0.95] \times [0.05,0.95]$ are used as interpolation points.

Because the linear function in 3D is reproduced exactly when linear polynomial terms are included in basis function, a harmonic function of 3D is considered, i.e.

$$f(x,y,z)=\sin x\cos y\sin z \tag{3.31}$$

The first-order partial derivative with respect to x is

$$f_{,x}(x,y,z)=\cos x\cos y\sin z \tag{3.32}$$

The approximated values of the field function and the first derivative with x for each interpolation point **x** can be obtained using interpolation as the follows,

$$\widetilde{f}(\mathbf{x})=\mathbf{\Phi}(\mathbf{x})\mathbf{F}_s=\sum_{i=1}^{n}\varphi_i f_i \tag{3.33}$$

$$\widetilde{f}_{,x}=\frac{\partial\mathbf{\Phi}(\mathbf{x})}{\partial x}\mathbf{F}_s=\sum_{i=1}^{n}\frac{\partial\varphi_i}{\partial x}f_i \tag{3.34}$$

where φ_i is the RPIM-MQ shape function, and n is the number of field nodes used in the support domain. Vector $\mathbf{F}_s$ collects the true nodal function values for these n field nodes, and f_i is the function value for the i^{th} field node.

The following norms are used as error indicators.

$$e=\frac{1}{N}\sum_{i=1}^{N}\left|\frac{\widetilde{f}_i-f_i}{f_i}\right| \tag{3.35}$$

$$e'=\frac{1}{N}\sum_{i=1}^{N}\left|\frac{\widetilde{f}^{\,i}_{,x}-f^{\,i}_{,x}}{f^{\,i}_{,x}}\right| \tag{3.36}$$

where N is the total number of the interpolation nodes.

The effects of two shape parameters, q and α_c, in the MQ-RBF are first studied. In the process of this study, Model-1 of support domain is used and $\alpha_s = 3.0$ is fixed in the study.

1) Effect of parameter q

In the study of the effect of q, $\alpha_c = 4.0$ is fixed. The average fitting errors e obtained for different values of q are plotted in Figure 3.1. It can be found that a more accurate result can be obtained when the value of q varies between 1 and 3 (but not 1, 2 and 3). When $q > 4.0$, the fitting error is found very large due to the badly conditioned moment matrix. However, if the value of q is identical to 1.0, 2.0, 3.0 and 4.0, the RPIM-MQ will fail due to the singularity of the moment matrix. In addition, if q is too close to 1.0, 2.0 or 3.0, the condition number of interpolation matrix of RPIM will become bigger, the moment matrix will be nearly singular and the results are not stable any more. The preferred value of parameter q is close to 1.0, 2.0 or 3.0, but not equal to these values. Therefore, in using RPIM shape functions, one has to strike a good balance between accuracy and stability (Liu, 2002).

2) Effect of parameter α_c

The effect of parameter α_c on the results of function fitting is shown in Figure 3.2. For comparison, two curves of function fitting errors obtained using $q = 1.03$ and $q = 2.83$ are both plotted in the figure. The value, $q = 1.03$, which is found by Wang and Liu

(2002b), performs the best for most 2D computational problems. The other value, $q = 2.83$, leads to the best result in the previous study of parameter q. It can be found, when $\alpha_c > 3.0$, the value of the fitting error is very small and changes little with respect to either the change of parameter α_c or q.

3) Convergence study

In the convergence study, Model-1 of the support domain is employed, $q = 1.03$ $\alpha_c = 4.0$ $\alpha_s = 3.0$ are fixed. The convergence curves with respect to nodal refinement are plotted in Figure 3.3. Note that h is actually the nodal spacing d_c, which is simply the distance between two neighboring nodes as the fields nodes are regularly and evenly distributed in this function fitting test. It can be found that RPIM has obtained very good convergence rates for fitting both function and its first-order derivative. However, the convergence process of the first-order partial derivative with x is not as stable as the process of the function.

It should be noted here that the interpolation error is only one part of total error in a meshfree method in solving a problem of computational mechanics. The studies of shape parameters presented in this section are only to check the interpolation quality and the reproducibility of using RPIM-MQ shape functions. The accuracy will be also studied in the following sections in the analysis of actual problems of computational mechanics.

3.5.2 A 3D cantilever beam

A 3D cantilever beam as shown in Figure 3.4 is studied to benchmark the present method. The left end of the beam is fixed and the right end is subjected to a parabolically distributed downward traction. The parameters are taken as $P=-1000$, $L=50$, $H=10$, $B=1$, $E=3.0\times10^7$ Pa and $v=0.3$. As the beam is relatively thin, a plane stress problem can be considered to yield the analytical solution (Timoshenko and Goodier, 1970). This analytical solution is used as the reference solution in the study.

The displacement components of the analytical solution are given by

$$u_x=-\frac{Py}{6EI}\left[(6L-3x)x+(2+\nu)(y^2-\frac{H^2}{4})\right] \tag{3.37}$$

$$u_y=\frac{P}{6EI}\left[3\nu y^2(L-x)+(4+5\nu)\frac{H^2x}{4}+(3L-x)x^2\right] \tag{3.38}$$

where the moment of the inertia I of the beam is given by $I=H^3/12$.

The stress components corresponding to above displacements are

$$\sigma_x=-\frac{P(L-x)y}{I} \tag{3.39}$$

$$\sigma_y=0 \tag{3.40}$$

$$\sigma_{xy}=\frac{P}{2I}\left[\frac{H^2}{4}-y^2\right] \tag{3.41}$$

1) Effect of shape parameters and dimension of support domain

In the following studies, the effects of parameters q , α_c and the dimension of the support domain on the displacements results are investigated via the problem of the

cantilever beam. The problem domain is represented by 1122 regularly distributed field nodes, and 500 hexahedron-shaped background cells are used for numerical integration. In each background cell, $4\times4\times4$ Gauss points are employed. The error indicator is defined as the follows

$$e_V = \frac{1}{N}\sum_{i=1}^{N}\left|\frac{V_i^{RPIM} - V_i^{reference}}{V_i^{reference}}\right| \tag{3.42}$$

where V_i denotes the displacement in y direction of the i^{th} node, N is the total number of field nodes and the superscripts *RPIM* and *reference* denote the RPIM and reference solutions respectively.

- Effect of parameter q

In the investigation of parameter q, α_c is fixed at 4.0. Model-1 of the support domain is used and α_s is fixed at 3.0. Errors defined in (3.42) for different values of q are computed and plotted in Figure 3.5. It can be found that when q in the range of $1.0 \sim 3.0$ (but not 1, 2, and 3), the value of error is very small and changes very little with respect to the change of q. The figure also shows that for this particular case, $q = 3.28$ leads to the best result, and, when $q > 3.28$, the error will significantly increase because of the big condition number of the moment matrix.

- Effect of parameter α_c

The effects of α_c is studied for a wide range of $1.0 \sim 10.0$ with Model-1 of the support domain employed and α_s is fixed at 3.0. Errors for different values of α_c are plotted in Figure 3.6. For comparison, two values of parameter q are employed. One value is 1.03, and the other one is 3.28, which has been found to produce the best result in the

previously study. The figure shows that when $\alpha_c > 3.0$, the method can obtain a more accurate and stable result, and the difference between the results, obtained using $q = 1.03$ and $q = 3.28$ respectively, is very little.

- Effect of the dimension of support domain

In the process of this study, $q = 1.03$ and $\alpha_c = 4.0$ are fixed. Two curves obtained using two models of the support domain respectively are plotted in Figure 3.7. Considering that too many nodes in the support domain will increase computational time, the use of $20 \sim 70$ nodes gives a better result for these two models of the support domain. The figure also shows that Model-2 performs better than Model-1. This can be explained as the follows. By using Model-1, fewer nodes will be used in the support domain when the point of interest is located near or at the boundaries. Using Model-2, there will not be such a problem, as a fixed number of nearby nodes are alwayse used.

It should be noted that more nodes are used in a local support domain for approximation compared with FEM, and usually the meshfree RPIM is computationaly more expensive. To improve the efficiency of the method, the skyline technique has been used in programming the RPIM code for three dimensional problems.

In the following studies, $q = 1.03$ and $\alpha_c = 4.0$ are used which have been found perform well in most 2D computational problems that have been investigated so far (Liu, 2002; Wang and Liu, 2002b); Model-2 is employed based on the studies previously.

2) Numerical results of the cantilever beam

In the analysis of the 3D cantilever beam, both a regular nodal distribution and an irregular nodal distribution, shown respectively in Figure 3.8 and Figure 3.9, are employed. For the regular nodal distributed model, there are totally 2223 field nodes and 1344 hexahedron-shaped background integration cells, in each tetrahedron cell, $4\times4\times4$ Gauss points are used to evaluate the stiffness matrix; for the irregular nodal distributed model, 1620 field nodes and 4447 tetrahedron-shaped background integration cells are used, 4 Gauss points are employed in each tetrahedron cell in the process of integration. As Model-2 of support domain is employed, 55 and 52 field nodes are involved in the support domains for regular and irregular nodal distribution respectively.

Figures 3.10~3.12 show the comparisons between the analytical solutions and the RPIM results, in which Figure 3.10 shows the distribution of displacement in y direction along the neutral axis, Figure 3.11 and Figure 3.12 show the distribution of the normal and shear stress along the middle line respectively. All these plots indicate that the results obtained using RPIM in 3D for both regular and irregular nodal distribution models are in good agreement with the reference solutions. Another conclusion is that, the irregularity of nodal distribution has little effect on the result of the RPIM.

3.5.3 Lame problem

The 3D Lame problem consists a hollow sphere with inner radius a and outer radius b and subjected to internal pressure p, as shown in Figure 3.13. For this benchmark problem, the analytical solution is available in polar coordinate system (Timoshenko and Goodier, 1970).

$$u_r = \frac{pa^3 r}{E\left(b^3 - a^3\right)}\left[(1-2\nu)+(1+\nu)\frac{b^3}{2r^3}\right] \tag{3.43}$$

$$\sigma_r = \frac{pa^3\left(b^3 - r^3\right)}{r^3\left(a^3 - b^3\right)} \tag{3.44}$$

$$\sigma_\theta = \frac{pa^3\left(b^3 + 2r^3\right)}{2r^3\left(b^3 - a^3\right)} \tag{3.45}$$

where r is the radius distance from the centroid of the sphere to the point of interest in the sphere.

As the problem is spherically symmetrical, only one-eighth of the sphere is modeled and symmetry conditions are imposed on the three planes of symmetry. The numerical solution of this problem has been calculated using the material parameters $E = 1.0$ Pa, $\nu = 0.3$, geometric parameters $a = 1$, $b = 2$ and internal pressure $p = 1$. Model-2 of support domain is adopted and 45 nodes are used in the local support domain. The problem domain is presented using 729 irregularly distributed nodes. The computed nodal displacements and stresses along the x axis are plotted in Figure 3.14 and Figure 3.15, respectively. It is observed that the RPIM obtains comparable numerical results compared with the analytical ones.

3.5.4 A 3D axletree base

In this example, the displacement analysis of an axletree base is studied using the present RPIM-3D code. As shown in Figure 3.16, the axletree base is symmetric about the $y-z$ plane, subjected to a uniformly distributed force along a line and fixed in the locations of four lower cylindrical holes and the bottom plane. The parameters are taken

as $E = 3.0 \times 10^7$ Pa and $v = 0.3$. The value of the uniformly distributed force is 5000. Numerical results at point K Line 1 and Line 2 (marked in Figure 3.16) will be examined in our study.

First, for the displacement distribution along Line 1, Line 2 and at point K, a reference solution is obtained using FEM software ABAQUS with a very fine mesh of high order elements (ten-node tetrahedron element). Then the displacement results are obtained using the RPIM and FEM (four-node tetrahedron element is employed) respectively using exactly the same distribution of nodes for comparison.

Figure 3.17 and Figure 3.18 show the displacement distribution along Line 1 and Line 2 obtained using the RPIM and the FEM respectively under the same condition (totally 4571 irregular distributed field nodes and 20561 tetrahedron-shaped background cells). It can be found that, the results obtained using the RPIM closely matches the corresponding reference solution and are much closer to the reference solutions than that obtained using FEM using a linear element.

The numerical solution of displacement in x direction of Point K (show in Figure 3.16) is obtained using both the RPIM and linear FEM via different nodal disttributioin. The numerical results are listed in Table 3.1 together with the reference one which is obtained using ABAQUS. It can be found that both the numerical solutions of RPIM and FEM converge to the reference with the increasing of field nodes. But the results of RPIM is closer to the reference one than the FEM, i.e., the RPIM obtains more accurate results compared with the FEM for this problem.

3.6 Remarks

The RPIM was extended to three dimensional problems in this chapter. Effect of parameters has been investigated in detail and some numerical examples of 3D solids have studied using the present method. Base on the study conducted, following conclusions can be drawn:

1) The RPIM shape functions constructed using RBF augmented with polynomial possess the following features in three dimensions.
    - The RPIM shape functions possess the Delta function property, which allows straightforward imposition of essential boundary conditions at nodes.
    - The RPIM shape functions are capable of reproducing what is contained in the basis, which is essential for any numerical method to produce accurate solution.
    - The RPIM shape functions have a good convergence capability. This allows the error of the approximation of function that is sufficiently smooth to approach zero when the nodal spacing is reduced sufficiently small.
2) Based on the study of function fitting and the numerical example, the remarks of the effect of some shape parameters are noted as follows.
    - For parameter q, the value in the range of $1.0 \sim 3.0$ (but not 1, 2, and 3) is recommended for 3D problems, and $q = 1.03$ is a robust choice, which has been found works well for 2D problems.
    - For parameter α_c, when its value is bigger than 3.0, the method can obtain a better result and $\alpha_c = 4.0$ is a robust and consistent choice in the RPIM.

- For the two models of the support domain presented in this chapter, Model-2 performs better for most 3D problems especially when the geometry of the domain is complicated. For Model-1, $\alpha_s = 3.0$ is recommended; for Model-2, $20 \sim 70$ nodes in the local support domain are preferred.

3) The numerical results of some 3D benchmark problem show that the RPIM can obtain very accurate results. The comparison study of the axletree has shown that the RPIM can be more accurate than the linear FEM for this particular problem. However, as more nodes are used in the local support domain for constructing RPIM shape functions, the RPIM is more expensive compared with the FEM.

In a summary, the RPIM is a very stable, robust and reliable numerical method for displacement and stress analysis of three dimensional solids.

Table 3.1 Comparison study on displacement results (u_x) of node K for the axletree base

Number of nodes	RPIM solution		FEM solution		Reference solution
	Numerical value	Relative error (%)	Numerical value	Relative error (%)	
1055	0.68969E-03	10.4380	0.59484E-03	22.7551	0.77007E-03
1936	0.71362E-03	7.3305	0.64067E-03	16.8037	
3009	0.74474E-03	3.2893	0.66332E-03	13.8624	
4108	0.75289E-03	2.2310	0.67795E-03	11.9625	
4571	0.76518E-03	0.6350	0.68951E-03	10.4614	

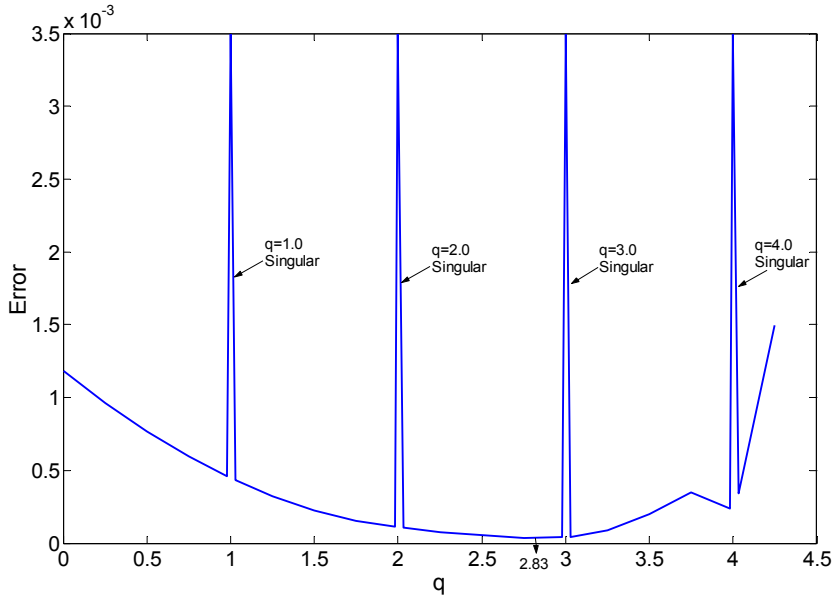

Figure 3.1 Error in function fitting using RPIM shape functions with different q (MQ-RBF augmented with linear polynomials is used with shape parameter $\alpha_c = 4.0$ and Model-1 of the support domain is useed with $\alpha_s = 3.0$).

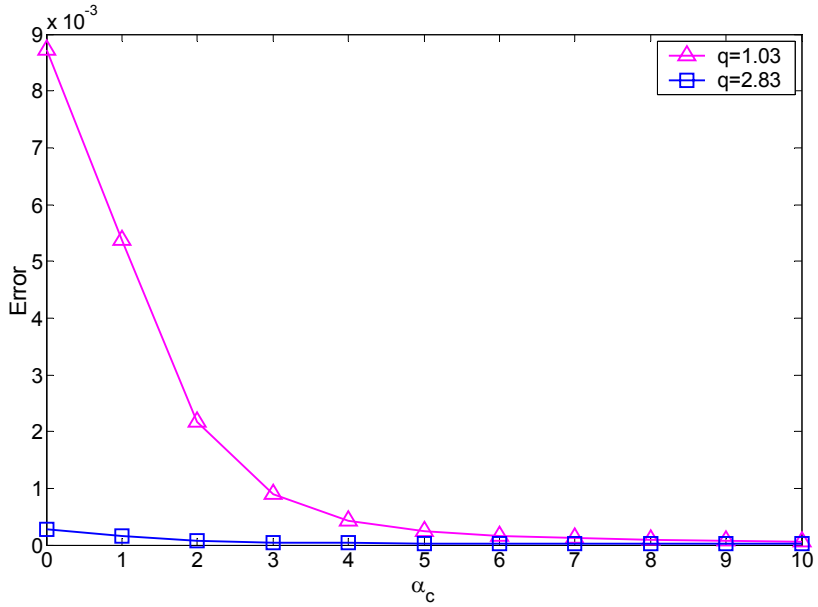

Figure 3.2 Error in function fitting using RPIM with different α_c (MQ-RBF augmented with linear polynomials is used and Model-1 of the support domain is used with $\alpha_s = 3.0$).

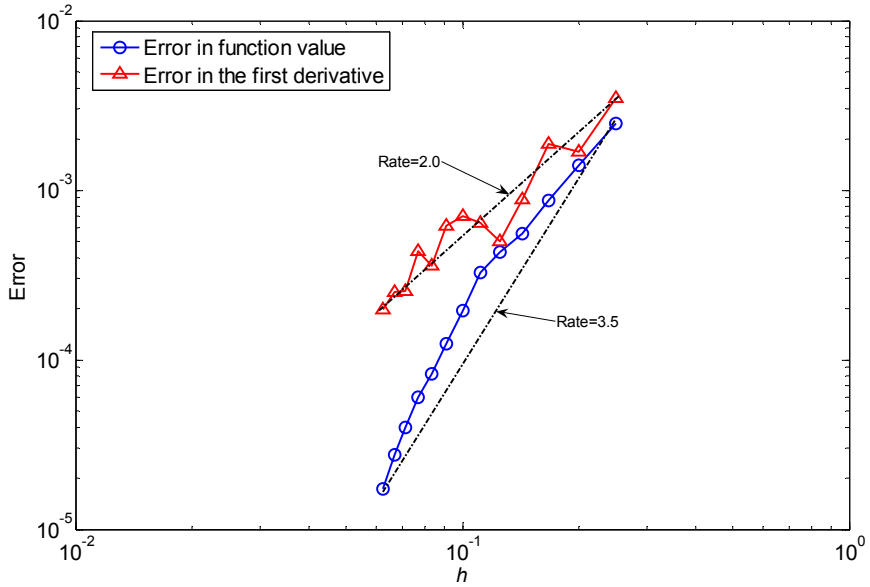

Figure 3.3 Convergence study of RPIM shape functions via function fitting (MQ-RBF augmented with linear polynomials is used with shape parameter: $q = 1.03$ and $\alpha_c = 4.0$; Model-1 of the support domain is used with $\alpha_s = 3.0$).

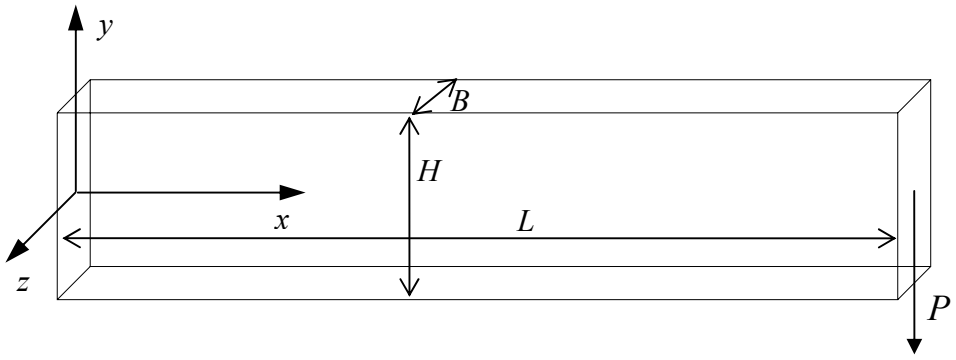

Figure 3.4 A 3D cantilever beam subjected to a parabolic downward traction at the right end

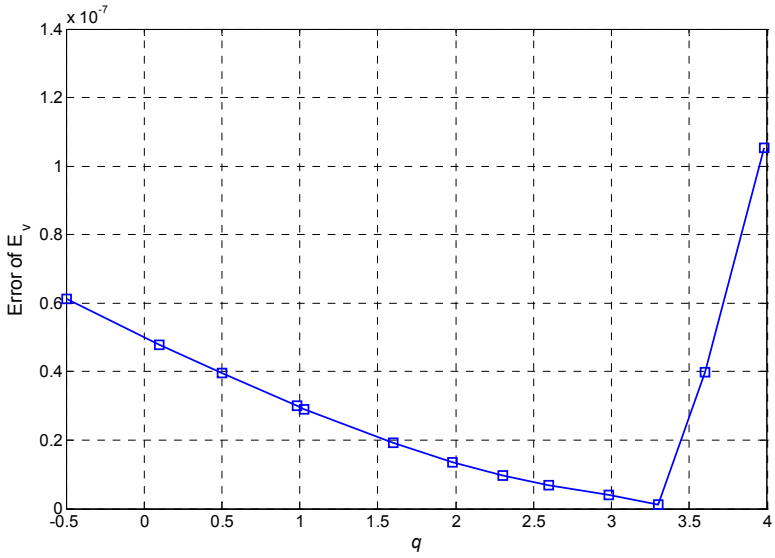

Figure 3.5 Effect of parameter q on the displacement results obtained using RPIM. (Error is defined by Equation (3.41); a total of 1122 regularly distributed field nodes and 500 hexahedron-shaped back ground cells are used; MQ-RBF augmented with linear polynomials is used with shape parameter $\alpha_c = 4.0$ and Model-1 of the support domain is used with $\alpha_s = 3.0$).

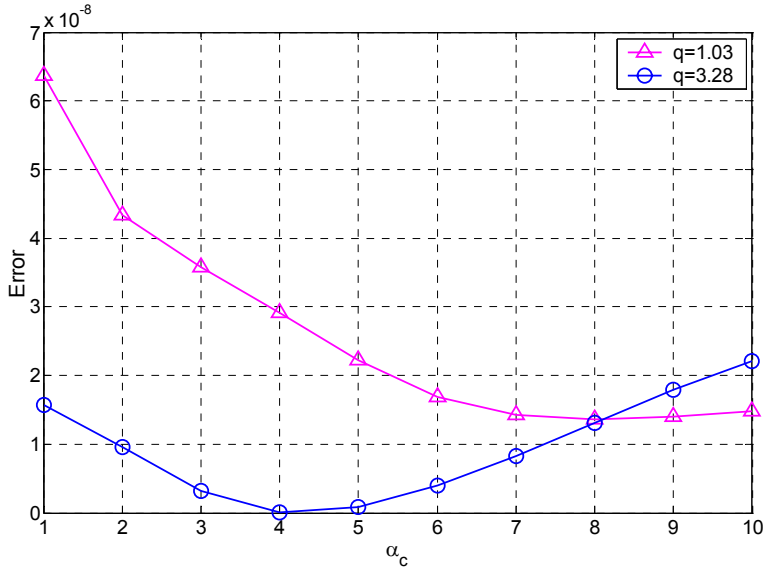

Figure 3.6 Effect of parameter α_c on the displacement results obtained using RPIM. (Error is defined by Equation (3.41); a total of 1122 regularly distributed field nodes and 500 hexahedron-shaped back ground cells are used; MQ-RBF augmented with linear polynomials is used with shape parameter $q = 1.03$ and Model-1 of the support domain is used with $\alpha_s = 3.0$).

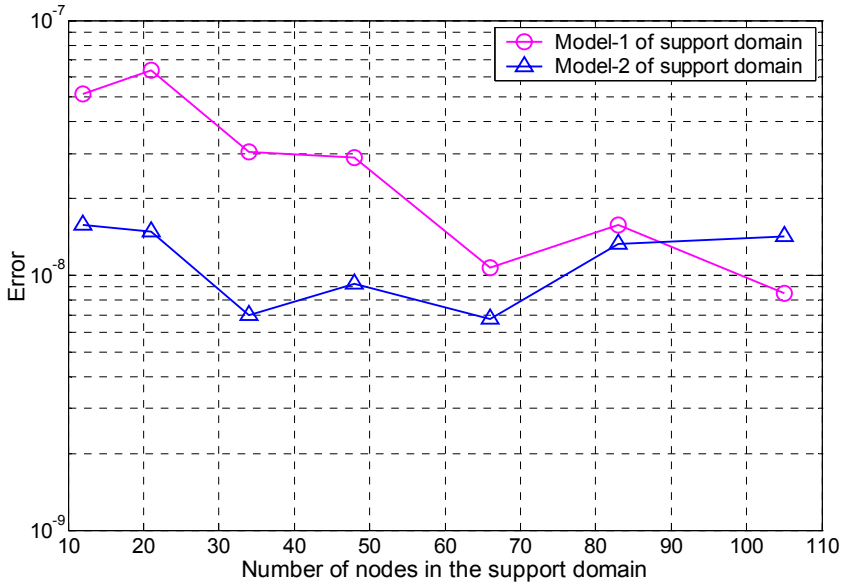

Figure 3.7 Effect of the dimension of the support domain on the RPIM (Error is defined by Equation (3.41); a total 1122 regularly distributed field nodes and 500 hexahedron-shaped back ground cells are used; MQ-RBF augmented with linear polynomials is used with shape parameter $q = 1.03$ and $\alpha_c = 4.0$).

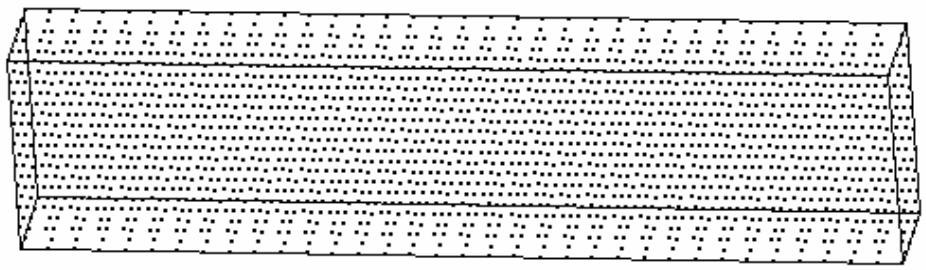

Figure 3.8 Regular nodal distribution for the cantilever (A total of 2223 regular field nodes and 1344 hexahedron-shaped background cells are used)

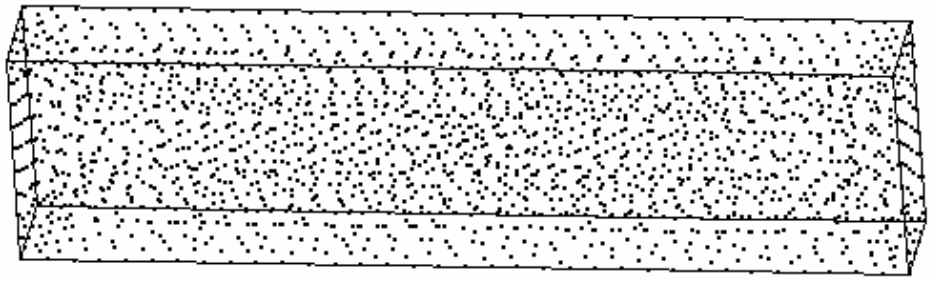

Figure 3.9 Irregular nodal distribution for the cantilever (A total of 1620 irregular field nodes and 4447 tetrahedron-shaped background cells are used)

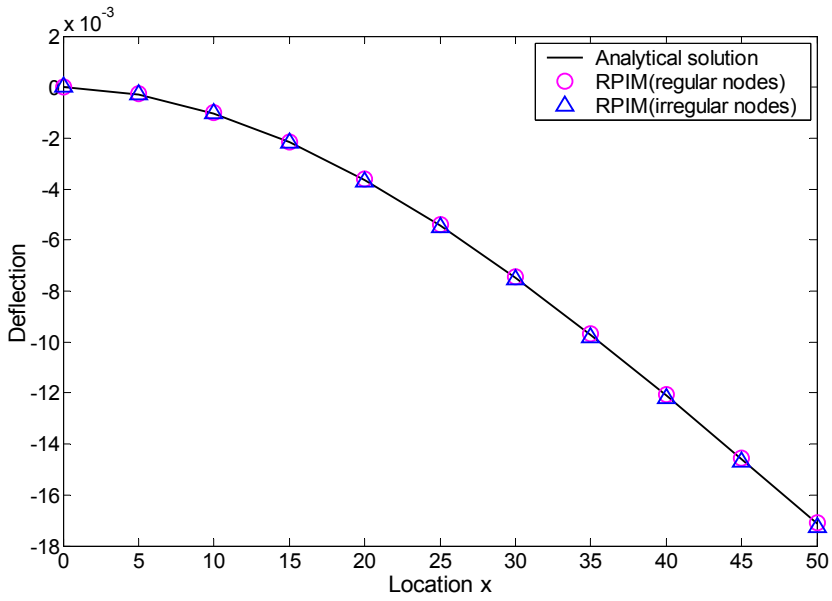

Figure 3.10 Displacement (u_y) distribution along the neutral axis (MQ-RBF augmented with linear polynomials is used with shape parameter $q = 1.03$ and $\alpha_c = 4.0$; Model-2 of the support domain is used, 52 and 55 field nodes are involved in the support domain for regular and irregular nodal distribution respectively).

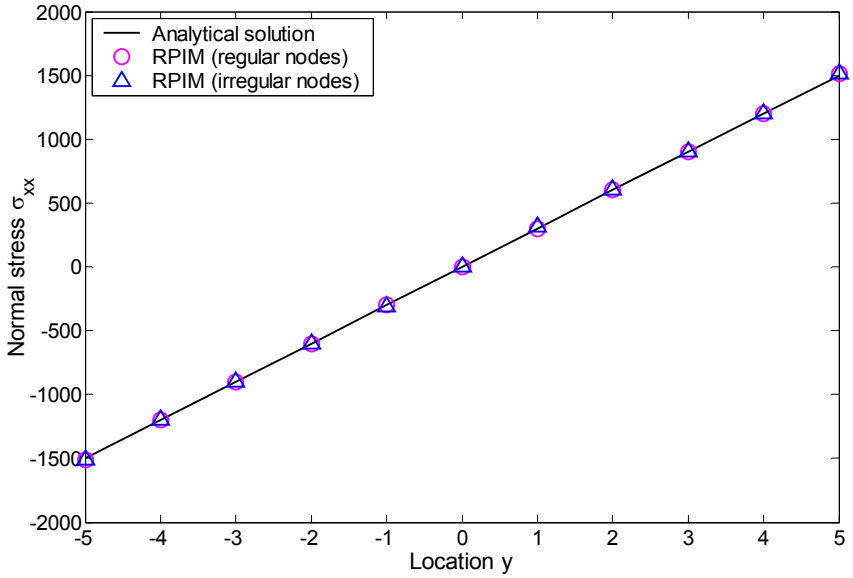

Figure 3.11 Normal stress distribution along the line of $x = L/2, z = 0.0$ (MQ-RBF augmented with linear polynomials is used with shape parameter $q = 1.03$ and $\alpha_c = 4.0$; Model-2 of the support domain is used, 52 and 55 field nodes are involved in the support domain for regular and irregular nodal distribution respectively).

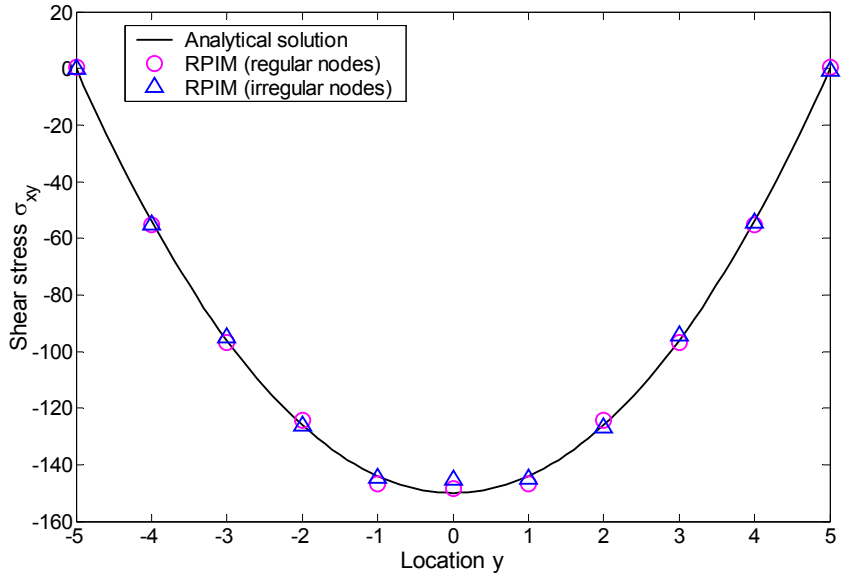

Figure 3.12 Shear stress distribution along the line of $x = L/2, z = 0.0$ (MQ-RBF augmented with linear polynomials is used with shape parameter $q = 1.03$ and $\alpha_c = 4.0$; Model-2 of the support domain is used, 52 and 55 field nodes are involved in the support domain for regular and irregular nodal distribution respectively).

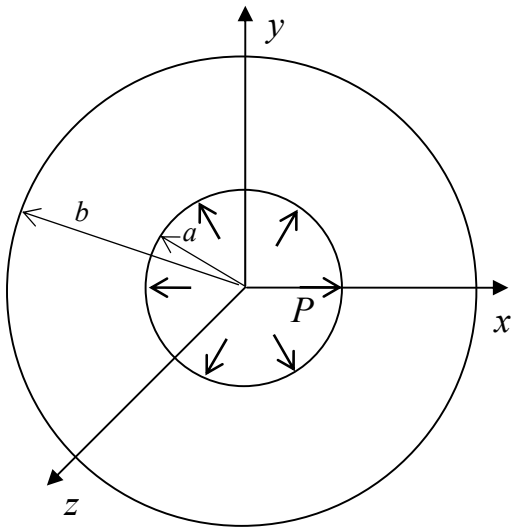

Figure 3.13 The Lame problem of a hollow sphere under internal pressure

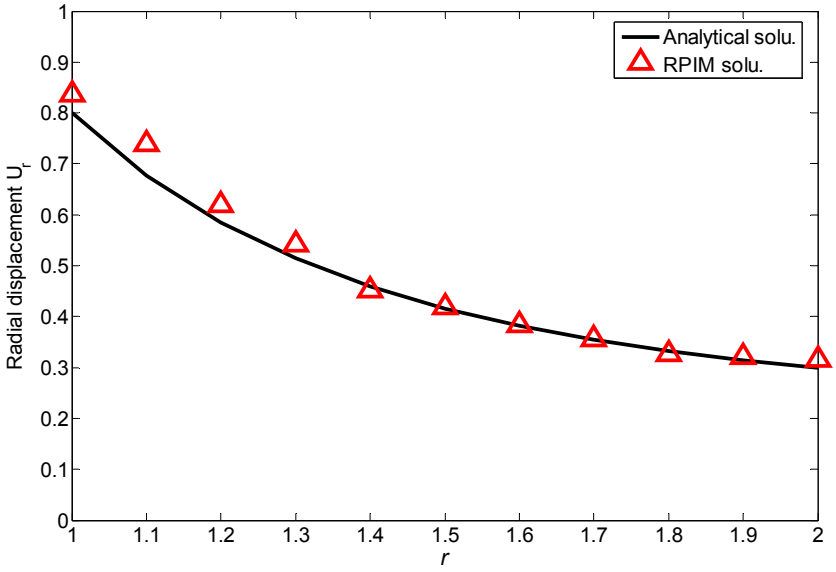

Figure 3.14 Distribution of the radial displacement along the *x* axis for the Lame problem

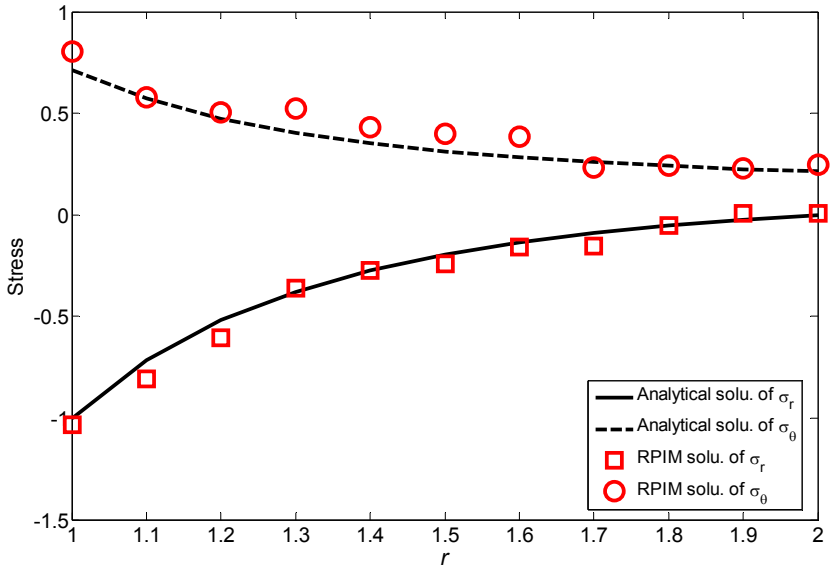

Figure 3.15 Distribution of the radial and tangential stresses along the *x* axis for the Lame problem

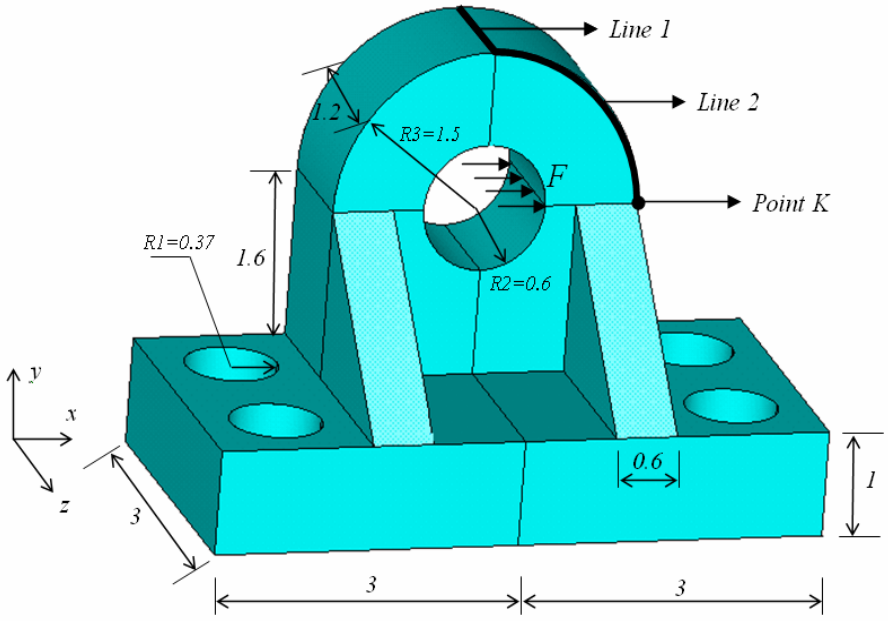

Figure 3.16 3D model of an axletree base

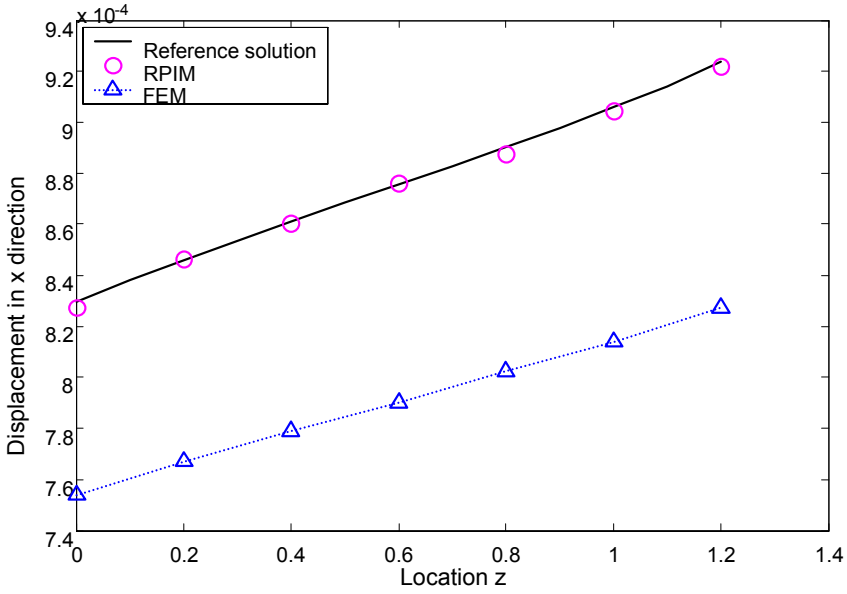

Figure 3.17 Distribution of displacement u_x along Line 1 of the axletree base

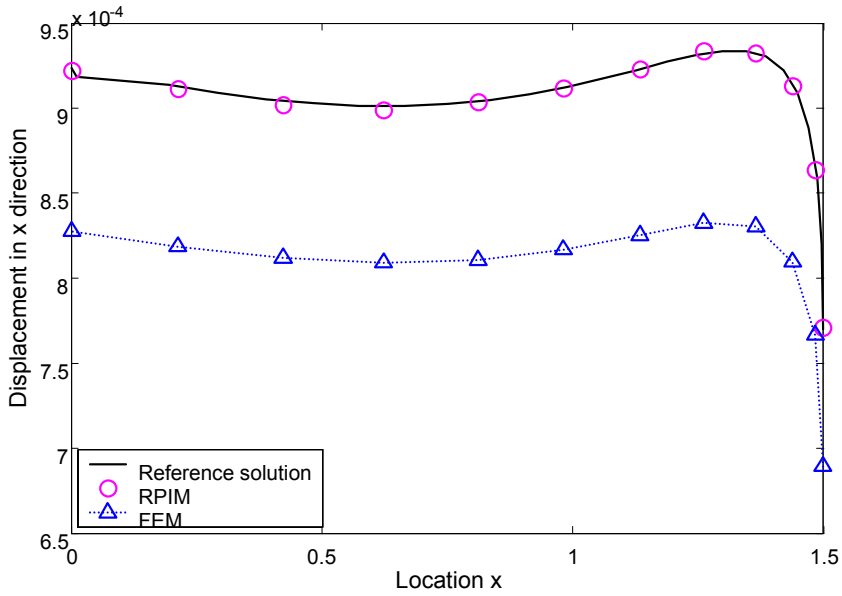

Figure 3.18 Distribution of displacement u_x along Line 2 of the axletree base

Chapter 4

A nodal integration technique for meshfree radial point interpolation method (NI-RPIM)

4.1 Introduction

Numerical integration plays an important role in the process of a meshfree weak form method. Gauss integration scheme is commonly used for integration of weak form methods. As we know, the finite element method uses Gauss quadrature in each element to integrate the weak form. For most of meshfree methods based on Galerkin weak form, error will be involved in the process of numerical integration due to the complexity involved in Gauss integration (Dolbow and Belytschko, 1999). Then some types of nodal integration schemes have been developed to perform the numerical integration.

The core idea of a nodal integration scheme is to use nodes as the integration sampling points. Nevertheless, a nodal integration scheme without extra measurement of stabilization, which is called 'direct nodal integration', may be plagued by spurious oscillation which also occurs in the finite difference method (Sze et al., 2004). To resolve this problem, attempts have been made by other authors. Beissel and Belytschko (Beissel and Belytschko, 1996) proposed a stabilized nodal integration scheme by adding a term, which contains the square of the residual of the governing equation, to the potential energy functional in the element-free Galerkin (EFG) framework. Another study by

Dolbow and Belytschko (Dolbow and Belytschko, 1999) examined the error of Gauss integration in Galerkon meshfree methods and demonstrated that considerable integration error will be produced when quadrature cells do not align with the local support domain for the construction of shape function. Bonet and Kulasegaram (Bonet and Kulasegaram, 1999) presented an integration correction to improve the accuracy of nodal integration. For linear patch test, correction terms are added to the shape function derivatives and the coefficients of correction terms at discrete nodes are solved by satisfying a linear patch test condition using an iterative procedure.

In this work, an alternative, stable and simply nodal integration technique for meshfree weak form methods is proposed and implemented in the process of numerical integration for the RPIM. In this nodal integration scheme, Taylor's expansion is used to serve as the stabilization terms, which have been employed in FEM (Liu et al., 1985) and other meshfree methods (Liu et al., 1996; Nagashima, 1999). In Nagashima's work, the MLS shape functions are used and first-order of Taylor series expansion to the strain matrix is employed for stabilization. In the present work, the formulation is based on the RPIM, the expansion is applied to the entirety of $\mathbf{B}^{\mathrm{T}}\mathbf{D}\mathbf{B}$ and it is expanded up to second-order. In this case, third-order derivatives of shape functions are required for linear elasticity problems. The RPIM shape functions created using RBFs perform well to the requirement, as it is one-piecely differentiable to any order in the integration domain (Liu, 2002). It is also noted that the expansion of $\mathbf{B}^{\mathrm{T}}\mathbf{D}\mathbf{B}$ to second-order is crucial, because the first order term will vanish for symmetrical integral domain and has no stabilization effect. The meshfree radial point interpolation method using the nodal integration scheme presented above is named as NI-RPIM. The NI-RPIM is examined in detail using a

number of benchmark examples, and applied to stress analysis of an automotive component. This integral scheme is formulated based on the simple Taylor series expansion and hence it is very easy to implement in any meshfree weak form method for stable nodal integration.

4.2 Discretized system equations

Consider a two-dimensional solid problem defined in domain Ω bounded by Γ ($\Gamma = \Gamma_t + \Gamma_u$), the governing equations of this problem can be expressed as follows (Liu, 2002).

Equilibrium equation:

$$\mathbf{L}^T \boldsymbol{\sigma} + \mathbf{b} = 0 \qquad \text{in } \Omega \tag{4.1}$$

Natural boundary condition:

$$\boldsymbol{\sigma} \cdot \mathbf{n} = \bar{\mathbf{t}} \qquad \text{on } \Gamma_t \tag{4.2}$$

Essential boundary condition:

$$\mathbf{u} = \bar{\mathbf{u}} \qquad \text{on } \Gamma_u \tag{4.3}$$

where $\mathbf{L}^{\mathrm{T}} = \begin{bmatrix} \dfrac{\partial}{\partial x} & 0 & \dfrac{\partial}{\partial y} \\ 0 & \dfrac{\partial}{\partial y} & \dfrac{\partial}{\partial x} \end{bmatrix}$ is differential operator; $\boldsymbol{\sigma}^T = \{\sigma_{xx} \quad \sigma_{yy} \quad \tau_{xy}\}$ is the stress vector, $\mathbf{u}^T = \{u \quad v\}$ is the displacement vector, $\mathbf{b}^T = \{b_x \quad b_y\}$ is the body force vector, $\bar{\mathbf{t}}$ is the prescribed traction on the natural boundaries, $\bar{\mathbf{u}}$ is the prescribed displacement on

the essential boundaries, and **n** is the vector of unit outward normal at a point on the natural boundary.

The unconstrained Galerkin weak form of Equation (4.1) is as follows (Liu, 2002),

$$\int_\Omega (\mathbf{L}\delta\mathbf{u})^{\mathrm{T}}(\mathbf{DLu})d\Omega - \int_\Omega \delta\mathbf{u}^{\mathrm{T}}\mathbf{b}d\Omega - \int_{\Gamma_t}\delta\mathbf{u}^{\mathrm{T}}\mathbf{t}d\Gamma = 0 \tag{4.4}$$

For linear elasticity, the material matrix $\mathbf{D}$ is expressed as follows,

$$\mathbf{D} = \frac{E}{1-v^2}\begin{bmatrix} 1 & v & 0 \\ v & 1 & 0 \\ 0 & 0 & \dfrac{1-v}{2} \end{bmatrix} \quad \text{For plane stress problem} \tag{4.5}$$

$$\mathbf{D} = \frac{E(1-v)}{(1+v)(1-2v)}\begin{bmatrix} 1 & \dfrac{v}{1-v} & 0 \\ \dfrac{v}{1-v} & 1 & 0 \\ 0 & 0 & \dfrac{1-2v}{2(1-v)} \end{bmatrix} \quad \text{For plane strain problem} \tag{4.6}$$

where E is Young's modulus and v is Poisson's ratio.

Substituting the RPIM approximation Equation (2.37) into Equation (4.4) yields,

$$\mathbf{Kd} = \mathbf{f} \tag{4.7}$$

where **d** is the vector of nodal displacement at all the unconstrained nodes and

$$\mathbf{K}_{ij} = \int_\Omega \mathbf{B}_i^{\mathrm{T}}\mathbf{D}\mathbf{B}_j d\Omega \tag{4.8}$$

$$\mathbf{f}_i = \int_{\Gamma_t}\varphi_i\bar{\mathbf{t}}d\Gamma + \int_\Omega \varphi_i\mathbf{b}d\Omega \tag{4.9}$$

in which

$$\mathbf{B}_i = \begin{bmatrix} \phi_{i,x} & 0 \\ 0 & \phi_{i,y} \\ \phi_{i,y} & \phi_{i,x} \end{bmatrix} \tag{4.10}$$

4.3 Nodal integration scheme based on Taylor's expansion

Consider now an integral,

$$I = \int_\Omega f(\mathbf{x}) d\Omega \tag{4.11}$$

where $f(\mathbf{x})$ is an arbitrary integrable function, which is, for example, a component of matrix $\mathbf{B}_i^{\mathrm{T}}\mathbf{D}\mathbf{B}_j$ given in Equation (4.8); Ω is the domain of the problem, that is represented by a set of N nodes distributed in the problem domain.

In a nodal integration scheme, the domain Ω is divided into a set of non-overlapping sub-domains $\Omega_i (i = 1,2,...,N)$, each of them includes a node, and $\Omega = \sum_{i=1}^{N} \Omega_i$. Then the integration, Equation (4.11), can then be expressed as

$$I = \sum_{i=1}^{N} \int_{\Omega_i} f(\mathbf{x}) d\Omega_i \tag{4.12}$$

In a meshfree method based on weak-form, a background mesh is needed for the implementation of numerical integration. For the present method, a background mesh is used for constructing the nodal integration domain for each node. The background mesh is not used for shape function construction which is constructed using a same set of nodes located in a local support domain. The independance of mesh from shape function construction has many advantages including the improvement in accuracy, which will be

observed later in examples. This fact has also been found in many other existing works (Belytschko et al., 1994; Atluri and Zhu, 1998; Chen et al., 2001). It is very clear that one does not have to use mesh for shape function construction. In the present work, the mesh is also only used for integration purpose.

The question now is how to evaluate $\int_{\Omega_i} f(\mathbf{x})d\Omega_i$ over the nodal integration domain Ω_i. Here a novel and simple approach based on the Taylor series extension is presented. The basic idea of this approach is to extend the integral function to some terms of Taylor series, and the integration will be approximately performed on these terms. Note that the integrand $f(\mathbf{x})$ is required to be differentiable within the integration domain when it is extended to be terms of Taylor series. Therefore, RPIM shape functions are constructed using the same set of nodes in each integration domain. A shape function so-constructed is one-piece, and hence is differentiable to any order in the integration domain. Note that the discontinuity will occur on the interfaces of the integration domains, and hence causes the non-conformability, which is omitted in this work, as it is controlled by the use of RBF shape functions with proper shape parameters (Liu, 2002). Note that this kind of non-conformability exists for all the meshfree methods based on weak-form and nodal integration even the ones using MLS shape functions, unless strain smoothing technique is used (Chen et al., 2001; Liu et al., 2005a; Liu and Zhang, 2006).

For comparison, the EFG method based on nodal integration is also coded, in which shape functions are obtained using the MLS method (Belytschko et al., 1994). For convenience, this method is named as NI-MLS. It is known that the MLS shape functions

can be constructed to satisfy the compatibility condition and the continuity of the field function approximation is ensured (Liu, 2002).

4.3.1 Formulations of nodal integration for 1D problems

To explain the method more clearly, the formulations for one-dimensional problems will be first presented. Based on Taylor series extension, a continuous function $f(x)$ can be approximated in the vicinity of a point x_0 as follows,

$$f(x) \approx f(x_0) + f^{'}(x_0)x + \frac{f^{''}(x_0)}{2!}x^2 \tag{4.13}$$

where the 3rd order and above are truncated.

The integration for the function $f(x)$ in the domain $(x_1 \le x \le x_2)$ can then be evaluated as,

$$\begin{aligned}\int_{x_1}^{x_2} f(x)dx &\approx \int_{x_1}^{x_2} (f(x_0) + f^{'}(x_0)x + \frac{1}{2}f^{''}(x_0)x^2)dx \\ &= \int_{x_1}^{x_2} f(x_0)dx + \int_{x_1}^{x_2} f^{'}(x_0)xdx + \frac{1}{2}\int_{x_1}^{x_2} f^{''}(x_0)x^2dx \\ &= f(x_0)(x_2 - x_1) + \frac{1}{2}f^{'}(x_0)(x_2^2 - x_1^2) + \frac{1}{6}f^{''}(x_0)(x_2^3 - x_1^3)\end{aligned} \tag{4.14}$$

Considering now a one-dimensional problem, the problem domain is presented by a set of nodes, as shown in Figure 4.1 and Figure 4.2. The integrand of $f(x)$ is now a component of the matrix $\mathbf{B}_i^T\mathbf{D}\mathbf{B}_j$ (see Equation (4.8)). When the field nodes are regularly distributed, by using Equation (4.14), the numerical integration for the i^{th} node can be performed as follows.

For an internal node, the integration can be applied as

$$\int_{-\frac{a}{2}}^{\frac{a}{2}} f(x)dx = f(x_i)(\frac{a}{2}+\frac{a}{2}) + \frac{1}{2}f^{'}(x_i)\left[(\frac{a}{2})^2 - (-\frac{a}{2})^2\right] + \frac{1}{6}f^{''}(x_i)\left[(\frac{a}{2})^3 - (-\frac{a}{2})^3\right]$$
$$= f(x_i)a + 0 + \frac{1}{24}f^{''}(x_i)a^3 \tag{4.15}$$

where a is the nodal spacing as shown in Figure 4.1.

For the node located at the left end, the integration will as

$$\int_{0}^{\frac{a}{2}} f(x)dx = f(x_i)(\frac{a}{2}-0) + \frac{1}{2}f^{'}(x_i)\left[(\frac{a}{2})^2 - 0\right] + \frac{1}{6}f^{''}(x_i)\left[(\frac{a}{2})^3 - 0\right]$$
$$= \frac{1}{2}f(x_i)a + \frac{1}{8}f^{'}(x_i)a^2 + \frac{1}{48}f^{''}(x_i)a^3 \tag{4.16}$$

For the node located at the right end of the 1D domain,

$$\int_{-\frac{a}{2}}^{0} f(x)dx = f(x_i)\left(0+\frac{a}{2}\right) + \frac{1}{2}f^{'}(x_i)\left[0-\left(-\frac{a}{2}\right)^2\right] + \frac{1}{6}f^{''}(x_i)\left[0-\left(-\frac{a}{2}\right)^3\right]$$
$$= \frac{1}{2}f(x_i)a - \frac{1}{8}f^{'}(x_i)a^2 + \frac{1}{48}f^{''}(x_i)a^3 \tag{4.17}$$

When the field nodes are irregularly distributed, Equations (4.15), (4.16) and (4.17) can be expressed as follows.

For an internal node:

$$\int_{-\frac{a}{2}}^{\frac{b}{2}} f(x)dx = f(x_i)(\frac{b}{2}+\frac{a}{2}) + \frac{1}{2}f^{'}(x_i)\left[(\frac{b}{2})^2 - (-\frac{a}{2})^2\right] + \frac{1}{6}f^{''}(x_i)\left[(\frac{b}{2})^3 - (-\frac{a}{2})^3\right]$$
$$= \frac{1}{2}f(x_i)(a+b) + \frac{1}{8}f^{'}(x_i)(b^2-a^2) + \frac{1}{48}f^{''}(x_i)(a^3+b^3) \tag{4.18}$$

For the node located at the left end:

$$\int_{0}^{\frac{c}{2}} f(x)dx = f(x_i)(\frac{c}{2}-0) + \frac{1}{2}f^{'}(x_i)\left[(\frac{c}{2})^2 - 0\right] + \frac{1}{6}f^{''}(x_i)\left[(\frac{c}{2})^3 - 0\right] \tag{4.19}$$

$$= \frac{1}{2} f(x_i)c + \frac{1}{8} f^{'}(x_i)c^2 + \frac{1}{48} f^{''}(x_i)c^3$$

For the node located at the right end:

$$\begin{aligned} \int_{-\frac{d}{2}}^{0} f(x)dx &= f(x_i)(0+\frac{d}{2}) + \frac{1}{2} f^{'}(x_i)\left[0-(-\frac{d}{2})^2\right] + \frac{1}{6} f^{''}(x_i)\left[0-(-\frac{d}{2})^3\right] \\ &= \frac{1}{2} f(x_i)d - \frac{1}{8} f^{'}(x_i)d^2 + \frac{1}{48} f^{''}(x_i)d^3 \end{aligned} \tag{4.20}$$

where a, b, c and d are nodal spacing for the irregularly distributed nodes as shown in Figure 4.2.

4.3.2 Formulations of nodal integration for 2D problems

Applying Taylor series extension, a two-dimensional (2D) continuous function $f(x, y)$ can be approximated in the vicinity of point (x_0, y_0) as follows,

$$f(x,y) \approx f(x_0,y_0) + (x\frac{\partial}{\partial x} + y\frac{\partial}{\partial y}) f(x_0,y_0) + \frac{1}{2!}(x\frac{\partial}{\partial x} + y\frac{\partial}{\partial y})^2 f(x_0,y_0) \tag{4.21}$$

The integration for function $f(x, y)$ over the nodal integration domain Ω_i can be expressed as,

$$\begin{aligned} \iint_{\Omega_i} f(x,y)d\Omega &\approx \iint_{\Omega_i} \left(f(x_0,y_0) + (x\frac{\partial}{\partial x} + y\frac{\partial}{\partial y}) f(x_0,y_0) + \frac{1}{2!}(x\frac{\partial}{\partial x} + y\frac{\partial}{\partial y})^2 f(x_0,y_0) \right) d\Omega \\ &= f(x_0,y_0)\iint_{\Omega_i} 1 d\Omega + f_{,x}(x_0,y_0)\iint_{\Omega_i} x d\Omega + f_{,y}(x_0,y_0)\iint_{\Omega_i} y d\Omega \\ &\quad + \frac{1}{2} f_{,xx}(x_0,y_0)\iint_{\Omega_i} x^2 d\Omega + f_{,xy}(x_0,y_0)\iint_{\Omega_i} xy d\Omega + \frac{1}{2} f_{,yy}(x_0,y_o)\iint_{\Omega_i} y^2 d\Omega \\ &= f(x_0,y_0)A_i + f_{,x}(x_0,y_0)M_{yi} + f_{,y}(x_0,y_0)M_{xi} \end{aligned} \tag{4.22}$$

$$+\frac{1}{2}f_{,xx}(x_0,y_0)M_{yyi}+f_{,xy}(x_0,y_0)M_{xyi}+\frac{1}{2}f_{,yy}(x_0,y_0)M_{xxi}$$

where A_i is the area of the nodal integration domain of the i^{th} node,

$$M_{xi}=\iint_{A_i}ydA_i \qquad M_{yi}=\iint_{A_i}xdA_i \tag{4.23}$$

are the area moments of 1st order for the integration domain of the i^{th} node, and

$$M_{xxi}=\iint_{A_i}y^2dA_i \qquad M_{yyi}=\iint_{A_i}x^2dA_i \qquad M_{xyi}=\iint_{A_i}xydA_i \tag{4.24}$$

are the area moments of 2nd order for the integration domain of the i^{th} node.

The integration for function $f(x,y)$ along the boundary line can be formulated as

$$\begin{aligned}\int_\Gamma f(x,y)dl&=\int_\Gamma\left(f(x_0,y_0)+(x\frac{\partial}{\partial x}+y\frac{\partial}{\partial y})f(x_0,y_0)+\frac{1}{2!}(x\frac{\partial}{\partial x}+y\frac{\partial}{\partial y})^2f(x_0,y_0)\right)dl\\&=f(x_0,y_0)\int_\Gamma 1dl+f_{,x}(x_0,y_0)\int_\Gamma xdl+f_{,y}(x_0,y_0)\int_\Gamma ydl\\&\quad+\frac{1}{2}f_{,xx}(x_0,y_0)\int_\Gamma x^2dl+f_{,xy}(x_0,y_0)\int_\Gamma xydl+\frac{1}{2}f_{,yy}(x_0,y_0)\int_\Gamma y^2dl\end{aligned} \tag{4.25}$$

To apply the nodal integration technique, a background cell is needed to divide the problem domain into nodal integration domains, each of which includes a node. When the nodes are regularly distributed, a rectangular domain can be used as the nodal integration domain Ω_i (illustrated in Figure 4.3), and the union of all the rectangles forms the problem domain. As shown in Figure 4.4, when the nodes are irregularly distributed, a tessellation can always be generated automatically by joining the centroids of the triangles and the mid-edge points (Ferzige and Peric, 1999).

According to Equation (4.22), the area A_i, the moments $M_{xi}, M_{yi}, M_{xxi}, M_{yyi}$ and M_{xyi} for the i^{th} field node can be calculated during the pre-process stage for later use in the

numerical integration, because they depend on only the geometry of the nodal integration domain.

4.4 Numerical examples

Several numerical examples are studied in this section. The materials used in the examples are all linear elastic with Young's modulus $E = 3.0 \times 10^7$ Pa and poisson's ratio $v = 0.3$. The error indicators in displacement and energy are respectively defined as follows,

$$e_d = \sqrt{\frac{\sum_{i=1}^{N} (u_i^{exact} - u_i^{numerical})^2}{\sum_{i=1}^{n} (u_i^{exact})^2}} \tag{4.26}$$

$$e_e = \frac{1}{A}\sqrt{\frac{1}{2}\int_{\Omega} \left(\boldsymbol{\varepsilon}^{exact} - \boldsymbol{\varepsilon}^{numerical}\right)^T \mathbf{D} \left(\boldsymbol{\varepsilon}^{exact} - \boldsymbol{\varepsilon}^{numerical}\right) d\Omega} \tag{4.27}$$

where the superscript *exact* notes the exact or analytical solution, *numerical* notes a numerical solution obtained using a numerical method including the present NI-RPIM, and A is the area of the problem domain.

4.4.1 A one-dimension bar subjected to body force

A simple benchmark problem of 1D bar subjected to body force is studied first. The governing equation and the boundary conditions are shown as follows.

$$E\frac{\partial^2 u(x)}{\partial x^2} + 10x = 0 \qquad (0 \le x \le 10) \tag{4.28}$$

$$u(0) = 0\,, \qquad u(10) = 0 \tag{4.29}$$

The analytical solution of this simple problem has the following polynomial form.

$$u(x) = -\frac{5}{3E}x^3 + \frac{500}{3E}x \tag{4.30}$$

In this study, eleven regularly distributed nodes are used. Solutions of field function u and its derivative du/dx are first obtained using the present method, and compared with the analytical solutions, as shown in Figure 4.5. It shows that the numerical solutions of both the function values and their first-order derivatives are in good agreement with the analytical solutions.

4.4.2 A one-dimensional problem with non-polynomial solution

In this study, the following problem is considered,

$$\frac{d^2u}{dx^2} + 25u = 0 \qquad (0 \le x \le 1) \tag{4.31}$$

$$u_{,x}(0) = u_{,x}(1) = 1 \tag{4.32}$$

The exact solution of $u(x)$ can be easily found as follows,

$$u(x) = \frac{\cos 5 - 1}{5\sin 5}\cos 5x + \frac{1}{5}\sin 5x \tag{4.33}$$

which is not in polynomial form.

The numerical solutions of $u(x)$ and $du(x)/dx$ are obtained using the present method with eleven regularly distributed nodes, and the results are shown in Figure 4.6 and Figure 4.7 together with the analytical solutions. A very good agreement is again

observed. A convergence study is also performed by using seven different nodal densities (4, 7, 13, 25, 49, 97 and 193 regular nodes). The error results of function value computed using Equation (4.26) is shown in Figure 4.8 against the average nodal spacing h. The convergence rate of NI-RPIM for this problem is about 1.94, which is the value of the slope of the line in Figure 4.8.

4.4.3 A cantilever beam

A benchmark problem of 2-D cantilever beam as shown in Figure 4.9 is now studied. The beam is subjected to a parabolic downward traction at the free end. As the beam has a unit thickness, it can be taken as a plane stress problem and the analytical solutions of displacement and stress components are shown as follows (Timoshenko and Goodier, 1970),

$$u_x = -\frac{Py}{6EI}\left[(6L-3x)x+(2+\nu)(y^2-\frac{D^2}{4})\right] \tag{4.34}$$

$$u_y = \frac{P}{6EI}\left[3\nu y^2(L-x)+(4+5\nu)\frac{D^2x}{4}+(3L-x)x^2\right] \tag{4.35}$$

where the moment of the inertia of the beam is given as $I = D^3/12$.

The stress components corresponding to above displacements are as,

$$\sigma_x = -\frac{p(L-x)y}{I} \tag{4.36}$$

$$\sigma_y = 0 \tag{4.37}$$

$$\sigma_{xy} = \frac{p}{2I}\left[\frac{D^2}{4}-y^2\right] \tag{4.38}$$

The values of the parameters are taken as: $L = 50, D = 10$ and $P = -1000$.

1) Effect of shape parameters

First, the effect of two shape parameters (q, α_c) in MQ-RBF that used to create the RPIM shape functions is studied through this benchmark problem. The problem domain is represented by 196 regular nodes and 181 irregular nodes (as shown in Figure 4.10). In the process of the study of q, α_c is fixed at 4.0, a circular local support domain is used, and α_s is fixed at 3.0. For different values of q (varies form 0.01 to 1.98), error of displacement defined in Equation (4.26) is computed using the present NI-RPIM method and plotted in Figure 4.11. Note that the value of q must not be an integer number, because it will cause the failure of the RPIM due to the singularity of the moment matrix (Liu, 2002). Figure 4.11 shows that a range of $0.4 \sim 1.0$ for parameter q will lead to better results for both regular and irregular nodes distribution. Based on previous study results (Liu, 2002), $q = 1.03$ was found good and hence is used in the present method. In the following study of effect of parameter α_c, a circular support domain is used and α_s is fixed at 3.0. Value of α_c varies form 1.0 to 7.0 and the errors of displacement obtained using the present method are plotted in Figure 4.12. The figure shows that a value of α_c around 4.0 will lead to better results for both regular and irregular nodes distributions. It is consistent with the previous conclusions obtained by other authors (Wang and Liu, 2002b; Liu et al., 2005). Therefore $\alpha_c = 4.0$ is used in this work for the following problems.

2) Effect of dimension of the local support domain

The dimension of the local support domain controls the number of field nodes used in the RPIM shape function construction, and can affect the numerical results. Values of shape parameters are fixed as $(q = 1.03, \alpha_c = 4.0)$, different values of α_s are examined and the displacement errors obtained for regular and irregular nodes distribution are plotted in Figure 4.13, respectively. Based on this study, α_s of 2.5~3.5 that includes 12~40 field nodes provides good results and is used in this work.

3) Numerical results of the cantilever beam

The beam is studied using both the regular and irregular modes of nodes distribution (shown in Figure 4.10). The numerical results of displacement in y direction along the neutral line and the shear stress along the middle line are obtained using the present method with 196 regular and 181 irregular nodes distribution and plotted in Figure 4.14 and Figure 4.15, respectively. The pictures show that the numerical solutions of displacement and stress components are all in good agreement with the analytical ones and the mode of nodal distribution has little effect on the results.

4) Comparison study of convergence and efficiency

To study the properties of convergence and efficiency, the cantilever beam is studied using three models of regular nodes (85, 297, and 1105 nodes distribution). Four different methods are used in the analysis: the traditional FEM with 4-node quadrilateral element, the original RPIM with Gauss integration scheme, the NI-MLS method and the present NI-RPIM. For the RPIM using Gauss integration, 2×2 Gauss points are employed for each quadrilateral background cell. The NI-MLS is formulated using linear and quadratic

polynomial basis functions respectively and they are labeled, respectively, as linear NI-MLS and quadratic NI-MLS in this work. The results of displacement and energy errors against h are plotted in Figure 4.16 for these four methods, where h is the average nodal spacing for the nodes distribution. The picture shows that the RPIM, the quadratic NI-MLS, and the present NI-RPIM is more accurate than the FEM and the linear NI-MLS. In Figure 4.17, the errors of the numerical results obtained using these four methods are plotted against the CPU time consumed, which shows the efficiency. It can be found that these three methods, i.e. the RPIM, the quadratic NI-MLS, and the NI-RPIM, are more efficient than the FEM. Compared with the original RPIM with Gauss integration, the NI-RPIM is more efficient when using the present simple nodal integration scheme.

4.4.4 An infinite plate with a hole

An infinite plate with a hole ($a = 10$) subjected to a tensile $(T_x = 10)$ is examined. Due to two-fold symmetry, only one quarter with the dimension of $b = 50$ is modeled, as shown in Figure 4.18. In the model, the analytical solutions of stress components are applied on the boundaries at $x = 50$ and $y = 50$. The essential boundary conditions are,

$$\begin{aligned} &u(x = 0) = 0, \quad (10 \le y \le 50) \\ &v(y = 0) = 0, \quad (10 \le x \le 50) \end{aligned} \tag{4.39}$$

The analytical solution of this problem is used below (Timoshenko and Goodier, 1970),

$$u_r = \frac{T_x}{4\mu}\left\{ r\left[\frac{(\kappa - 1)}{2} + \cos(2\theta)\right] + \frac{a^2}{r}\left[1 + (1 + \kappa)\cos(2\theta)\right] - \frac{a^4}{r^3}\cos(2\theta)\right\} \tag{4.40}$$

$$u_\theta = \frac{T_x}{4\mu}\left[(1-\kappa)\frac{a^2}{r} - r - \frac{a^4}{r^3}\right]\sin(2\theta) \tag{4.41}$$

where

$$\mu = \frac{E}{2(1+v)} \qquad \kappa = \begin{cases} 3-4v & \text{Plane strain} \\ \dfrac{3-v}{1+v} & \text{Plane stress} \end{cases} \tag{4.42}$$

The stress components corresponding to the analytical displacements are

$$\sigma_{xx} = T_x\left\{1 - \frac{a^2}{r^2}\left[\frac{3}{2}\cos(2\theta) + \cos(4\theta)\right] + \frac{3a^4}{2r^4}\cos(4\theta)\right\} \tag{4.43}$$

$$\sigma_{yy} = -T_x\left\{\frac{a^2}{r^2}\left[\frac{1}{2}\cos(2\theta) - \cos(4\theta)\right] + \frac{3a^4}{2r^4}\cos(4\theta)\right\} \tag{4.44}$$

$$\sigma_{xy} = -T_x\left\{\frac{a^2}{r^2}\left[\frac{1}{2}\sin(2\theta) + \sin(4\theta)\right] - \frac{3a^4}{2r^4}\sin(4\theta)\right\} \tag{4.45}$$

In this study, the problem is analyzed as plane stress and the domain is represented by 489 irregularly distributed nodes. The numerical displacement solutions along two boundary lines $(x = 0; y = 0)$ and the normal stress solutions along the line $(x = 0)$ are plotted in Figure 4.19 and Figure 4.20, respectively. Figure 4.19 shows that the displacement results obtained using the present method are in a very good agreement with the analytical solutions for this benchmark problem. Figure 4.20 shows that the NI-RPIM obtains a comparable stress solution. The figure shows that the numerical solution of stress components near the right end of the edge is not very good compared with the analytical solution. For the point of interest along the edge, fewer nodes are used in the local support domain and it will cause the worse results as shown in Figure 4.20.

4.4.5 Internal pressurized hollow cylinder

A hollow cylinder subjected to internal pressure (shown in Figure 4.21) is also analyzed. The cylinder is of internal radius $a = 10$, outer radius $b = 25$, and internal pressure $p = 100$. Plain strain condition is considered and the analytical solutions can be written as (Timoshenko and Goodier, 1970),

$$u_r = \frac{pa^2}{E\left(b^2 - a^2\right)r}\left[(1-v)r^2 + (1+v)b^2\right] \tag{4.46}$$

$$\sigma_r = \frac{a^2 p}{b^2 - a^2}\left(1 - \frac{b^2}{r^2}\right) \tag{4.47}$$

$$\sigma_\theta = \frac{a^2 p}{b^2 - a^2}\left(1 + \frac{b^2}{r^2}\right) \tag{4.48}$$

The problem is discretized by 123 irregularly distributed nodes (shown in Figure 4.21). The numerical solutions using the present method are plotted in Figure 4.22 and Figure 4.23. The figures show that both the displacement and stress solutions obtained using the present NI-RPIM method, coincide well with the analytical ones.

4.4.6 An automotive part: connecting rod

A typical connecting rod used in automobiles, as shown in Figure 4.24, is studied using the NI-RPIM. The value of the pressure is 100 units. As shown in Figure 4.25, the rod is discretized using 592 irregularly distributed nodes. Along the middle dashed line (shown in Figure 4.24), the displacement and the normal stress components in x direction of the nodes are plotted. Because the exact solution is not available, the reference solution is

obtained using the FEM with a very fine mesh of 7756 6-node triangular elements. The numerical solutions obtained using the present method are plotted in Figure 4.26 and Figure 4.27 with the reference ones. The figures show that, the present method can obtain very good results of both the displacement and stress components.

4.5 Remarks

In this chapter, a nodal integration technique for meshfree radial point interpolation method (NI-RPIM) is presented. This method employs radial basis functions (RBFs) augmented with polynomials to construct shape functions. Galerkin weak form is used and a nodal integration scheme based on Taylor series extension is introduced to perform the numerical integration. Some numerical examples are examined and the effects of shape parameters as well as the dimension of the local support domains are investigated. From the research work, the following conclusions can be drawn.

- The RPIM Shape functions generated using RBFs augmented with polynomials possess the Delta function property, which allows straightforward imposition of essential boundary conditions at nodes.
- Based on the study of examples in this chapter and the previous works on RPIM, $q = 1.03$ and $\alpha_c = 4$ are recommended for NI-RPIM.
- For the circular support domain, $\alpha_s = 2.5 \sim 3.5$ which includes 12 ~ 40 field nodes are suggested.
- The benchmark numerical examples show that the results obtained using the present nodal integration technique is accurate and stable.

- Compared with the linear FEM, the NI-RPIM is more accurate and efficient; compared with the original RPIM using Gauss integration scheme, the NI-RPIM can achieve higher convergence rate and efficiency; compared with the NI-MLS, the NI-RPIM performs much better than the linear NI-MLS and is almost in the same level of performance of quadratic NI-MLS.

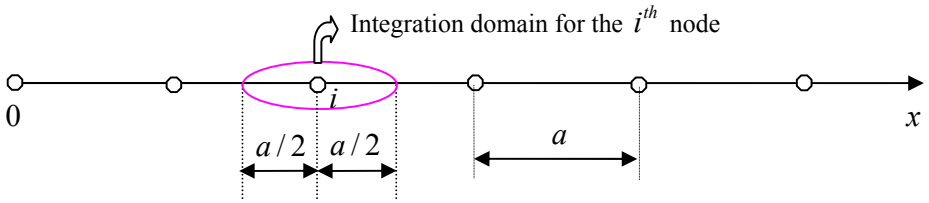

Figure 4.1 Nodal integration domain for regularly distributed nodes for 1D problem

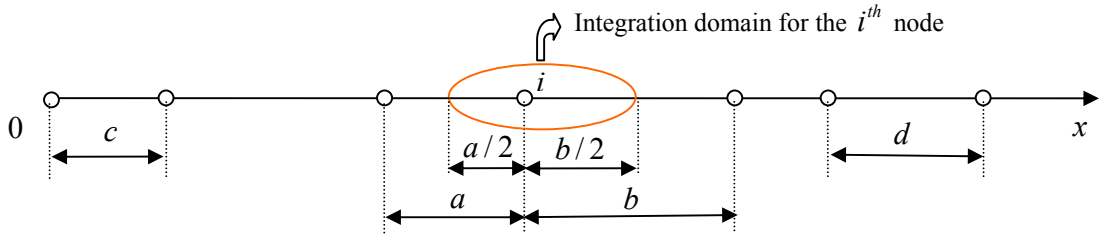

Figure 4.2 Nodal integration domain for irregularly distributed nodes for 1D problem

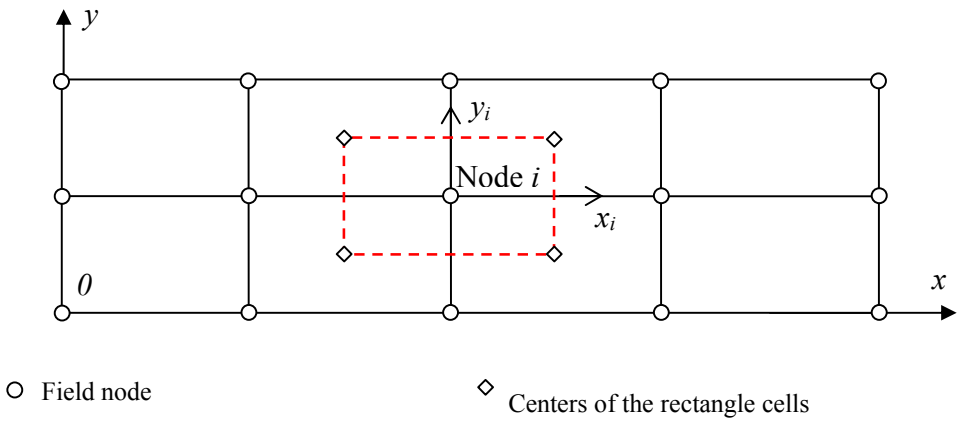

Figure 4.3 Illustration of rectangular background cells and integral domain for node i in two dimensions

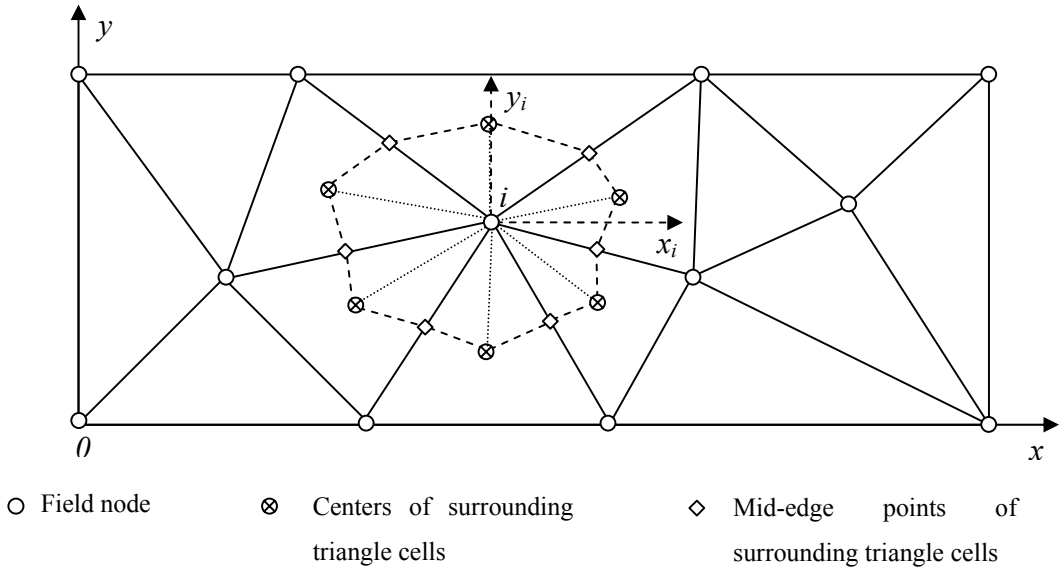

Figure 4.4 Illustration of triangular background cells and the integral domain for node i in two dimensions

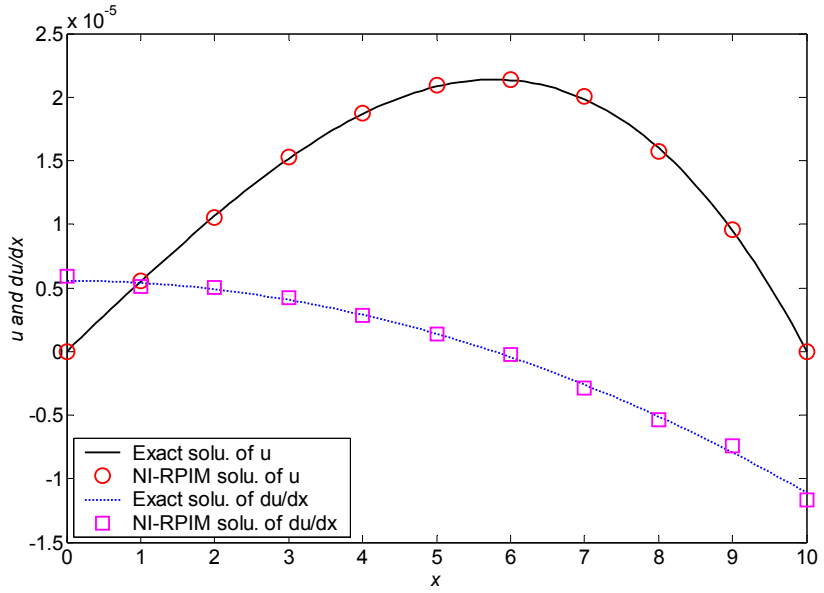

Figure 4.5 Exact and numerical solutions of u and du/dx for the one-dimensional bar problem

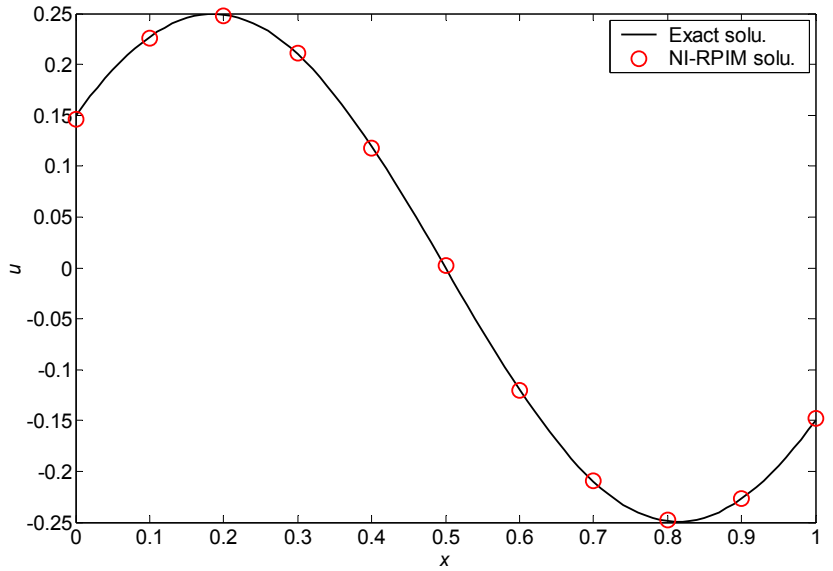

Figure 4.6 Exact and numerical solutions of u for the one-dimensional problem with trigonometric form of solution

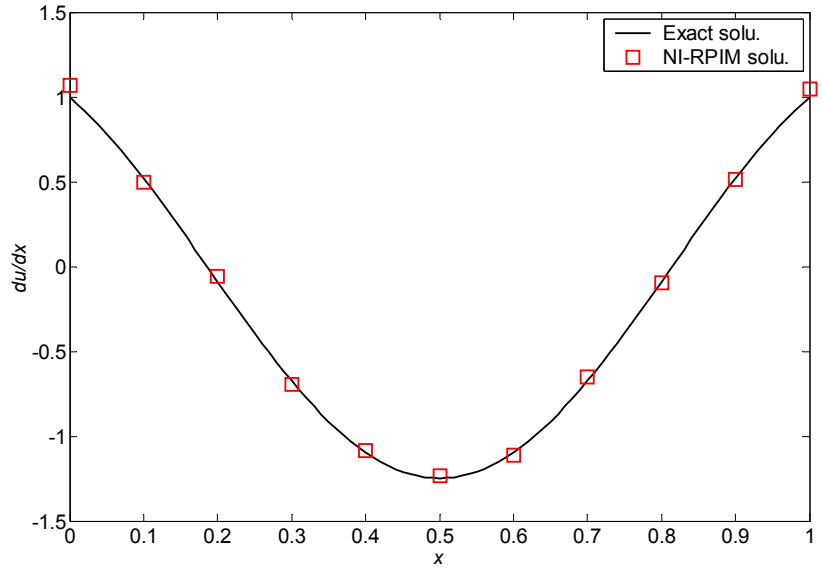

Figure 4.7 Exact and numerical solutions of du/dx for the one-dimensional problem with trigonometric form of solutions

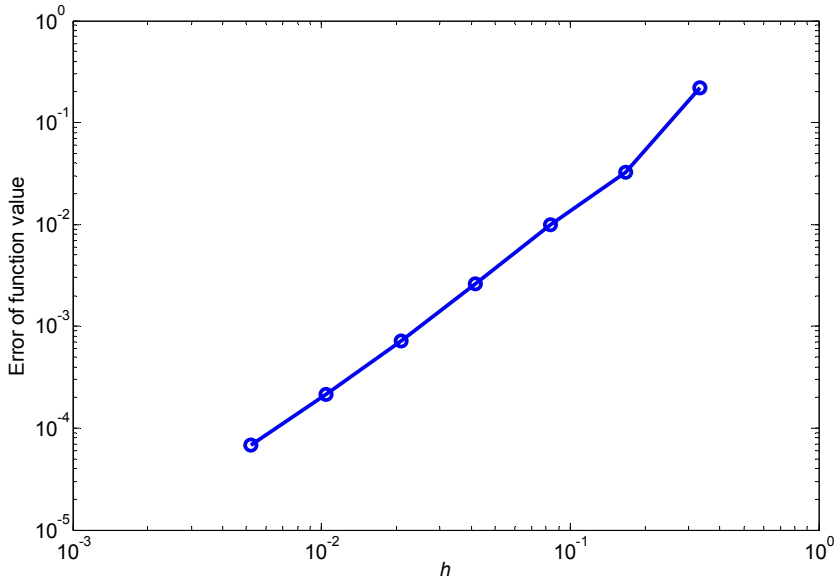

Figure 4.8 The convergence study of the present method by using the one-dimensional bar problem (The convergence rate is about 1.94)

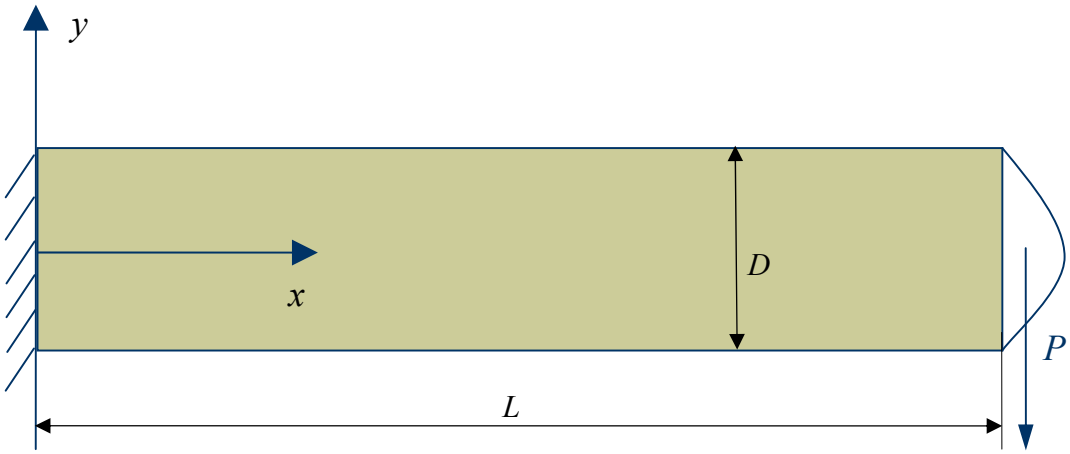

Figure 4.9 Cantilever beam subjected to a parabolic traction at the free end

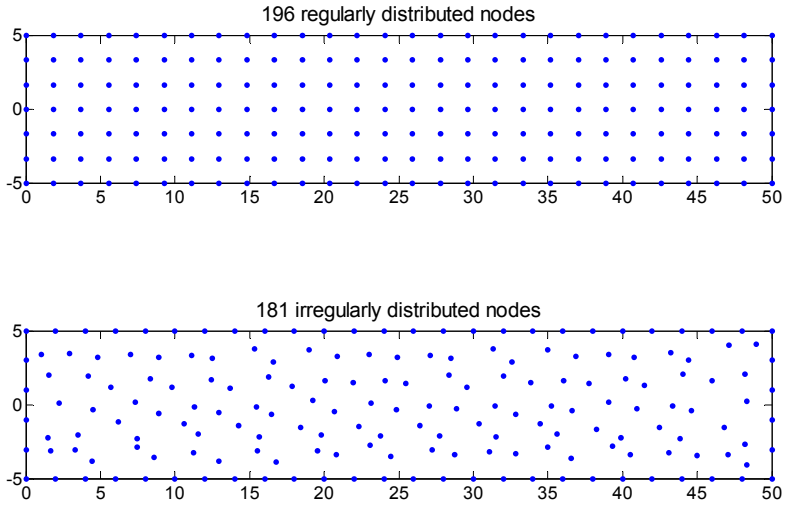

Figure 4.10 Illustration of regular and irregular nodes distribution for the problem of cantilever beam

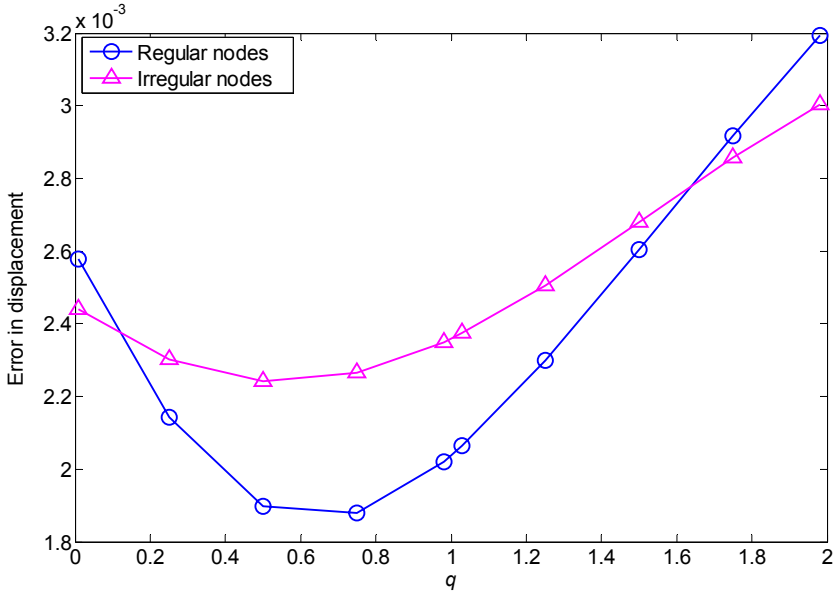

Figure 4.11 Effect of parameter q on the displacement results for the cantilever beam (196 and 181 nodes are used for regular and irregular nodes distribution; $\alpha_c = 4.0$ and $\alpha_s = 3.0$).

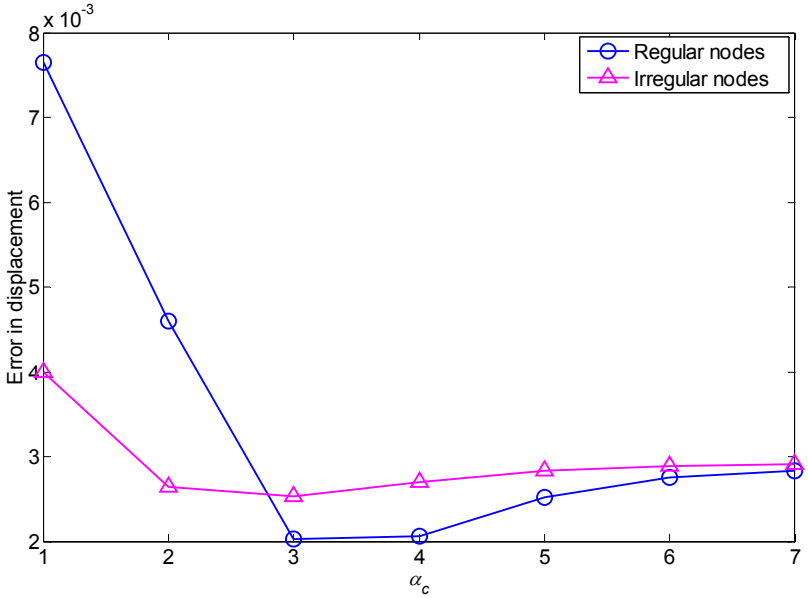

Figure 4.12 Effect of parameter α_c on the displacement results for the cantilever beam (196 and 181 nodes are used for regular and irregular nodes distribution; $q = 1.03$ and $\alpha_s = 3.0$).

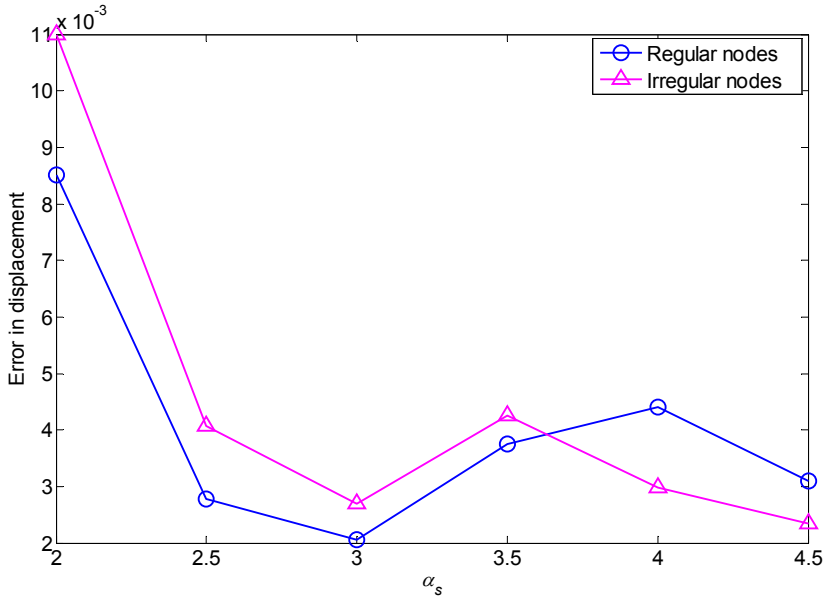

Figure 4.13 Effect of dimension of the local support domain on the displacement results for the cantilever beam (196 and 181 nodes are used for regular and irregular nodes distribution; $\alpha_c = 4.0$ and $q = 1.03$).

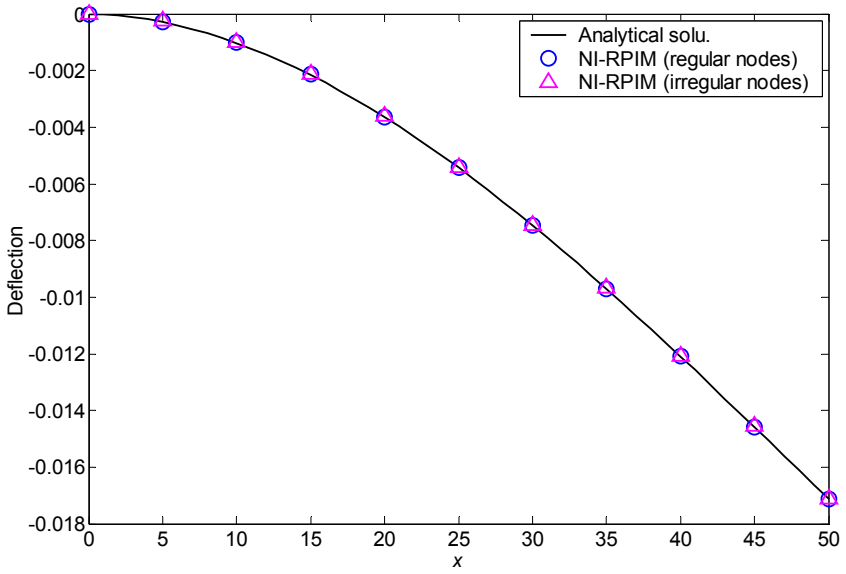

Figure 4.14 Deflection distribution along the neutral line of the cantilever beam

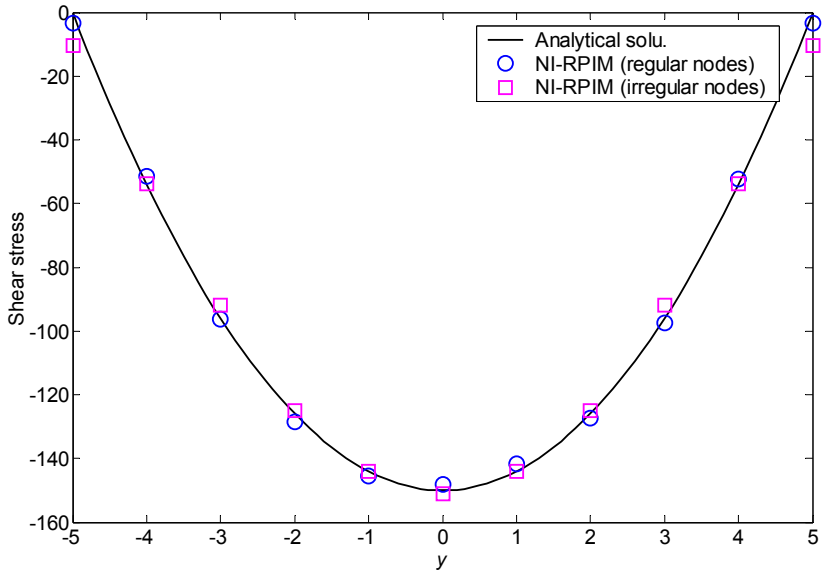

Figure 4.15 Shear stress distribution along the line $\left(x = L/2\right)$ of the cantilever beam

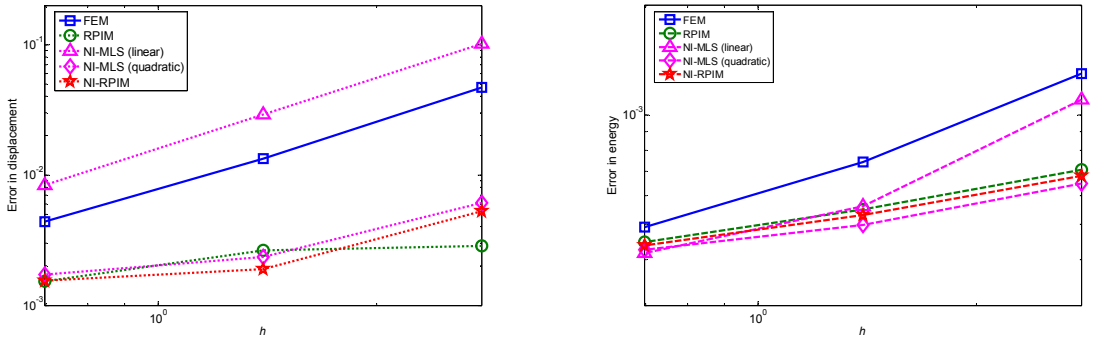

Figure 4.16 Comparison of convergence of four different methods, i.e. the FEM, the RPIM, the NI-MLS and the NI-RPIM. (The cantilever beam is used for examination. In the FEM, 4-node quadrilateral element is used; in the RPIM, Gauss integration is used with the parameters of $\alpha_c = 4.0$, $q = 1.03$ and $\alpha_s = 3.0$; in the NI-MLS, linear and quadratic polynomial basis functions are both used with the cubic weight function; in the NI-RPIM, the present nodal integration technique is used with the parameters of $\alpha_c = 4.0$, $q = 1.03$ and $\alpha_s = 3.0$.)

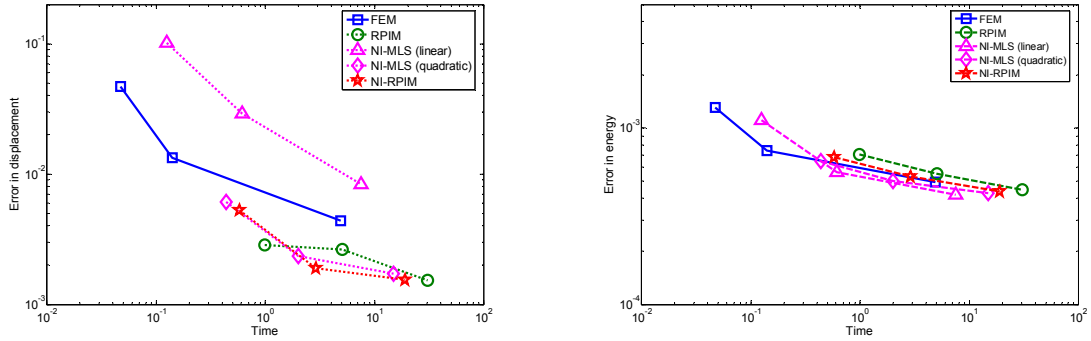

Figure 4.17 Comparison of efficiency of four different methods, i.e. the FEM, the RPIM, the NI-MLS and the NI-RPIM. (The cantilever beam is used for examination. In the FEM, 4-node quadrilateral element is used; in the RPIM, Gauss integration is used with the parameters of $\alpha_c = 4.0$, $q = 1.03$ and $\alpha_s = 3.0$; in the NI-MLS, linear and quadratic polynomial basis functions are both used with the cubic weight function; in the NI-RPIM, the present nodal integration technique is used with the parameters of $\alpha_c = 4.0$, $q = 1.03$ and $\alpha_s = 3.0$)

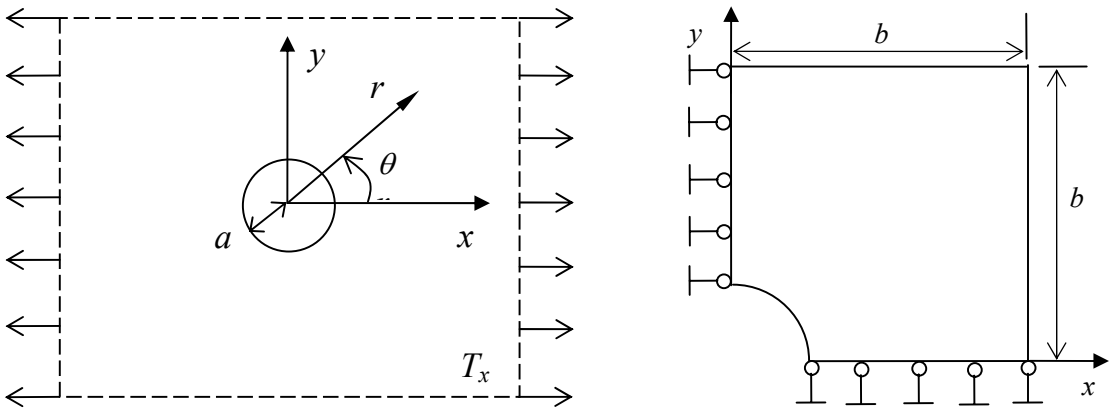

Figure 4.18 A quarter model of an infinite plate with a hole subjected to a tensile force

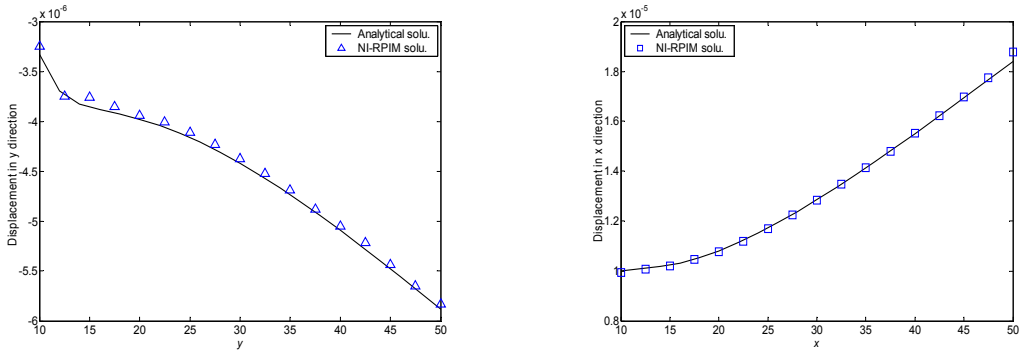

Figure 4.19 Displacement distribution along two boundary lines ($x = 0$ and $y = 0$)

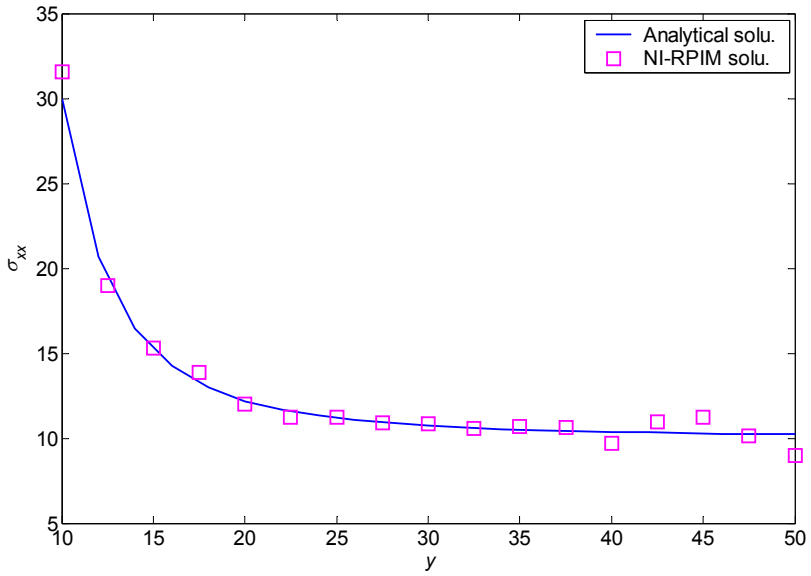

Figure 4.20 Stress distribution along the boundary line $(x = 0)$

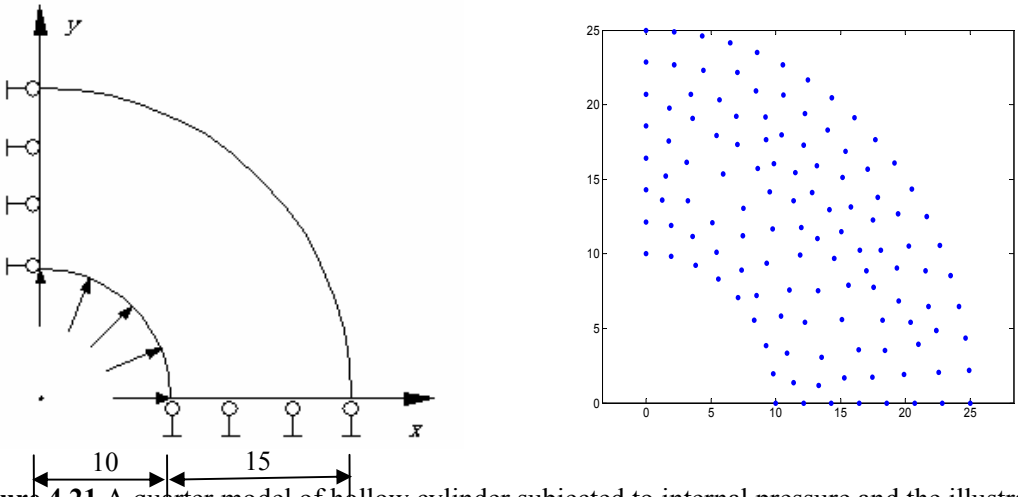

Figure 4.21 A quarter model of hollow cylinder subjected to internal pressure and the illustration of nodes distribution of 123 nodes

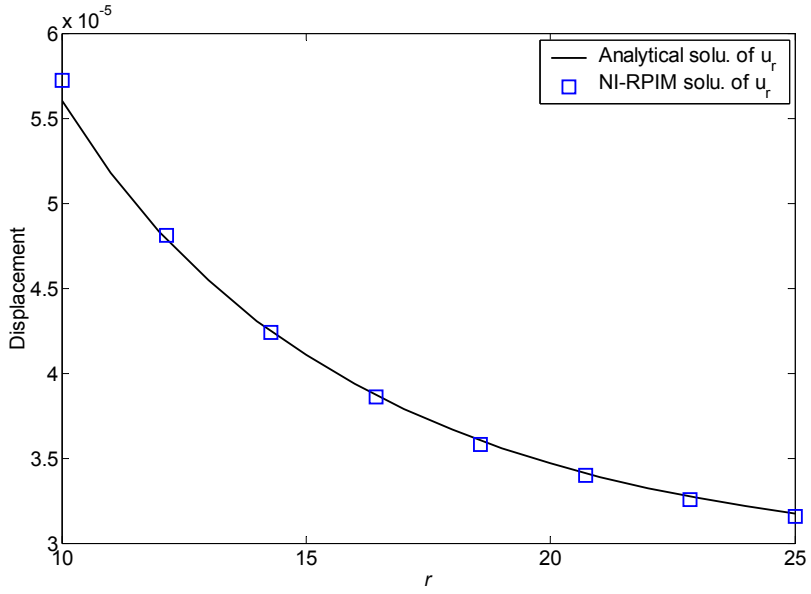

Figure 4.22 Displacement distribution along the boundary line $(x = 0)$

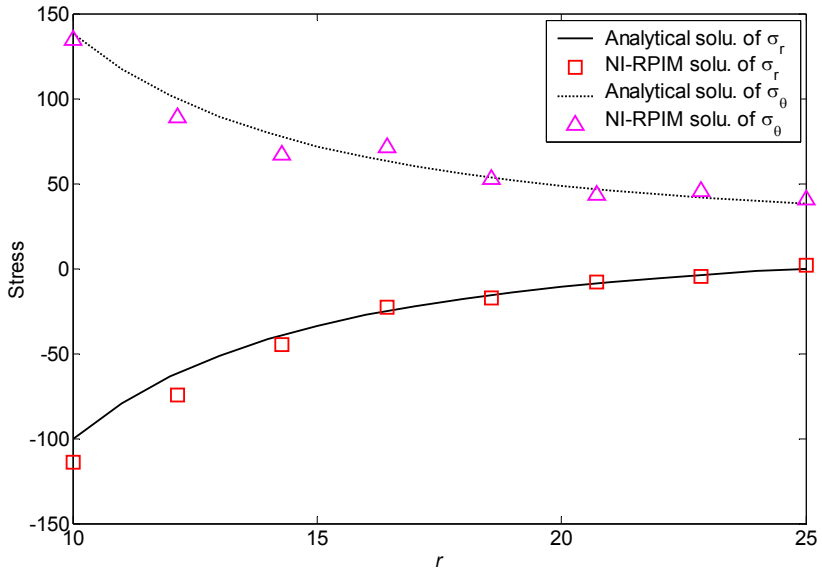

Figure 4.23 Stress distribution along the boundary line $(x = 0)$

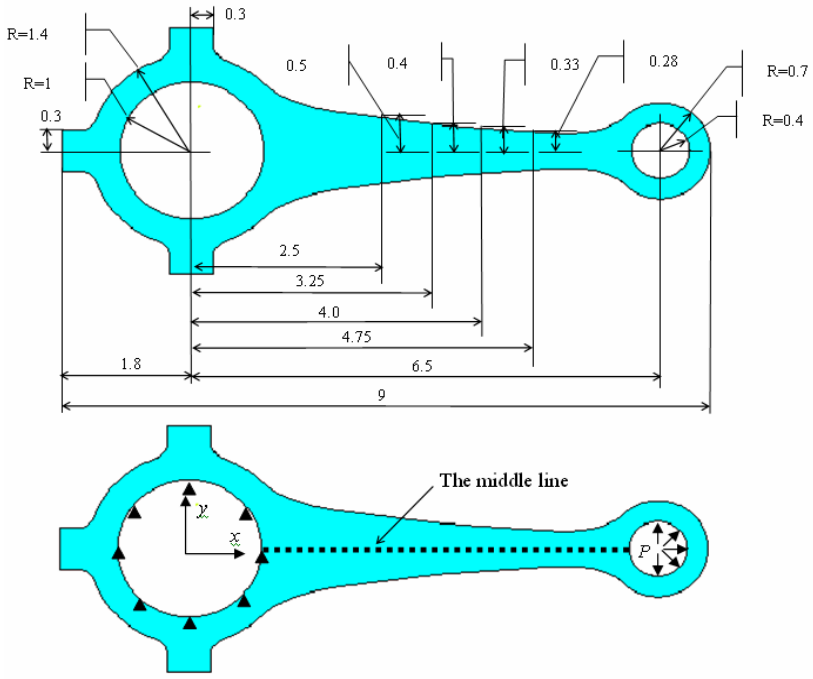

Figure 4.24 Model of the connecting rod used in automobiles

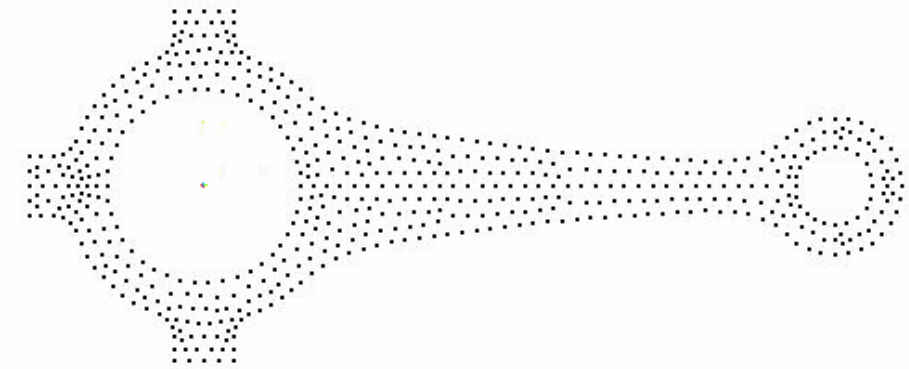

Figure 4.25 Nodal distribution for the connecting rod problem

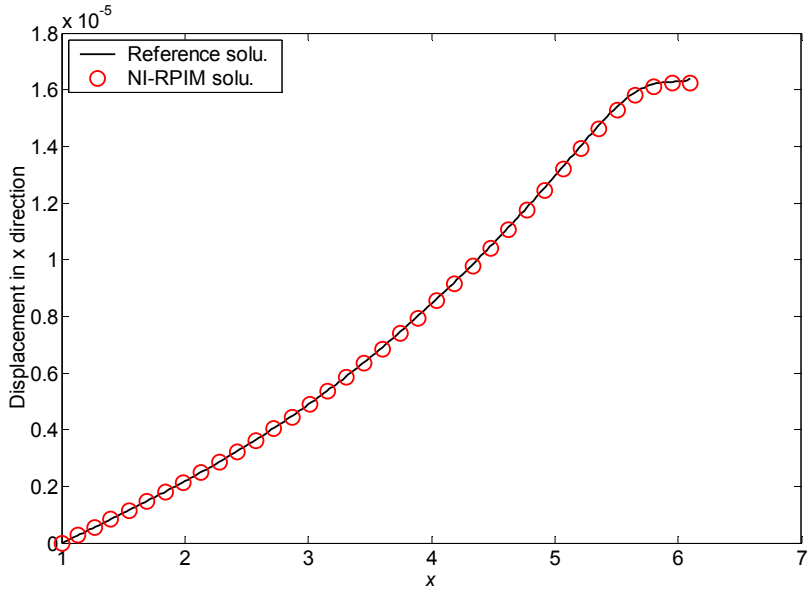

Figure 4.26 Displacement distribution along the middle line

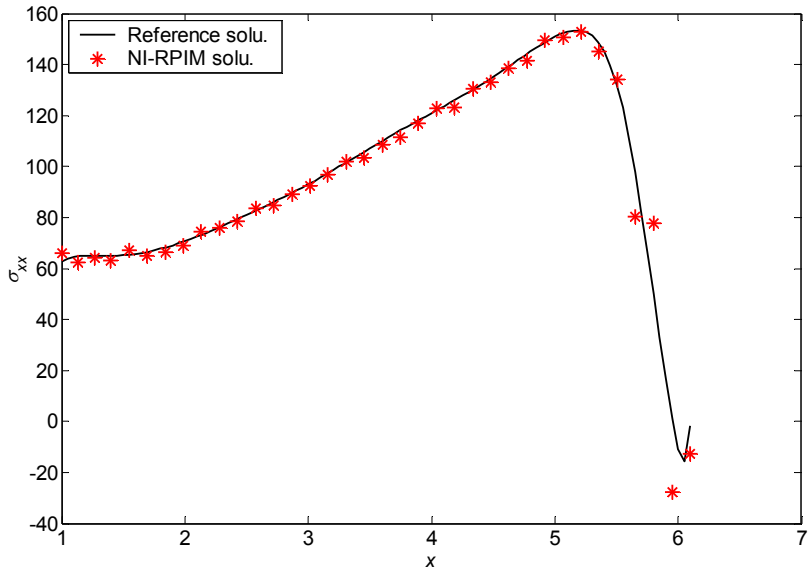

Figure 4.27 Normal stress (σ_{xx}) distribution along the middle line

Chapter 5

Linearly conforming point interpolation method (LC-PIM) for two-dimensional problems

5.1 Introduction

The traditional finite element method (FEM) has been used most widely for engineering problems. It is well known that the FEM provides a lower bound in energy norm for the exact solution to elasticity problems. It is, however, much more difficult to bound the solution from above for general problems in elasticity, and it has been a dream of many decades to find a systematical way to obtain an upper bound of the exact solution. This chapter presents a linearly conforming point interpolation method (LC-PIM) with a very important property: it provides general means to obtain an upper bound solution in energy norm for elasticity problems (Liu and Zhang, 2006).

The LC-PIM is evolved from the meshfree point interpolation method (PIM). The PIM was originally formulated based on the Galerkin weak-form with PIM shape functions constructed using a small set of nodes located in a local support domain with simple interpolation (details can be found in Chapter 2). The unique feature of PIM is that the shape functions possess Delta function property, which allows straightforward imposition of point essential boundary conditions. So far, two types of PIM have been developed by Liu and his coworkers, i.e., polynomial PIM which uses the polynomial

terms as the basis functions and radial point interpolation method which uses radial basis functions (RBFs).

Chen and his coworkers have developed a stabilized nodal integration scheme in which a strain smoothing operation is performed (Chen et al., 2001). Liu and his coworkers have developed a linearly conforming radial point interpolation method (LC-RPIM) by incorporating the nodal integration scheme with the original radial point interpolation method (RPIM) (Liu et al., 2006b). In the present work, a linearly conforming point interpolation method (LC-PIM) is formulated, in which the polynomial PIM shape functions are employed and the stabilized nodal integration scheme with strain smoothing operation is used for numerical integration. To construct polynomial PIM shape function, a scheme for the selection of local supporting nodes based on background cells is suggested, which can always ensure the moment matrix is invertible. The generalized Galerkin weak form is used for creating discretized system equations, and the stabilized nodal integration scheme with strain smoothing is used to perform the numerical integration.

In this chapter, the weak form for the LC-PIM based on the generalized two-field variational principle will be first derived. Then it will be proved that LC-PIM is variationally consistent. Finally, the upper bound property in energy norm for the LC-PIM will be demonstrated through a number of numerical examples.

5.2 Briefing on the finite element method (FEM)

5.2.1 Basic formulation

The standard formulation of finite element method (FEM) (Zienkiewicz et al. 2000; Liu and Quek, 2003) will be first briefed, as the formulation will be referenced in this chapter for times. In the FEM, the displacement field is assumed, and the discrete set of algebraic equations of FEM are generated from the following energy functional.

$$J(\mathbf{u}) = \int_{\Omega} \boldsymbol{\varepsilon}^T \mathbf{D} \boldsymbol{\varepsilon} d\Omega - \int_{\Omega} \mathbf{u}^T \mathbf{b} d\Omega - \int_{\Gamma_t} \mathbf{u}^T \hat{\mathbf{t}} d\Gamma \tag{5.1}$$

where $\boldsymbol{\varepsilon}$ is the stain obtained using the compatibility equation, $\mathbf{u} \in H^1(\Omega)$ are trial functions with corresponding test function of $\delta\mathbf{u} \in H_0^1(\Omega)$. Here $H^1(\Omega)$ denotes the Sobolev space of functions with square integrable derivatives in Ω, and $H_0^1(\Omega)$ is the subset of $H^1(\Omega)$. In the numerical implementations, the FEM divides the domain Ω into a number of elements, and the following trial functions are used.

$$\tilde{\mathbf{u}}(\mathbf{x}, \mathbf{d}) = \sum_{i \in n_e} \boldsymbol{\Phi}_i(\mathbf{x}) \mathbf{d}_i \tag{5.2}$$

where n_e is the set of nodes of the element containing $\mathbf{x}$, $\mathbf{d}_i = \begin{bmatrix} u_{xi} & u_{yi} \end{bmatrix}^T$ is the vector of nodal displacements, and $\boldsymbol{\Phi}$ is a matrix of shape functions.

$$\boldsymbol{\Phi}_i(\mathbf{x}) = \begin{bmatrix} \varphi_i(\mathbf{x}) & 0 \\ 0 & \varphi_i(\mathbf{x}) \end{bmatrix} \tag{5.3}$$

in which $\varphi_i(\mathbf{x})$ is the shape function for node *i*. Using the compatibility equations and Equation (5.2), the strain of FEM approximation is given by

$$\tilde{\boldsymbol{\varepsilon}}(\mathbf{x},\mathbf{d}) = \mathbf{L}_d \tilde{\mathbf{u}}(\mathbf{x},\mathbf{d}) = \sum_{i\in n_e} \underbrace{\mathbf{L}_d \boldsymbol{\Phi}_i(\mathbf{x})}_{\tilde{\mathbf{B}}_i} \mathbf{d}_i = \sum_{i\in n_e} \tilde{\mathbf{B}}_i \mathbf{d}_i \tag{5.4}$$

with the strain matrix of FEM defined as

$$\tilde{\mathbf{B}}_i(\mathbf{x}) = \mathbf{L}_d \boldsymbol{\Phi}_i(\mathbf{x}) = \begin{bmatrix} \dfrac{\partial \varphi_i(\mathbf{x})}{\partial x} & 0 \\ 0 & \dfrac{\partial \varphi_i(\mathbf{x})}{\partial y} \\ \dfrac{\partial \varphi_i(\mathbf{x})}{\partial y} & \dfrac{\partial \varphi_i(\mathbf{x})}{\partial x} \end{bmatrix} \tag{5.5}$$

where $\mathbf{L}_d$ is a matrix of differential operator defined as

$$\mathbf{L}_d = \begin{bmatrix} \frac{\partial}{\partial x} & 0 \\ 0 & \frac{\partial}{\partial y} \\ \frac{\partial}{\partial y} & \frac{\partial}{\partial x} \end{bmatrix} \tag{5.6}$$

The stationary conditions of functional J give the following standard Galerkin weak form.

$$\delta J(\mathbf{u}) = \int_\Omega (\delta\boldsymbol{\varepsilon})^T \mathbf{D}\boldsymbol{\varepsilon} d\Omega - \int_\Omega (\delta\mathbf{u})^T \mathbf{b} d\Omega - \int_{\Gamma_t} (\delta\mathbf{u})^T \hat{\mathbf{t}} d\Gamma = 0 \tag{5.7}$$

By substituting the approximations $\tilde{\mathbf{u}}$ into Equation (5.7) and invoking the arbitrariness of virtual nodal displacements, the standard discretized algebraic system equation can be obtained as follows.

$$\tilde{\mathbf{K}}\tilde{\mathbf{d}} = \tilde{\mathbf{f}} \tag{5.8}$$

where $\tilde{\mathbf{d}}$ is the vector of nodal displacement of FEM at all the unconstrained nodes, $\tilde{\mathbf{K}}$ is the (global) stiffness matrix of FEM that is assembled using

$$\tilde{\mathbf{K}}_{ij} = \int_{\Omega} \tilde{\mathbf{B}}_i^T \mathbf{D} \tilde{\mathbf{B}}_j d\Omega \tag{5.9}$$

and $\tilde{\mathbf{f}}$ is the vector of nodal forces at the unconstrained nodes that is assembled using

$$\tilde{\mathbf{f}}_i = \int_{\Omega} \mathbf{\Phi}_i^T(\mathbf{x}) \mathbf{b} d\Omega + \int_{\Gamma_t} \mathbf{\Phi}_i^T(\mathbf{x}) \hat{\mathbf{t}} d\Gamma \tag{5.10}$$

5.2.2 Some properties of FEM

Some properties of FEM are presented in this section, as these properties will be used in the following work.

Remark 5.2.1 Lower-bound property: The strain energy obtained from the FEM solution based on assumed displacements that are fully compatible is a lower bound of the exact strain energy. This property can be shown in the following.

The strain energy obtained from the FEM solution can be written as

$$\tilde{U}(\tilde{\mathbf{d}}) = \int_{\Omega} \frac{1}{2} \tilde{\boldsymbol{\varepsilon}}^T \mathbf{D} \tilde{\boldsymbol{\varepsilon}} \, d\Omega = \frac{1}{2} \tilde{\mathbf{d}}^T \tilde{\mathbf{K}} \tilde{\mathbf{d}} \tag{5.11}$$

Let the *exact* strain energy defined as

$$U_0 = \int_{\Omega} \frac{1}{2} \boldsymbol{\varepsilon}_0^T \mathbf{D} \boldsymbol{\varepsilon}_0 d\Omega \tag{5.12}$$

where $\boldsymbol{\varepsilon}_0$ is the exact solution of strains of the problem, which relates to the exact solution of displacement $\mathbf{u}_0$ in the form of $\boldsymbol{\varepsilon}_0 = \mathbf{L}_d \mathbf{u}_0$. For an FEM solution from solving Equation (5.8) based on assumed displacement that is fully compatible, the total potential energy at the stationary point can be written as

$$\tilde{J}(\tilde{\mathbf{d}}) = \frac{1}{2}\tilde{\mathbf{d}}^T\tilde{\mathbf{K}}\tilde{\mathbf{d}} - \tilde{\mathbf{d}}^T \underbrace{\tilde{\mathbf{f}}}_{\tilde{\mathbf{K}}\tilde{\mathbf{d}}} = -\frac{1}{2}\tilde{\mathbf{d}}^T\tilde{\mathbf{K}}\tilde{\mathbf{d}} = -\tilde{U}(\tilde{\mathbf{d}}) \tag{5.13}$$

As the FEM solution of a compatible model is based on the minimum total potential energy principle, it arrives

$$\tilde{J} = -\tilde{U} \geq J_0 = -U_0 \tag{5.14}$$

or

$$\tilde{U}\left(\tilde{\boldsymbol{\varepsilon}}\right) \leq U_0\left(\boldsymbol{\varepsilon}_0\right) \tag{5.15}$$

which means that the strain energy obtained from an FEM solution is a lower bound of the exact solution of strain energy.

Remark 5.1 implies that the strain energy obtained from the displacement-based fully compatible FEM solution is always an underestimate of the exact strain energy, and the displacement is always a lower bound of the exact solution in the "K norm" (or strain energy). Similar discussions on the lower bound property of FEM can be found in Zienkiewicz and Tlaylor's book (2000).

The above lower bound property of FEM valid for all types of elements as long as the displacement field is compatible. In this work, however, only linear triangular elements (that is compatible) are used in the FEM.

Remark 5.2.2 Monotonic property: For given a sequence of n_m meshes $M_1, M_2, \cdots, M_{n_m}$, in which the nodes in M_i contains that in $M_{i-1}\left(i = 2,3,\cdots,n_m\right)$, the following inequalities then stand

$$\widetilde{U}\left(\widetilde{\boldsymbol{\varepsilon}}_{M_1}\right) \leq \widetilde{U}\left(\widetilde{\boldsymbol{\varepsilon}}_{M_2}\right) \leq \cdots \leq \widetilde{U}\left(\widetilde{\boldsymbol{\varepsilon}}_{M_{nm}}\right) \leq U_0\left(\boldsymbol{\varepsilon}_0\right) \tag{5.16}$$

where $\tilde{\boldsymbol{\varepsilon}}_{m_i}$ is the FEM compatible solution of strains obtained using mesh m_i. This property can be shown easily using the arguments give by Oliveira (1968).

Remark 5.2.3 Reproducibility property: If the exact solution lives in the space of the shape functions used in Equation (5.2), the FEM solution of compatible model will be exact.

This property of FEM can be shown easily using the arguments given in Oliveira (1968) and Liu (2003).

5.3 Formulations of LC-PIM

5.3.1 Construction of PIM shape functions

In the polynomial PIM presented in Chapter 2, the shape functions are constructed using the point interpolation method (PIM) with a group of nodes in the local support domain of the point of interest. In the present LC-PIM, a scheme for selecting nodes for constructing PIM shape functions is proposed based on the background cells (Liu et al., 2005a). In the simplest setting of LC-PIM, background cells of 3-node triangles are employed for the construction of shape functions. When linear interpolation is used, any point of interest located in a cell is approximated using the three vertexes of this triangle, which is as same as the interpolation process in the conventional FEM. In the present work, the use of the simplest linear interpolation will be focused, that means the same interpolations as in the linear FEM are used. Without the loss of generality and for the convenience of the later discussion, the general procedure of forming the PIM shape functions will be reviewed.

Considering a problem in the domain Ω that is represented using a set of scattered nodes, the field variable $u(\mathbf{x})$ can be approximated using

$$u^h(\mathbf{x}) = \sum_{i=1}^{n} p(\mathbf{x}) a_i = \mathbf{p}^{\mathrm{T}}(\mathbf{x})\mathbf{a} \tag{5.17}$$

where $\mathbf{x} = [x \quad y]$ for 2D problems, $\mathbf{p}^{\mathrm{T}}(\mathbf{x}) = [1 \quad x \quad y \quad \cdots]$ is the vector of n terms of polynomial bases chosen from the Pascal's triangle, and $\mathbf{a} = [a_1 \quad a_2 \quad \cdots \quad a_n]$ is a vector of the unknown coefficients. Using n field nodes at $\mathbf{x}_i=[x_i, y_i]$, i=1,2, .. n, in the support domain of the $\mathbf{x}$, and enforcing Equation (5.17) passing through these three nodes, the shape functions can then be obtained as follows.

$$\mathbf{\Phi}(\mathbf{x}) = [1 \quad x \quad y \quad \cdots] \begin{bmatrix} 1 & x_1 & y_1 & \cdots \\ 1 & x_2 & y_2 & \cdots \\ \vdots & \vdots & \vdots & \vdots \\ 1 & x_n & y_n & \cdots \end{bmatrix}^{-1} \tag{5.18}$$

The approximation of the displacement at $\mathbf{x}$ can then be interpolated using the shape functions as

$$u^h(\mathbf{x}) = \mathbf{\Phi}^{\mathrm{T}}(\mathbf{x})\mathbf{U}_{\mathrm{s}} = [\varphi_1(\mathbf{x}) \quad \varphi_1(\mathbf{x}) \quad \cdots \quad \varphi_n(\mathbf{x})]\mathbf{U}_{\mathrm{s}} \tag{5.19}$$

where $\mathbf{U}_s = \{u_1 \quad u_2 \quad \cdots \quad u_n\}^T$ is the vector that collects the values of field variables at the n nodes. The explicit forms of the linear shape functions are exactly the same as that in the FEM using triangular elements that can be found in any textbook on FEM. The shape functions has therefore the Delta function property

$$\varphi_I(\mathbf{x}_J) = \delta_{IJ} \tag{5.20}$$

where δ_{IJ} is the Kronecker delta, and the partitions of unity property.

$$\sum_{I=1}^{NP} \varphi_I(\mathbf{x}) = 1 \tag{5.21}$$

The property of the Delta function allows straightforward imposition of point essential boundary conditions.

Note that the derivatives of the shape functions are basically constants and can be easily obtained, but they are not required in the LC-PIM formulation due to the use of strain smoothing technique in the process of nodal integration (Liu et al., 2005a).

5.3.2 Discretized system equations

The LC-PIM uses the generalized Galerkin weak form that can be expressed as

$$\int_{\Omega} \delta\left(\tilde{\boldsymbol{\varepsilon}}(\mathbf{u})\right)^T \mathbf{D}\left(\tilde{\boldsymbol{\varepsilon}}(\mathbf{u})\right) d\Omega - \int_{\Omega} \delta\mathbf{u}^T \mathbf{b} d\Omega - \int_{\Gamma_t} \delta\mathbf{u}^T \hat{\mathbf{t}} d\Gamma = 0 \tag{5.22}$$

The overall procedure of the LC-PIM is as follows. Firstly it is assumed that the displacement is approximated using Equation (5.19), which implies that the displacement at any point in the problem domain is interpolated using the PIM shape functions created using the nodes in the support domain of the point. Then the strain field is assumed using the assumed displacement field for each of the node, and hence the strain is not independent of the displacement. The strain energy (corresponding the first term in Equation (5.22)) in the problem domain is then calculated using the assumed strain. A set of discretized algebraic system equation can be obtained in the following matrix form.

$$\tilde{\mathbf{K}}\tilde{\mathbf{d}} = \tilde{\mathbf{f}} \tag{5.23}$$

In obtaining the integrations over the problem domain Ω need to be performed based on the nodes. The detailed procedure leading to Equation (5.23) is given in the next sub-section.

For the convenience in the derivation, the same set of shape functions for both FEM and LC-PIM are used, and therefore the assumed displacement in LC-PIM is also $\tilde{\mathbf{u}}$ defined in Equation (5.2), and $\tilde{\mathbf{f}}$ and $\hat{\mathbf{f}}$ are also the same. In the following there will thus no difference between $\tilde{\mathbf{f}}$ and $\hat{\mathbf{f}}$. Note that the resultant strains $\tilde{\boldsymbol{\varepsilon}}$ in FEM and the assumed strains $\hat{\boldsymbol{\varepsilon}}$ in LC-PIM are different, and so are the solution of the nodal displacements for FEM $\tilde{\mathbf{d}}$ and that of LC-PIM $\hat{\mathbf{d}}$.

5.3.3 Nodal integration scheme with strain smoothing operation

In the LC-PIM, the integration required in the weak form Equation (5.22) is performed based on each of the nodes in the problem domain, and a stabilized nodal integration scheme (Chen et al., 2001) is used in the LC-PIM. In such nodal integration process, the problem domain Ω is divided into smoothing domains $\Omega = \Omega_1 \cup \Omega_2 \cup \cdots \cup \Omega_N$ in which N is the number of total field nodes located in the entire problem domain. The smoothing domain Ω_k for each node is created by connecting sequentially the mid-edge-point to the centroids of the surrounding triangles of the node as shown in Figure 5.1 (Ferzige and Peric, 1999).

Introducing the smoothing operation, the strains to be used in Equation (5.22) is assumed to be the *smoothed* strain for node k defined by

$$\widehat{\boldsymbol{\varepsilon}}_k \equiv \widehat{\boldsymbol{\varepsilon}}\ \left(\mathbf{x}_k\right) = \int_{\Omega_k} \boldsymbol{\varepsilon}\left(\mathbf{x}\right) \widehat{\mathbf{W}}\left(\mathbf{x}-\mathbf{x}_k\right) d\Omega \tag{5.24}$$

where $\widehat{\mathbf{W}} = \begin{bmatrix} \widehat{W} & \widehat{W} & \widehat{W} \end{bmatrix}$ is a diagonal matrix of smoothing function $\widehat{W}$. For simplicity, the smoothing function is taken as

$$\widehat{W}\left(\mathbf{x}-\mathbf{x}_k\right) = \begin{cases} 1/A_k & \mathbf{x} \in \Omega_k \\ 0 & \mathbf{x} \notin \Omega_k \end{cases} \tag{5.25}$$

where $A_k = \int_{\Omega_k} d\Omega$ is the area of smoothing domain for node k.

Substituting Equation (5.25) into Equation (5.24) and integrating by parts, the smoothed strain can be calculated using

$$\widehat{\boldsymbol{\varepsilon}}_k = \frac{1}{A_k}\int_{\Omega_k} \boldsymbol{\varepsilon}\left(\mathbf{x}\right) d\Omega = \frac{1}{A_k}\int_{\Gamma_k} \mathbf{L}_n \mathbf{u}\left(\mathbf{x}\right) d\Gamma = \widehat{\boldsymbol{\varepsilon}}_k\left(\mathbf{u}\right) \tag{5.26}$$

where $\mathbf{L}_n^T = \begin{bmatrix} n_x & 0 & n_y \\ 0 & n_y & n_x \end{bmatrix}$ is the matrix of unit outward normal, Γ_k is the boundary of the smoothing domain for node k and n_i is the i^{th} components of the outward normal vector on Γ_k. Equation (5.26) states that the assumed strain $\widehat{\boldsymbol{\varepsilon}}_k$ is a function of assumed displacement $\mathbf{u}^h$.

Substituting Equation (5.19) into Equation (5.26), the smoothed strain can be written in the following matrix form of nodal displacements.

$$\widehat{\boldsymbol{\varepsilon}}_k = \sum_{i \in N_{infl}} \widehat{\mathbf{B}}_i\left(\mathbf{x}_k\right) \mathbf{U}_i \tag{5.27}$$

where N_{infl} is the number of nodes in the influence domain of node k (including node k). When linear shape functions are used, it is the number of nodes that are directly

connected to node k in the triangular mesh (see, Figure 5.1). In Equation (5.27), the $\widehat{\mathbf{B}}_i(\mathbf{x}_k)$ is termed as the *smoothed* strain matrix that is calculated using

$$\widehat{\mathbf{B}}_i(\mathbf{x}_k)=\begin{bmatrix} \widehat{b}_{ix}(\mathbf{x}_k) & 0 \\ 0 & \widehat{b}_{iy}(\mathbf{x}_k) \\ \widehat{b}_{iy}(\mathbf{x}_k) & \widehat{b}_{ix}(\mathbf{x}_k) \end{bmatrix} \tag{5.28}$$

Using the Gauss integration along each segment of boundary Γ_k, the integration in above equation can be calculated as

$$\widehat{b}_{il}=\frac{1}{A_k}\sum_{m=1}^{N_s}\left[\sum_{n=1}^{N_g} w_n\varphi_i(\mathbf{x}_{mn})n_l(\mathbf{x}_m)\right] \quad (l=x,y) \tag{5.29}$$

where N_s is the number of segments of the boundary Γ_k, N_g is the number of Gauss points used in each segment, and w_n is the corresponding weight number of Gauss integration scheme. In the LC-PIM using linear shape functions, $n_g=1$ is used. The entries in sub-matrices of the stiffness matrix **K** in Equation (5.23) is then expressed as

$$\widehat{\mathbf{K}}_{ij}=\sum_{k=1}^{N}\widehat{\mathbf{K}}_{ij(k)} \tag{5.30}$$

where the summation means an assembly process as we practice in the FEM, and $\widehat{\mathbf{K}}_{ij(k)}$ is the stiffness matrix associated with node k that is computed using

$$\widehat{\mathbf{K}}_{ij(k)}=\int_{\Omega_k}\widehat{\mathbf{B}}_i^{\mathrm{T}}\mathbf{D}\widehat{\mathbf{B}}_j d\Omega=\widehat{\mathbf{B}}_i^{\mathrm{T}}\mathbf{D}\widehat{\mathbf{B}}_j A_k \tag{5.31}$$

The entries (in sub-vectors of nodal forces) of the force vector $\widehat{\mathbf{f}}$ in Equation (5.23) can be simply expressed as

$$\widehat{\mathbf{f}}_i = \sum_{k \in N_{infl}} \widehat{\mathbf{f}}_{i(k)} \tag{5.32}$$

The above integration is also performed by a summation of integrals over smoothing domains, and hence is $\widehat{\mathbf{f}}_i$ is an assembly of nodal force vectors at the surrounding nodes of node *k*.

$$\widehat{\mathbf{f}}_{i(k)} = \int_{\Gamma_{t(k)}} \varphi_i \hat{\mathbf{t}} d\Gamma + \int_{\Omega_{(k)}} \varphi_i \mathbf{b} d\Omega \tag{5.33}$$

Note again that the force vector obtained in LC-PIM is the same as that in the FEM, if the same order of shape functions are used. Therefore, it is shown again that there is not difference between $\tilde{\mathbf{f}}$ and $\widehat{\mathbf{f}}$.

5.3.4 Comparison between LC-PIM and FEM

The FEM and the LC-PIM are compared in the following sub-section.

Remark 5.3.1 When FEM and LC-PIM use the same triangular mesh, one has the same set of nodes for nodal displacements, and the same size in the discrete system equations and the number of unknowns. The interpolation of displacements in both FEM and LC-PIM are essentially the same. The stiffness matrices have the same sparsity and bandwidth, if the same numbering system for the nodes is used. The stiffness matrices obtained using both FEM and LC-PIM are symmetric positive definite (SPD), if sufficient constraints are applied to eliminate the rigid body movement. The displacement field in both FEM and LC-PIM are compatible in the global problem domain. Note that when higher order interpolation schemes are used, FEM and LC-PIM will depart: FEM

uses element-based interpolation, but LC-PIM has overlapping in the use of nodes for interpolation.

Remark 5.3.2 The shape functions used in FEM and LC-PIM are all have the property of the Delta function, which allows straightforward imposition of essential boundary conditions.

Remark 5.3.3 The integration in FEM is element based, but the integration in LC-PIM is nodal smoothing domain based.

Remark 5.3.4 Both FEM and LC-PIM can reproduce linear displacement field exactly and hence pass the standard patch test (to machine accuracy), if shape functions of at least 1^{st} order are used. This allows both FEM and LC-PIM converge to the exact solution of any higher order field.

Remark 5.3.5 The FEM is capable of reproducing any high order field, as long as the field lives in the space of the FEM shape functions; LC-PIM can only approximate the high order field, even if high order shape functions are used. In FEM the strains in the element are obtained using the compatibility equations and Equation (5.2), and hence it is a fully compatible mode; In the LC-PIM, however, the strains in the smoothing cells are obtained using Equation (5.27), and hence will not be compatible within the smoothing cells, in terms of satisfying the displacement-strain relations.

Remark 5.3.6 The FEM solution does not in general satisfy the equilibrium conditions locally (either at any point in the elements or element-wise). The LC-PIM solution, on the other hand, satisfies the equilibrium equations (free of body force) at any point within the smoothing domain, for each of the smoothing domains, and hence at any point in the entire problem domain. However, on the interfaces of the smoothing domains, only the

displacement compatibility is ensured. Therefore, the LC-PIM behaves very much like an *equilibrium model*, but not exactly an equilibrium model. It is a combination of equilibrium model and compatible model.

Remark 5.3.7 FEM model using triangular elements behaviors very "stiff", and stress result is in general not very accurate; The LC-PIM model using exactly the same triangular mesh behaviors much softer, and stress result is in general more accurate.

Remark 5.3.8 In terms of convergence rate, for the same problem with same mesh, the LC-PIM obtains similar value of convergence rate in displacement norm. The convergence rate in energy norm of the LC-PIM with linear elements is, in theory, between 1.0 and 2.0, which is higher than that of the FEM model with compatible linear elements.

Remark 5.3.9 In terms of computational efficiency, for the same problem of same mesh the CPU time required by FEM and LC-PIM are in the same level. For a solution of same accuracy in stress, the LC-PIM is more efficient.

Remark 5.3.10 The displacement-based fully compatible FEM model provides the lower bound for the solution (in energy norm), and the LC-PIM provides the upper bound of the solution which will be discussed intensively in the following sections.

5.4 Variational principle for LC-PIM

5.4.1 Weak form for LC-PIM

In this section, the weak form for the LC-PIM will be discussed in detail. Firstly two independent field variables are assumed: strain field and the displacement field, and the generalized Reissner's two-field variational principle (Pian and Wu, 2006) is used as:

$$J(\mathbf{u},\boldsymbol{\varepsilon}) = -\int_{\Omega}\frac{1}{2}\boldsymbol{\varepsilon}^T\mathbf{D}\boldsymbol{\varepsilon}d\Omega - \int_{\Omega}\left(\mathbf{L}_d^T\boldsymbol{\sigma}+\mathbf{b}\right)^T\mathbf{u}d\Omega + \int_{\Gamma_u}\mathbf{t}^T\hat{\mathbf{u}}d\Gamma - \int_{\Gamma_t}\left(\hat{\mathbf{t}}-\mathbf{t}\right)^T\mathbf{u}d\Gamma \tag{5.34}$$

where $\boldsymbol{\varepsilon}$ is the assumed strain vector, the stresses $\boldsymbol{\sigma}$ is dependent on the strains $\tilde{\boldsymbol{\varepsilon}}$ through the stress-strain relation $\boldsymbol{\sigma}=\mathbf{D}\boldsymbol{\varepsilon}$, $\mathbf{t}$ is the traction on the boundary that is depending on the stress $\boldsymbol{\sigma}$ in the form of

$$\mathbf{L}_n^T\boldsymbol{\sigma} = \mathbf{t} \tag{5.35}$$

Using the Green's divergence theorem, the second term in the right-hand side of Equation (5.34) can be further express as

$$\int_{\Omega}\left(\mathbf{L}_d^T\boldsymbol{\sigma}+\mathbf{b}\right)^T\mathbf{u}d\Omega = \int_{\Gamma}\mathbf{L}_n^T\boldsymbol{\sigma}\mathbf{u}d\Gamma - \int_{\Omega}\boldsymbol{\sigma}^T\left(\mathbf{L}_d\mathbf{u}\right)d\Omega + \int_{\Omega}\mathbf{b}^T\mathbf{u}d\Omega \tag{5.36}$$

Substituting Equation (5.36) into Equation (5.34) gives

$$\begin{aligned} J(\mathbf{u},\boldsymbol{\varepsilon}) = &-\int_{\Omega}\frac{1}{2}\boldsymbol{\varepsilon}^T\mathbf{D}\boldsymbol{\varepsilon}d\Omega - \int_{\Gamma}\mathbf{L}_n^T\boldsymbol{\sigma}\mathbf{u}d\Gamma + \int_{\Omega}\boldsymbol{\sigma}^T\left(\mathbf{L}_d\mathbf{u}\right)d\Omega \\ &-\int_{\Omega}\mathbf{b}^T\mathbf{u}d\Omega + \int_{\Gamma_u}\mathbf{t}^T\hat{\mathbf{u}}d\Gamma - \int_{\Gamma_t}\left(\hat{\mathbf{t}}-\mathbf{t}\right)^T\mathbf{u}d\Gamma \end{aligned} \tag{5.37}$$

To split the 2nd term of the integration over the entire boundary to two integrations over the displacement boundary Γ_u and over the stress boundary Γ_t, and then rearranging these terms in Equation (5.37) gives

$$J(\mathbf{u},\boldsymbol{\varepsilon}) = -\int_{\Omega}\frac{1}{2}\boldsymbol{\varepsilon}^T\mathbf{D}\boldsymbol{\varepsilon}d\Omega + \int_{\Omega}\boldsymbol{\sigma}^T\left(\mathbf{L}_d\mathbf{u}\right)d\Omega - \int_{\Omega}\mathbf{b}^T\mathbf{u}d\Omega - \int_{\Gamma_t}\hat{\mathbf{t}}^T\mathbf{u}d\Gamma$$
$$-\int_{\Gamma_u}\left(\mathbf{L}_n^T\boldsymbol{\sigma}-\mathbf{t}^T\right)\hat{\mathbf{u}}d\Gamma - \int_{\Gamma_t}\left(\mathbf{L}_n^T\boldsymbol{\sigma}-\mathbf{t}^T\right)\mathbf{u}d\Gamma \tag{5.38}$$

Invoking now Equation (5.35) and using $\boldsymbol{\sigma} = \mathbf{D}\boldsymbol{\varepsilon}$, it arrived at

$$J(\mathbf{u},\boldsymbol{\varepsilon}) = -\int_{\Omega}\frac{1}{2}\boldsymbol{\varepsilon}^T\mathbf{D}\boldsymbol{\varepsilon}d\Omega + \left(-\int_{\Omega}\mathbf{b}^T\mathbf{u}d\Omega - \int_{\Gamma_t}\hat{\mathbf{t}}^T\mathbf{u}d\Gamma\right) + \int_{\Omega}\left(\boldsymbol{\varepsilon}^T\mathbf{D}\right)\left(\mathbf{L}_d\mathbf{u}\right)d\Omega \tag{5.39}$$

Note that Equation (5.39) is similar to the modified Hellinger-Reissner variational principle with strains $\tilde{\boldsymbol{\varepsilon}}$ and displacements $\mathbf{u}$ as independent field variables (Pian and Wu, 2006).

Using Equation (5.26), the functional of single displacement variable in the following form is obtained.

$$J(\mathbf{u}) = \underbrace{-\int_{\Omega}\frac{1}{2}\left(\hat{\boldsymbol{\varepsilon}}(\mathbf{u})\right)^T\mathbf{D}\left(\hat{\boldsymbol{\varepsilon}}(\mathbf{u})\right)d\Omega}_{\hat{U}(\mathbf{u})} + \underbrace{\left(-\int_{\Omega}\mathbf{b}^T\mathbf{u}d\Omega - \int_{\Gamma_t}\hat{\mathbf{t}}^T\mathbf{u}d\Gamma\right)}_{W(\mathbf{u})} + \underbrace{\int_{\Omega}\left(\hat{\boldsymbol{\varepsilon}}^T\mathbf{D}\right)\underbrace{\left(\mathbf{L}_d\mathbf{u}\right)}_{\boldsymbol{\varepsilon}(\mathbf{u})}d\Omega}_{V_{\hat{\boldsymbol{\varepsilon}}}(\mathbf{u})} \tag{5.40}$$
$$= -\hat{U}(\mathbf{u}) + W(\mathbf{u}) + V_{\hat{\boldsymbol{\varepsilon}}}(\mathbf{u})$$

where $\hat{U}(\mathbf{u})$ is the strain energy potential with smoothed strains, $W(\mathbf{u})$ is the work potential of external force, and $V_{\hat{\boldsymbol{\varepsilon}}}(\mathbf{u})$ is the strain energy potential of the smoothed strains on the assumed displacement field. Let's now examine in detail $V_{\hat{\boldsymbol{\varepsilon}}}(\mathbf{u})$ in the LC-PIM setting, through which the following remark is proved.

Theorem 5.1 The LC-PIM is variationally consistent, and the generalized Galerkin weak form Equation (5.22) is variationally valid weak form for the LC-PIM.

Proof

In the process of the nodal integration used in LC-PIM, the problem domain Ω is divided into smoothing domains $\Omega = \Omega_1 \cup \Omega_2 \cup \cdots \cup \Omega_N$ and each of which contains a node. The smoothing domain Ω_k for the k^{th} node is created by connecting sequentially the mid-edge-point to the centroids of the surrounding triangles of the node as shown in Figure 5.1. Note that due to the smoothing operation, the assumed strains $\widehat{\boldsymbol{\varepsilon}}_k$ are constants in Ω_k and the corresponding stresses $\widehat{\boldsymbol{\sigma}}_k = \mathbf{D}\widehat{\boldsymbol{\varepsilon}}_k$ are thus also constant in Ω_k. Therefore, $\boldsymbol{\sigma}$ is bounded and continuous in each of the smoothing domain Ω. Due to the fact that the shape functions used in Equation (5.19) are linear functions, the strain $\boldsymbol{\varepsilon}$ is also a continuous function in each of the domain Ω. It can be obtained that

$$V_{\tilde{\varepsilon}}(\mathbf{u}) = \int_{\Omega} \tilde{\boldsymbol{\varepsilon}}^T \mathbf{D}\boldsymbol{\varepsilon} d\Omega = \int_{\Omega} \tilde{\boldsymbol{\varepsilon}}^T \mathbf{D}\left(\mathbf{L}_d \mathbf{u}\right) d\Omega = \sum_{k=1}^{N} \int_{\Omega_k} \tilde{\boldsymbol{\varepsilon}}_k^T \mathbf{D}\left(\mathbf{L}_d \mathbf{u}\right) d\Omega \tag{5.41}$$

Using Green's divergence theorem for each smoothing domain Ω_k, and the fact that $\mathbf{L}^T\left(\widehat{\boldsymbol{\varepsilon}}_k^T \mathbf{D}\right)$ vanishes in Ω_k, it arrived at

$$\begin{aligned} V_{\tilde{\varepsilon}}(\mathbf{u}) &= \sum_{k=1}^{N} \left[\int_{\Gamma_k} \left(\widehat{\boldsymbol{\varepsilon}}_k^T \mathbf{D}\right)\left(\mathbf{L}_n \mathbf{u}\right) d\Gamma - \int_{\Omega_k} \underbrace{\left(\mathbf{L}_d^T (\widehat{\boldsymbol{\varepsilon}}_k^T \mathbf{D})\right)^T}_{=0,\ \text{in}\ \Omega_k} \mathbf{u} d\Omega \right] \\ &= \sum_{k=1}^{N} \int_{\Gamma_k} \widehat{\boldsymbol{\varepsilon}}_k^T \mathbf{D}\left(\mathbf{L}_n \mathbf{u}\right) d\Gamma \end{aligned} \tag{5.42}$$

Again since $\widehat{\boldsymbol{\varepsilon}}_k$ is constant in Ω_k, then

$$V_{\tilde{\varepsilon}}(\mathbf{u}) = \sum_{k=1}^{N} \left(\widehat{\boldsymbol{\varepsilon}}_k^T \mathbf{D}\right) \underbrace{\int_{\Gamma_k} \left(\mathbf{L}_n \mathbf{u}\right) d\Gamma}_{\bar{\boldsymbol{\varepsilon}}_k A_k} = \sum_{k=1}^{N} \widehat{\boldsymbol{\varepsilon}}_k^T \mathbf{D} \widehat{\boldsymbol{\varepsilon}}_k A_k = \int_{\Omega} \widehat{\boldsymbol{\varepsilon}}^T \mathbf{D} \widehat{\boldsymbol{\varepsilon}}\ d\Omega = 2\widehat{U}(\mathbf{u}) \tag{5.43}$$

In deriving above equation, Equation (5.26) was used. Equation (5.43) means that the LC-PIM satisfies the orthogonal conditions (Simo and Hughes, 1998):

$$\int_{\Omega} \tilde{\boldsymbol{\varepsilon}}^T \mathbf{D} \boldsymbol{\varepsilon} d\Omega = \int_{\Omega} \tilde{\boldsymbol{\varepsilon}}^T \mathbf{D} \hat{\boldsymbol{\varepsilon}} \, d\Omega \tag{5.44}$$

which implies that LC-PIM is variationally consistent.

Substituting Equation (5.43) into Equation (5.40), the following energy functional for the LC-PIM can be obtained.

$$J(\mathbf{u}) = \int_{\Omega} \frac{1}{2} \left(\hat{\boldsymbol{\varepsilon}}(\mathbf{u})\right)^T \mathbf{D} \left(\hat{\boldsymbol{\varepsilon}}(\mathbf{u})\right) d\Omega - \int_{\Omega} \mathbf{b}^T \mathbf{u} d\Omega - \int_{\Gamma_t} \hat{\mathbf{t}}^T \mathbf{u} d\Gamma \tag{5.45}$$

This is a mixed variational principle of the assumed strain method (Simo and Hughes, 1998), and the corresponding weak form is Equation (5.22).

Note that the difference between the standard Galerkin weak form and the generalized Galerkin weak form, is that in the standard Galerkin weak form the compatible strains obtained using $\boldsymbol{\varepsilon} = \mathbf{L}\mathbf{u}$ are used, but in the generalized Galerkin weak form the assumed strain $\hat{\boldsymbol{\varepsilon}}$ is used, that is, in the case of LC-PIM, given by Equation (5.27). In general, the assumed strain may not satisfy the orthogonal condition Equation (5.44), and the formulation based on the generalized Galerkin weak form will not be variationally consistent. A variationally inconsistent formulation can work well, if it is energy consistent such as the smoothed finite element method (SFEM) proposed by Liu et al. (2006 c, d). The SFEM is formulated by incorporating cell-wise strain smoothing operation into standard compatible finite element method (FEM). When the number of smoothing cells of the elements is a finite number larger than 1, the SFEM solutions are not variationally consistent but energy consistent and can also work well. A detailed proof for this conclusion has been provided by Liu and his coworkers (Liu et al., 2007b). On the other hand, a variationally consistent formulation does not in general guarantee a stable solution. A typical example is the SFEM with SC=1 can have hour-glass

instability for some problems (see, Liu et al., 2007a, b). The reason is that due to the use of assumed strain $\tilde{\boldsymbol{\varepsilon}}$ instead of the compatible strain $\boldsymbol{\varepsilon}$, the formulation becomes incompatible. Hence, it is well possible that the resultant stiffness matrix (still symmetric) can have zero eigenvalues even if physically sufficient support is imposed. The LC-PIM works very well, and any zero eigenvalues or unstable modes for all the example problems studied so far using triangular background meshes has not been discovered.

It is well known in FEM (Zienkiewicz and Taylor, 2000) that if the number of independent relations provided by all integration points must be no less than the number of unknowns, or the stiffness matrix **K** must be singular or containing as zero-eigenvalue. This concept has also been applied to analyze meshfree methods (Liu, 2002). Considering now the present LC-PIM for 2D problems, there are three independent strain relations at each node and the total number of independent equations generated in LC-PIM will be $3N$, where N is the total number of field nodes in the whole problem domain. The number of unknown variables should be $2N–N_f$, where N_f is the number of constrained degrees of freedoms. It is obvious that the LC-PIM always satisfy the requirement mentioned above, which concludes that the LC-PIM will not encounter the problem of zero eigenvalues or unstable modes. This is also confirmed by the results of all the numerical examples. The LC-PIM will have no zero-energy modes and always be stable as long as the problem is well-posed (physically sufficient support is imposed).

5.4.2 Upper bound property of LC-PIM

It was discovered that the solution of LC-PIM has always been the upper bound of the exact solution in energy norm, which will also be demonstrated in all the examples given in the next section. To understand this property, the relationship of solutions of a LC-PIM model, a FEM model and the exact model are closely examined.

1) LC-PIM vs. FEM

Lemma 5.1 For any given admissible displacement field $\mathbf{u}$, the strain potential $\hat{U}(\mathbf{u})$ for a LC-PIM model obtained using the smoothed strains is no-larger than the strain potential $\tilde{U}(\mathbf{u})$ for a FEM model of compatible displacements:

$$\hat{U}(\mathbf{u}) \le \tilde{U}(\mathbf{u}) \tag{5.46}$$

in which

$$\begin{aligned} \hat{U}(\mathbf{u}) &= \int_{\Omega} \frac{1}{2} \hat{\boldsymbol{\varepsilon}}^T(\mathbf{u}) \mathbf{D} \hat{\boldsymbol{\varepsilon}}(\mathbf{u}) d\Omega \\ \tilde{U}(\mathbf{u}) &= \int_{\Omega} \frac{1}{2} \tilde{\boldsymbol{\varepsilon}}^T(\mathbf{u}) \mathbf{D} \tilde{\boldsymbol{\varepsilon}}(\mathbf{u}) d\Omega \end{aligned} \tag{5.47}$$

where $\hat{\boldsymbol{\varepsilon}}$ is the smoothed strain obtained in LC-PIM using Equation (5.27) and $\tilde{\boldsymbol{\varepsilon}}$ is the strain obtained in FEM.

Proof

It is examined that

$$\begin{aligned}
&\int_\Omega \frac{1}{2}\left(\hat{\boldsymbol{\varepsilon}}-\tilde{\boldsymbol{\varepsilon}}\right)^T \mathbf{D}\left(\hat{\boldsymbol{\varepsilon}}-\tilde{\boldsymbol{\varepsilon}}\right)d\Omega \\
&=\int_\Omega \frac{1}{2}\hat{\boldsymbol{\varepsilon}}^T\mathbf{D}\hat{\boldsymbol{\varepsilon}}d\Omega-\int_\Omega \frac{1}{2}\hat{\boldsymbol{\varepsilon}}^T\mathbf{D}\tilde{\boldsymbol{\varepsilon}}d\Omega-\int_\Omega \frac{1}{2}\tilde{\boldsymbol{\varepsilon}}^T\mathbf{D}\hat{\boldsymbol{\varepsilon}}d\Omega+\int_\Omega \frac{1}{2}\tilde{\boldsymbol{\varepsilon}}^T\mathbf{D}\tilde{\boldsymbol{\varepsilon}}d\Omega \\
&=\int_\Omega \frac{1}{2}\hat{\boldsymbol{\varepsilon}}^T\mathbf{D}\hat{\boldsymbol{\varepsilon}}d\Omega-\int_\Omega \hat{\boldsymbol{\varepsilon}}^T\mathbf{D}\tilde{\boldsymbol{\varepsilon}}d\Omega+\int_\Omega \frac{1}{2}\tilde{\boldsymbol{\varepsilon}}^T\mathbf{D}\tilde{\boldsymbol{\varepsilon}}d\Omega
\end{aligned} \tag{5.48}$$

Using the orthogonal condition Equation (5.44) that holds for any $\boldsymbol{\varepsilon}$, and the fact that $\tilde{\boldsymbol{\varepsilon}}$ is a special case of $\boldsymbol{\varepsilon}$, and $\mathbf{D}$ is SPD, it can be obtained that

$$\underbrace{\int_\Omega \frac{1}{2}\left(\hat{\boldsymbol{\varepsilon}}-\tilde{\boldsymbol{\varepsilon}}\right)^T \mathbf{D}\left(\hat{\boldsymbol{\varepsilon}}-\tilde{\boldsymbol{\varepsilon}}\right)d\Omega}_{\geq 0}=\int_\Omega \frac{1}{2}\tilde{\boldsymbol{\varepsilon}}^T\mathbf{D}\tilde{\boldsymbol{\varepsilon}}d\Omega-\int_\Omega \frac{1}{2}\hat{\boldsymbol{\varepsilon}}^T\mathbf{D}\hat{\boldsymbol{\varepsilon}}d\Omega\geq 0 \tag{5.49}$$

which gives Equation (5.46).

Equation (5.46) can be written in discrete form of arbitrary (but admissible) nodal displacement $\mathbf{d}$ as

$$\underbrace{\frac{1}{2}\mathbf{d}^T\hat{\mathbf{K}}\mathbf{d}}_{\hat{U}(\mathbf{d})}\leq\underbrace{\frac{1}{2}\mathbf{d}^T\tilde{\mathbf{K}}\mathbf{d}}_{\tilde{U}(\mathbf{d})} \tag{5.50}$$

Corollary 5.1 For any admissible assumed nodal displacement field $\mathbf{d}$, total potential $\tilde{J}(\mathbf{d})$ for FEM model is no-less than that $\hat{J}(\mathbf{d})$ for LC-PIM model:

$$\tilde{J}(\mathbf{d})\geq\hat{J}(\mathbf{d}) \tag{5.51}$$

where

$$\begin{aligned}
\tilde{J}(\mathbf{d})&=\frac{1}{2}\mathbf{d}^T\tilde{\mathbf{K}}\mathbf{d}-\mathbf{d}^T\tilde{\mathbf{f}} \\
\hat{J}(\mathbf{d})&=\frac{1}{2}\mathbf{d}^T\hat{\mathbf{K}}\mathbf{d}-\mathbf{d}^T\hat{\mathbf{f}}
\end{aligned} \tag{5.52}$$

Proof

This is natural consequence of Lemma 5.1, based on the fact that $\tilde{\mathbf{f}}$ and $\hat{\mathbf{f}}$ are the same.

Theorem 5.2 When the same mesh is used, the strain energy obtained from the LC-PIM solution is no-less than that from the FEM solution based on compatible displacement model.

$$\hat{U}\left(\hat{\mathbf{d}}\right) \geq \tilde{U}\left(\tilde{\mathbf{d}}\right) \tag{5.53}$$

where

$$\begin{aligned} \hat{U}\left(\hat{\mathbf{d}}\right) &= \frac{1}{2}\hat{\mathbf{d}}^T\hat{\mathbf{K}}\hat{\mathbf{d}} \\ \tilde{U}\left(\tilde{\mathbf{d}}\right) &= \frac{1}{2}\tilde{\mathbf{d}}^T\tilde{\mathbf{K}}\tilde{\mathbf{d}} \end{aligned} \tag{5.54}$$

The equality is true when LC-PIM and FEM produces the exact solutions, or all the nodal-based smoothing covers only on element.

Proof

Based on Lemma 5.1 (see Equation (5.46)), it is obtained that for *any* admissible **d**:

$$\underbrace{\mathbf{d}^T\tilde{\mathbf{K}}\mathbf{d} - \mathbf{d}^T\hat{\mathbf{K}}\mathbf{d}}_{\geq 0} = \mathbf{d}^T\left(\tilde{\mathbf{K}} - \hat{\mathbf{K}}\right)\mathbf{d} \geq 0 \tag{5.55}$$

Equation (5.55) implies that matrix $\left(\tilde{\mathbf{K}} - \hat{\mathbf{K}}\right)$ is SPD. In mechanics, it implies that $\tilde{\mathbf{K}}$ is "stiffer" than $\hat{\mathbf{K}}$. In addition, the solution of FEM can be written as

$$\tilde{\mathbf{d}} = \tilde{\mathbf{K}}^{-1}\tilde{\mathbf{f}} \tag{5.56}$$

at which the $\tilde{J}\left(\mathbf{d}\right)$ is stationary. The solution of LC-PIM can be written as

$$\hat{\mathbf{d}} = \hat{\mathbf{K}}^{-1}\tilde{\mathbf{f}} \tag{5.57}$$

at which the $\hat{J}(\mathbf{d})$ is stationary. Note here that the fact that $\hat{\mathbf{f}} = \tilde{\mathbf{f}}$ is used. At the stationary point, it can be obtained for FEM

$$\tilde{J}(\tilde{\mathbf{d}}) = \frac{1}{2}\tilde{\mathbf{d}}^T\tilde{\mathbf{K}}\tilde{\mathbf{d}} - \tilde{\mathbf{d}}^T\tilde{\mathbf{f}} = \underbrace{-\frac{1}{2}\tilde{\mathbf{d}}^T\tilde{\mathbf{K}}\tilde{\mathbf{d}}}_{\tilde{U}(\tilde{\mathbf{d}})} = -\frac{1}{2}\tilde{\mathbf{d}}^T\tilde{\mathbf{f}} = \underbrace{-\frac{1}{2}\tilde{\mathbf{f}}^T\tilde{\mathbf{K}}^{-1}\tilde{\mathbf{f}}}_{\tilde{U}(\tilde{\mathbf{d}})} \tag{5.58}$$

and for LC-PIM

$$\hat{J}(\hat{\mathbf{d}}) = \frac{1}{2}\hat{\mathbf{d}}^T\hat{\mathbf{K}}\hat{\mathbf{d}} - \hat{\mathbf{d}}^T\tilde{\mathbf{f}} = \underbrace{-\frac{1}{2}\hat{\mathbf{d}}^T\hat{\mathbf{K}}\hat{\mathbf{d}}}_{\tilde{U}(\hat{\mathbf{d}})} = -\frac{1}{2}\hat{\mathbf{d}}^T\tilde{\mathbf{f}} = \underbrace{-\frac{1}{2}\tilde{\mathbf{f}}^T\hat{\mathbf{K}}^{-1}\tilde{\mathbf{f}}}_{\tilde{U}(\hat{\mathbf{d}})} \tag{5.59}$$

The difference of between the strain energies of FEM and LC-PIM solution becomes

$$\hat{U}(\hat{\mathbf{d}}) - \tilde{U}(\tilde{\mathbf{d}}) = \frac{1}{2}\tilde{\mathbf{f}}^T\hat{\mathbf{K}}^{-1}\tilde{\mathbf{f}} - \frac{1}{2}\tilde{\mathbf{f}}^T\tilde{\mathbf{K}}^{-1}\tilde{\mathbf{f}} = \frac{1}{2}\tilde{\mathbf{f}}^T\underbrace{\left(\hat{\mathbf{K}}^{-1} - \tilde{\mathbf{K}}^{-1}\right)}_{SPD}\tilde{\mathbf{f}} \geq 0 \tag{5.60}$$

which gives Equation (5.53).

In the working of Equation (5.60), the fact that $\left(\hat{\mathbf{K}}^{-1} - \tilde{\mathbf{K}}^{-1}\right)$ is SPD is used. This can be proven based on the facts at $\hat{\mathbf{K}}$, $\tilde{\mathbf{K}}$, and $\left(\tilde{\mathbf{K}} - \hat{\mathbf{K}}\right)$ are all SPD (see, Equation (5.55)).

2) LC-PIM vs. exact model

It has been found that not only $\hat{U}(\hat{\mathbf{d}}) \geq \tilde{U}(\tilde{\mathbf{d}})$, but also $\hat{U}(\hat{\mathbf{d}}) \geq U(\boldsymbol{\varepsilon}) \geq \tilde{U}(\tilde{\mathbf{d}})$ is true except for a few trivial cases, meaning the solution of LC-PIM gives the upper bound of the exact solution in energy norm. The fact will be stated in Theorem 5.3 that follows the following Lemma.

Lemma 5.2 For any (admissible) displacement $\mathbf{u}$, the strain potential $\widehat{U}(\mathbf{u})$ for a LC-PIM model is no-larger than that $U(\mathbf{u})$ for the exact model:

$$\widehat{U}(\mathbf{u}) \le U(\mathbf{u}) \tag{5.61}$$

where

$$\begin{aligned} \widehat{U}(\mathbf{u}) &= \int_\Omega \frac{1}{2}\widehat{\boldsymbol{\varepsilon}}^T(\mathbf{u})\mathbf{D}\widehat{\boldsymbol{\varepsilon}}(\mathbf{u})d\Omega \\ U(\mathbf{u}) &= \int_\Omega \frac{1}{2}\boldsymbol{\varepsilon}^T(\mathbf{u})\mathbf{D}\boldsymbol{\varepsilon}(\mathbf{u})d\Omega \end{aligned} \tag{5.62}$$

Proof

It is examined that

$$\begin{aligned} &\int_\Omega \frac{1}{2}\left(\widehat{\boldsymbol{\varepsilon}}-\boldsymbol{\varepsilon}\right)^T\mathbf{D}\left(\widehat{\boldsymbol{\varepsilon}}-\boldsymbol{\varepsilon}\right)d\Omega \\ &= \int_\Omega \frac{1}{2}\widehat{\boldsymbol{\varepsilon}}^T\mathbf{D}\widehat{\boldsymbol{\varepsilon}}d\Omega - \int_\Omega \frac{1}{2}\widehat{\boldsymbol{\varepsilon}}^T\mathbf{D}\boldsymbol{\varepsilon}d\Omega - \int_\Omega \frac{1}{2}\boldsymbol{\varepsilon}^T\mathbf{D}\widehat{\boldsymbol{\varepsilon}}d\Omega + \int_\Omega \frac{1}{2}\boldsymbol{\varepsilon}^T\mathbf{D}\boldsymbol{\varepsilon}d\Omega \\ &= \int_\Omega \frac{1}{2}\widehat{\boldsymbol{\varepsilon}}^T\mathbf{D}\widehat{\boldsymbol{\varepsilon}}d\Omega - \int_\Omega \widehat{\boldsymbol{\varepsilon}}^T\mathbf{D}\boldsymbol{\varepsilon}d\Omega + \int_\Omega \frac{1}{2}\boldsymbol{\varepsilon}^T\mathbf{D}\boldsymbol{\varepsilon}d\Omega \end{aligned} \tag{5.63}$$

Using the orthogonal condition Equation (5.44), and the fact that **D** is SPD, it arrives at

$$\underbrace{\int_\Omega \frac{1}{2}\left(\widehat{\boldsymbol{\varepsilon}}-\boldsymbol{\varepsilon}\right)^T\mathbf{D}\left(\widehat{\boldsymbol{\varepsilon}}-\boldsymbol{\varepsilon}\right)d\Omega}_{\ge 0} = \int_\Omega \frac{1}{2}\boldsymbol{\varepsilon}^T\mathbf{D}\boldsymbol{\varepsilon}d\Omega - \int_\Omega \frac{1}{2}\widehat{\boldsymbol{\varepsilon}}^T\mathbf{D}\widehat{\boldsymbol{\varepsilon}}d\Omega \ge 0 \tag{5.64}$$

which gives Equation (5.61).

Corollary 5.2 For any assumed admissible nodal displacement field $\mathbf{d}$, total potential $J(\mathbf{d})$ for the exact model is no-less than that $\widehat{J}(\mathbf{d})$ for LC-PIM model:

$$J(\mathbf{d}) \ge \widehat{J}(\mathbf{d}) \tag{5.65}$$

where

$$J(\mathbf{d}) = \frac{1}{2}\mathbf{d}^T\mathbf{K}\mathbf{d} - \mathbf{d}^T\mathbf{f}$$
$$\widehat{J}(\mathbf{d}) = \frac{1}{2}\mathbf{d}^T\widehat{\mathbf{K}}\mathbf{d} - \mathbf{d}^T\widehat{\mathbf{f}} \tag{5.66}$$

Proof

This is natural consequence of Lemma 5.2, based on the fact that $\mathbf{f}$ and $\widehat{\mathbf{f}}$ are the same.

Theorem 5.3 The strain energy obtained from the LC-PIM solution has the following relationship with the exact strain energy:

$$\widehat{U}(\widehat{\mathbf{d}}) \geq U(\mathbf{d}_0) \tag{5.67}$$

where $\widehat{\mathbf{d}}$ is the solution of a LC-PIM model which is obtained using shape functions constructed using bases containing the exact solution, and $\mathbf{d}_0$ is exact nodal displacement sampled using the exact displacement field $\mathbf{u}_0$.

Proof

Consider a problem with exact solution of $\mathbf{u}_0$. Let $\mathbf{d}_0$ be the corresponding solution at the nodes of the mesh used in the LC-PIM model for the same problem. The exact solution $\mathbf{u}_0$ can then always be written in the form of

$$\mathbf{u}_0(\mathbf{x}, \mathbf{d}) = \sum_{i \in n_e} \mathbf{\Phi}_{ei}(\mathbf{x})\mathbf{d}_{0i} \tag{5.68}$$

where n_e is the set of nodes of the element containing $\mathbf{x}$, $\mathbf{d}_{0i}$ is the vector of nodal displacements of the exact solution, and $\mathbf{\Phi}_{ei}(\mathbf{x})$ is the matrix of the shape functions that

are constructed using bases contains the exact that returns $\mathbf{u}_0$ for the given $\mathbf{d}_{0i}$ within the element. Considering an arbitrary displacement field defined by

$$\mathbf{u}(\mathbf{x},\mathbf{d}) = \sum_{i\in n_e} \mathbf{\Phi}_{ei}(\mathbf{x})\mathbf{d}_i \tag{5.69}$$

where $\mathbf{d}_i$ is the vector of arbitrary nodal displacements. This means that there is a special FEM model that uses the exact shape function, which should produce the exact solution of nodal displacement (Remark 5.2.3). Following the arguments in proving Theorem 5.2, it can be obtained that

$$\hat{U}(\hat{\mathbf{d}}) - U(\mathbf{d}_0) \geq 0 \tag{5.70}$$

which is Equation (5.67).

3) The battle of softening and stiffening effects

Theorem 5.3 implies that LC-PIM can provide an upper bound for the exact solution in energy norm, under the condition that $\mathbf{\Phi}_{ei}(\mathbf{x})$ is used. In mechanics, what this means is that the smoothing operation providing a *softening* effect to the solids or structure, so that the displacement $\hat{\mathbf{d}}$ obtained by LC-PIM is "larger" (in $\mathbf{K}$ norm) than that of the exact solution.

In the practice of using LC-PIM for a general problem, however, finding $\mathbf{\Phi}_{ei}(\mathbf{x})$ is not always practical. Therefore, the usual PIM shape functions (or, in special cases, the FEM shape functions) are used. The use of any (compatible) shape functions in the place of the exact shape functions will, on the other hand, provide a *stiffening* effect to the model. The

battle between the softening and stiffening effects will determine whether a LC-PIM model can in fact provide an upper bound solution to the problem.

The *softening effect* depends on the following situations in a LC-PIM model.

- The number of elements that connected to a node of a smoothing domain: The more the elements, the more the smoothing effects. As shown in Figure 5.1, at node k, there are five elements connected, and at the corner node q, however, only two elements are connected. In an extreme case, if the smoothing domain is defined for each element to perform the smoothing operation (Ω_k is further divided to five sub-domains: each for an element), there will no softening effect at all. In this case, the LC-PIM and FEM gives naturally the same results, and the LC-PIM will not provide an upper bound, but a lower bound solution.
- The number of nodes being smoothed. In LC-PIM, one does not have to perform the smoothing operation for all the nodes. If the smoothing is selectively performed, the softening effect will propositionally depends on the number of nodes participated in the smoothing operation.
- The number of nodes used in the problem domain or density of the background cells. When a small number of nodes are used, the displacements approximated using the PIM shape functions in a smoothing domain deviates far from the exact solution, resulting in a heavy smoothing to the strain field, and hence a strong softening effect. On the other hand, When a large number of nodes are used, the displacements approximated using the PIM shape functions in a smoothing domain is more close to the exact solution, resulting less smoothing effects, and hence less softening effect. At

the extreme of infinitely small elements are used, the smoothing effects will diminish and the LC-PIM solution (also the FEM solution) will approach to the exact solution.

The *stiffening effect* depends on the following situations in a LC-PIM model.

- The order of the PIM shape functions used in the displacement approximation. When high order PIM shape functions are sued, the displacements approximated using the PIM shape functions in a smoothing domain is closer to the exact solution of displacements, which reduces the stiffening effect, and vice versa.
- The number of nodes used in the problem domain. When a small number of nodes are used, the displacements approximated using the PIM shape functions in a smoothing domain deviates far from the exact solution, the stiffening effect is therefore large, and vice verse. At the extreme of infinitely small elements are used, the stiffening effects will diminish and the LC-PIM solution (also the FEM solution) will approach to the exact solution.

Generally, the softening effect provided by the smoothing in a LC-PIM model is more significant than the stiffening effects. This is because the smoothing is a zero order approximation that is lower than the at least first order approximation of the displacement resulting in the stiffening effect. Therefore, the LC-PIM always produces an upper bound solution except the following cases:

- Only one element is used. In this case, only element participates in smoothing, which should not have any smoothing effects, and hence the solutions of LC-PIM and FEM are the same, and LC-PIM gives a lower bound solution.

- For the Fraeijs de Veubeke's particular cases (Debongine et al., 1995), in which homogeneous equiirbium condition is applied, LC-PIM and FEM will provide lower and upper bound respectively.

In the numerical study, it has been found that LC-PIM can produce upper bound solutions for all the problems studied, except the very special case mentioned above. Intensive numerical studies have been conducted and reported in the following section to confirm the properties of the LC-PIM with a focus on the important upper bound property.

5.5 Numerical examples

5.5.1 Standard patch test

For a numerical method working for solid mechanics problems, the sufficient requirement for convergence is to pass the standard patch test (Zienkiewicz and Taylor, 2000). Therefore, the first example is the standard patch test using the present LC-PIM. The problem is studied in a 10×10 square domain, and the displacements are prescribed on all outside boundaries by the following linear function.

$$\begin{aligned} u_x &= 0.6x \\ u_y &= 0.6y \end{aligned} \tag{5.71}$$

The patch test is presented using regular and irregular nodes as shown in Figure 5.2. The errors in displacement norm as defined in Equation (4.26) are found to be 1.65×10^{-15} and 1.80×10^{-15} for these two models of nodes distributions respectively. This example demonstrates numerically that, the LC-PIM will monotonically converge due to its ability to reproduce linear fields and the use of the Galerkin weak form.

5.5.2 Cantilever beam

A cantilever beam which has been studied in Chapter 4 (shown in Figure 4.9) is studied using the LC-PIM. The beam is of length L and height D, and subjected to a parabolic traction on the right edge. As the beam is assumed to have unit thickness, analytical solution based on plane stress theory is available (Timoshenko and Goodier, 1970) and shown in Equations (4.34)-(4.38). In the present study, the parameters are of $E = 3.0 \times 10^7$ Pa, $v = 0.3$, $L = 50$, $D = 10$ and $P = -1000$.

To investigate the effect of the irregularity of nodal distribution, three models of 420 distributed nodes with different status of irregularity (shown in Figure 5.3) are studied using the LC-PIM. The results of deflection along the neutral line and the shear stress along the line $(x = L/2)$ of the beam are plotted together with the analytical solutions in Figure 5.4. It can be observed that the numerical results of these three models obtained using the LC-PIM are all in good agreement with the analytical ones, and the irregularity of the nodal distribution has litter effect on the numerical results.

To study the convergence and efficiency properties of the LC-PIM, three models with regularly distributed nodes (105, 369 and 1377 nodes respectively) have been studied. For comparison, the problem has also been studied using the linear FEM with the same models. According to Equations (4.26) and (4.27), errors in displacement and energy norms are calculated and have been plotted against the average nodal spacing (h) in Figure 5.5. It can be found that the LC-PIM obtains a similar accuracy and convergence rate in displacement compared with the linear FEM. But for the results in energy norm, solutions of the LC-PIM will be more accurate and achieve much higher convergence rate. In Figure 5.6, the errors in displacement and energy norms are plotted against the

time consumed, which shows the efficiency of the method. It can be observed that the LC-PIM is as efficient as the linear FEM in terms of displacement results but is more efficient in terms of stress results.

It is known that if a fully (both displacements and displacement-strain relations) compatible model is used, the convergence rate in energy norm should be, in theory, 1.0 (for linear fields assumed); and if a fully equilibrium model is used, the convergence rate in energy norm should be, in theory, 2.0. In the LC-PIM, the strain smoothing is performed, which creates an "equilibrium" state locally inside the smoothing cells. On all the interfaces of the smoothing cells, however, the equilibrium is not ensured and only the compatibility of displacements is ensured. Therefore, the rate of convergence in energy norm should be, in theory, between 1.0 and 2.0. The actual value will be problem dependent. For this cantilever beam problem, the convergence rate in energy norm for the LC-PIM is 1.42 (shown in Figure 5.5), which also demonstrated this theory.

To investigate the upper bound property on strain energy of the LC-PIM numerically, strain energy of the model is calculated according to the following formulation.

$$U = \int_{\Omega} \frac{1}{2} \boldsymbol{\varepsilon}^T \mathbf{D} \boldsymbol{\varepsilon} d\Omega \tag{5.72}$$

Figure 5.7 shows the convergence status of the strain energies against the increase of Degree of Freedom (DOF) for both the FEM and the LC-PIM. The reference solution of the strain energy is obtained using the analytical solutions of stress components. It can be clearly found that the strain energy of the FEM model is always smaller than the reference one; on the contrary, the strain energy of the LC-PIM model is always bigger compared with the reference one. The figure also shows that with the increase of DOF,

strain energy of the FEM model and the LC-PIM model will converge to the reference solution from the lower and upper points respectively. This 2D example shows clearly the very important fact that one now can bound the exact solution from both sides.

5.5.3 Infinite plate with a circular hole

An infinite plate with a central circular hole and subjected to a unidirectional tensile is studied (as shown in Figure 4.18). Due to its two-fold symmetry, one quarter is modeled. Symmetry conditions are imposed on the left and bottom edges, and the inner boundary of the hole is traction free. For this benchmark problem, the analytical solution is available (Timoshenko and Goodier, 1970) and can be found in Equations (4.40)-(4.45). In the present study, plane stress is considered with the parameters $E = 3.0 \times 10^7$ Pa, $v = 0.3$ $a = 1$, $b = 5$ and $T_x = 10$.

The problem domain is first discretized with 1330 nodes and the computed results of displacement and stress components along the bottom and left edges are plotted with the analytical solutions (as shown in Figure 5.8 and Figure 5.9). It is observed that all the numerical results obtained using the LC-PIM are in good agreement with the analytical solutions.

Next, the problem domain is presented with four models of irregularly distributed nodes (577, 1330, 2850 and 3578 nodes respectively). The convergence rates in displacement and energy norms are demonstrated in Figure 5.10 for both the FEM and the LC-PIM. Again it can be seen that for the displacement results, the LC-PIM and the FEM obtain similar accuracy and achieve almost equal convergence rate; but for the

stress results in energy norm, the LC-PIM could get better accuracy and achieve much higher convergence rate. Figure 5.11 shows the errors of the numerical results against the time consumed. It is observed that the LC-PIM and the linear FEM obtain similar efficiency for displacement results but the former is more efficient than the latter for stress results.

The strain energy for each model is calculated according to Equation (5.72). As shown in Figure 5.12, strain energy of the FEM model is always smaller than the reference one and converges from the lower point with the increase of DOF. On the contrary, strain energy of the LC-PIM model is always bigger than the reference one and converges from above.

5.5.4 Semi-infinite plane

A semi-infinite plane subjected to a uniform pressure within a finite range $(-a \le x \le a)$ is studied (as shown in Figure 5.13). Plane strain condition is considered and the analytical stresses are given by

$$\sigma_{xx} = \frac{p}{2\pi}\left[2(\theta_1 - \theta_2) - \sin 2\theta_1 + \sin 2\theta_2\right] \tag{5.73}$$

$$\sigma_{yy} = \frac{p}{2\pi}\left[2(\theta_1 - \theta_2) + \sin 2\theta_1 - \sin 2\theta_2\right] \tag{5.74}$$

$$\sigma_{xy} = \frac{p}{2\pi}(\cos 2\theta_1 - \cos 2\theta_2) \tag{5.75}$$

The directions of θ_1 and θ_2 are referred in Figure 5.13. The corresponding displacements can be given by

$$u_x = \frac{p(1-v^2)}{\pi E}\left[\frac{1-2v}{1-v}\left[(x+a)\theta_1 - (x-a)\theta_2\right] + 2y\ln\frac{r_1}{r_2}\right] \tag{5.76}$$

$$u_y = \frac{p(1-v^2)}{\pi E}\left\{\frac{1-2v}{1-v}\left[y(\theta_1-\theta_2) + 2H\arctan\frac{1}{c}\right] + 2(x-a)\ln r_2 - 2(x+a)\ln r_1 + 4a\ln a + 2a\ln(1+c^2)\right\} \tag{5.77}$$

where $H = ca$ is the distance from the origin to the point $0'$ where the vertical displacement is assumed to be zero and c is a coefficient.

Due to the symmetry about $y\text{-}axis$, the problem is modeled with a $5a \times 5a$ square with $a = 0.2$, $c = 100$ and $p = 1\,\text{MPa}$. The parameters are taken as $E = 3.0 \times 10^7\,\text{Pa}$ and $v = 0.3$. The left and bottom edges are constrained using exact displacement while the right side is subjected to tractions computed from the analytical solutions.

The problem domain has been discretized with four models of nodes distributions (322, 651, 1252 and 2551 nodes respectively) and the convergence rates in displacement and energy norms have also been calculated for the LC-PIM and the FEM. As shown in Figure 5.14, the LC-PIM and the FEM obtain similar accuracy and convergence rate for displacement calculation, but the former could get better accuracy and achieve higher convergence rate for energy calculation. As it has been discussed previously, the convergence rate in energy norm of LC-PIM should be, in theory, between 1.0 and 2.0. In this example, the convergence rate in energy norm is 0.98 (shown in Figure 5.14). Strain energy calculated based on numerical results have been plotted against DOF in Figure 5.15. It can be seen again that the LC-PIM possesses the upper bound property on strain energy, i.e., strain energy of the LC-PIM model is always bigger than the exact one and converges to it with the increase of DOF.

5.5.5 Square plate subjected to uniform pressure and body force

A square plate shown in Figure 5.16 is studied. The plate is constrained on the left, the right and the bottom edges. It is subjected to uniform pressure along the top edge and body fore of $b^T = \{0 \quad -1\}$. The problem is considered as plane stress with $E = 3.0 \times 10^7$ Pa and $\nu = 0.3$.

The problem is descritized with four models of 145, 313, 545 and 841 nodes respectively. The property of upper bound on strain energy for the LC-PIM is also investigated similarly as previous examples. As the analytical solution is not available for this problem, the reference value of strain energy is obtained using the FEM with a very fine mesh (8238 nodes). The calculated strain energy has been plotted against the DOF in Figure 5.17. Again, it can be observed that the LC-PIM possesses the property of upper bound on strain energy.

5.5.6 An automotive part: connecting rod

Finally, a typical connecting rod used in automobiles, as shown in Figure 4.24, is studied again using the LC-PIM. The rod is constrained along the left circle and subjected to a uniform radial pressure of 100. The parameters are of $E = 3.0 \times 10^7$ Pa and $\nu = 0.3$. As the exact solution is not available, a reference solution of strain energy is obtained using the FEM with very fine mesh (total 11226 nodes).

The problem is presented using four models of nodes distribution, i.e., 592, 1150, 1660 and 2244 nodes. The calculated strain energy has been plotted against the increase of

DOF in Figure 5.18. For this practical problem with complicated shape, the LC-PIM is found again to possess the property of upper bound on strain energy.

5.6 Remarks

In this chapter, a linearly conforming point interpolation method (LC-PIM) has been formulated for 2D solid mechanics problems. The LC-PIM employs the polynomial basis to construct shape functions. The generalized Galerkin weak form is used to create discretized system equations and a stabilized nodal integration scheme with strain smoothing operation is used to perform the numerical integration. It has been proved theoretically that

- Polynomial PIM shape function obtained using linear interpolation can be constructed as same as in the FEM using triangle element, which is very simple.
- The LC-PIM is variationally consistent, and the generalized Galerkin weak form is a valid weak form for generating the discretized system equations.
- The LC-PIM solution (in energy norm) is always no-less than that of FEM.
- The LC-PIM solution (in energy norm) is no-less than that of exact solution except a few trivial cases.

Intensive studies have been then conducted, and it has been confirmed numerical that

- The LC-PIM solution (in energy norm) is always no-less than that of FEM for all cases studied, without exception.
- LC-PIM solution (in energy norm) is no-less than that of exact solution except a few trivial cases: only one element is used, and the smoothing domain is reduced.

Using the LC-PIM together with the FEM, there is now a systematical way to numerically obtain both upper and lower bounds of the exact solution to elasticity problems.

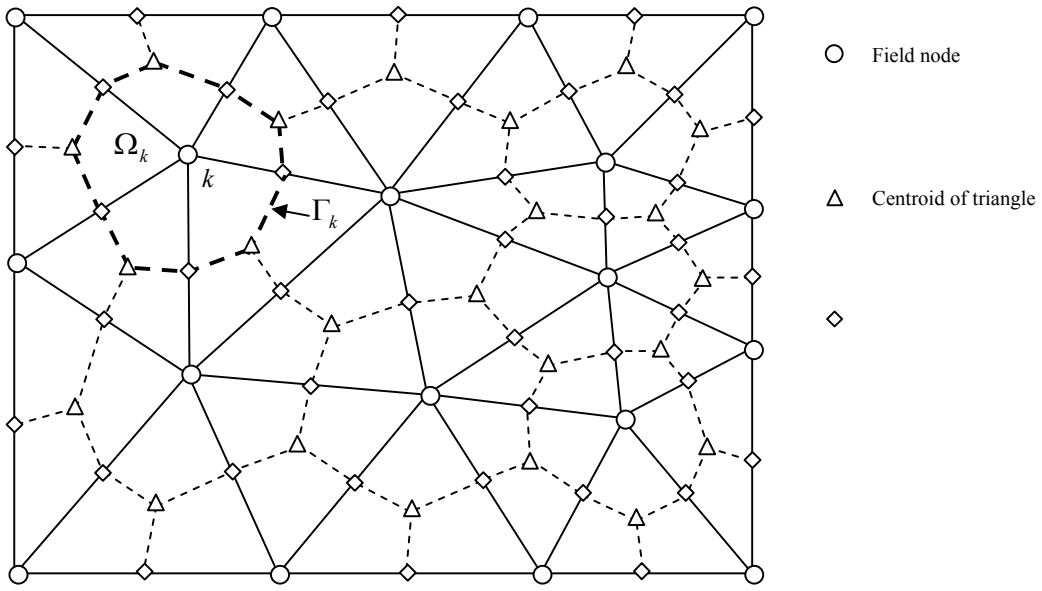

Figure 5.1 Illustration of the background triangular cells and the smoothing domains created by sequentially connecting the centroids with the mid-edge-points of the surrounding triangles of a node.

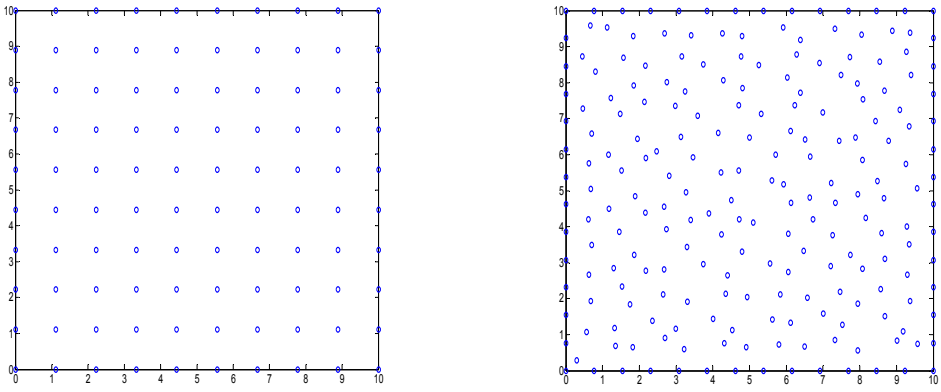

(a): 100 regularly distributed nodes (b): 109 irregularly distributed nodes

Figure 5.2 Nodes distribution for the standard patch test

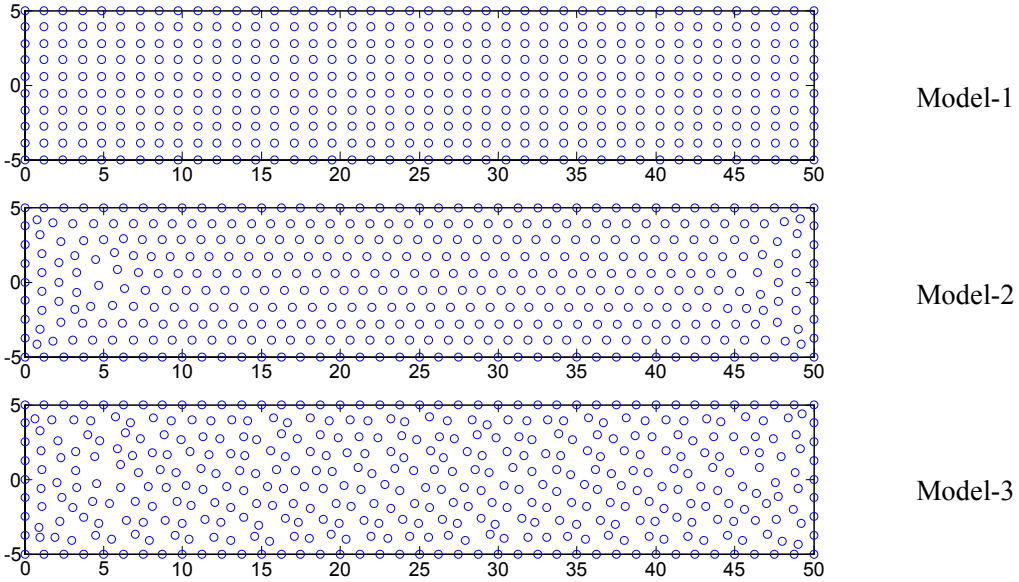

Figure 5.3 Three models of 420 nodes with different irregularity for the cantilever beam

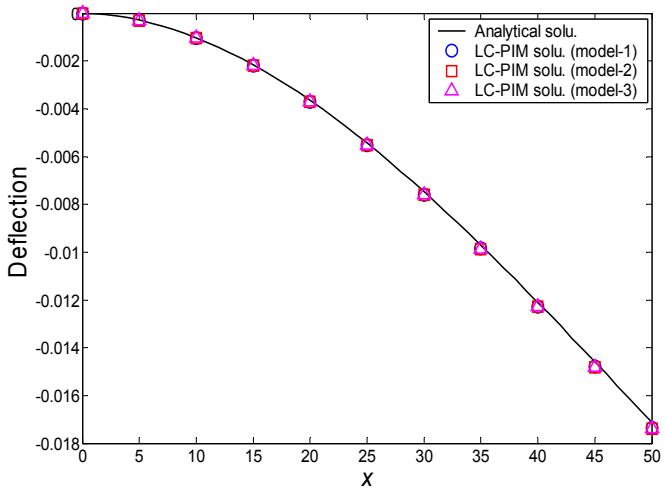

(a) Deflection distribution along the neutral line

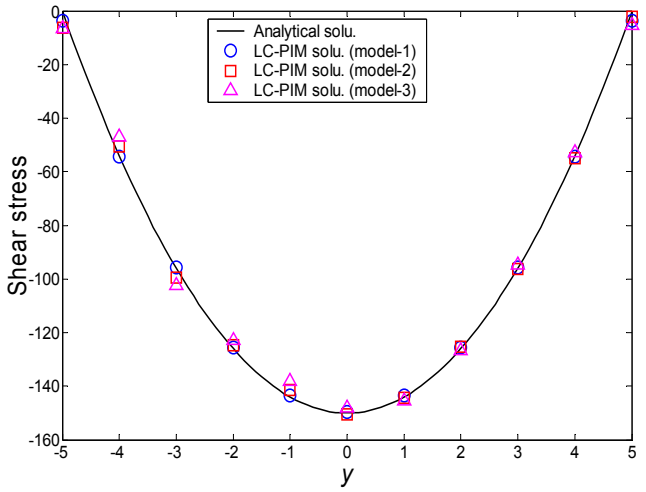

(b) Shear stress distribution along the lien of $x = L/2$

Figure 5.4 Numerical results obtained using the LC-PIM with three models of different status of irregularity

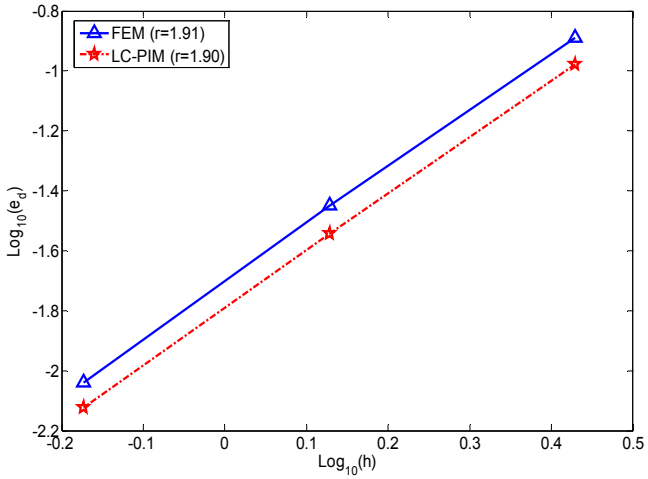

(a) Comparison of convergence rate in displacement norm

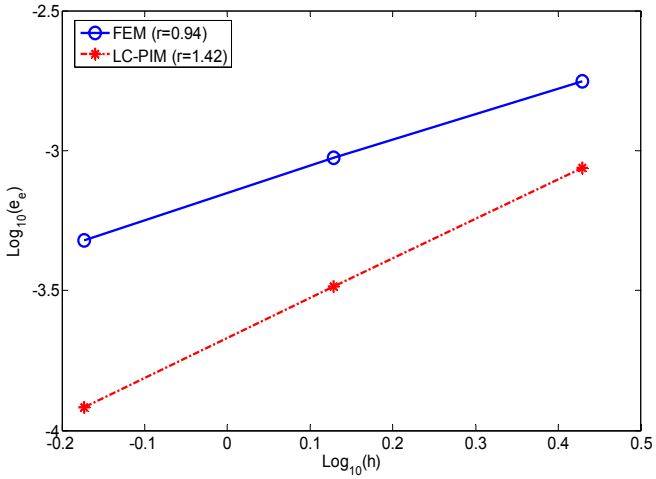

(b) Comparison of convergence rate in energy norm

Figure 5.5 Comparison of convergence rate between the FEM and the LC-PIM via the problem of cantilever beam

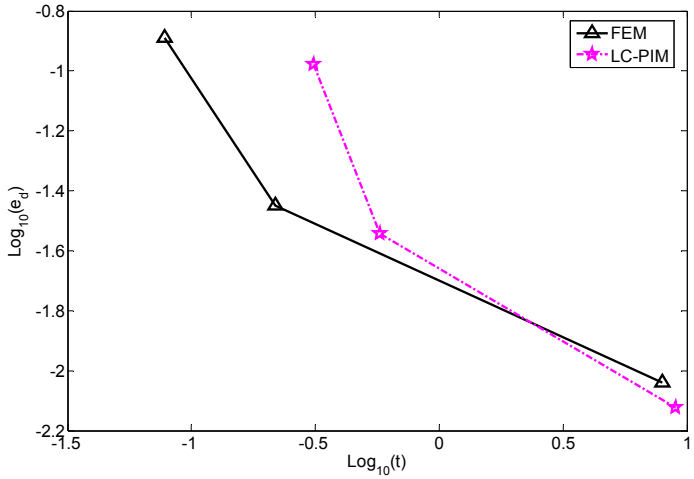

(a) Comparison of efficiency in displacement norm

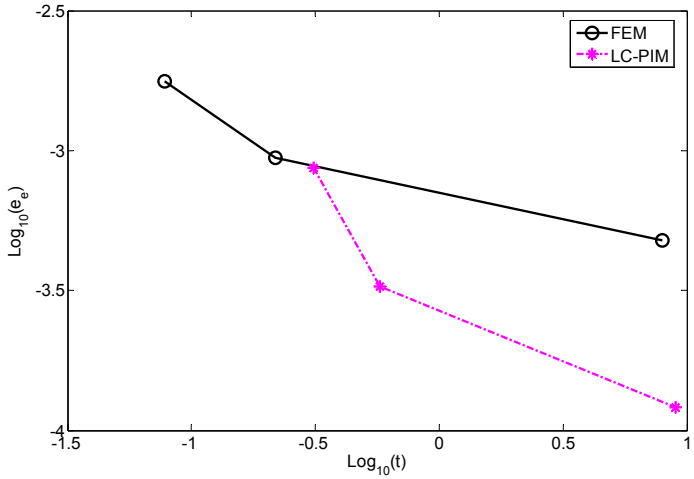

(b) Comparison of efficiency in energy norm

Figure 5.6 Comparison of efficiency between the FEM and the LC-PIM via the problem of cantilever beam

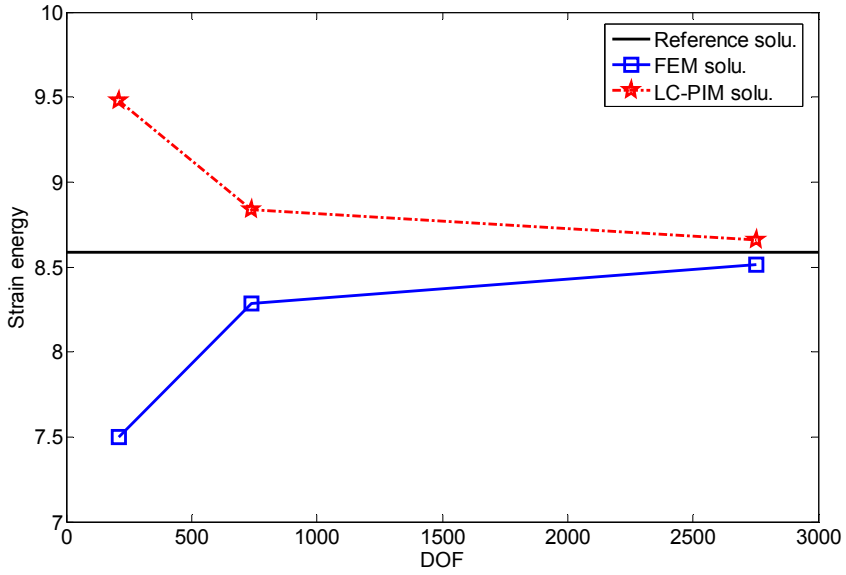

Figure 5.7 Study of the property of upper bound on strain energy for the LC-PIM via the problem of a cantilever beam

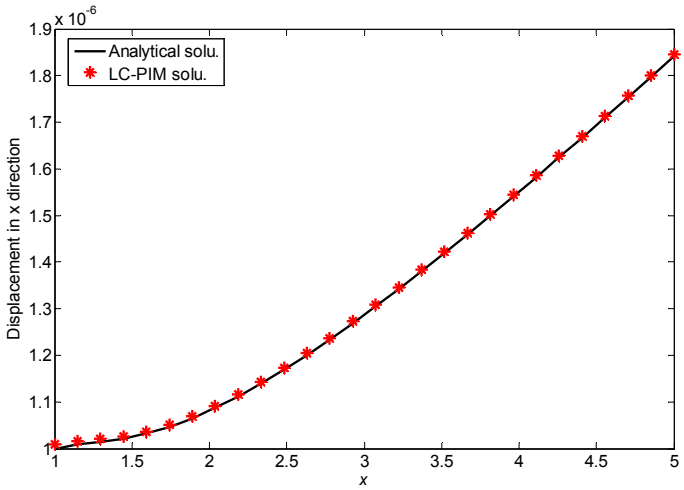

(a) Distribution of displacement (u) along the bottom edge

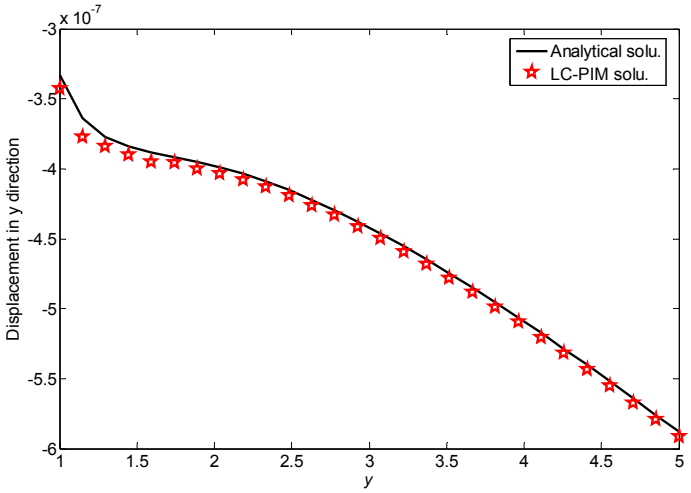

(b) Distribution of displacement (v) along the left edge

Figure 5.8 Distribution of the displacement results obtained using the LC-PIM

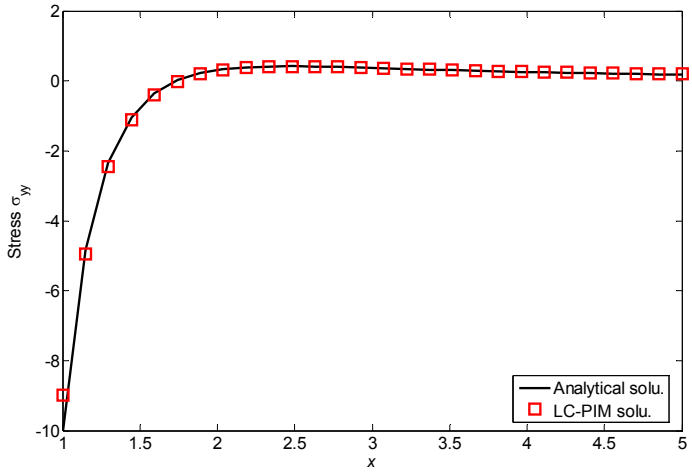

(a) Distribution of stress (σ_{yy}) along the bottom edge

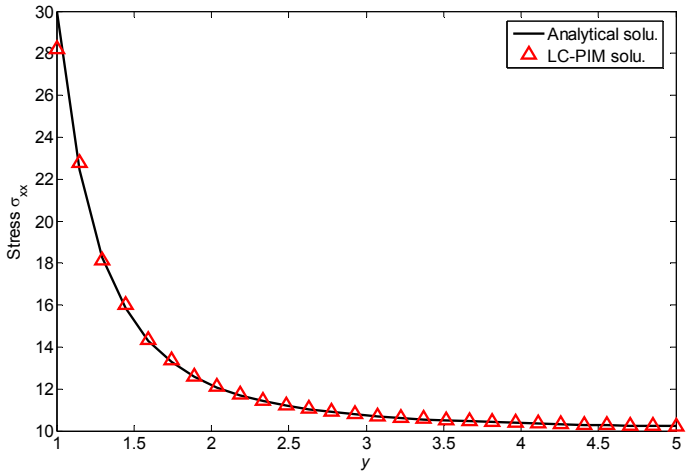

(b) Distribution of stress (σ_{xx}) along the left edge

Figure 5.9 Distribution of the stress results obtained using the LC-PIM

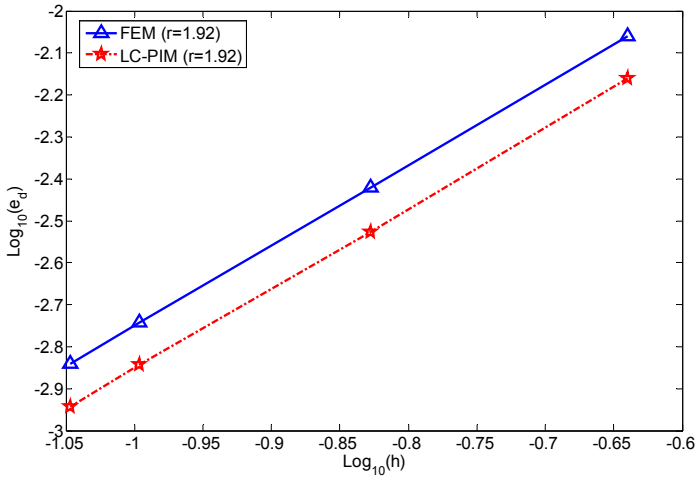

(a) Comparison of convergence rate in displacement norm

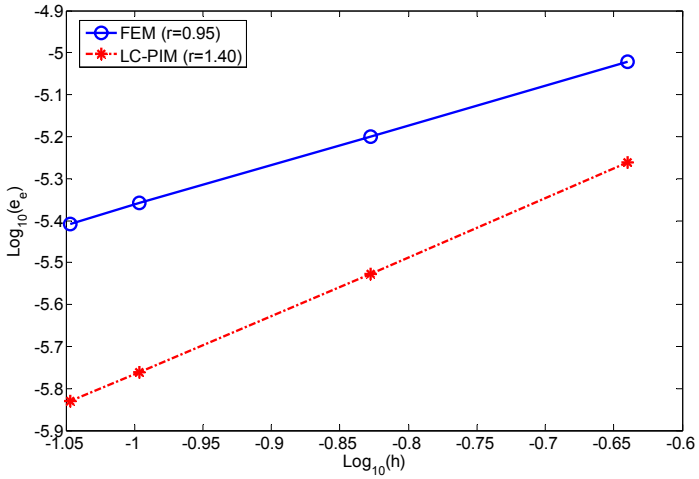

(b) Comparison of convergence rate in energy norm

Figure 5.10 Comparison of convergence rate between the FEM and the LC-PIM via the problem of an infinite plate with a hole

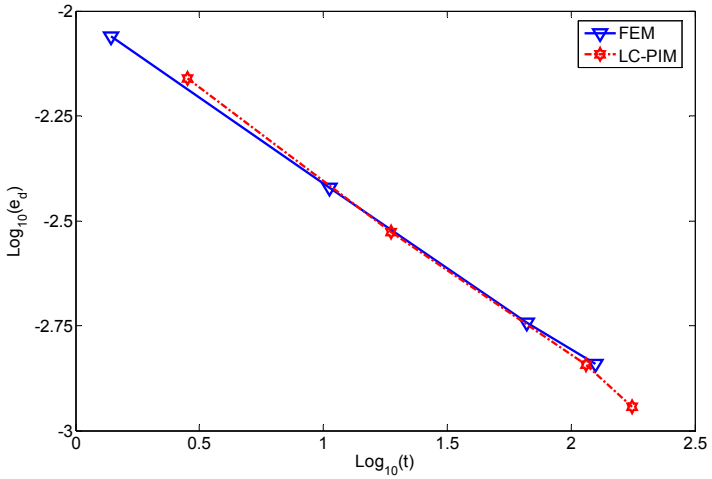

(a) Comparison of efficiency in displacement norm

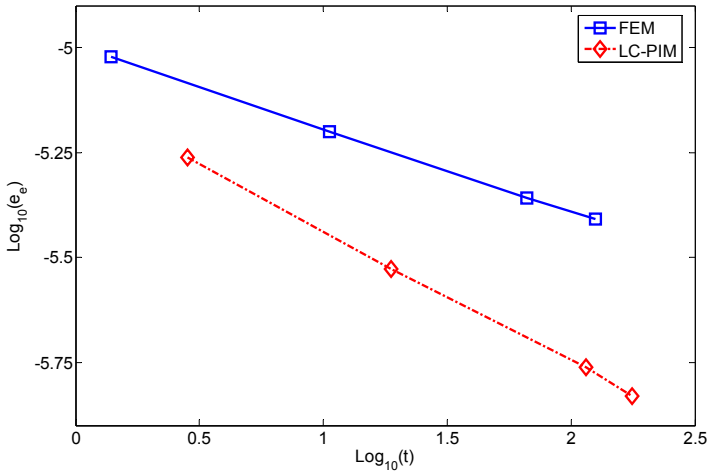

(b) Comparison of efficiency in energy norm

Figure 5.11 Comparison of efficiency between the FEM and the LC-PIM via the problem of an infinite plate with a hole

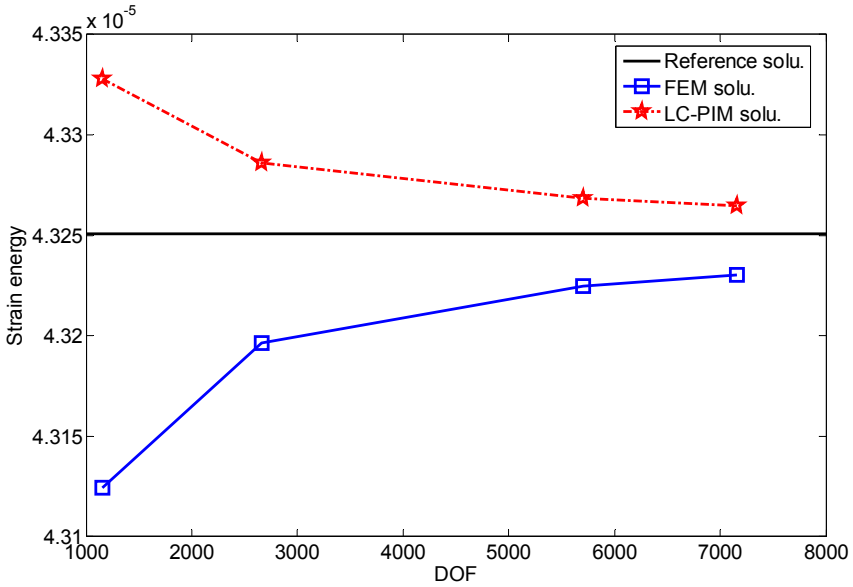

Figure 5.12 Study of the property of upper bound on strain energy for the LC-PIM via the problem of an infinite plate with a hole

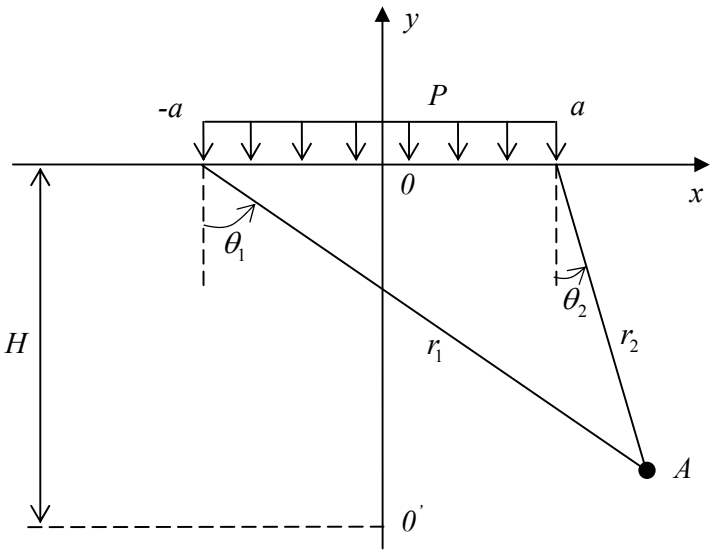

Figure 5.13 Semi-infinite plane subjected a uniform pressure

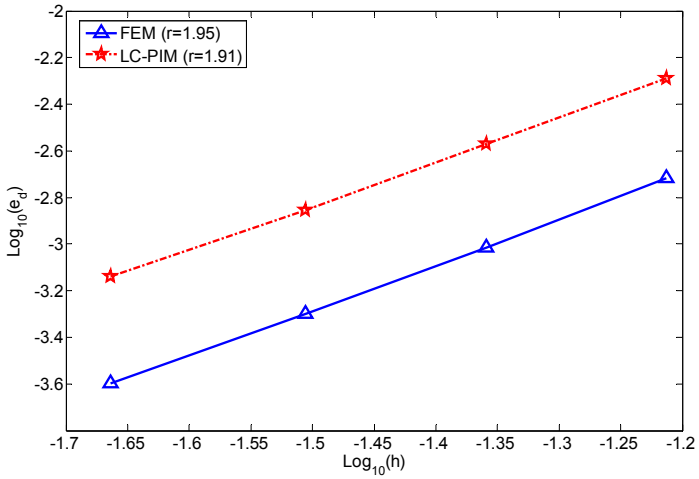

(a) Comparison of convergence rate in displacement norm

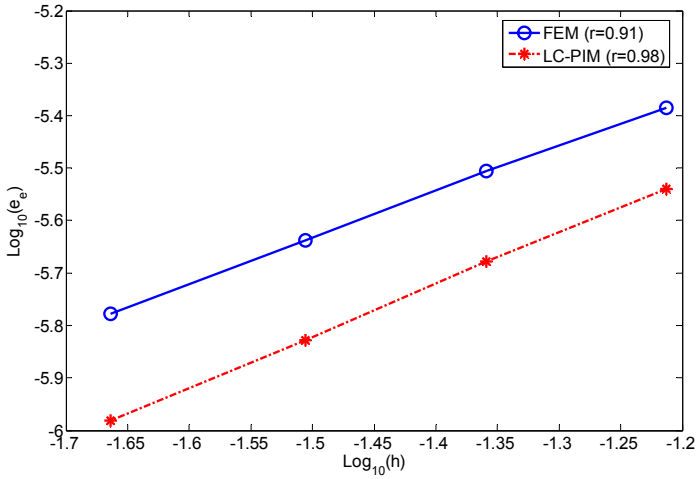

(b) Comparison of convergence rate in energy norm

Figure 5.14 Comparison of convergence rate between the FEM and the LC-PIM via the problem of semi-infinite plane

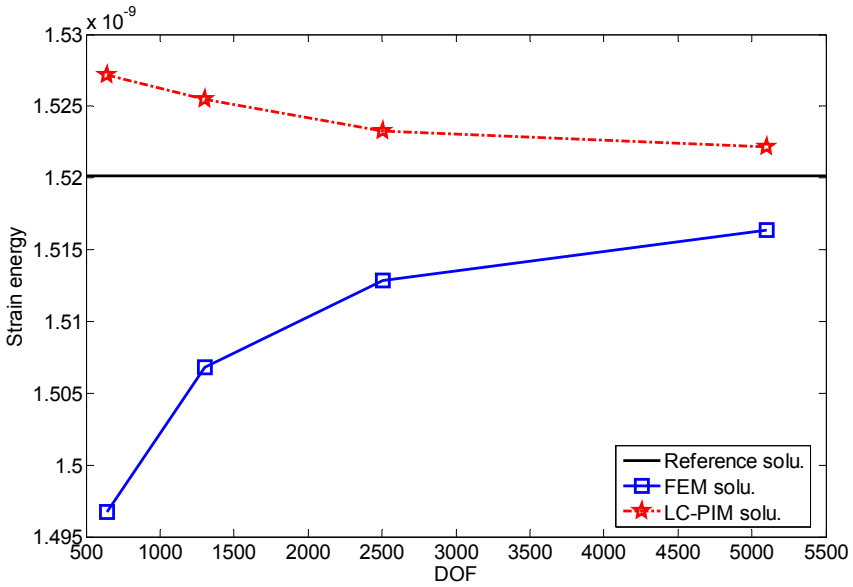

Figure 5.15 Study of the property of upper bound on strain energy for the LC-PIM via the problem of semi-infinite plane

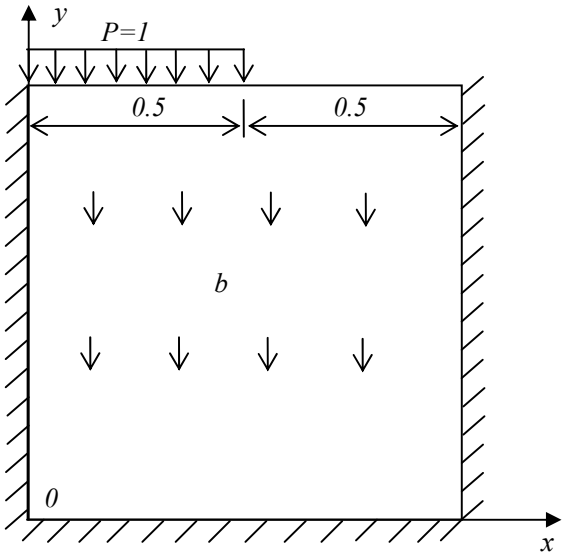

Figure 5.16 A square plate subjected to uniform pressure and body force

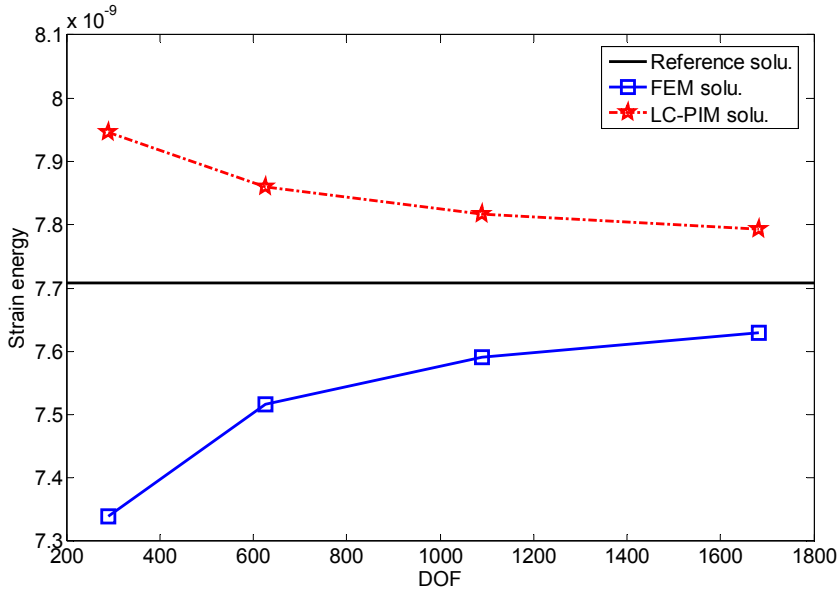

Figure 5.17 Study of the property of upper bound on strain energy for the LC-PIM via the problem of square plate subjected to uniform pressure and body force

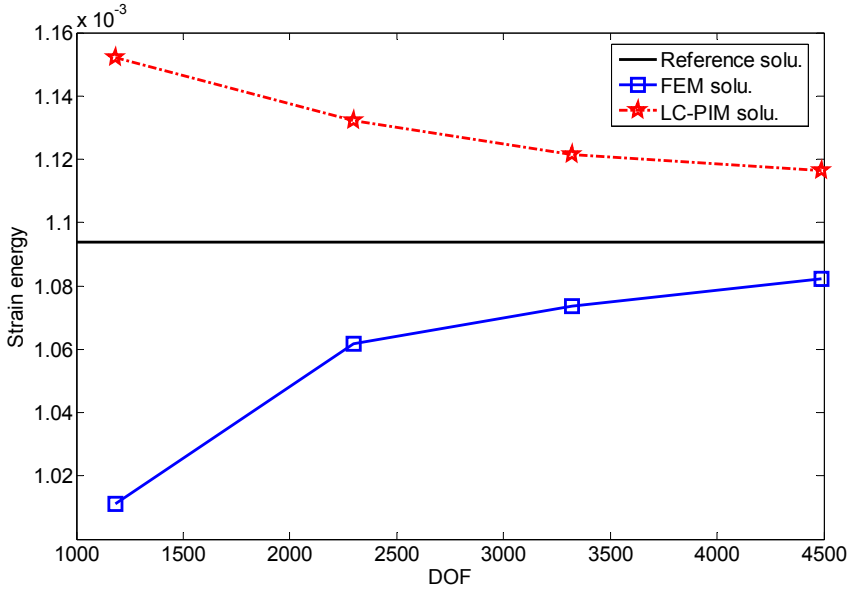

Figure 5.18 Study of the property of upper bound on strain energy for the LC-PIM via the problem of connecting rod

Chapter 6

Linearly conforming point interpolation method (LC-PIM) for three-dimensional problems

6.1 Introduction

The linearly conforming point interpolation method (LC-PIM) for 2D problems has been proposed and investigated thoroughly in Chapter 5. In the LC-PIM, the approximation of the variable is performed by simple point interpolation using polynomial basis functions and the singularity problem of the moment matrix can be successfully resolved. The generalized Galerkin weak form is used for creating discretized system equations, and a stabilized nodal integration scheme with strain smoothing technique is used to perform the numerical integration. The LC-PIM can guarantee linear exactness and monotonic convergence in energy norm for the numerical solutions. Furthermore, it has been found that the LC-PIM possesses the property of upper bound on strain energy (details see Chapter 5).

In this chapter, the LC-PIM will be extended for three-dimensional problems. In this framework, a background cell of four-node tetrahedron is employed and shape functions are constructed using linear polynomial basis functions. The stabilized nodal integration scheme with strain smoothing is extended to 3D problems and volume integrals involving shape function gradients are recast into surface integrals involving only shape functions.

The present method can guarantee the linear exactness in energy norm of the numerical solution and is computationally efficient.

6.2 Polynomial point interpolation method in three-dimensions

Consider a 3D continuous function $u(\mathbf{x})$, it can be approximated in the vicinity of $\mathbf{x}$ as follows.

$$u^h(\mathbf{x}) = \sum_{i=1}^{n} p_i(\mathbf{x}) a_i = \mathbf{p}^{\mathrm{T}}(\mathbf{x})\mathbf{a} \tag{6.1}$$

where $p_i(\mathbf{x})$ is polynomial basis function of $\mathbf{x} = [x, y, z]^{\mathrm{T}}$, n is the number of polynomial terms, and $\mathbf{a} = \{a_1, a_2, \cdots, a_n\}^{\mathrm{T}}$, in which a_i is the corresponding coefficient yet to be determined. The polynomial basis $p_i(\mathbf{x})$ is usually built utilizing the Pascal's triangles, and a complete basis is preferred because of the requirement of higher possible order of consistency. The complete polynomial basis of order 1 and order 2 in three dimensions can be written in the following forms.

$$\begin{aligned} \mathbf{p}^{\mathrm{T}}(\mathbf{x}) &= \{1 \quad x \quad y \quad z\} \\ \mathbf{p}^{\mathrm{T}}(\mathbf{x}) &= \{1 \quad x \quad y \quad z \quad x^2 \quad y^2 \quad z^2 \quad xy \quad yz \quad zx\} \end{aligned} \tag{6.2}$$

The coefficients $\mathbf{a}$ in Equation (6.1) can then be determined by enforcing $u(\mathbf{x})$ to be the nodal values at these n nodes in the support domain of $\mathbf{x}$, which leads to the following n equations:

$$\begin{cases} u(x_1,y_1,z_1)=a_1+a_2x_1+a_3y_1+a_4z_1+\ldots+a_np_n(\mathbf{x}_1) \\ u(x_2,y_2,z_2)=a_1+a_2x_2+a_3y_2+a_4z_2+\ldots+a_np_n(\mathbf{x}_2) \\ \vdots \\ u(x_n,y_n,z_n)=a_1+a_2x_n+a_3y_n+a_4z_n+\ldots+a_np_n(\mathbf{x}_n) \end{cases} \tag{6.3}$$

In matrix form, it can be written as

$$\mathbf{U}_s=\mathbf{P}_n\mathbf{a} \tag{6.4}$$

where $\mathbf{U}_s$ is the vector of nodal functional values in the support domain,

$$\mathbf{U}_s=\{u_1 \quad u_2 \quad u_3 \quad \ldots \quad u_n\}^{\mathrm{T}} \tag{6.5}$$

$\mathbf{P}_n$ is the 3D polynomial moment matrix given by

$$\mathbf{P}_n=\begin{bmatrix} 1 & x_1 & y_1 & z_1 & \ldots & p_n(\mathbf{x}_1) \\ 1 & x_2 & y_2 & z_2 & \ldots & p_n(\mathbf{x}_2) \\ 1 & x_3 & y_3 & z_3 & \ldots & p_n(\mathbf{x}_3) \\ \vdots & \vdots & \vdots & \vdots & \ddots & \vdots \\ 1 & x_n & y_n & z_n & \ldots & p_n(\mathbf{x}_n) \end{bmatrix} \tag{6.6}$$

Assuming the existence of $\mathbf{P}_n^{-1}$, a unique solution for $\mathbf{a}$ can be obtained as

$$\mathbf{a}=\mathbf{P}_n^{-1}\mathbf{U}_s \tag{6.7}$$

Substituting Equation (6.7) back into Equation (6.1) yields

$$u^h(\mathbf{x})=\mathbf{P}^{\mathrm{T}}(\mathbf{x})\mathbf{P}_n^{-1}\mathbf{U}_s=\sum_{i=1}^{n}\varphi_iu_i=\boldsymbol{\Phi}^{\mathrm{T}}(\mathbf{x})\mathbf{U}_s \tag{6.8}$$

where $\boldsymbol{\Phi}(\mathbf{x})$ is the vector of PIM shape functions in three-dimensions:

$$\boldsymbol{\Phi}^{\mathrm{T}}(\mathbf{x})=\{\varphi_1(\mathbf{x}) \quad \varphi_2(\mathbf{x}) \quad \ldots \quad \varphi_n(\mathbf{x})\} \tag{6.9}$$

The k^{th} derivative of the shape functions can be easily obtained, but they are not required in the LC-PIM formulations due to the use of strain smoothing operation as it has been discussed in Chapter 5.

In the present LC-PIM for 3D problems, linear monomials are used to serve as the basis functions. Same as in the FEM, four vertexes of the background tetrahedron cell are taken to perform the interpolation of the interest points located inside the cell. This can be easily implemented and can always ensure the invertibility of the moment matrix, as long as the four vertexes of the tetrahedron are not on a plane.

6.3 The stabilized nodal integration scheme in three-dimensions

As presented in Chapter 5, the generalized Galerkin weak form is used and the discretized system equations can be obtained as shown in Equation (5.15). To perform the numerical integration, a stabilized nodal integration scheme has been proposed in Chapter 5 for 2D problems. In this section, this nodal integration scheme will be extended for 3D problems as follows.

In the process of the nodal integration, the problem domain Ω is divided into N smoothing domains $\Omega_k \left(k = 1,\ldots,N\right)$, in which N is the total number of field nodes. The smoothing domain for each field node is centered by the node and constructed based on the background cells of four-node tetrahedrons. As illustrated in Figure 6.1, the sub-domain of the smoothing domain for node k located in the particular cell j can be obtained by connecting the mid-edge-points, the centroids of the surface triangles and the centroid of cell j. Finding out other sub-domains located in the surrounding cells of

node k and the smoothing domain for node k can be constructed by uniting all these sub-domains.

Applying the nodal integration scheme, the domain integration of the stiffness matrix can be performed numerically as follows.

$$\widehat{\mathbf{K}}_{ij} = \sum_{k=1}^{N} \widehat{\mathbf{K}}_{ij(k)} \tag{6.10}$$

in which

$$\widehat{\mathbf{K}}_{ij(k)} = \int_{\Omega_k} \widehat{\mathbf{B}}_i^{\mathrm{T}} \mathbf{D} \widehat{\mathbf{B}}_j d\Omega = \widehat{\mathbf{B}}_i^{\mathrm{T}} \mathbf{D} \widehat{\mathbf{B}}_j V_k \tag{6.11}$$

where V_k is the volume of the smoothing domain for the k^{th} node and $\widehat{\mathbf{B}}$ is the smoothed strain matrix that can be formulated as follows.

Introducing the smoothing operation, the strain to be used in the Galerkin weak form is assumed to be smoothed strain for node k (Chen et al., 2001)

$$\widehat{\boldsymbol{\varepsilon}}_k \equiv \widehat{\boldsymbol{\varepsilon}}\ (\mathbf{x}_k) = \int_{\Omega_k} \boldsymbol{\varepsilon}(\mathbf{x}) \widehat{\mathbf{W}}(\mathbf{x} - \mathbf{x}_k) d\Omega \tag{6.12}$$

where $\widehat{\mathbf{W}}$ is the matrix of smoothing functions.

For simplicity, the smoothing function is taken as

$$\widehat{\mathbf{W}}(\mathbf{x} - \mathbf{x}_k) = \begin{cases} 1/V_k & \mathbf{x} \in V_k \\ 0 & \mathbf{x} \notin V_k \end{cases} \tag{6.13}$$

where $V_k = \int_{\Omega_k} d\Omega$ is the volume of the smoothing domain for node k.

Substituting Equation (6.13) into Equation (6.12) and integrating by parts, yields

$$\widehat{\boldsymbol{\varepsilon}}_k = \frac{1}{V_k} \int_{\Omega_k} \boldsymbol{\varepsilon}(\mathbf{x}) d\Omega = \frac{1}{V_k} \int_{\Gamma_k} \mathbf{L}_n \mathbf{u}(\mathbf{x}) d\Gamma = \widehat{\boldsymbol{\varepsilon}}_k(\mathbf{u}) \tag{6.14}$$

where $\mathbf{L}_n^T = \begin{bmatrix} n_x & 0 & 0 & n_y & 0 & n_z \\ 0 & n_y & 0 & n_x & n_z & 0 \\ 0 & 0 & n_z & 0 & n_y & n_x \end{bmatrix}$ is the matrix of unit outward normal, Γ_k is the boundary surface of the smoothing domain for node k. Introducing the PIM shape functions into Equation (6.14), the smoothed strain can be written in the following matrix form.

$$\widehat{\boldsymbol{\varepsilon}}_k = \sum_{i \in N_{infl}} \widehat{\mathbf{B}}_i(\mathbf{x}_k)\mathbf{U}_i \tag{6.15}$$

Where N_{infl} is the number of nodes in the influence domain of node k (including node k). When linear shape functions are used, it is the number of nodes that are directly connected to node k. In three-dimensional space,

$$\widehat{\mathbf{B}}_i(\mathbf{x}_k) = \begin{bmatrix} \widehat{b}_{ix}(\mathbf{x}_k) & 0 & 0 \\ 0 & \widehat{b}_{iy}(\mathbf{x}_k) & 0 \\ 0 & 0 & \widehat{b}_{iz}(\mathbf{x}_k) \\ \widehat{b}_{iy}(\mathbf{x}_k) & \widehat{b}_{ix}(\mathbf{x}_k) & 0 \\ 0 & \widehat{b}_{iz}(\mathbf{x}_k) & \widehat{b}_{iy}(\mathbf{x}_k) \\ \widehat{b}_{iz}(\mathbf{x}_k) & 0 & \widehat{b}_{ix}(\mathbf{x}_k) \end{bmatrix} \tag{6.16}$$

$$\widetilde{b}_{il} = \frac{1}{V_k}\int_{\Omega_k} \varphi_i(\mathbf{x}) n_l(\mathbf{x}) d\Omega \qquad (l = x, y, z) \tag{6.17}$$

Applying Gauss integration among each part of the surface Γ_k of smoothing domain Ω_k, the above equation can be written in algebraic form as

$$\widehat{b}_{il} = \frac{1}{V_k}\sum_{m=1}^{N_s}\left[\sum_{n=1}^{N_g} w_n\left(\varphi_i(\mathbf{x}_{mn}) n_l(\mathbf{x}_m)\right)\right] \tag{6.18}$$

where N_s is the number of surface areas of smoothing domain Ω_k, N_g is the number of Gauss points distributed in each area, and w_n is the corresponding weight number of Gauss integration scheme. In the present method, $N_g = 4$ is used which means that 2×2 Gauss points is used for integration on each quadrangular surface area of the smoothing domain.

6.4 Numerical examples

Some 3D numerical examples will be studied in this section using the present LC-PIM. The error indicators in displacement and energy norms defined as in Equations (4.26) and (4.27) are used to evaluate the numerical solutions.

6.4.1 Linear patch test

For a numerical method working for solid mechanics problems, the sufficient requirement for convergence is to pass the standard patch test (Zienkiewicz and Taylor, 2000). Therefore, the first example is the standard patch test using the present LC-PIM. The problem is studied in a cubic domain with the dimension of $10 \times 10 \times 10$, and the displacements are prescribed on all outside boundaries by the following linear function.

$$\begin{cases} u_x = 0.6x \\ u_y = 0.6y \\ u_z = 0.6z \end{cases} \tag{6.19}$$

The linear patch test is first conducted using a set of nodes distributed in the cubic domain, i.e., eight nodes located on the vertexes of the cube and the ninth node locates

inside. By changing the location of the ninth node inside the cube, displacement error as defined in Equation (4.26) has been calculated and listed in Table 6.1. It can be found that the present method can pass the linear patch test regardless the location of the ninth node. This result numerically proves the stability of the LC-PIM.

Second, the problem domain has been represented using both 125 regularly and 166 irregularly distributed nodes as shown in Figure 6.2. For these two models, the errors in displacement are found to be 1.2837×10^{-15} and 1.2036×10^{-15} respectively, which reach almost the level of the computer precision. The results show that the displacements of all the interior nodes follow "exactly" the same function of the imposed displacement. This example demonstrates numerically that the present LC-PIM can monotonically converge due to its ability to reproduce linear fields and the use of the Galerkin weak form.

6.4.2 A 3D cantilever beam

A 3-D cantilever beam under a parabolic traction on the right edge is studied using the LC-PIM. As shown in Figure 6.3, the beam is of $L=10$, $H=1$, $B=1$, $P=-100$ and with the parameters of $E=3.0\times10^{7}$ Pa and $\nu=0.3$. Since the beam is relatively thin, analytical solutions based on the plane stress (shown in Equations 3.77-3.41) can be used approximately as reference solutions (Timoshenko and Goodier, 1970).

The problem domain has been presented using both 775 regularly and 874 irregularly distributed nodes (as shown in Figure 6.4), and computed distribution of defection along the neutral line and shear stress (τ_{xy}) along the mid-line $(x=L/2, z=0)$ are plotted together with the reference solutions in Figure 6.5 and Figure 6.6, respectively. It can be

found that the numerical results obtained using the present LC-PIM with both regular and irregular nodal distribution models are in very good agreement with the reference ones.

The problem is discretized using four models of nodes distribution, i.e., 163,439,874 and 1304 nodes. The calculated strain energy has been plotted against the increase of DOFs in Figure 6.7 for both the FEM and LC-PIM, in wihcih the reference strain energy is calculated by using the reference solutions of stress components shown in Equations 3.77-3.41. For this 3D problem, it is found that LC-PIM also produces an upper bound solution, while the FEM produces the lower bound.

6.4.3 3D Lame problem

The 3D Lame problem which has been studied in Chapter 3 (shown in Figure 3.13) is studied again using the present LC-PIM. As the problem is spherically symmetrical, only one-eighth of the sphere is modeled and symmetry conditions are imposed on the three planes of symmetry. The related parameters are taken as $E = 1.0\,\text{Pa}, v = 0.3$, $a = 1$, $b = 2$ and $P = 1$. The problem domain is presented using 1304 irregularly distributed nodes. The computed nodal displacements and stresses along the x axis are plotted in Figure 6.8 and Figure 6.9, respectively. It can be clearly seen that the numerical results agree well with the analytical ones.

Furthermore, to investigate the properties of convergence and efficiency of the present LC-PIM for 3D problems, four models of 173, 317, 729, and 1304 irregularly distributed nodes are employed. For each model of nodes distribution, the error in energy of the numerical results is calculated according to the definition in Equation (4.27). For

comparison, the FEM using linear four-node tetrahedron element is also employed to study the problem with the same nodes distributions. As shown in Figure 6.10, the results of error in energy norm against h are plotted for both the FEM and the present LC-PIM, where h is the average nodal spacing of the nodes distribution. It can be found obviously that these two methods reach similar rates of convergence, but the LC-PIM obtains more accurate results compared with the linear FEM for this problem. In Figure 6.11, the energy errors of the numerical results obtained using these two methods are plotted against the CPU time consumed, which shows performance of numerical methods. It can be found that the LC-PIM is clearly more efficient than the linear FEM for this problem.

Figure 6.12 shows that for this 3D problem with, LC-PIM has again produced an upper bound solution: stain energy of LC-PIM solution is no-less than the strain energy of the reference solution and convergences to it with the increase of DOFs, while FEM solution convergences from below to the reference solution.

6.4.4 3D Kirsch problem

A 3D Kirsch problem is considered to examine the stress distribution in the vicinity of a small cavity in an infinite cube subjected to far field uniform tension, as illustrated in Figure 6.13. The analytical solution for the normal stress (σ_{zz}) in the plane $z=0$ is given as (Timoshenko and Goodier, 1970):

$$\sigma_{zz}=\sigma_0\left[1+\frac{4-5v}{2(7-5v)}\left(\frac{a}{r}\right)^3+\frac{9}{2(7-5v)}\left(\frac{a}{r}\right)^5\right] \tag{6.20}$$

where r is the radial distance from the centroid of the cube to the point of interest.

The problem is modeled for $a=1$, $b=10$ and $\sigma_0=1$ with the parameters of $E=3.0\times10^7$ Pa and $v=0.3$. The problem domain is presented with total 1256 irregularly distributed nodes. Figure 6.14 shows the comparison between the analytical solution and the numerical solution for the normal stress σ_{zz} along the x axis. It can be clearly found again that the LC-PIM solution is in excellent agreement with the analytical ones.

6.4.5 An automotive part: rim

A typical rim used in automotive industry is modeled and studied using the present LC-PIM. As shown in Figure 6.15, the rim is of inner radius 2, outer radius 19 and a thickness of 3. It is constrained in three dimensions along the inner annulus and a uniform pressure of 100 is applied on the outer annulus of 60^o. The parameters are taken as $E=3.0\times10^7$ Pa and $v=0.3$. As no analytical solution is available for this problem, a reference solution is obtained using the FEM software ABAQUS with a very fine mesh, in which the four-node tetrahedeon elements are used with total 16715 nodes distributed in the problem domain. The problem domain is represented using 7972 nodes and the numerical solutions of stress components of nodes located on the plane of $z=0$ are plotted in the form of contour. Figure 6.16, Figure 6.17 and Figure 6.18 show the comparison of the stress contour between the reference solutions and the numerical ones for σ_{xx}, σ_{yy} and τ_{xy}, respectively. It can be seen that the results obtained using the LC-PIM match well with the reference ones.

6.4.6 Riser connector

The final example comes from a real offshore project of Floating Production and Storage Unit (FPSO). Fluid transfer between FPSO and subsea pipeline is carried out through a kind of flexible pipe called riser, which is attached to FPSO shipside by riser connector. The simplified model of riser connector is shown in Figure 6.19 with the load being applied on the top flange of riser connector. The boundary conditions are defined at the end of I-beams where riser connector is supported by other structures. This riser connector is made of steel material with Young's modulus $E = 2.0 \times 10^5$ N/mm^2, Poisson's ratio $v = 0.32$.

Reference solution of this problem is obtained using the FEM software ABAQUS with 4-node tetrahedron elements via very fine mesh (total 27072 nodes), and the contour of elemental Von Mises stress is plotted in Figure 6.20 in the deformed shape of the riser connector. For the purpose of comparison, this problem is studied using both the present LC-PIM and the linear FEM via the same nodes distribution (total 2228 nodes). The numerical results of the elemental Von Mises stress obtained by using these two methods are plotted in the form of contour, shown in Figure 6.21 and Figure 6.22, respectively. It can be found that, although the riser connector is presented with less than one tenth of the reference nodes distribution, the LC-PIM solution matches well with the reference one and is closer to it than that of the linear FEM.

6.5 Remarks

In this chapter, the linearly conforming point interpolation method (LC-PIM) is formulated for three dimensional problems. The present LC-PIM employs polynomial basis functions for field approximation and the shape functions have the property of Kronecker delta function. The generalized Galerkin weak form is used and a stabilized nodal integration scheme with strain smoothing technique is employed to perform the numerical integration. Some examples are studied numerically using the present method. Either for the benchmark problems which have the analytical solutions, or for the practical example with the complicated shapes, the LC-PIM can always obtain very stable and accurate results in terms of both displacements and stresses. The following remarks can be made.

- Shape functions are generated using the polynomial basis functions and have the property of Kronecher delta function, which allows straightforward imposition of point essential boundary conditions.
- With the implementation of strain smoothing technique, the LC-PIM using the nodal integration scheme can get stable numerical results.
- Using the technique of strain smoothing, field gradients are computed directly using shape functions itself and no derivative of shape function is needed. This property can reduce the requirement on the smoothness of shape functions, which allows the LC-PIM to get accurate stress solutions, even using low order shape functions.

- The present LC-PIM guarantees a linear exactness of the numerical solutions, which is also proven numerically by the standard patch test. This property ensures the stability and the convergence of the LC-PIM.
- Compared with the FEM using the linear tetrahedron element, the LC-PIM can achieve a higher accuracy and better efficiency for the problems studied.
- The LC-PIM possesses the upper bound property on strain energy for three-dimensional problems.

Table 6.1 Displacement error of the linear patch

Location of node 9	(5,5,5)	(9.9,9.9,9.9)	(9.9,9.9,0.1)	(0.1,5,5)	(5,5,0.1)
Error in displacement	2.5807E-16	2.0467D-14	1.4951D-14	2.4072D-16	1.5590D-16

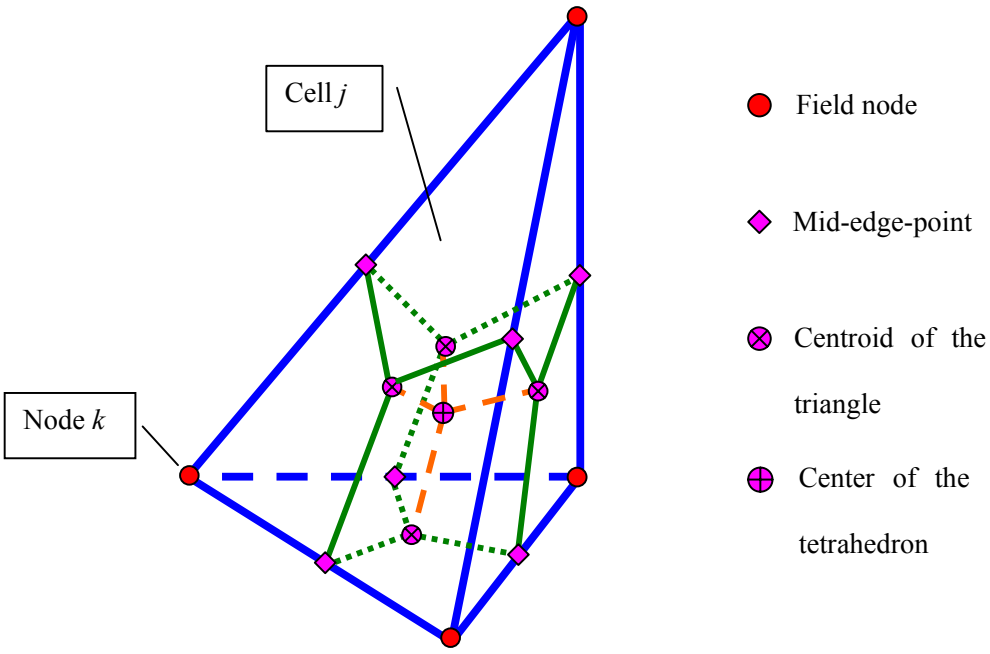

Figure 6.1 Illustration of background four-node tetrahedron cell and one of the sub-smoothing-domain for node k located in cell j created by connecting the mid-edge-points, the centroids of the surface triangles and the centroid of the tetrahedron.

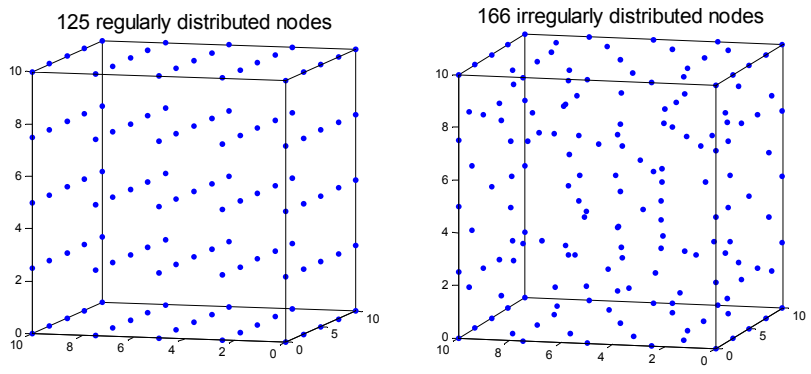

Figure 6.2 Illustration of nodal distributions of a cube for the standard patch test

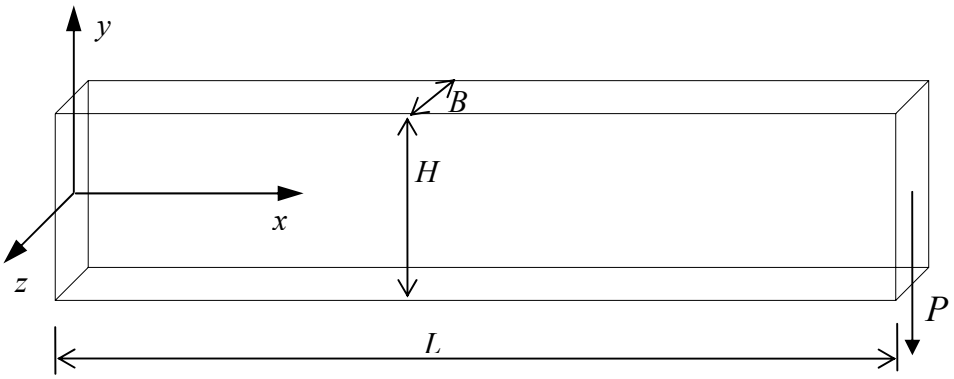

Figure 6.3 A 3D cantilever beam subjected to a parabolic traction on the right edge.

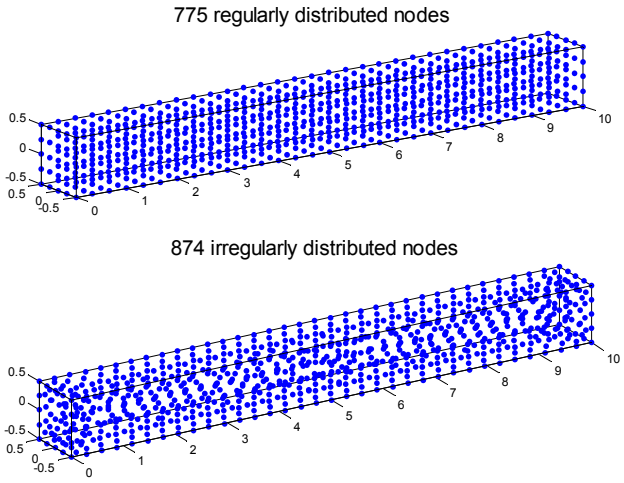

Figure 6.4 Illustration of nodal distributions of the 3D cantilever beam

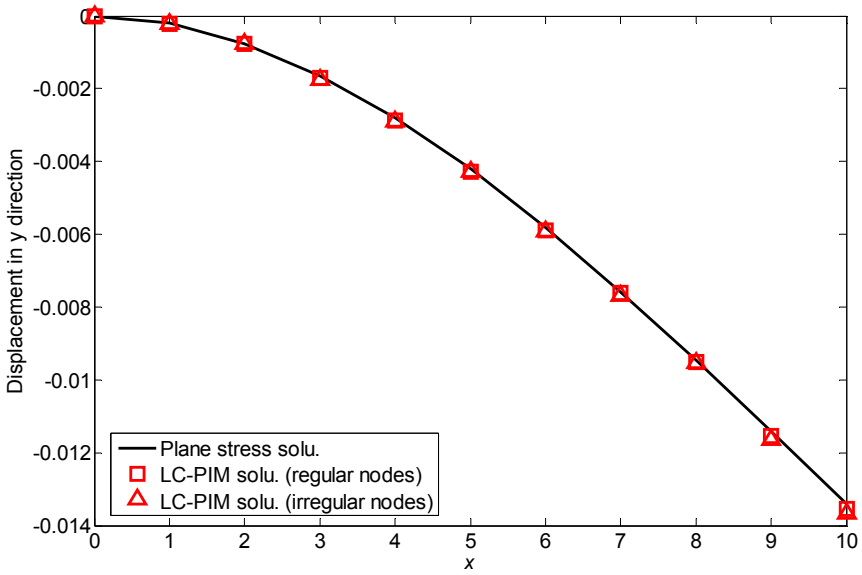

Figure 6.5 Deflection distribution along the neutral line of the 3D cantilever beam

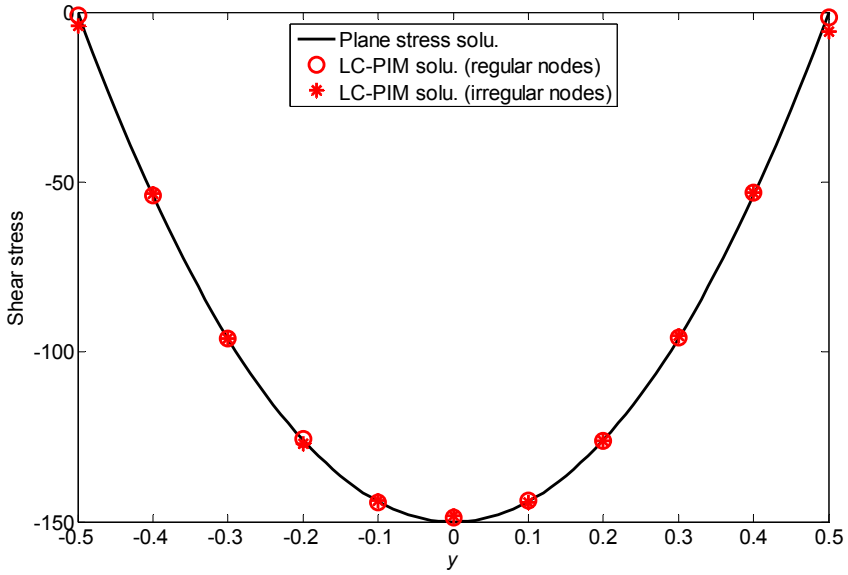

Figure 6.6 Shear stress distribution along the line of $(x = L/2, z = 0)$ of the 3D cantilever beam

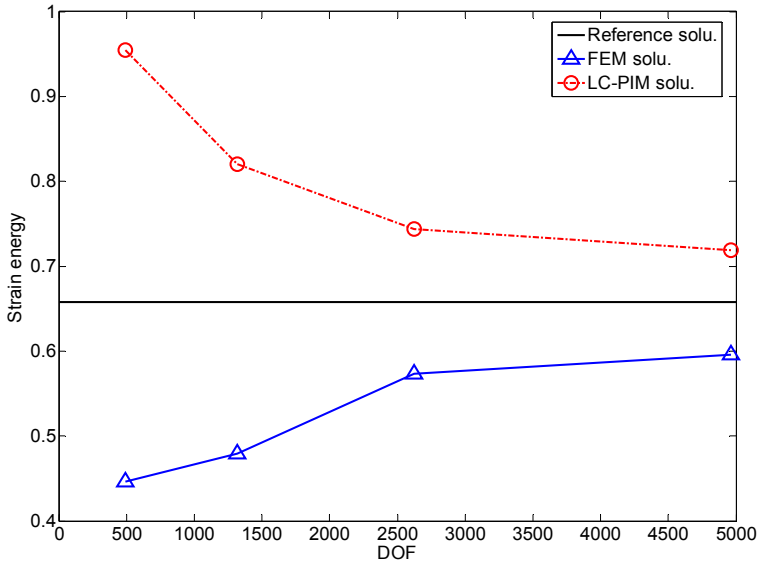

Figure 6.7 Study of the upper bound property on strain energy for the LC-PIM via the 3D cantilever problem

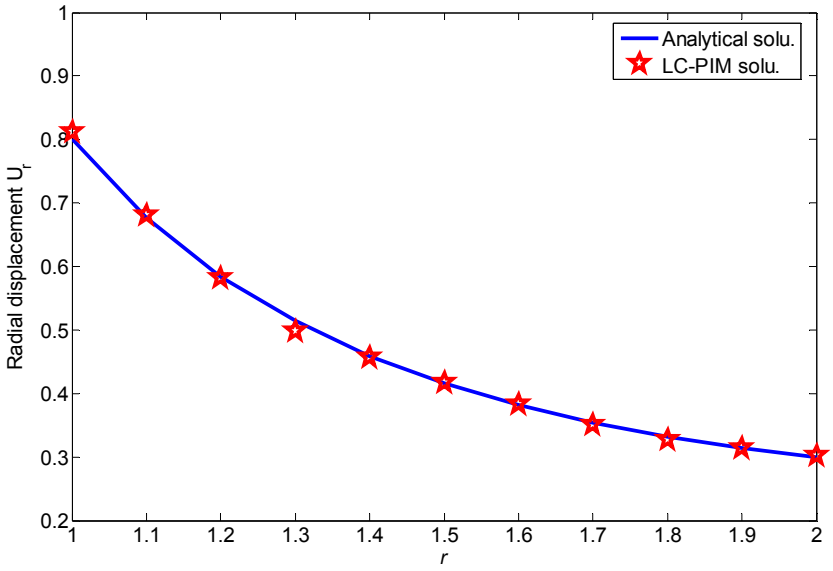

Figure 6.8 Distribution of the radial displacement along the x axis for the 3D Lame problem

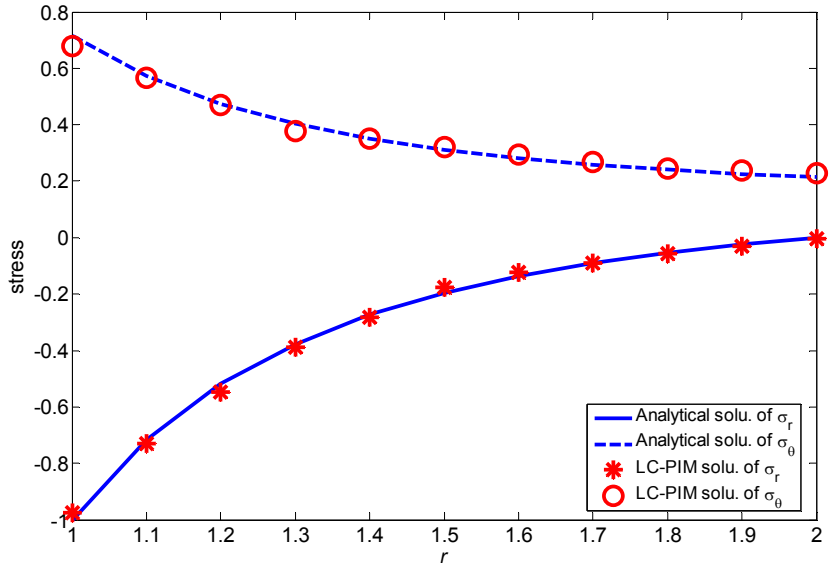

Figure 6.9 Distribution of radial and tangential stresses along the x axis for the 3D Lame problem

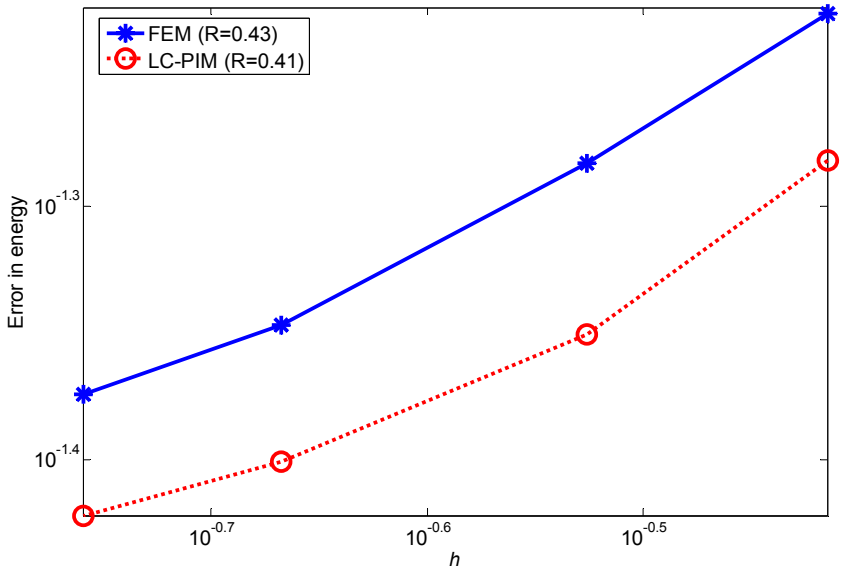

Figure 6.10 Comparison of convergence between FEM and LC-PIM via the Lame problem with the same nodes distribution

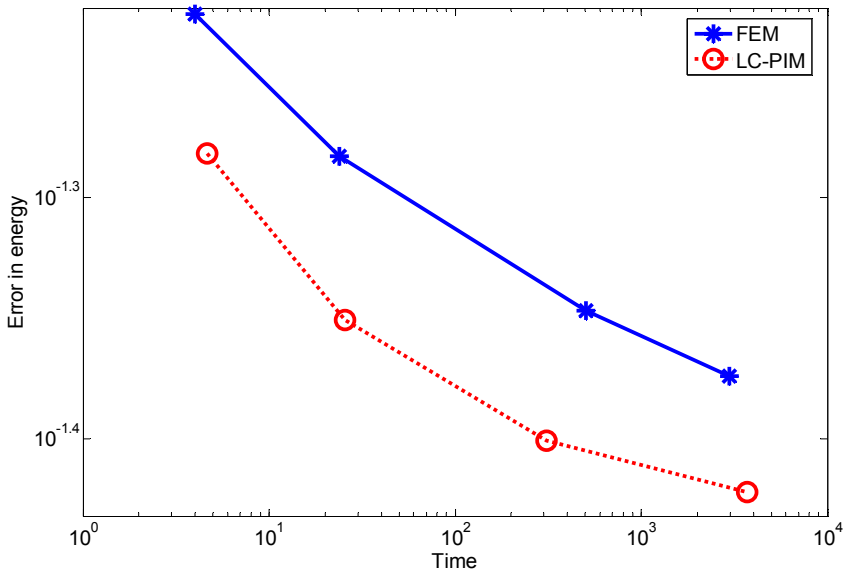

Figure 6.11 Comparison of efficiency between FEM and LC-PIM via the Lame problem with the same nodes distribution

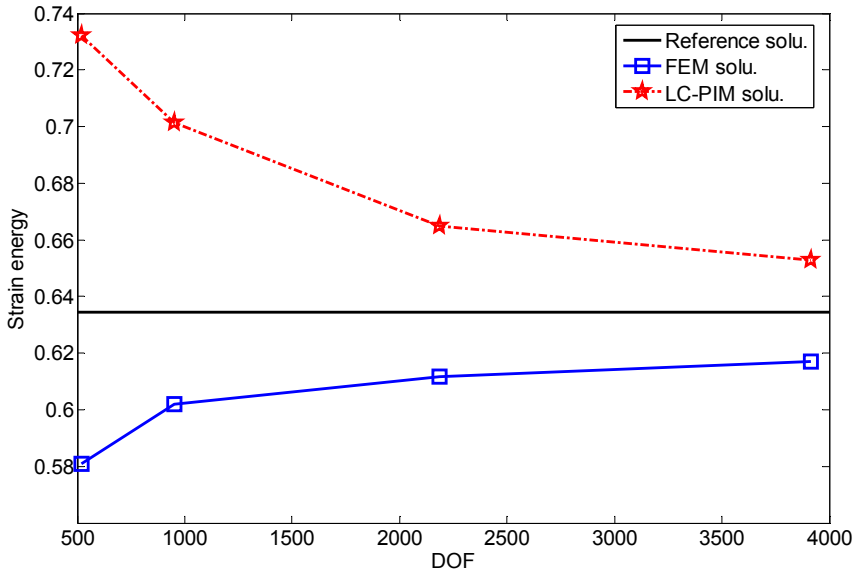

Figure 6.12 Study of the upper bound property on strain energy for the LC-PIM via the 3D Lame problem

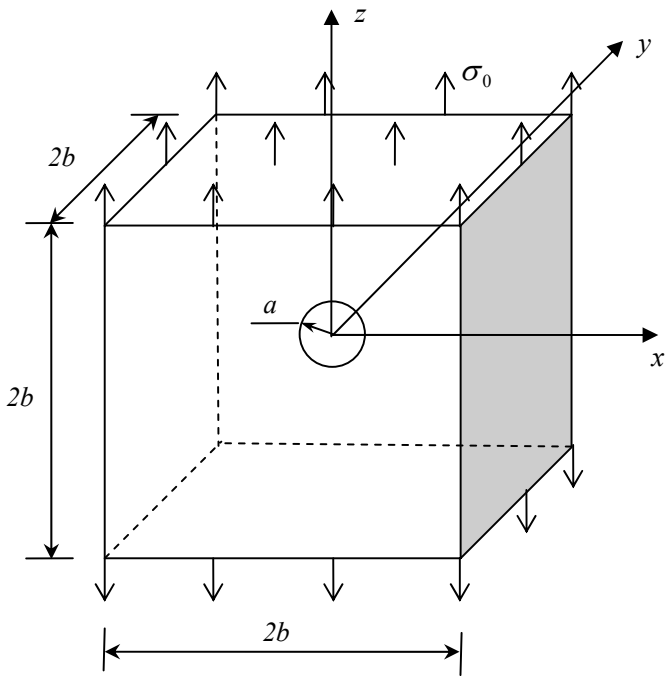

Figure 6.13 3D Kirsch problem: a cube with a spherical cavity subjected to a uniform tension

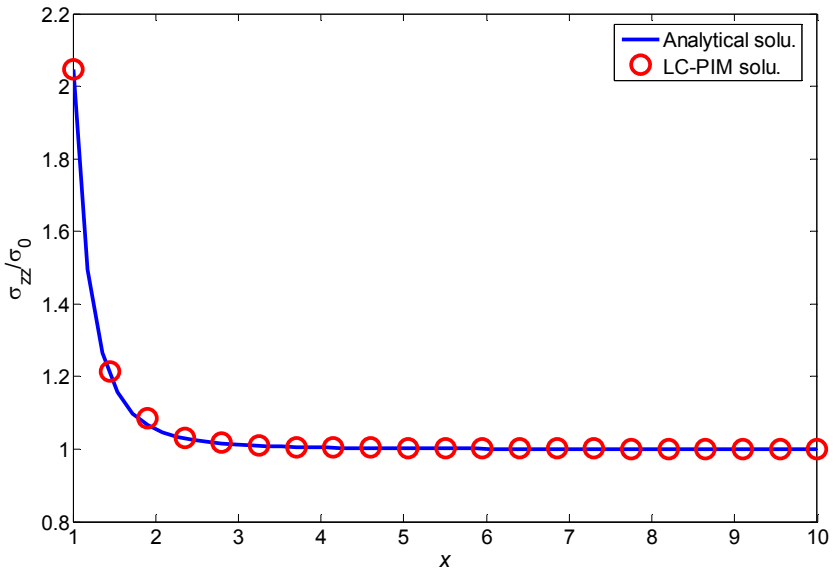

Figure 6.14 Distribution of σ_{zz} along the x axis for the Kirsch problem

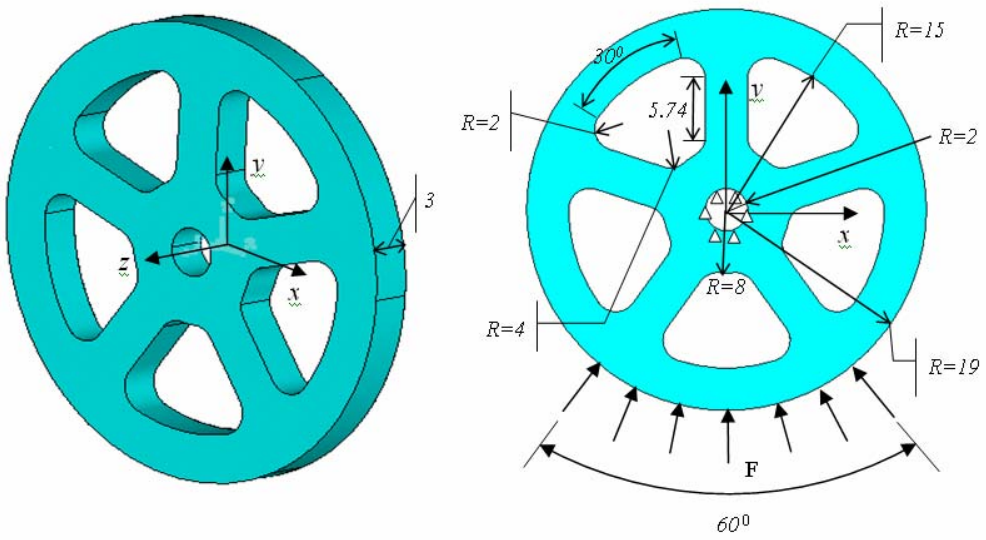

Figure 6.15 Simplified model of an automotive rim.

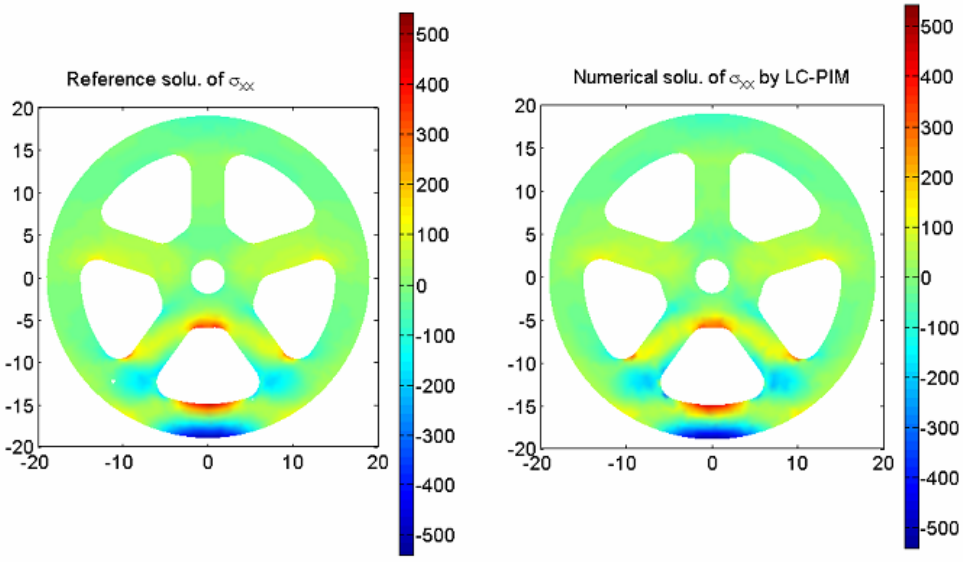

Figure 6.16 Stress contour of σ_{xx} on the plane $z = 0$ for the rim problem

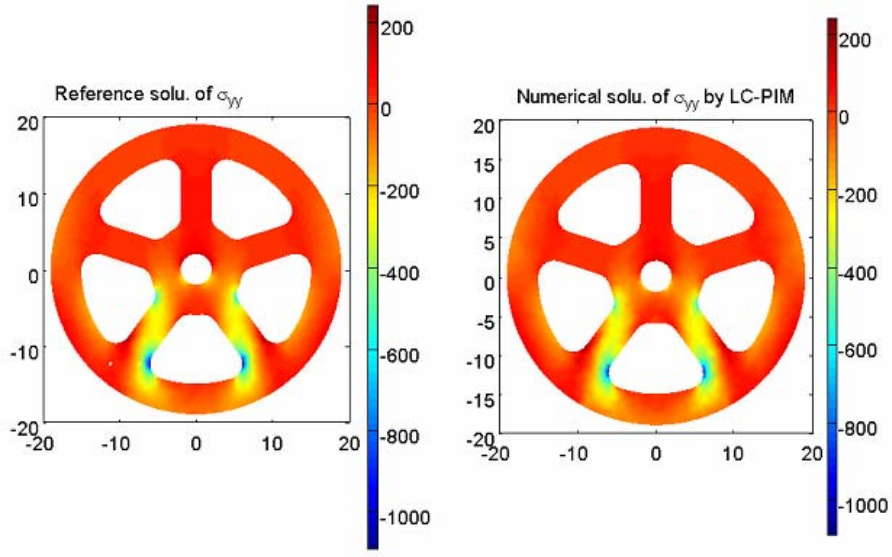

Figure 6.17 Stress contour of σ_{yy} on the plane $z = 0$ for the rim problem

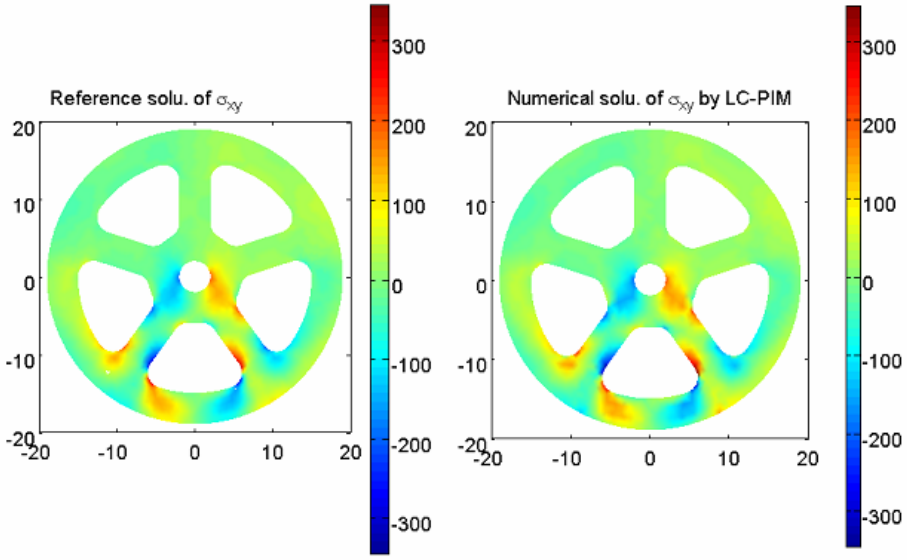

Figure 6.18 Stress contour of σ_{xy} on the plane $z = 0$ for the rim problem

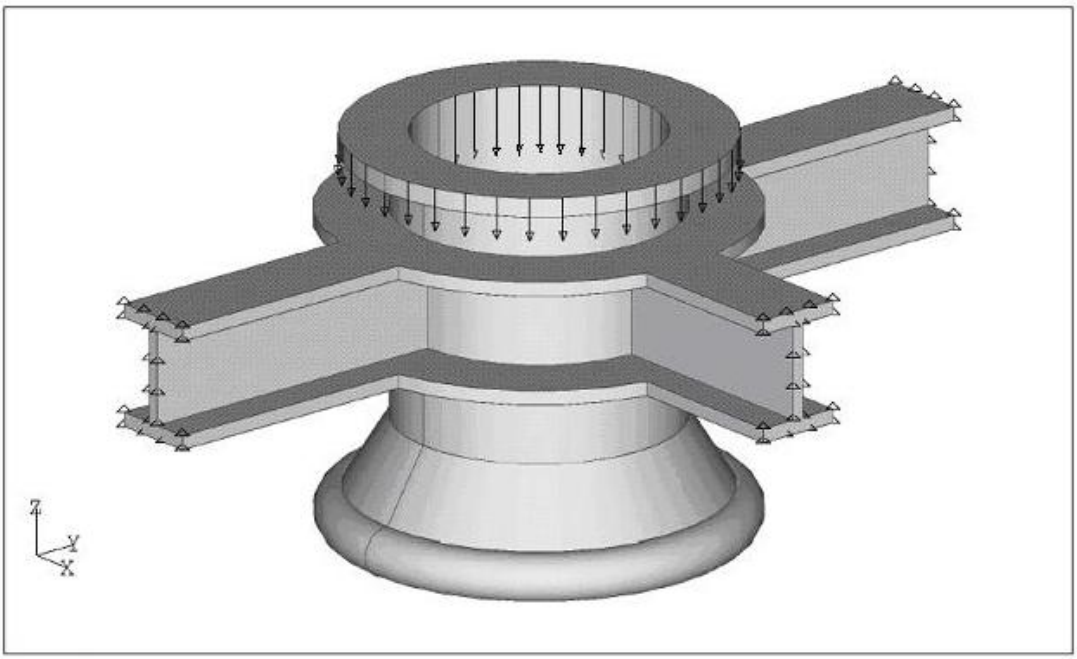

Figure 6.19 Simplified model of the three-dimensional riser connector

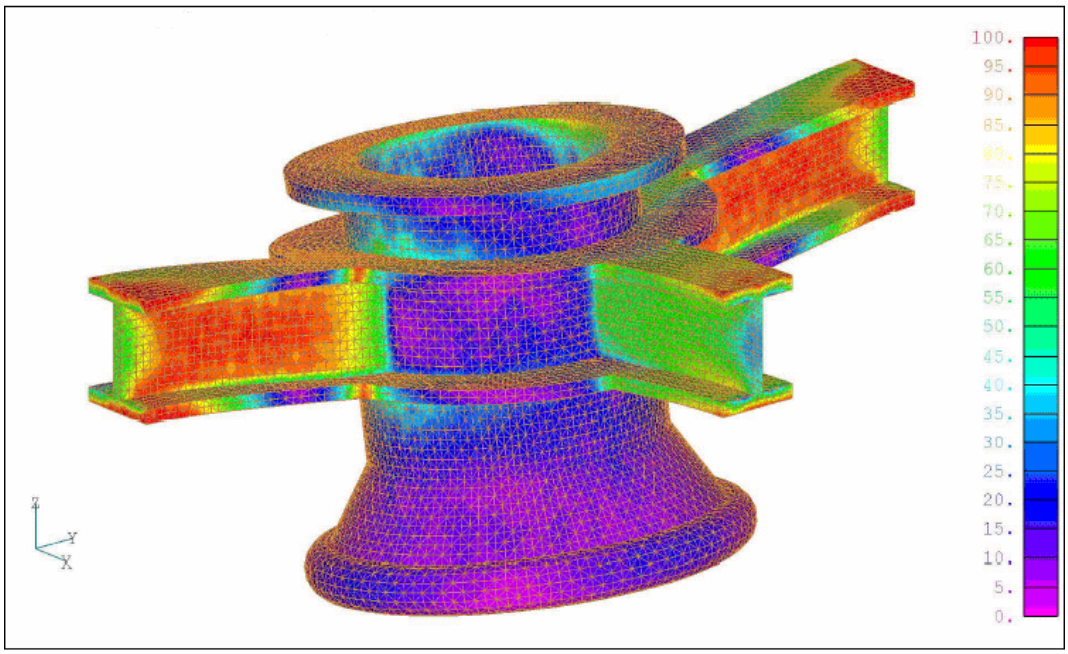

Figure 6.20 Reference solution of contour for elemental Von Mises stress obtained using FEM software (ABAQUS) via fine mesh

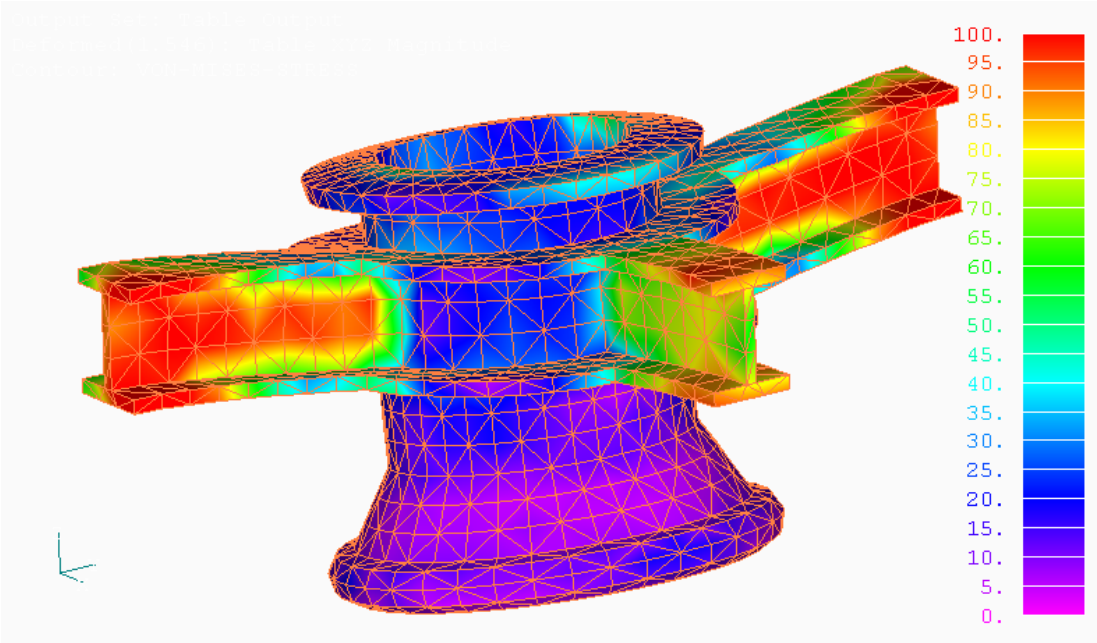

Figure 6.21 Contour of elemental Von Mises stress obtained using LC-PIM via coarse mesh

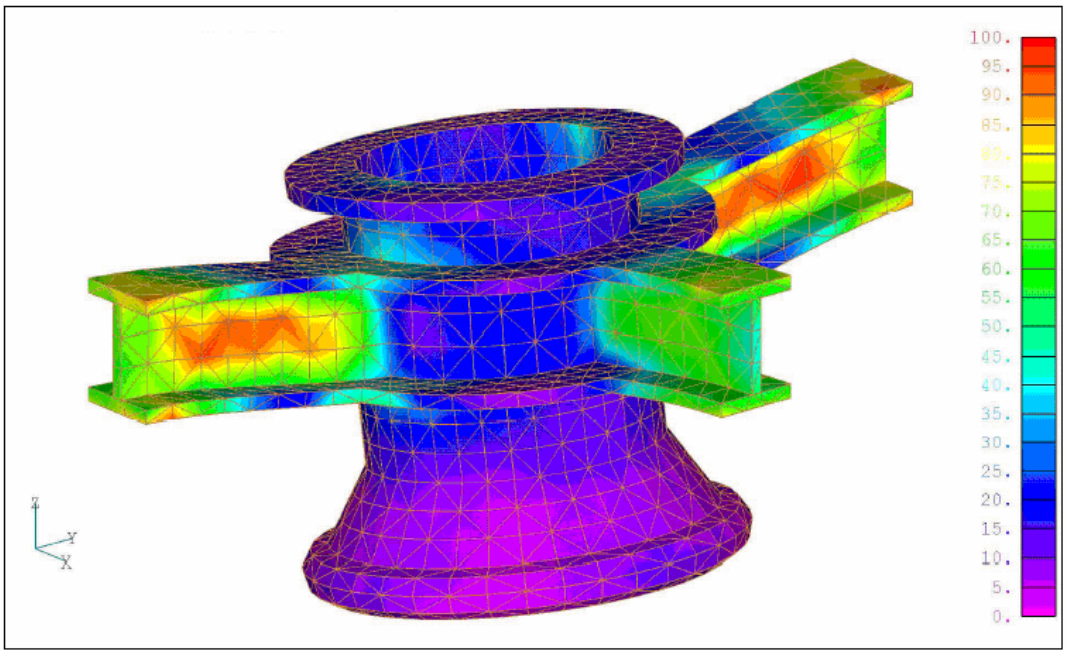

Figure 6.22 Contour of elemental Von Mises stress obtained using FEM via coarse mesh

Chapter 7

Adaptive analysis using the linearly conforming point interpolation method (LC-PIM)

7.1 Introduction

In this chapter, an adaptive procedure using the linearly conforming point interpolation method (LC-PIM) is introdued. Adaptive analysis has been adequately used in the traditional FEM and various procedures for error estimate and refinement have been developed. In particular, two distinct types of error indicator or estimators are used: recovery based error estimators and residual based error estimators. Recovery is the process that can improve the accuracy by a posteriori treatment of the numerical data (Zienkiewicz and Taylor, 2000). The recovery based error indicator was introduced by Zienkiewicz and Zhu (1987) and has been widely used in the finite element method. A thorough state of the posteriori error estimation, including limits of usual error measures, has been proposed by Gratsch and Bathe recently (2005). The residual based error estimators were developed by making use of the residuals of the numerical approximation, either explicitly or implicitly. Many works have been done on this type of error estimators (Babuska and Reinboldt, 1978; Bank and Weiser, 1985; Verfurth, 1989; Ainsworth and Oden, 1993). There are various procedures of the refinement and they may be broadly classified into two categories: *h*-type refinement and *p*-type refinement

(Zienkiewicz and Taylor, 2000). In an *h*-type refinement, the same class of elements will continue to be used but are changed in size to provide maximum economy in reaching the desired solution. In a *p*-type refinement, elements of same size are used and simply increase the order of the polynomial functions.

For most meshfree methods, as they evaluate field variables entirely based on a group of discrete nodes and require no predefined nodal connectivity, then field nodes can be moved, inserted and deleted freely. This is particularly suitable for adaptive analysis. So far, many procedures of adaptive analysis have been developed for meshfree methods. Duarte and Oden (1996) derived an error estimate that involves only the computation of interior residuals and the residuals for Neumann boundary conditions for the *h*-*p* cloud method. For the EFG method, Chung and Belytschko have proposed an error estimate which is based on the difference between the values of projected stresses and the stresses given directly by the EFG method (Chung and Belytschko, 1998). More in-depth study about refinement procedures in EFG has been conducted by Lee and Zhou (2003). In the context of the reproducing kernel particle method (RKPM), Liu et al., (1997) have proposed approaches based on the residual errors. You et al. (2003) have developed an approach by utilizing the reproducing kernel as a low-pass filter and the corresponding high-pass filter is used to identity the locations of high gradient. Yvonnet et al. (2006) have proposed an adaptive procedure with the error indicator based on natural neighbor recovery stress in the context of the constrained natural element method (C-NEM). Liu and Tu (2002) have also developed an error estimate based on the energy of individual cells. For each cell, computing cell energy and reference cell energy are generated based

on a same stress field by using two different integration schemes; the difference between the two energy values is used as the basic measure of error level.

As presented in Chapters 5 and 6, the LC-PIM not only maintains the unique feature brought by the use of shape functions of Delta function property, but also guarantees linear exactness and monotonic convergence in energy norm for the numerical solutions. Compared to the linear FEM, the LC-PIM can give both better accuracy and higher convergence rate, especially for stress results (Liu et al., 2005a; Zhang et al., 2006b; Liu and Zhang, 2006). However, in the LC-PIM frame work, these types of error estimates cannot be used directly, because the use of strain smoothing has made the matter trickier. Therefore, a proper error estimate needs to be devised. The objective of the present work is to develop an effective adaptive procedure for the LC-PIM. First, an efficient error indicator is defined which works properly in the framework of the LC-PIM. A corresponding refinement scheme is then proposed for adaptive analysis. In the present procedure, background triangular cells that can always be generated automatically are used and an error indicator based on residuals of the strong-form governing equations is used to evaluate the residual error of each triangular cell (Kee et al., 2006). Then new nodes will be added in the cell whose residual error exceeds the critical value. The Delaunay algorithm is finally used to reform the background cells and the analysis will be advanced to the next stage. As the formulations of the LC-PIM has been presented in detail in Chapters 5 and 6, only the adaptive procedure, including the definition of the error estimate and the refinement strategy, is introduced in the flowing sections.

7.2 Adaptive procedure

A good error indicator and an appropriate refinement strategy should be the two important issues for an adaptive procedure. In the present work, an error estimate based on the residual error of the strong-form governing equations and a simple refinement strategy based on the background triangular cells have been used for adaptive analysis using the LC-PIM.

7.2.1 Error indicator based on residual error

The error indicator proposed by Kee et al. (2006, 2007) is evaluated based on the residual error of the governing equations. Consider a two dimensional problem that is governed by the following partial differential equation in terms of displacements:

$$C(u)+b=0 \tag{7.1}$$

where $C(\ )$ is a differential operator. Then the residual error for a cell, say cell i, can be calculated as

$$\eta_i = \frac{1}{3} A_i \left\| C(u)+b \right\|_{L_2} \tag{7.2}$$

where A_i is the area of the i^{th} cell.

Note that in the process of calculating residual errors using Equation (7.1), second order derivatives of displacement variables are involved. But for the present LC-PIM, same as the linear FEM, the second order derivatives of shape functions will be zero. So the meshfree radial point interpolation method (RPIM) is employed for the calculating of this error estimate (Kee et al., 2006, 2007). As presented in Chapter 2, the RPIM shape

functions created using RBFs are piecewisely differentiable to any order in the local support domain (Liu, 2002) hand have been found works well for the calculation of the present error indicator (Kee et al, 2006).

7.2.2 Refinement strategy

According to the residual error of each cell, an adaptive procedure can then be implemented as illustrated in Figure 7.1. In the process of the adaptive refinement, there are two issues should be noted.

1) Definition of local critical value

In the present study, a maximum number of the adaptive steps is predefined and adaptive refinements may proceed until the number of steps equals this maximum number. In the process of each adaptive step, a local critical value of residual error is involved which is defined as

$$\eta_{lc} = \kappa_l \eta_{lm} \tag{7.3}$$

where η_{lc} is the local critical value of residual error for a particular adaptive step, κ_l is a constant number and η_{lm} is the maximum value of residual error throughout all the background cells at this adaptive step.

2) Refinement scheme

In each adaptive step, refinement is performed by simply adding nodes in the cell whose residual error is greater than the critical value (means $\eta_i > \eta_{lc}$). In advance, the background triangular cells are classified into interior and edge cells, which have been

defined in Chapter 5. An interior cell is a cell that has no edge on the boundaries of the problem domain, and an edge cell is a cell that has at least one edge on the boundaries. For example, cell a and cell b are interior and edge cells respectively (shown in Figure 7.2). Then if an interior cell needs to be refined, a new node will be added at the centroid of the triangle; for an edge cell, two new nodes will be added at the centroid and the midpoint of the edge which is on the boundaries (Illustrated in Figure 7.2). Finally, the formation of the new background mesh is performed using Delaunay technique based on the new nodal configuration and the third picture in Figure 7.2 is only a sketch. This refinement sheme is very simple and has been proven effective for all the cases studien in the following section. In addition, this simple procedure has an advantage that the information at the nodes of old mesh is preserved.

7.3 Numerical examples

To investigate the performance of the present adaptive procedure for LC-PIM, several numerical examples are studied in this section.

7.3.1 Infinite plate with a circular hole

A benchmark problem for adaptive analysis is studied here, which is an infinite plate with a central circular hole and subjected to unidirectional tensile (as shown in Figure 4.18). Plane stress is considered with Young's modulus $E = 3.0 \times 10^7$ Pa and $v = 0.3$. The parameters are taken as $a = 1$ and $T_x = 10$. As the problem has two-fold symmetry, only

the upper right quadrant is studied with $b = 5$. The analytical solutions for this problem are available as shown in Equations (4.40)-(4.45).

To study the effectiveness of the present adaptive procedure, uniformly refined models as shown in Figure 7.3 are also considered. For the adaptive LC-PIM, $\kappa_l = 0.05$ is used and 6 steps of adaptive refinement is performed. Furthermore, the present problem has also been studied using linear FEM with both uniform and adaptive models. For the adaptive procedure using the FEM, the same refinement algorithm as used in adaptive LC-PIM is used with same tolerant values. The results of FEM and LC-PIM with both uniform and adaptive models are shown in Figure 7.4 and Figure 7.5, in which the energy errors calculated using Equation (4.27) are plotted with respect to degree of freedom (DOF) and h respectively. Here h is taken as the average nodal spacing for different nodal configurations. First, these two figures show us that the adaptive models for both LC-PIM and FEM obtain much higher convergence rate compared to the uniformly refined modes. This has demonstrated the effectiveness of the proposed adaptive procedure. Second, compared with the linear FEM, the LC-PIM achieves a better accuracy and higher convergence rate for both uniform and adaptive models (1.55 and 2.2 for uniform and adaptive models respectively). This conclusion is consistent with the previous work which has been presented in Chapter 5.

Figure 7.6 shows the nodal configuration of the results of adaptive refinement. From the figure it can be found that the refinement is activated in the regions with a significant stress concentration.

7.3.2 Short cantilever plate

A short cantilever plate is studied, which is a rather simple model example and was also analyzed in the work of Ainsworth and Oden (1997). The problem domain is a unit square and subjected to unit pressure along the upper side (shown in Figure 7.7). Plane strain is considered with $E = 1.0$ and $v = 0.3$. The exact solution of the strain energy for this problem is known as $S = 1.3797453$. The analytical solution of displacement components for this problem is not available, and the value of point A, $u_y(A) = 2.875323$, is used as the reference one which was provided in the work of Steeb et al. (2002).

This problem has also been studied with both uniformly refined models of 81, 289 and 1089 nodes respectively and adaptive models. For the adaptive study, $\kappa_l = 0.05$ is used and the adaptive refinement is performed for 4 steps. As shown in Figure 7.8, the relative errors of $u_y(A)$ and strain energy are plotted against the DOF for both uniform and adaptive refinements. Again the results show that the LC-PIM with adaptive refinement convergences faster than that based on uniform refinement with the increase of DOF. Figure 7.9 shows the nodal distributions for the adaptive procedure at each step. It can be found that refinement is focusing on the two corners where the concentration of stress occurs.

7.3.3 Mode-I crack problem

A mode-I crack problem is considered, whose geometry is shown in Figure 7.10. The exact stress solution in the crack tip neighborhood is given as follows (Perrone et al., 1978)

$$\sigma_{xx} = \frac{\mathrm{K_I}}{\sqrt{2\pi r}}\cos\frac{\theta}{2}\left(1-\sin\frac{\theta}{2}\sin\frac{3\theta}{2}\right) \tag{7.4}$$

$$\sigma_{yy} = \frac{\mathrm{K_I}}{\sqrt{2\pi r}}\cos\frac{\theta}{2}\left(1+\sin\frac{\theta}{2}\sin\frac{3\theta}{2}\right) \tag{7.5}$$

$$\sigma_{xy} = \frac{\mathrm{K_I}}{\sqrt{2\pi r}}\sin\frac{\theta}{2}\cos\frac{\theta}{2}\cos\frac{3\theta}{2} \tag{7.6}$$

where $\mathrm{K_I}$ is the stress intensity factor and it is assumed $\mathrm{K_I} = \sqrt{2\pi}$ in the present case. As the problem is symmetric about x axis, only the upper half of the plate is modeled for analysis (shown in Figure 7.10). To extend the exact solution to the whole domain, exact traction which can be obtained using Equations (7.4)-(7.6), will be imposed on the outer sides (the upper, the right and the left sides). The symmetric conditions are imposed on the bottom edge as shown in Figure 7.10. The problem is considered as plain strain problem with the parameters $E = 3.0\times10^7$ Pa, $v = 0.3$ and $a = 1$.

The problem is studied using the LC-PIM with both uniform and adaptive models. For the uniform refinement, three models with 153, 561 and 1326 nodes are studied. The adaptive analysis is performed for 4 steps with $\kappa_l = 0.05$ and the results are compared with that obtained using uniform models. The first picture in Figure 7.11 shows the energy errors of the numerical solutions calculated using Equation (4.27) against DOF for both uniform and adaptive models, and the second picture shows the situation of relative

errors of strain energy. The results of these two indexes indicate that the adaptive model convergences much faster than the uniform model. Figure 7.12 shows the nodal configurations at each adaptive step for the whole plate, where the nodes distribution in the lower half plate is obtained by reflection. It can be found that more nodes may centralize around the tip of the creak as singularity appears at that point.

7.3.4 L-shaped plate

A L-shaped plate subjected to uniform tensile force in the horizontal direction is studied. As shown in Figure 7.13, the plate is constrained in x and y directions along the right and upper sides respectively. This is also a benchmark problem to examine an adaptive scheme as singularity will occur at point A. The plate is studied as a plane stress problem with the parameters as $E = 3.0\times10^7$ Pa, $v = 0.3$, $a = 5$ and $p = 10$.

The L-shaped plate is studied using the LC-PIM with both uniform and adaptive models. For the uniform refinement, the problem domain is presented using 109, 369 and 1430 nodes respectively. For the adaptive procedure, 6 steps of adaptive refinement are performed with $\kappa_l = 0.05$ and the nodal configuration at each step is shown in Figure 7.14. The figure shows that the present adaptive procedure can accurately catch the steep gradient of stresses and the occurrence of refinement is properly concentrated around point A. This problem is also studied by using the FEM with a very fine mesh of linear triangular element (total 13654 nodes) and the calculated value of strain energy is used to compute the relative errors against the LC-PIM solutions obtained using both uniform and adaptive models. In Figure 7.15, the relative errors of strain energy are plotted

against the DOF for the results of uniform and adaptive refinements and it indicates again that the present adaptive procedure convergences much faster than the traditional uniform refinement. In Figure 7.16, contours of stress components at the finalstep of the adaptive refinement are compared with the results of the FEM using 13654 distributed nodes. It can be found that the stress components at the final adaptive step (only 750) nodes are in good agreement with the FEM results which are obtained using uniform modle with a very fine mesh. In checking the nodal spacing near the stress concentration corner, it is found that the nodal spacing of the uniform model of 13654 nodes is 0.08, and that of the adaptive model of 750 nodes is 0.072. This shows that the present adaptive procedure uses nodes where most needed. It indicate again the effectiveness of the proposed adaptive procedure using the LC-PIM.

7.4 Remarks

An efficient error indicator and the associated refinement scheme within the framework of the linearly conforming point interpolation method (LC-PIM) are presented in this chapter. The LC-PIM which employs the nodal integration scheme with strain smoothing technique can guarantee linear exactness and monotonic convergence in energy norm for the numerical results. Compared with the linear FEM, the LC-PIM obtains better accuracy and achiever higher convergence rate. The error estimate used in the present adaptive procedure is calculated based on the residual error of the strong-form governing equations. The results of some benchmark problems show that the present adaptive procedure using the LC-PIM can accurately catch the appearance of the steep

gradient of stresses and the occurrence of refinement is concentrated properly. Compared to the results of uniformly refined models, the results of adaptive models can convergence much faster. All the results have demonstrated the effectiveness of the present adaptive procedure for the LC-PIM.

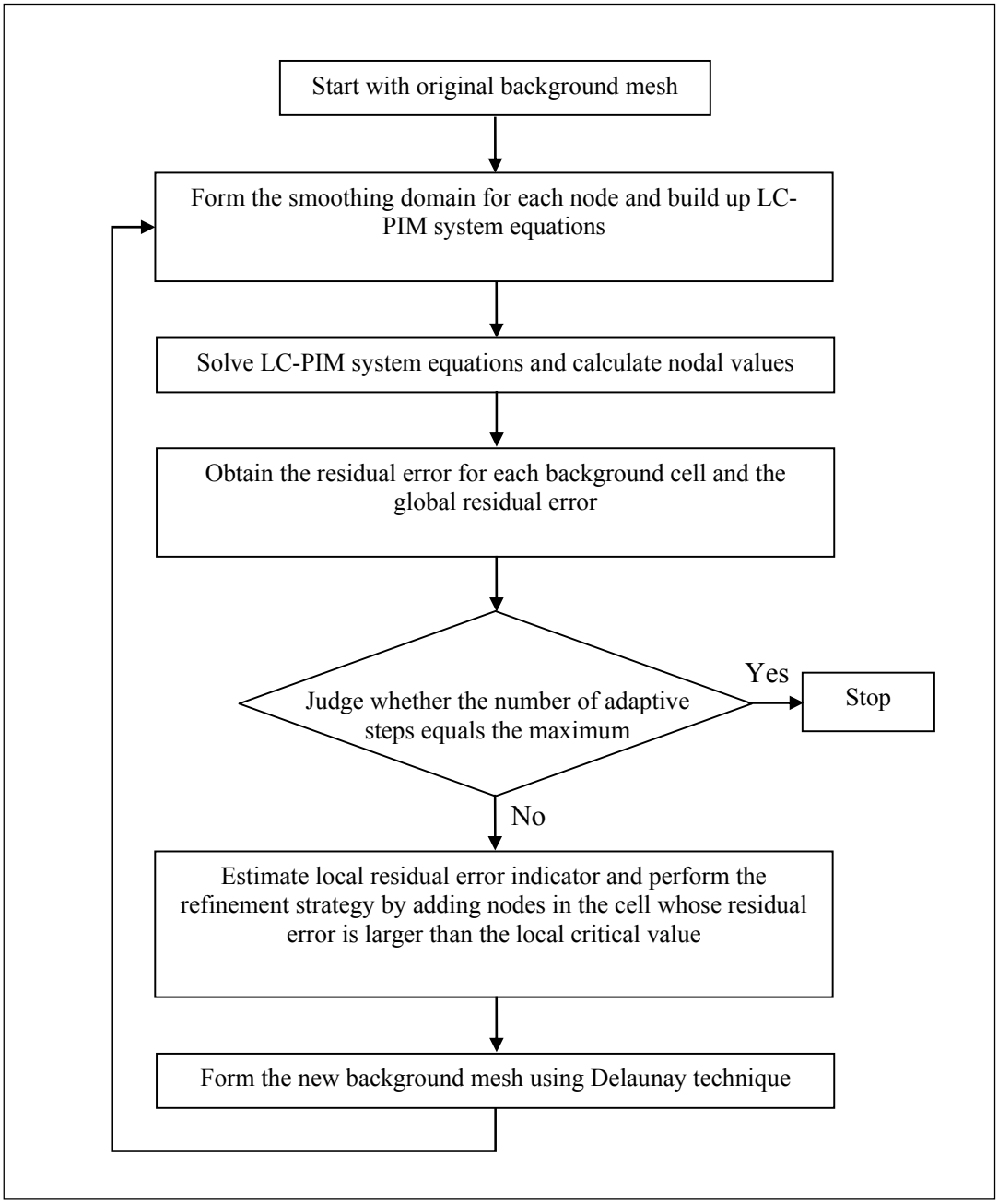

Figure 7.1 Illustration of the flow chart for the adaptive procedure using LC-PIM

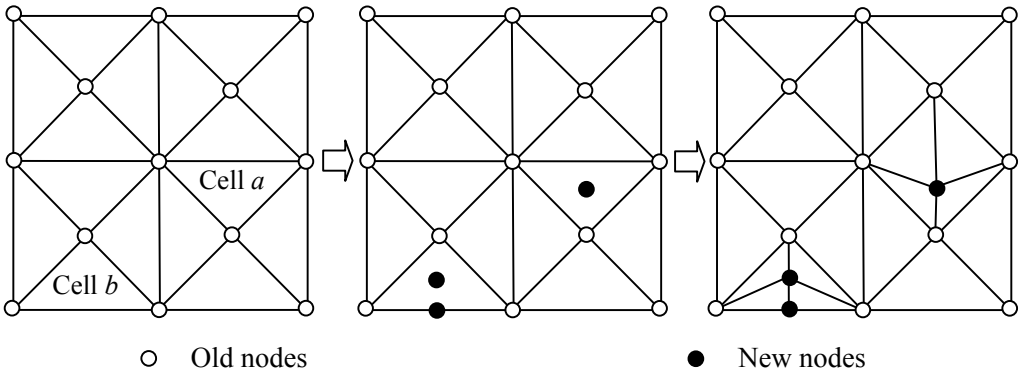

Figure 7.2 Illustration of refinement strategy

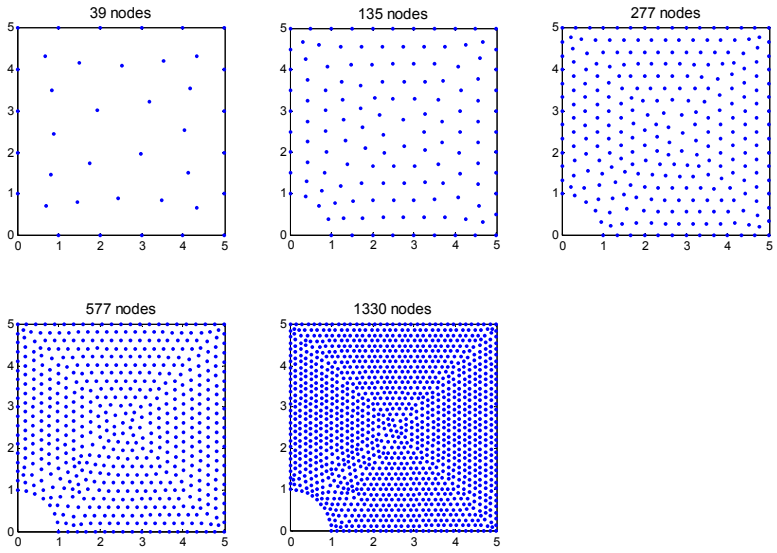

Figure 7.3 Sequence of uniformly refined models for the quarter model of the plate

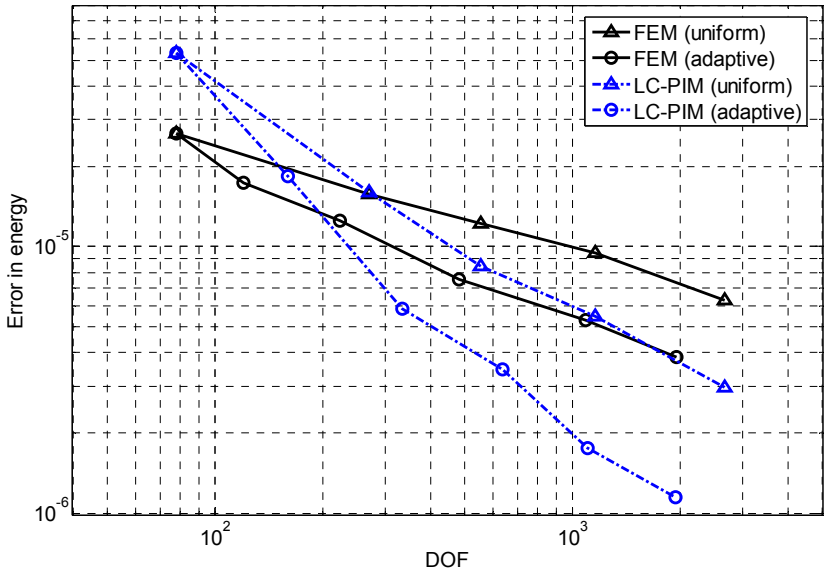

Figure 7.4 Comparison study of the convergence property by plotting the errors in energy against the DOF

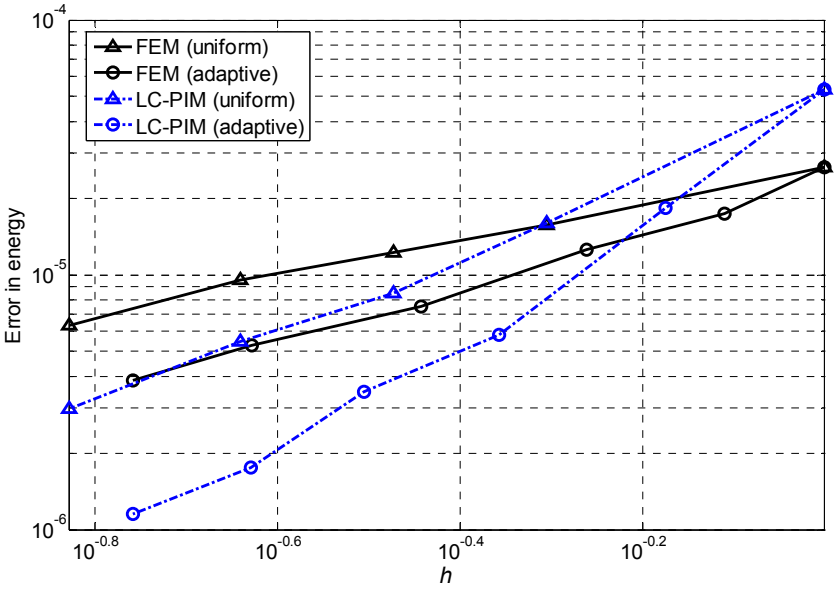

Figure 7.5 Comparison study of the convergence property by plotting the errors in energy against 'h'

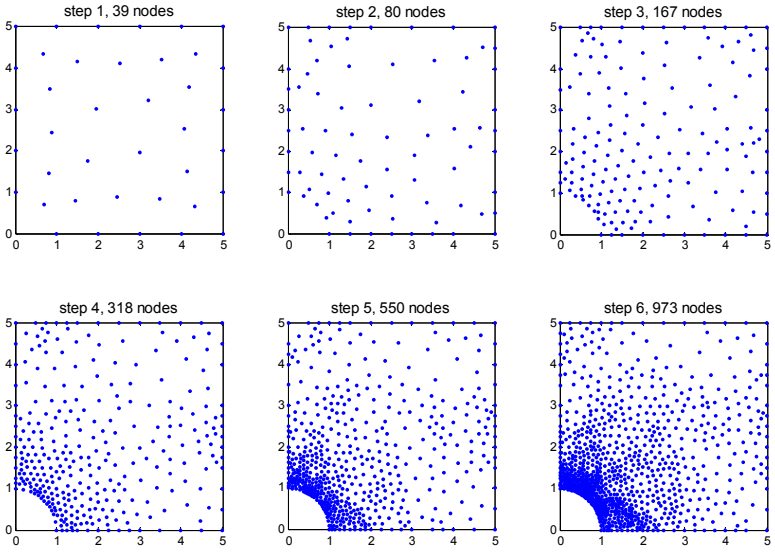

Figure 7.6 Sequence of adaptive refinement models for the quarter of the plate

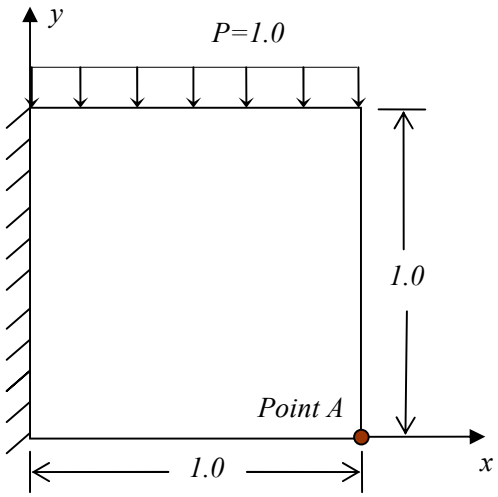

Figure 7.7 Short cantilever plate

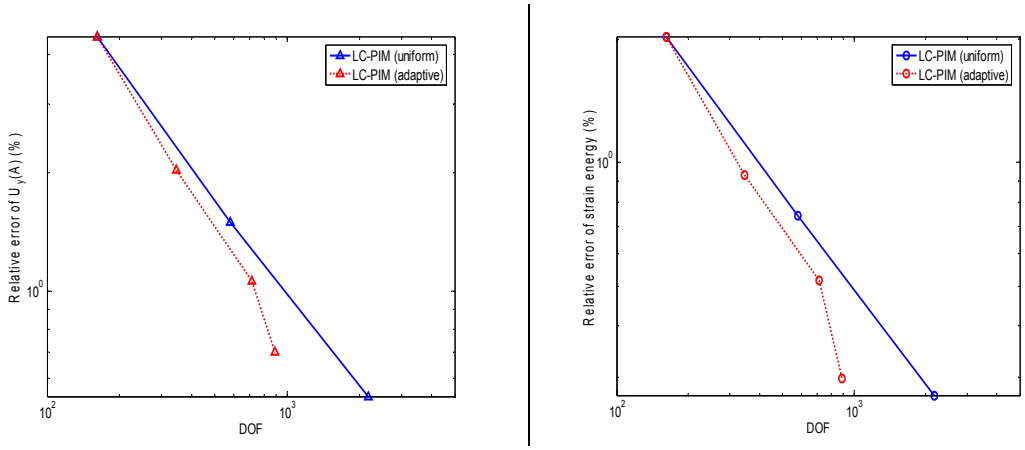

Figure 7.8 Comparison between uniform and adaptive models for the short cantilever plate

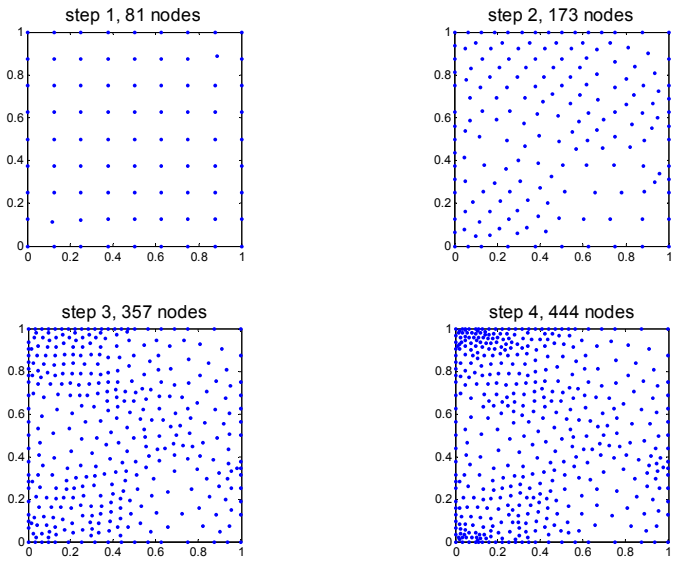

Figure 7.9 Sequence of adaptive refinement models for the short cantilever plate

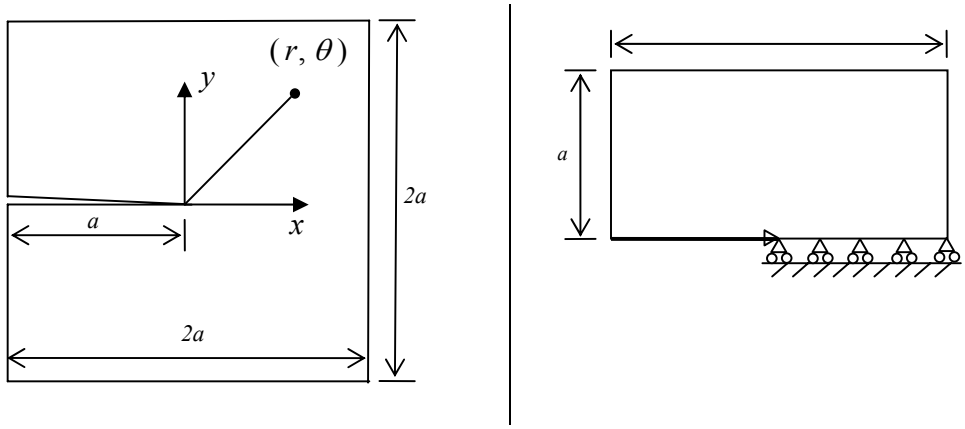

Figure 7.10 Geometry of the Mode-I crack problem and its half model

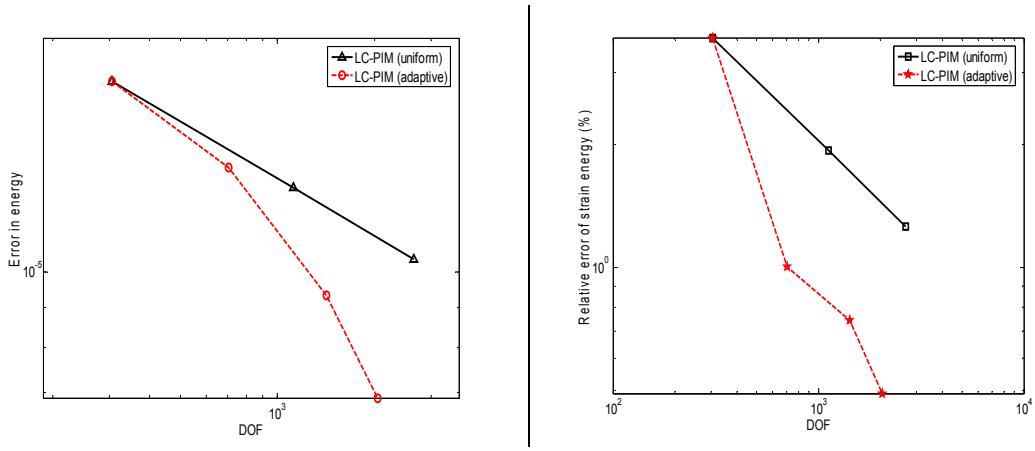

Figure 7.11 Comparison between uniform and adaptive models for the Mode-I crack problem

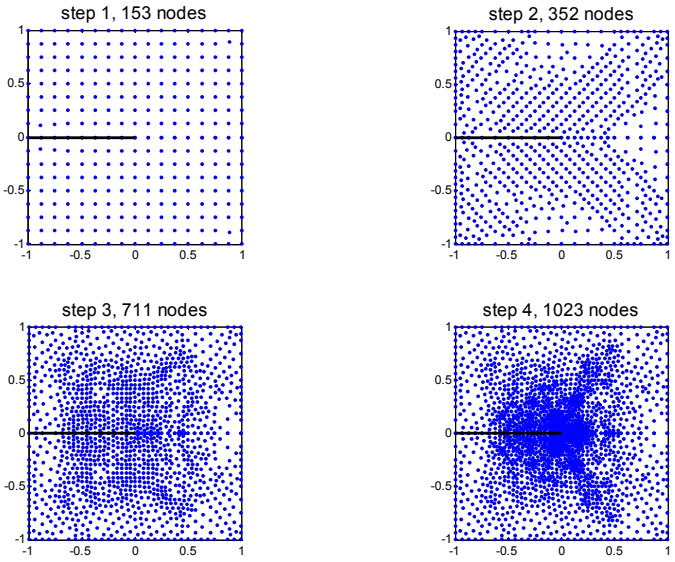

Figure 7.12 Sequence of adaptive refinement models for the Mode-I crack problem

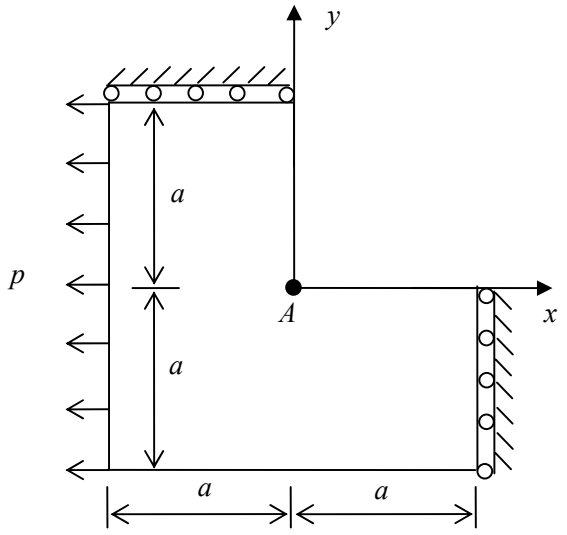

Figure 7.13 L-shaped plate subjected to uniform tensile stress

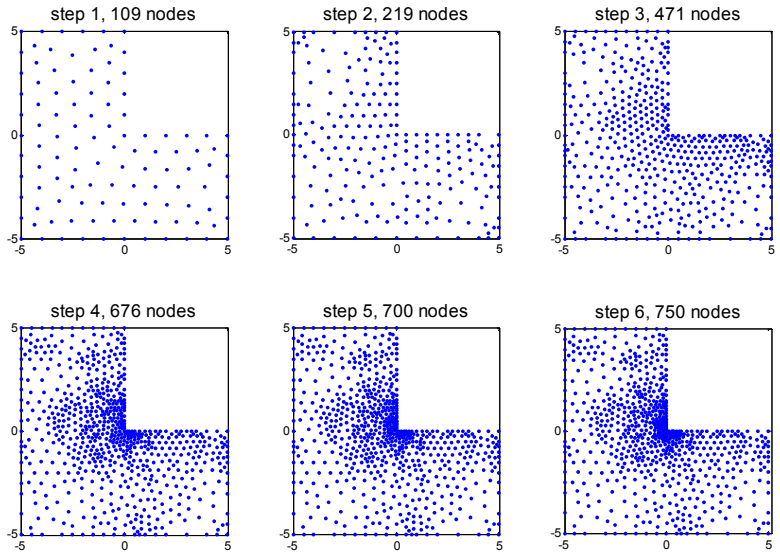

Figure 7.14 Sequence of adaptive refinement models for the L-shaped plate

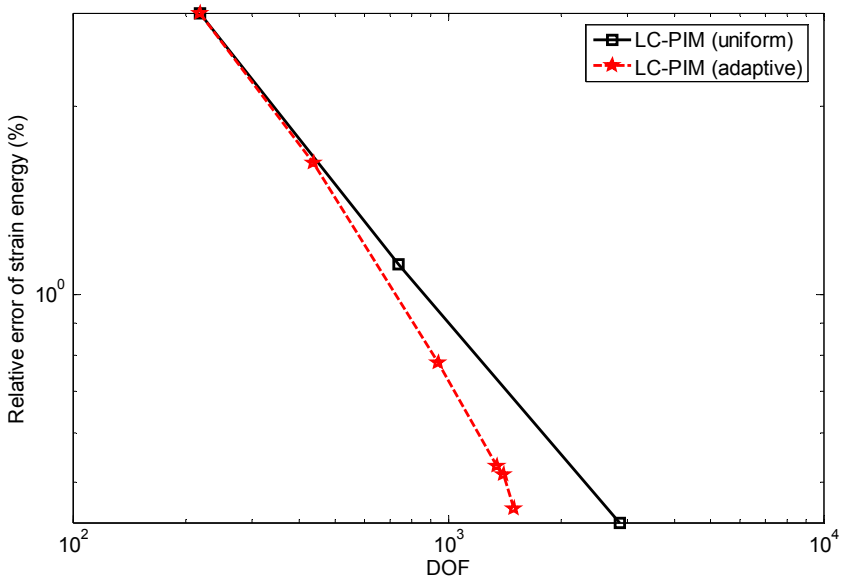

Figure 7.15 Comparison between uniform and adaptive models for the L-shaped plate

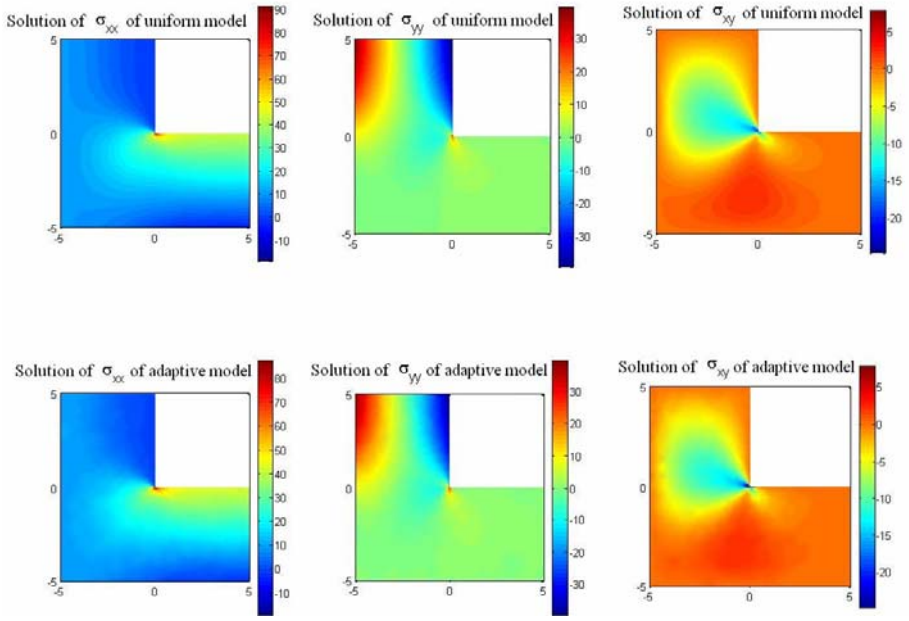

Figure 7.16 Comparison of stress distributions (the results are obtained by using FEM with uniform model of 13654 nodes and adaptive model of 750 nodes respectively)

Chapter 8

Conclusions and recommendations

8.1 Concluding remarks

This study has focused on the development of new meshfree methods and the application of these methods for three-dimensional problems and adaptive analysis. Through the studies, following conclusions are drawn:

1) The meshfree radial point interpolation method (RPIM) has been extended for three-dimensional problems. The RPIM shape functions constructed using RBF augmented with polynomial possess the Delta function property which allows the straightforward imposition of essential boundary conditions at nodes. The RPIM shape function can reproduce what is contained in the basis and has a good convergence. Via the study of the numerical examples, the following values are recommended for the shape parameters used in the MQ-RBF for 3D problems, i.e. $q = 1.03$ and $\alpha_c = 4$. Two models of the support domain have been presented and Model-2 performs better for most 3D problems especially when the geometry of the domain is complicated. For Model-1, $\alpha_s = 3.0$ is recommended; for Model-2, $20 \sim 70$ nodes in the local support domain are preferred. The numerical results show that the RPIM can obtain higher accuracy than the linear FEM and has a good performance for solving 3D elastic problems.

2) A nodal integration technique for the radial point interpolation method (NI-RPIM) has been proposed. The nodal integration scheme is based on Taylor's expansion. The expansion is applied to the entirety of $\mathbf{B}^{\mathrm{T}}\mathbf{D}\mathbf{B}$ and expanded up to second-order. In this case, third-order derivatives of shape functions are required for linear elasticity problems. The RPIM shape functions created using RBFs fit well to the requirement, as it is one-piecely differentiable to any order in the integration domain. The NI-RPIM can obtain very stable results. Effect of the parameters is investigated, and $q = 1.03$ and $\alpha_c = 4$ are recommended for the NI-RPIM. For the circular support domain, $\alpha_s = 2.5 \sim 3.5$ which includes 12 ~ 40 field nodes are suggested. Compared with the linear FEM, the NI-RPIM is more accurate and efficient for the problems studied; compared with the original RPIM using Gauss integration, the NI-RPIM can achieve higher convergence rate and better efficiency; compared with the NI-MLS, the NI-RPIM performs much better than the linear NI-MLS and shows similar performance as quadratic NI-MLS.

3) A linearly conforming point interpolation method (LC-PIM) has been developed. Polynomial PIM shape function used in the LC-PIM is obtained using linear interpolation as same as in the FEM using triangle element, which is very simple and easily to be performed. The PIM shape functions possess many properties (for example, the Kronecker delta function property) and most numerical techniques and treatments developed in the FEM can be utilized with minor modifications. A generalized Galerkin weak form is derived for the LC-PIM and a stabilized nodal integration scheme with strain smoothing operation is used for the numerical integration. The LC-PIM can guarantee linear exactness and monotonic convergence

in energy norm for the numerical solutions. The LC-PIM is proved to be variationally consistent. Furthermore, the LC-PIM has been found to possess the property of providing an upper bound on strain energy. A number of numerical examples have been studied and the properties mentioned above have been demonstrated numerically.

4) The linearly conforming point interpolation method (LC-PIM) has been extended for three-dimensional problems. The 3D LC-PIM also possesses the attractive properties as the 2D one, such as the Delta functions property for the PIM shape function and the linear exactness for the numerical solutions. Compared with the FEM using the linear tetrahedron element, the LC-PIM can achieve better accuracy and higher efficiency.

5) An adaptive analysis procedure using the linearly conforming point interpolation method (LC-PIM) has been proposed. An error indicator based on residual error together with a simple refinement scheme has been introduced. Some benchmark problems for adaptive analysis have been studied. The results show that the present adaptive procedure using the LC-PIM can accurately catch the appearance of the steep gradient of stresses and the occurrence of refinement will be concentrated properly. Compared to the results of uniformly refined models, the results of adaptive models converge much faster. All the results have demonstrated the validity and effectiveness of the adaptive procedure for the LC-PIM.

8.2 Recommendations for further work

Based on the work presented in the thesis, following aspects will be recommended for future and further research:

1) Many types of meshfree methods have been developed. These methods have provided us a number of numerical techniques and extended our minds for construction of numerical methods. It is promising to incorporate these ideas and techniques with the traditional numerical methods (such as FEM) and to develop more effective and robust numerical methods.

2) Further research work should be done on the linearly conforming point interpolation method (LC-PIM). The LC-PIM has shown very attractive properties for both 2D and 3D elasticity problems and has been applied in the adaptive analysis. One side, more work should be done to further study the theoretical aspects of the LC-PIM. The other side, the LC-PIM is expected to be applied for more types of problems to utilize its good properties.

3) Some new numerical methods have been proposed in this work and they have shown good properties for solving linear elasticity problems. It is desirable to extend these methods to deal with the nonlinear problems and coupling problems.

4) The development of meshfree methods for industrial application is expected to be done in the future. In this thesis, some numerical cases come from practical application have been studied and satisfying results have been obtained. However, there are still a lot of technical problems need to be solved before they become an efficient tool for practical analysis. In addition, a robust and efficient commercial software package should be developed.

References

Ainsworth M, Oden JT (1993), A unified approach to a posteriors error estimation using element residual methods. Numerische Mathematik, 65: 23-50.

Aluru NR (2000), A point collocation method based on reproducing kernel approximations. International Journal for Numerical Methods in Engineering, 47: 1083-1121.

Armando DC, Oden JT (1995), Hp clouds – a meshles method to solve boundary value problems. TICAM Report 95-05, University of Texas at Austin.

Atluri SN (2004), The meshless method (MLPG) for domain & BIE discretizations. Tech science press, USA.

Atluri SN, Cho JY, Kim HG (1999a), Analysis of thin beams, using the meshless local Petrov-Galerkin (MLPG) method, with generalized moving least squares interpolation. Computational Mechanics, 24: 334-347.

Atluri SN, Kim HG, Cho JY (1999b), A critical assessment of the truly meshless local Petrov-Galerkin (MLPG), and local boundary integral equation (LBIE) methods. Computational Mechanics, 24: 348-372.

Atluri SN, Sladek J, Sladek V, Zhu T (2000), Local boundary integral equation (LBIE) and it's meshless implementation for linear elasticity. Computational Mechanics, 25(2): 180-198.

Atluri SN, Zhu T (1998), A new meshless local Petrov-Galerkin (MLPG) approach in computational mechanics. Computational Mechanics, 22: 117-127.

Atluri SN, Zhu T (2000), The meshless local Petrov-Galerkin (MLPG) approach for solving problems in elasto-statics. Computational Mechanics, 25: 169-179.

Babuska I, Melenk JM (1997), The partition of unity method. International Journal for Numerical Methods in Engineering, 40(4): 727-758.

Babuska I, Rheinboldt C (1978), A-posteriori error estimates for the finite element method. International Journal for Numerical Methods in Engineering, 12: 1597-1615.

Bank RE, Weiser A (1985), Some a posteriori error estimators for elliptic partial differential equations. Mathematics of Computation, 44: 283-301.

Beissel S, Belytschko T (1996), Nodal integration of the element-free Galerkin method. Computer Methods in Applied Mechanics and Engineering, 139: 49-74.

Belytschko T, Krongauz Y, Organ D, Fleming M, Krysl P (1996a), Meshless methods: an overview and recent development. Computer Methods in Applied Mechanics and Engineering, 139: 3-47., 74: 111-126.

Belytschko T, Krongauz Y, Organ D, Liu WK (1996b), Smoothing and accelerated computations in the element free Galerkin method. Journal of Computational and Applied Mathematics, 74: 111-126.

Belytschko T, Krysl P, Krongauz Y (1997), A three-dimensional explicit element-free Galerkin method. International Journal for Numerical Methods in Fluids, 24(12): 1253-1270.

Belytschko T, Lu YY, Gu L (1994a), Element-free Galerkin methods. International Journal for Numerical Methods in Engineering, 37:229-256.

Belytschko T, Lu YY, Gu L (1994b), Fracture and crack growth by element-free Galerkin methods. Modeling and Simulation in Materials Science and Engineering, 2(3A): 519-534.

Belytschko T, Lu YY, Gu L (1995a), Crack propagation by element free Galerkin methods. Engineering Fracture Mechanics, 51: 295-315.

Belytschko T, Lu YY, Gu L (1995b), Element free Galerkin methods for static and dynamic fracture. International Journal of Solids and Structures, 32: 2547-2570.

Belytschko T, Organ D, Krongauz Y (1995c), Coupled finite element-element-free Galerkin method. Computational Mechanics, 17: 186-195.

Benz W (1988), Applications of smoothed particle hydrodynamics (SPH) to astrophysical problems. Computer Physics Communications, 48: 97-105.

Bonet J, Kulasegaram S (1999), Correcton and stabilization of smoothed particle hydrodynamics methods with applications in metal forming simulation. International Journal for Numerical Methods in Engineering, 47: 1189-1214.

Chati MK, Mukherjee S (2000), The boundary node method for three-dimensional problems in potential theory. International Journal for Numerical Methods in Engineering, 47: 1523-1547.

Chati MK, Mukherjee S, Mukherjee YX (1999), The boundary node method for three-dimensional linear elasticity. International Journal for Numerical Methods in Engineering, 46: 1163-1184.

Chen JS, Pan C, Wu CT (1997), Large deformation analysis of rubber based on a reproducing kernel particle method. Computational Mechanics, 19: 153-168.

Chen JS, Pan C, Wu CT, Liu WK (1996), Reproducing kernel particle methods for large deformation analysis of nonlinear structures. Computer Methods in Applied Mechanics and Engineering, 139: 195-227.

Chen JS, Roque C, Pan C, Button ST (1998), Analysis of metal forming process based on meshless method. Journal of Material Processing Techonology, 80-81: 642-646.

Chen JS, Wu CT, Yoon S, You Y (2001), A stabilized conforming nodal integration for Galerkin mesh-free methods. International Journal for Numerical Methods in Engineering, 50: 435-466.

Chen XL (2003), Meshfree techniques for plate structures. PhD thesis. National University of Singapore.

Cheng M, Liu GR (2002), A novel finite point method for flow simulation. Internationa Journal for Numerical Methods in Fluids, 39(12): 1161-1178.

Ching HK, Batra RC (2001), Determination of crack tip fields in linear elastostatics by the meshless local Petrov-Galerkin (MLPG) method. CMES-Computer Modeling in Engineering & Science, 2(2): 273-290.

Cho JY, Kim HG, Atluri SN (2001), Analysis of shear flexible beams, using the meshless local Petrov-Galerkin method based on locking-free formulation. Engineering Computations, 18(1/2): 215-240.

Chorin AJ (1973), Numerical study of slightly viscous flow. Journal of Fluid Mechanics, 57: 785-796.

Chung HJ, Belytschko T (1998), An error estimate in the EFG method. Computational Mechanics 21: 91-100.

Cingoski V, Miyamoto N, Yamashita H (1998), Element-free Gakerkin method for electromagnetic field computations. IEEE Transactions on Magnetics, 34(5), Part 1: 3236-3239.

Cleary PW (1998), Modeling confined multi-material heat and mass flows using SPH. Applied Mathematical Modeling, 22: 981-993.

Dai KY, Liu GR, Han X, Li Y (2006), Inelastic analysis of 2D solids using a weak-form RPIM based on deformation theory. Computer Methods in Applied Mechanics and Engineering, 195: 4179-4193.

Dai KY, Liu GR, Lim KM, Han X, Du SY (2004), A meshfree radial point interpolation method for analysis of functionally graded material (FGM) plates. Computational Mechanics, 34(3): 213-223.

De S, Bathe KJ (2000), The method of finite spheres. Computational Mechanics, 25: 329-345.

Debongnie JF, Zhong HG, Beckers P (1995), Dual analysis with general boundary conditions. Computer Methods in Applied Mechanics and Engineering, 122: 183-192.

Dolbow J, Belytschko T (1999), Numerical integration of the Galerkin weak from in meshfree methods. Computational Mechanics, 23: 219-230.

Duarte CA, Oden JT (1996), An hp adaptive method using clouds. Computer Methods in Applied Mechanics and Engineering, 139: 237-262.

Durate CA, Oden JT (1996), An H-p adaptive method using clouds. Computer Methods in Applied Mechanics and Engineering, 139: 237-262.

Ferziger JH, Peric M (1999), Computational methods for fluid dynamics. Springer, Berlin, Germany.

Gingold RA, Moraghan JJ (1977), Smooth particle hydrodynamics: theory and applications to non-spherical stars. Man. Not. Roy. Astron. Soc., 181: 375-389.

Girault V (1974), Theory of a GDM on irregular networks. SIAM J. Num. Anal., 11: 260-282.

Golberg MA, Chen CS, Bowman H (1999), Some recent results and proposals for the use of radial basis functions in the BEM. Engineering Analysis with Boundary Elements, 23: 285-296.

Gordon WJ, Wixom JA (1978), Shepard's method of 'Metric Interpolation' to bivariate and multivariate data. Mathematics of Computation, 32: 253-264.

Gratsch T, Bathe KJ (2005), A posteriori error estimation techniques in practical finite element analysis. Computers and Structures, 83: 235-265.

Gu YT, Liu GR (2001), A local point interpolation method for static and dynamic analysis of thin beams. Computer Methods in Applied Mechanics and Engineering, 190: 5515-5528.

Gu YT, Liu GR (2002), A boundary point interpolation method for stress analysis of solids. Computational Mechanics, 28: 47-54.

Gu YT, Liu GR (2003), A boundary radial point interpolation method (BRPIM) for 2-D structural analyses. Structural Engineering and Mechanics, 15(5): 535-550.

Gu YT, Liu GR (2005), A meshfree weak-strong (MWS) form method for time dependent problems. Computational Mechanics, 35: 134-145.

Hardy RL (1990), Theory and applications of multiquadrics-biharmonic method (20 years of discovery 1968-1988). Computers & Mathematics with Applications, 19: 163-208.

Hegen D (1996), Element-free Galerkin methods in combination with finite element approaches. Computer Methods in Applied Mechanics and Engineering, 135: 143-166.

Jun SA (1996), Meshless method for nonlinear solid mechanics. RIKEN Review, 14: 33-34.

Kee BBT, Liu GR, Zhang GY, Lu C (2007), A residual based error estimator using radial basis functions. Finite Elements in Analysis and Design, (submitted)

Kee Bernard BT, Liu GR, Lu C (2006), A regularized least-squares radial point collocation method (RLS-RPCM) for adaptive analysis. Computational Mechanics (in press).

Kothnur VS, Mukherjee S, Mukherjee YX (1999), Two-dimensional linear elasticity by the boundary node method. International Journal of Solids and Structures, 36: 1129-1147.

Krysl P, Belytschko T (1995), Analysis of thin plates by the element-free Galerkin method. Computational Mechanics, 17(1-2): 26-35.

Krysl P, Belytschko T (1996), Analysis of thin shells by the element-free Galerkin method. International Journal of Solids and Structrues, 33(20-22): 3057-3080.

Lancaster P, Salkauskas K (1981), Surfaces generated by moving least squares methods. Mathematics of Computation, 37: 141-158.

Lee CK, Zhou CE (2003), On error estimation and adaptive refinement for element free Galerkin method: part I: stress recovery and a posteriori error estimation. Computers & Structrues, 82(4-5): 413-428.

Lee CK, Zhou CE (2003), On error estimation and adaptive refinement for element free Galerkin method: part II: adaptive refinement. Computers & Structrues, 82(4-5): 429-443.

Li H, Wang QX, Lam KY (2004), A variation of local point interpolation method (vLPIM) for analysis of microelectromechanical systems (MEMS) device. Engineering Analysis with Boundary Elements, 28(10): 1261-1270.

Libersky LD, Petscheck AG (1991), Smoothed particle hydrodynamics with strength of materials. In H. Trease, J. Fritts and W. Crowley eds., Proceeding of The Next Free Lagrange Conference, Springer-Verlag, NY, 395: 248-257.

Libersky LD, Randles PW, Carney TC (1995), SPH calculations of fragmentation. Proceedings of 3rd US Congress on Computational Mechanics, Dallas, TX.

Lin H, Atluri SN (2000), Analysis of incompressible Navier-Stokes flows by the meshless MLPG method. CMES-Computer Modeling in Engineering & Science, 2(2): 117-142.

Liszka T, Orkisz J (1980), The finite difference methods at arbitrary irregular grids and its applications in applied mechanics. Computers & Structures, 11: 83-95.

Liu GR (2002), A point assembly method for stress analysis for solid. International Journal of Solids and Structures, 39: 261-276.

Liu GR (2002), Meshfree methods: Moving Beyond the Finite Element Method. CRC press, Boca Baton, USA

Liu GR, Chen XL (2001), A mesh-free method for static and free vibration analyses of thin plates of complicated shape. Journal of Sound and Vibration, 241(5): 839-855.

Liu GR, Dai KY, Lim KM, Gu YT (2002a), A point interpolation mesh free method for static and frequency analysis of two-dimensional piezoelectric structures. Computational Mechanics, 29(6): 510-519.

Liu GR, Dai KY, Lim KM, Gu, YT (2003), A radial point interpolation method for simulation of two-dimensional piezoelectric structures. Smart Materials and Structures, 12: 171-180.

Liu GR, Dai KY, Nguyen TT (2007a), A smoothed finite element method for mechanics problems. Computational Mechanics, 39: 859-877.

Liu GR, Gu YT (1999), A point interpolation method. In Porc. 4th Asia-Pacific Conference on Computational Mechanics, December, Singapore, 1009-1014.

Liu GR, Gu YT (2001a), A point interpolation method for two-dimensional solids. International Journal for Numerical Methods in Engineering, 50: 937-951.

Liu GR, Gu YT (2001b), A local point interpolation method for stress analysis of two-dimensional solids. Structural Engineering and Mechanics, 11(2): 221-236.

Liu GR, Gu YT (2001c), A local radial point interpolation method (LR-PIM) for free vibration analyses of 2-D solids. Journal of Sound and Vibration, 246(1): 29-46.

Liu GR, Gu YT (2002), Comparisons of two meshfree local point interpolation methods for structural analyses. Computational Mechanics, 29: 107-121.

Liu GR, Gu YT (2003a), A matrix triangularization algorithm for point interpolation method. Computer Methods in Applied Mechanics and Engineering, 192(19): 2269-2295.

Liu GR, Gu YT (2003b), A meshfree method: Meshfree Weak-Strong (MWS) form method, for 2-D solids. Computational Mechanics, 33(1): 2-14.

Liu GR, Gu YT (2004), Assessment and applications of point interpolation methods for computational mechanics. International Journal for Numerical Methods in Engineering, 59: 1373-1397.

Liu GR, Gu YT (2005), An Introduction to Meshfree Methods and Their Programming. Springer, Dordrecht, The Netherlands.

Liu GR, Gu YT, Tu ZH, Huang XM, Wang JG, Wu YG (2002), MFree2D. http://www.nus.edu.sg/ACES.

Liu GR, Kee Bernard BT (2006), A stabilized least-squares radial point collocation method (LS-RPCM) for adaptive analysis, Computer Method in Applied Mechanics and Engineering, (in press).

Liu GR, Li Y, Dai KY, Luan MT, Xue W (2006b), A linearly conforming RPIM for 2D solid mechanics. International Journal of Computational Methods, 3(4): 401-428.

Liu GR, Liu MB (2003), Smoothed Particle hydrodynamics-A meshfree particle method. World Scientific, Singapore.

Liu GR, Nguyen TT, Dai KY, Lam KY (2007b), Theoretical aspects of the smoothed finite element method (SFEM). International Journal for Numerical Methods in Engineering, 71: 902-930.

Liu GR, Quek SS (2003), The finite element method: a practical course. Butterworth Heinemann: Oxford.

Liu GR, Tu ZH (2001), MFree2D: an adaptive stress analysis package based on mesh-free technology. First MIT Conference on Computational Fluid and Solid Mechanics, June, MIT, 327-329.

Liu GR, Tu ZH (2002), An adaptive procedure based on background cells for meshless methods. Computer Methods in Applied Mechanics and Engineering, 191: 1923-1943.

Liu GR, Wu YL (2002), Application of local radial point interpolation method (LRPIM) to impressible flow simulation. International Journal for Numerical Methods in Fluids, (submitted)

Liu GR, Wu YL, Ding H (2004), Meshfree Weak-Strong (MWS) form method and its application to incompressible flow problems. International Journal for Numerical Methods in Fluids, 46: 1025-1047.

Liu GR, Yan L, Wang JG, Gu YT (2002b), Point interpolation method based on local residual formulation using radial basis functions. Structural Engineering and Mechanics, 14(6): 713-732.

Liu GR, Yang KY (1998), A penalty method for enforce essential boundary conditions in element free Galerkin method. In Proc. Of the 3rd HPC Asia'98, Singapore: 715-721.

Liu GR, Zhang GY (2007), Upper bound solution to elasticity problems: a unique property of the linearly conforming point interpolation method (LC-PIM). International Journal for Numerical Methods in Engineering, (acceped).

Liu GR, Zhang GY, Dai KY, Wang YY, Zhong ZH, Li GY, Han X (2005a), A linearly conforming point interpolation method (LC-PIM) for 2D solid mechanics problems. International Journal of Computational Methods, 2(4): 645-665.

Liu GR, Zhang GY, Gu YT, Wang YY (2005b), A meshfree radial point interpolation method (RPIM) for three-dimensional solids. Computational Mechanics, 36(6):421-430.

Liu GR, Zhang GY, Wang YY, Zhong ZH, Li GY, Han X (2006a), A nodal integration technique for meshfree radial point interpolation method (NI-RPIM). International Journal of Solids and Structures, 44: 3840-3860.

Liu L, Tan VBC (2002), A meshfree method for dynamics analysis of thin shells. Advances in Meshfree and X-FEM methods (Liu GR ed.): 90-95.

Liu MB, Liu GR, Zong Z, Lam KY (2003), Smoothed particle hydrodynamics for numerical simulation of underwater explosions. Computational Mechanics, 30(2): 106-118.

Liu WK, Chen Y, Jun S, Chen JS, Belytschko T, Pan C, Uras RA, Chang CT, (1996), Overview and applicatons of the reproducing kernel particle methods. Arvhives of Computational Methods in Engineering State of the Art Review, 3: 3-80.

Liu WK, Jun S (1998), Multiple scale reproducing kerkel particle method for large deformation problems. International Journal for Numerical Methods in Engineering, 141: 1339-1679.

Liu WK, Jun S, Sihling DT, Chen Y, Hao W (1997b), Multiresolution reproducing kernel particle method for computational fluid dynamics. International Journal for Numerical Methods in Fluids, 24(12): 1391-1415.

Liu WK, Jun S, Zhang YF (1995), Reproducing kernel particle methods. International Journal for Numerical Methods in Engineering, 20: 1081-1106.

Liu WK, Li SF, Belytschko T (1997a), Moving least-square reproducing kernel methods .1. Methodology and convergence. Computer Methods in Applied Mechanics and Engineering 143(1-2): 113-154.

Liu WK, Ong JS, Uras RA (1985), Finite element stabilization matrices-a unification approach. Computer Methods in Applied Mechanics and Engineering, 53: 13-46.

Lu YY, Belytschko T, Tabbara M (1994), A new implementation of the Element Free Galerkin method. Computer Methods in Applied Mechanics and Engineering, 113: 397-414.

Lu YY, Belytschko T, Tabbara M (1995), Element-free Galerkin method for wave propagation and dynamic fracture. Computer Methods in Applied Mechanics and Engineering, 126: 131-153.

Lucy L (1977), A numerical approach to testing the fission hypothesis. The Astronomical Journal, 82: 1013-1024.

Mclain DH (1974), Drawing contours from arbitrary data points. Comput. J., 17: 318-324.

Melenk JM, Babuska I (1996), The partition of unity finite element method: basic theory and applications. Computer Methods in Applied Mechanics and Engineering, 139: 289-314.

Monaghan JJ (1982), Why particle methods work. SIAM Journal on Scientific and Statistical Computing, 3(4): 422-433.

Monaghan JJ (1992), Smoothed particle hydrodynamics. Annual Review of Astronomy and Astrophysics, 30: 543-574.

Monaghan JJ (1995), Simulating gravity currents with SPH lock gates. Applied Natgenatucs Reports and Preprints, Monash University.

Monaghan JJ, Lattanzio JC (1985), A refined particle method for astrophysical problems. Astronomy and Srtophsics, 149: 135-143.

Morris JP (1996), A study of the stability properties of smoothed particle hydrodynamics. Publications Astronomical Society of Australia, 13(1): 97-102.

Mukherjee YX, Mukherjee S (1997), Boundary node method for potential problems. International Journal for Numerical Methods in Engineering, 40: 797-815.

Nagashima Y (1999), Node-by-node meshless approach and its applications to structural analysis. International Journal for Numerical Methods in Engineering, 46: 341-385.

Nayroles B, Touzot G, Villon P (1992), Generalizing the finite element method: diffuse approximation and diffuse elements. Computational Mechanics, 10: 307-318.

Oliveira Eduardo R De Arantes E (1968), Theoretical foundations of the finite element method. International Journal of Solids and Structures, 4: 929-952.

Onate E, Idelsohn S, Zienkiewicz OZ, Taylor RL (1996), A finite point method in computational mechanics. Applications to convective transport and fluid flow. International Journal for Numerical Methods in Engineering, 39: 3839-3867.

Pavlin V, Perrone N (1975), Finite difference energy techniques for arbitrary meshes. Computational Structure, 5: 45-58.

Perrone N, Liebowitz H, Mulville D, Plikey W (1978). Fracture mechanics. Charlottesville: University Press of Virginia.

Pian THHH, Wu CC (2006), Hybrid and Incompatible finite element methods. CRC Press: Boca Raton.

Powell MJD (1922), The theory of radial basis function approximation in 1990. Advances in Numerical Analysis, Eds. FW. Light, 303-322.

Randles PW, Libersky LD (1996), Smoothed Particle Hydrodynamics some recent improvements and applications. Computer Methods in Applied Mechanics and Engineering, 138: 375-408.

Schaback R (1994), Approximation fo polynomials by radial basis functions. Laurent PJ, Mehaute Le, Schumaker LL (Eds) Wavelets, images and surface fitting, Wellesley, MA: 459-466.

Simo JC, Hughes TJR (1998), Computational Inelasticity. Springer-Verlag: New York.

Steeb H, Maute A, Ramm E (2002). Goal-oriented error estimation in solid mechanics. In: Error-controlled adaptive finite elements in solid mechanics, 211-261. John Wiley & Sons Ltd, West Sussex, England.

Swegle JW, Hicks DL, Attaway SW (1995), Smoothed particle hydrodynamics stability analysis. Journal of Computational Physics, 116: 123-134.

Sze KY, Chen JS, Sheng N, Liu XH (2004), Stabilized conforming nodal integration: exactness and variational justification. Finite Elements in Analysis and Design, 41: 147-171.

Timoshenko SP, Goodier JN (1970), Theory of Elasticity (3rd edition). McGraw-hill, New York.

Uras RA, Chang CT, Chen Y, Liu WK (1997), Multiresolution reproducing kernel particle method in acoustics. Journal of Computational Acoustics, 5: 71-94.

Verfurth R (1989), A posteriori error estimators for the stokes equations. Numerische Mathematik, 55: 309-325.

Wang JG, Liu GR (2000), Radial point interpolation method for elastoplastic problems, In Porc. 1st International Conference on Structural Stability and Dynamics, December 7-9, Taipei, Taiwan: 703-708.

Wang JG, Liu GR (2002a), A point interpolation meshless method based on radial basis functions. International Journal for Numerical Methods in Engineering, 54: 1623-1648.

Wang JG, Liu GR (2002b), On the optimal shape parameters of radial basis functions used for 2-D meshless methods. Computer Methods in Applied Mechanics and Engineering, 191: 2611-2630.

Wang JG, Liu GR, Lin P (2002), Numerical analysis of Biot's consolidation process by radial point interpolation method. International Journal of Solids and Structures, 39(6): 1557-1573.

Wang JG, Liu GR, Wu YG (2001), A point interpolation method for simulating dissipation process of consolidation. Computer Methods in Applied Mechanics and Engineering, 190(45): 5907-5922.

Wang JG, Liu GR, Wu YG (2001), A point interpolation method for simulating dissipation process of consolidation. Computer Methods in Applied Mechanics and Engineering, 190(45): 5907-5922.

Wang JG, Liu, GR (2000), Radial point interpolation method for elastoplastic problems. International Conference on Structural Stability and Dynamics, December 7-9, Taipei, Taiwan, 703-708.

Wendland H (1998), Error estimates for interpolation by compactly supported radial basis functions of minimal degree. Journal of Approximation Theory, 93: 258-396.

Wu YL, Liu GR (2003), A meshfree formulation of local radial point interpolation method (LRPIM) for incompressible flow simulation. Computational Mechanics, 30(5-6): 355-365.

Xiao JR, Mccarthy MA (2003a), A local Heaviside weighted meshless method for two-dimensinal solids using radial basis functions. Computational Mechanics, 31(3-4): 301-315.

Yang KY (1999), Development of meshfree techniques for stress analysis. National University of Singapore, Thesis of M. Eng.

You Y, Chen JS, Lu H (2003), Filters, reproducing kernel, and adaptive meshfree method. Computational Mechanics, 31(3-4):P 316-326.

Yvonnet J, Coffignal G, Ryckelynck D, Lorong PH, Chinesta F (2006), A simple error indicator for meshfree methods based on natural neighbors. Computers and Structures, 84: 1301-1312.

Zhang GY, Liu GR, Kee Bernard BT, Wang YY (2006a), An adaptive analysis procedure using the linearly conforming point interpolation method (LC-PIM). International Journal of Solids and Structrues, (revised).

Zhang GY, Liu GR, Wang YY, Huang HT, Zhong ZH, Li GY, Han X (2006b), A linearly conforming point interpolation method (LC-PIM) for three-dimensional elasticity problems. International Journal for Numerical Methods in Engineering, (accepted).

Zhang X, Song KZ, Lu MW, Liu X (2000), Meshless methods based on collocation with radial basis functions. Computational Mechanics, 26(4): 333-343.

Zhu T, Atluri SN (1998), A modified collocation & a penalty formulation for enforcing the essential boundary conditions in the element free Galerkin method. Computational Mechanics, 21: 211-222.

Zhu T, Zhang JD, Atluri SN (1998a), Local boundary integral equation (LBIE) method in computational mechanics, and a meshless discretization approach. Computational Mechanics, 21(3): 223-235.

Zhu T, Zhang JD, Atluri SN (1998b), Meshless local boundary integral equation (LBIE) method for solving nonlinear problems. Computational Mechanics, 22(2): 174-186.

Zhu T, Zhang JD, Atluri SN (1999), A meshless numerical method based on the local boundary integral equation (LBIE) to solve linear and non-linear boundary value problems. Engineering Analysis with Boundary Elements, 23(5-6): 375-389.

Zienkiewicz OC, Taylor RL (2000), The finite element method (5^{th} edition). Butterworth Heinemann, Oxford, UK.

Zienkiewicz OC, Zhu JZ (1987), A simple error estimator and adaptive procedure for practical engineering analysis. International Journal for Numerical Methods in Engineering, 24: 337-357.

Publications arising from thesis

1. Liu GR, **Zhang GY**, Gu YT, Wang YY (2005), A meshfree radial point interpolation method (RPIM) for three-dimensional solids. *Computational Mechanics,* 36(6):421-430.

2. Liu GR, **Zhang GY**, Dai KY, Wang YY, Zhong ZH, Li GY, Han X (2005), A linearly conforming point interpolation method (LC-PIM) for 2D solid mechanics problems. *International Journal of Computational Methods,* 2(4): 645-665.

3. Liu GR, **Zhang GY**, Wang YY, Zhong ZH, Li GY, Han X (2006), A nodal integration technique for meshfree radial point interpolation method (NI-RPIM). *International Journal of Solids and Structures*, 44: 3840-3860.

4. **Zhang GY**, Liu GR, Wang YY, Huang HT, Zhong ZH, Li GY, Han X (2006), A linearly conforming point interpolation method (LC-PIM) for three-dimensional elasticity problems. *International Journal for Numerical Methods in Engineering,* (accepted).

5. **Zhang GY**, Liu GR, Kee Bernard BT, Wang YY (2006), An adaptive analysis procedure using the linearly conforming point interpolation method (LC-PIM). *International Journal of Solids and Structures,* (revised).

6. Liu GR, **Zhang GY** (2007), Upper bound solution to elasticity problems: a unique property of the linearly conforming point interpolation method (LC-PIM). *International Journal for Numerical Methods in Engineering,* (accepted).

7. Kee BBT, Liu GR, **Zhang GY**, Lu C (2007), A residual based error estimator using radial basis functions. *Finite Elements in Analysis and Design,* (submitted)